Climate, topography and erosion in the Nepal Himalayas

Cristoff Andermann

N° d'ordre : 4379

ANNÉE 2011

UNIVERSITÉ DE RENNES 1

TECHNISCHE UNIVERSITÄT BERGAKADEMIE FREIBERG

THÈSE / UNIVERSITÉ DE RENNES 1
sous le sceau de l'Université Européenne de Bretagne

En Cotutelle Internationale avec
TU Bergakademie Freiberg, Allemagne

pour le grade de

DOCTEUR DE L'UNIVERSITÉ DE RENNES 1

Mention: Sciences fe la Terre

Ecole doctorale Sciences de la Matière Rennes

présentée par

Christoff ANDERMANN

préparée à l'unité de recherche UMR6118
Geosciences Rennes
Université de Rennes 1

Climate, topography and erosion in the Nepal Himalayas

Thèse soutenue à Rennes le 19.10.2011

devant le jury composé de :

Jérôme LAVE
D.R. CNRS, CRPG – Nancy, France / *rapporteur*

Bodo BOOKHAGEN
Ass. Prof. UC Santa Barbar, USA / *rapporteur*

Philippe DAVY
D.R. CNRS, Universite de Rennes 1 / *examinateur*

Lothar RATSCHBACHER
Prof. TU Bergakademie Freiberg, Allemagne / *examinateur*

Stéphane BONNET
MC HDR (Prof.), Universite de Rennes 1 / *directeur de thèse*

Richard GLOAGUEN
Ass. Prof. TU Bergakademie Freiberg, Allemagne / *directeur de thèse*

Preface

My PhD thesis is constructed around four topics of research, of which one is already published, one is in review, a third close to be submitted and a fourth in preparation. I have chosen to present this work in form of research articles, because I feel the diverse subjects are easier to read, when presented in a compact way accompanied with their associated introduction and methods. However, I like to excuse some possible redundancy, caused by the need to introduce each article again in full. Although, I present this work and all the results as my work, I have to acknowledge the contributions of my co-authors. Without their contribution this work would not have been possible.

Abstract

Erosion processes in large mountain belts are controlled by tectonic uplift and the spatial distribution of topography and precipitation. The aim of this work is to understand more in detail the influence of precipitation on erosion in the Nepal Himalayas. Here, the Indian Summer Monsoon defines a very clear cyclic seasonality, with two well separated and long-lasting seasons, one very wet and one very dry. I will investigate here: 1) the evaluation of precipitation datasets, 2) the transfer of precipitation to river discharge, 3) the mobilization and transport of material from the analysis of a unique suspended sediment dataset, and 4) the determination of millennial time-scale erosion rates using comsogenic isotopes.

1) High-quality precipitation observations with good spatio-temporal coverage are needed to investigate the possible impact of precipitation on erosion. I evaluate five gridded precipitation data sets and show that the APHRODITE dataset, derived from gauge data interpolation performs best in the Himalayas.

2) The transfer of precipitation into rivers involves temporary water storage in different reservoirs, where different residence times influence the hydrological cycle. I observe an annual anticlockwise precipitation-discharge hysteresis loop, revealing more river discharge than precipitation during the falling limp of the monsoon season. This implies the temporal storage of water in a fractured basement aquifers, whose storage capacity is $\sim 28\ km^3$ at the scale of Nepal.

3) I present a new suspended sediment data compilation, with daily resolution for the major rivers in the Nepal Himalayas. I show that suspended sediment concentrations vary through the seasons describing an annual clockwise hysteresis effect. This hysteresis effect disappears when comparing suspended sediment fluxes directly with direct storm discharge, revealing a linear relationship. All river basins show the same erosion behavior when data are normalized by drainage area and mean sediment flux,. Erosion rates calculated from a new rating model, based on direct discharge, range between 0.1 and 5.9 mm/yr. The rivers in the Nepal Himalayas are supply limited and the hillsopes as contributing source are transport limited. This results provide some new insights on erosion mechanisms in the Himalayas.

4) I present mean catchment erosion rates, calculated from in-situ produced ^{10}Be cosmogenic isotope concentration. The calculated erosion rates range between 0.2 and 4.4 mm/yr within five large streams in Nepal and several tributary catchments. I show an unreported systematic difference be-

tween tributary and main streams erosion rates, suggesting that the system is not in an equilibrium state. However, this effect could be also due to bias in the calculation of the erosion rates.

Acknowledgement

Over the three years of my PhD thesis at Geosciences Rennes, France, and the TU Bergakademie Freiberg, Germany, I have met many interesting and challenging people who all have contributed in one way or the other to the success of this work. Thanks are due to all of them. These three years have been just perfect, I have learned a tremendous amount and felt home.

I would like to start acknowledging my two supervisors Stephane Bonnet and Richard Gloaguen, first for your confidence and support, and secondly for the freedom you gave me to develop my own research and interests. Thank you Richard and Stephane, you have been a perfect team.

Furthermore, I would like to thank Alain Crave for accompanying me on the field in Nepal and for all the challenging discussions on hydrology and transport of sediments, Laurent Longuevergne who contributed to some interesting and highly "pertinent" aspects of my work, and Philippe Davy not only for supporting me financially at the end of my PhD but also for challenging my work. I have to say thanks to Silke Merchel for teaching me in cosmogenic nuclide sample preparation and the good time I had whenever I showed up in Dresden with some more samples to prepare. Thanks also to Regis Braucher, Didier Bourles and Vincent Godard for analyzing my samples and your help to turn the results into denudation rates.

The three years would have been only half the fun without all the friends in Rennes. Just to name few persons who have been directly involved in my work: Delphine and Laure who were perfect office mates during the first year and especially Delphine who taught me quite a bit of my Matlab scripting skills. Thank you Etienne, Pietro and Romain to take me into your office when I found myself on the corridor and thank you for the good discussions and help. Thanks also to Martine Bouhnik-Le Coz for your help in the lab, Jean-Jacques Kermarec for the technical support and Dimitri Lague for discussions. Marc Jolivet, Kerry Gallagher and Guillaume Dupont-Nivet for corrections on parts of the manuscript. Finally, I have to thank Eline for her final checks and of course for giving me a very good reason to come to Rennes.

On the Freiberg side, I have been maybe less often present and many conversations had to be via Skype and chat, nevertheless their contribution is of no less importance. Mathias who helped with handling the precipitation datasets and being with me in the field, Faisal for the online Matlab help and providing TecDEM. Eric and Malte for the exchange on data processing and them asking me to clean and explain my scripts did have definitely some positive feedback. I would like to thank Alex

for discussions and her introduction to the mineral separation lab. I also have to thank Storchi and Ina, Paul and Nadja as well as Claude-Alexander and Olaf to not let me sleep on the street during my visits to Freiberg. Finally I have to thank the Namaste Nepal S-GMbH, namely Stefen Judersleben for exciting me to go to Nepal in the first place.

I would like to thank Bodo Bookhagen for our discussions and his readiness to share his data with me, Jerome Lave for his help whenever I had some questions on Nepal and especially for collecting some sand samples for me. I also have to thank Maarten Lupker for our discussions and exchange on results.

I have to thank all friends and colleagues from Nepal who always helped to support me on my field visits. In particular, Keshav Sharma from the Department of Hydrology and Meteorology Nepal who explained me Himalayan hydrology and gave me access to data. Isabelle Providolli from ICIMOD for allowing me kindly to use their facilities, helping me to get the PARDYP data and supporting me on my visits to the PARDYP watersheds. Same thanks have to go to Madhav Dakhal who accompanied me whenever he got some time and who put me in contact with the PARDYP partners. Roshan M. Bajrachary form the Kathmandu University was always ready to discuss with me as well as signing letters of support to ship my samples to Europe. Bikram Sthapit from the Bhotekoshi Power Company for sending always the newest data on suspended sediment loads. I would like the thank Bishar and Devraj, both for being such good helpers in the field. Thank you Shivendra and Rajani for always welcoming me in Kathmandu and all the good time we had together. Thanks also to Sanam *Raj* for your help and interest.

Last but not leased I have to thank all the organizations who contributed financially to my PhD thesis. Especially I have to thank the German exchange service DAAD for providing me a three year scholarship to carry out my PhD in Rennes. I have to thank the French-German University DFH/UFA in Saarbrücken to support my binational PhD with a three year travel grant. I have to thank the supporters *Freunde und Förderer* of the TU Bergakademie Freiberg as well as the *Region de Bretagne* for providing conference travel support.

Contents

List of Figures

List of Tables

Chapter 1

Introduction

1.1 Erosion in mountain belts

Mountain evolution depends on the rather complex interplay between tectonics, climate and erosion [*Willett*, 1999; *Molnar*, 2003; *Reiners et al.*, 2003; *Whipple*, 2009], (Fig. 1.1). Tectonics set the initial condition lifting material upwards [*Molnar*, 2003] and erosion acts as the destructive counterpart, thinning the orogen by removing material [*Whipple*, 2009] and shaping landscape [*Molnar*, 2003]. Climate is highly influenced by mountains [*Roe*, 2003] and might have a first order control on erosion [*Reiners et al.*, 2003]. Erosion in return exerts a direct influence on tectonic [*Whipple*, 2009; *Willett*, 1999]. The interaction of these three processes results in the topographic expression of mountain relief [e.g. *Bonnet and Crave*, 2003; *Grujic et al.*, 2006]. However, until today this is a rather hypothetical conceptual picture, based on a manifold of empirical, experimental and numerical studies [*Whipple*, 2009], which still have to be tested in detail, and the question of how these forces are connected remains still to be understood.

Knowledge on mountain building processes has numerous implications in fundamental geological sciences as well as in applied engineering. The east-west orientation of the Himalayan range forms an orographic barrier, potentially controlling the global monsoon circulation [*Boos and Kuang*, 2010]. Weathering of silicate rocks and erosion processes are a major CO_2 sink controlling largely the global carbon budget and thus climate [*Raymo and Ruddiman*, 1992; *France-lanord and Derry*, 1997; *Galy et al.*, 2007]. Even plate motion might be influenced by erosion-precipitation interaction at the plate margins [*Iaffaldano et al.*, 2011]. Mountain relief has furthermore implicit impact on catastrophic events, land degradation and floods. High mountains also host glaciers and are therefore important freshwater reservoirs [*Immerzeel et al.*, 2010].

In the following two chapters, I will discuss the state of the art research of the three fundamental processes with focus on erosion and climate in large mountain belts. Starting from continental scale over mountain ranges to detailed regional studies.

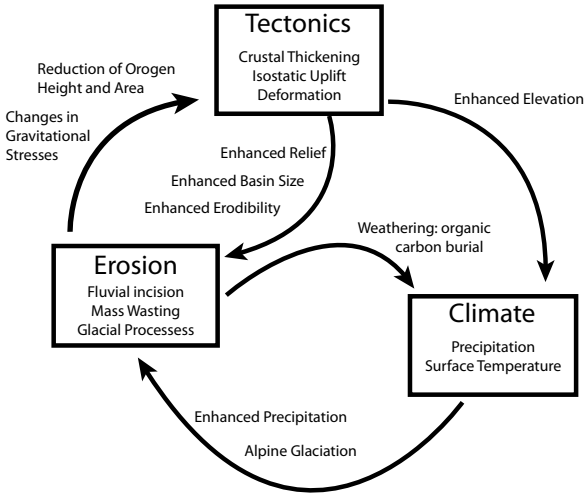

Figure 1.1: *Feedback loop illustration of the three fundamental Earth Surface Processes process in earth surface processes; erosion, climate and tectonics. [from Willett et al., 2006]*

1.2 General context

Tectonic - climate - erosion interactions

Relating continental scale erosion[I] and deposition with tectonic activity and climate through geological time, provides information on the process of landscape evolution [*Schumer and Jerolmack*, 2009]. The debate of how precipitation controls erosion and consequently the tectonic activities, is a long lasting debate [e.g. *Molnar*, 2003; *Whipple*, 2009]. Over the last twenty years this field of research gained more attention in Earth sciences, motivated by the new suggestion of [*Molnar and England*, 1990] that climate change has exerted a strong control on the Cenozoic change in surface processes. The increased supply of terrigenous sediments into oceans during the late Cenozoic (Fig. 1.2) has triggered a controversial debate about the role of tectonic, erosion and climate change in the evolution of the Earth [e.g. *Hays et al.*, 1976; *Molnar and England*, 1990; *Derry and France-Lanord*, 1996; *Molnar*, 2004; *Clift et al.*, 2008a; *Willenbring and von Blanckenburg*, 2010]. Analysis of sedimentary cores from large ocean basins revealed that over the last ~ 5 *Myr* sediment supply to the ocean basins has increased dramatically [e.g. *Molnar and England*, 1990]. The increased sedimentation rates coincide with decreasing global atmospheric CO_2 concentration (Fig. 1.2) and consequently with atmospheric cooling. Earlier, *Hays et al.* [1976] have interpreted it as a evidence of a global intensification of tectonic activity, accompanied by increasing relief energy and hence, high erosion rates and CO_2 consumption due silicate weathering. Later, *Molnar and England* [1990] questioned this evidence and interpreted the high sediment influxes in the

[I]Erosion integrates all involved processes that remove mass from Earth and make it transportable. It can be seen as a natural intrinsic process forming landscape. Erosion includes mechanical/chemical weathering and dissolution. Denudation refers only to a mass or volume removed (by erosion). Denudation can be directly measured as a length or a volume removed over time.

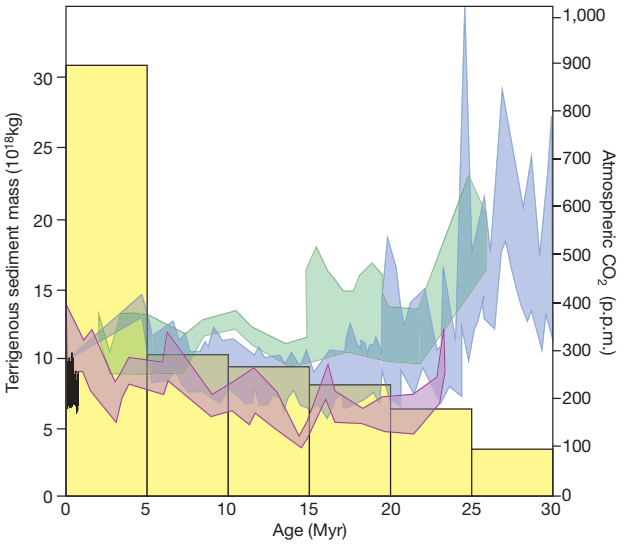

Figure 1.2: *Cenozoic terringenous sediment supply to the oceans (yellow bars, binned in 5 Myr time steps) and atmospheric CO_2 concentration determined from different markers (purple: planktonic foraminifera, green: C_3 plants, blue: alkenones, and black: ice cores) [from Willenbring and von Blanckenburg, 2010]*

light of climate change and isostatic rebound of continental crust, causing flexural surface uplift[II]. In this sense, increased erosion rates are the result of a stormier climate and of large scale glaciation due to low temperatures rather than the consequence of high relief [*Molnar*, 2004]. The argument that plant fossils, which are indicators of warmer climates are found at high elevation, do provides evidence for the Cenozoic accelerated uplift can be as well explained by climate change [*Molnar and England*, 1990]. For example the plant fossils are not necessarily brought to their current elevation by uplift, it could well be that climate has just simply changed. In contrast, recent work by *Willenbring and von Blanckenburg* [2010] question the evidence of increased sediment input. Their arguments is that $^{10}Be/^{9}Be$ ratios in seawater bearing sediments do not show any increase in chemical weathering and the apparent increased sedimentation rate might well be only an observational biased side effect. Indeed, estimating sedimentation volumes from point observations of drilling cores is tricky and many processes, such as consumption by subduction, compaction by overburden and remobilization have to be corrected [*Sadler*, 1999; *Molnar*, 2004; *Schumer and Jerolmack*, 2009; *Willenbring and von Blanckenburg*, 2010]. However, *Willenbring and von Blanckenburg* [2010] make the basic assumption that weathering rates and physical erosion rates are straightforward linked, which might not be true in a rapidly

[II]When talking about uplift one has to distinguish between three different processes: (1) Surface uplift is the change of mean elevation with respect to the geoid. (2) Rock uplift is the vertical displacement of individual rocks (units) with respect to the geoid and (3) exhumation is the vertical movement of rocks with respect to the surface. Thus, surface uplift equals rock uplift minus exhumation [*Molnar and England*, 1990].

evolving mountain belt such as the Himalayas or in Taiwan. For example *Summerfield and Hulton* [1994] show that the contribution of chemical weathering rates to the total denudation rate varies considerably between different settings. Furthermore, the consumption of large quantities of CO_2 can thoroughly take place in form of organic detritus burial, and does not necessarily need to involve silicate weathering [*Galy and France-Lanord*, 2001]. From a global point of view, the interpretation of fundamental processes is highly controversial and limits our understanding on the evolution of climate and large mountain belts.

Depending on the local tectonic settings and the climatic condition, relief and mountain structure might develop completely differently. Many efforts have been done in applying experimental and numerical models, together with empirical evaluations, in order to understand the involved processes. Erosion is a crucial process linking climate and tectonics and acts like a transmitter of the signals.

Erosion unloads the crust and shapes landscape at the same time. As a results of decreasing burden the crust reacts by rebounding in a flexural manner, and thus lifting the surface. *Schaffer et al.* [1998] have demonstrated this conceptual reactions in the Laramide mountain range, in the western United States. They related mountain summit erosion with valley erosion, which is roughly one magnitude faster. Therefore, relief increases simply as a function of relative erosion rates. But at the same time, erosion removes mass from the region and due to isostatic response landscape elevation increases. This concept describes how erosion alters landscape, both relief and elevation, without any active tectonic and climatic forcing *Schaffer et al.* [1998].

In compressional and active orogens such as the Himalayas, Taiwan, Southern Alps of New Zealand or the European Alps, the interplay of the involved surface processes is more complex. In this areas, very high erosion rates coincide with high uplift rates, which might be influenced by precipitation distribution or vice versa [*Willett*, 1999; *Whipple*, 2009]. In a widely recognized coupled deformation-erosion model, *Willett* [1999] has studied crustal deformation and strain localisation under the impact of surface processes (climate and erosion) that perturb topography (Fig. 1.3 a and b). His numerical experiments demonstrate how precipitation can focus tectonic activity at continental plate margins by enhanced erosion activity. As illustrated in Figure 1.3, the exhumation front is oriented towards the main moisture arrival. If the leeward side of the system coincides with the fixed overriding plate of the model, exhumation appears to be more localised (Fig. 1.3 a). If moisture arrives from the side of the subducting plate (Fig. 1.3 b), the exhumation front is broadened.

Based on the earlier work of *Royden* [e.g. 1996], *Beaumont et al.* [2001] proposed a highly debated model for the Himalayan - Tibetan Plateau system in central Asia (Fig. 1.4). The authors propose a thermo-mechanical model explaining the exhumation of the Himalayan range driven by erosion. In this model, intensive monsoon precipitation at the subduction front causes extensive denudation. Due to high erosion rates, hot and low-viscose rocks surface from an inter-crustal layer, or are literally drawn from under the plateau, building the High Himalayan peaks. This positive feedback has been termed as channel flow [*Bird*, 1991]. In the case of the Himalayas, the erosion induced channel flow is capable

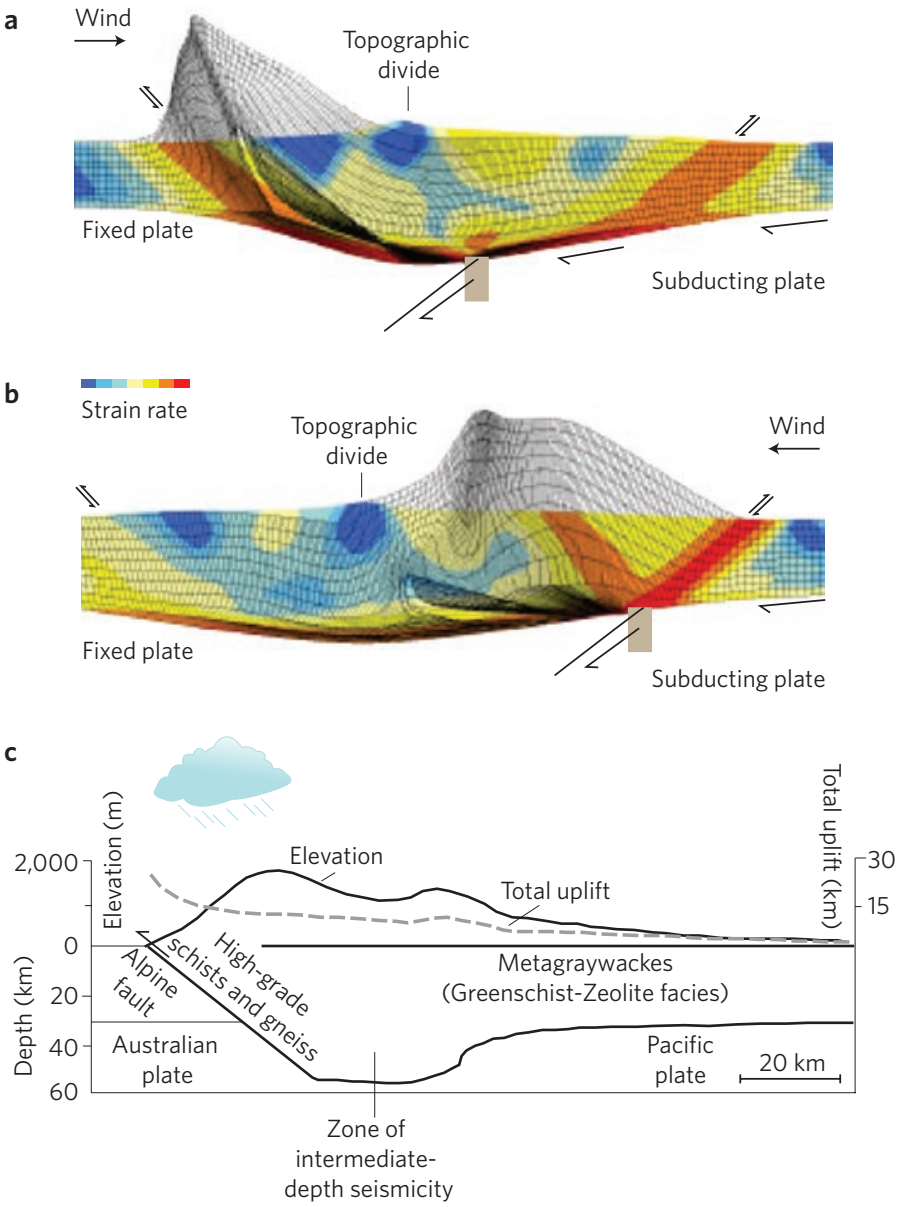

Figure 1.3: *Interplay between tectonics, erosion and climate demonstrated by the numerical model of Willett [1999]. The model describes how crustal deformation and strain rate (color coding) evolves in response to unidirectional moisture flux on the examples of the Southern Alps of New Zealand. Grey colored zone illustrates the exhumed material which has been eroded during the numeric run. a) If major moisture transport arrives from the west, exhumation is forced to the west of the topographic divide. Exhumation is focused on the active thrust fault. b) In the case of moisture-laden air arriving from the east, both exhumation and uplift are focused to the east of the topographic divide. The thrust fault in the east becomes nearly inactive. c) Illustration of observed topographic and tectonic structure [from Koons, 1990], matching the numerical experiment. Note that in the experiment (a) exhumation is much more localized than in experiment (b) [from Whipple, 2009].*

of explaining many observed features (e.g. rapid exhumation, dome intrusion). However, their model lacks real field evidence [*Harrison*, 2006; *Whipple*, 2009]. Nevertheless, the model presents a possible connection of how climate might drive erosion and hence, tectonic movements, within active mountain ranges and high plateau construction. In particular the question, if localized monsoon precipitation can maintain sufficient high erosion rates along the mountain front, that a channel flow model demands, remains to be evaluated [*Harrison*, 2006]. Indeed, *Burbank et al.* [2003] contest that climate and erosion in the Himalayas are linked and propose that tectonic rock uplift is controlling erosion.

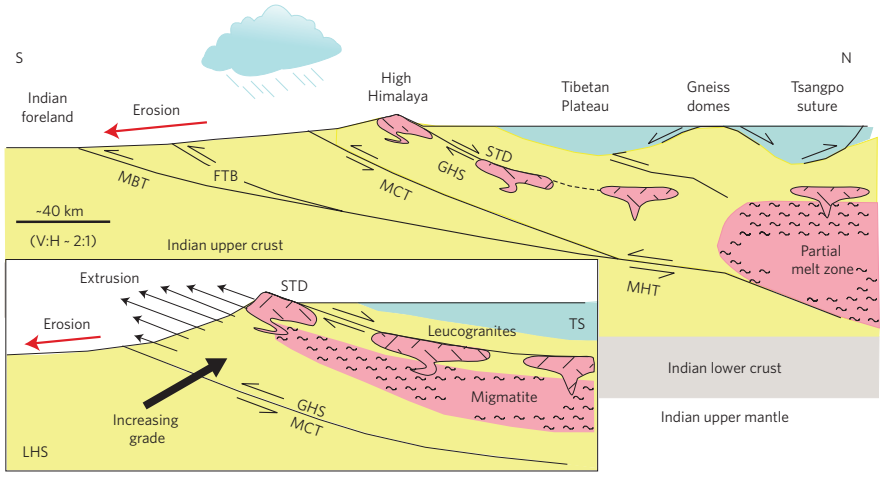

Figure 1.4: *Schema of the erosion driven Himalayan channel flow model, as proposed by Beaumont et al. [2001], 2:1 vertical exaggerated. In this model, highly ductile and hot crustal material (pink) is extracted along the main structural system by erosional forcing. This is illustrated in the unscaled inset. Abbreviation are: Main Boundary Thrust MBT, Fold Thrust Belt FTB, Main Himalayan Thrust MHT, Main Central Thrust MCT, South Tibetan Detachment STD, Lesser Himalayan Sequence LHS, Great Himalayan Sequence GHS an Tethyan Sequence TS [from Whipple, 2009]*

Precipitation seams to exert a strong influence on erosion [e.g. *Reiners et al.*, 2003]. However, geochronological measurements and field observations struggle to proof the link between tectonic exhumation and precipitation. *Reiners et al.* [2003] demonstrate that in the Washington Cascades, modern precipitation distribution fits well with spatial pattern of erosion. Their Apatite (U-Th)/He model erosion rates are highest where precipitation is highest, and decrease to the west and east in a similar fashion as mean annual rainfall. However, it is not clear if the differential exhumation rate is an expression of simple isostasy or some other mechanical response. *Dadson et al.* [2003] report that long-term erosion patterns for the Taiwan orogen are linked to localized tectonic deformation. They find that short term erosion events correlate well with seismic activity and typhoon precipitation. However this, is less surprising since these kind of events only trigger erosion in already destabilized locations, such as over-steepened mountain terrain. I will discuss this more in detail later. In the NW Himalayas,

Thiede et al. [2004] demonstrated using Apatite fission track dating that precipitation (present day) and exhumation rates are linked. But in their second more complete study [*Thiede et al.*, 2009] the authors contradict their earlier observations and find only poor spatial correlation between exhumation and precipitation. Though, the most resent findings [*Deeken et al.*, 2011] for the same region, incorporating the previous results [*Thiede et al.*, 2004, 2009], suggest a dynamic coupling between tectonics and surface processes. These different findings in the same region, based on basically the same kind of measurements, highlights the converse problematic of interpretation. Although, these previous examples are field observations, they can not provide information on the physics of the erosion processes, but are only interpret measurements in this context. Eventually, the supposed coupling might only be coincidence, given the different time scales the data represents. In any case, it is clear that the acting processes have to be explored more in detail.

In summary, the fundamental question of what is controlling shape and speed of mountain building on a continental and orogene scale is still highly debated and current state of the art research can not really clarify the "chicken or egg" [*Molnar and England*, 1990] question. It is probably undeniable that climate-erosion-and tectonic are connected. So far, the knowledge on the involved feedback processes is merely hypothetical. Real measurements and field observations of these processes, both short-term and long-term, are needed to quantify the existing models. In particular the assumption that erosion efficiency increases with precipitation has not yet been demonstrated [*Whipple*, 2009]. Therefore, the role of water has to be further investigated [*Molnar*, 2003].

1.3 Controls on erosion rates and patterns

Erosion is the displacement of rock, soils and minerals to a different position by loosing potential energy. It can take place by physical and/or chemical processes and involves often a transport media such as water and/or wind. The process of erosion depends mainly on local settings, such as physiography of the terrain, lithology and the availability of the transport media. Additionally, life can catalyse erosion processes considerably. For example, chemical weathering might be strongly influenced by the presence of bacteria, which can accelerate dissolution processes. However, in this thesis I will mainly focus on erosion processes by physical erosion. Chemical weathering and dissolution may be important [*Galy and France-Lanord*, 2001] but in most case they are a minor fraction [*Summerfield and Hulton*, 1994].

1.3.1 Erosion measurements

Measuring erosion, notable denudation, is one of the fundamental disciplines in geomorphology. In this paragraph, I will give a principle overview of three techniques to determine erosion fluxes from direct field measurements and analysis of field samples: 1) Erosion rates from measurements of sediment fluxes in rivers, 2) erosion rates from cosmogenic nuclide analysis, and 3) erosion rates from

low-temperature thermochronology (fission tracks and (U-Th)/He) analysis. Strictly speaking, rates from low-temperature thermochronology are cooling ages, but under certain assumptions, erosion rates can be calculated (will be explained below). Each method is representative of a different time scale, from very recent ($\lesssim 10^2$ years), over intermediate ($10^3 - 10^5$ years), to long time (typical longer than 10^5 years), respectively.

Erosion rates from sediment fluxes

All the eroded material in a drainage basin is normally transported by rivers until it reaches its final sink [e.g. *Ahnert*, 1970]. Thus, if significant internal storage and/or transport by wind can be neglected, it is possible to estimate present-day erosion rates of the whole contributing area by measuring the mass of eroded material transported in the river. Material can be transported in three different ways: 1) As bedload, creeping and saltation of material along the river bed, 2) in suspension within the water column of the river and 3) in chemical dissolved form. In order to estimate the complete mass flux leaving the basin, each parameter has to be measured separately, which is in many cases difficult or impossible. Bedload is not constant over time and varies depending on local conditions, such as river bed inclination, velocity and the upstream settings [*Turowski*, 2010]. In particular in large rivers, this fraction is difficult to measure for instrumental reasons. Suspended sediment flux is normally measured as the depth integrated mean concentration. However, sediment concentration is not homogeneously distributed over the river cross section, tampering the results. Dissolved load can be measured from a water sample by classical element analysis. The proportional contribution of dissolved load to the total flux varies considerably between regional settings [e.g. *Summerfield and Hulton*, 1994].

The large disadvantage of this methodology is the considerable effort of labour and time, since measurements have to be conducted continuously in order to obtain a reliable estimation. Secondly, sampling intervals might not always be representative and in particular bedload is not always measurable. However, measuring sediment fluxes provides high temporal information on the erosion processes. Single events can be for example related to precipitation events, earthquakes or human impact *Dadson et al.* [2003]; *Fuller et al.* [2003]; *Morehead* [2003]. Typically these kind of measurements are available for > 30 years, however, in most remote areas they are almost inexistent.

Sediments are deposited in lowlands, lakes or man made structures (e.g. water reservoirs or retaining dams). If these kind of traps are monitored, large-scale erosion rates can be estimated from the simple volumetric storage variation. For example *Dadson et al.* [2003] and *Wulf et al.* [2010] have used sedimentation volumes to calibrate and correct their suspended measurements for bedload contribution and to validate their results. The dissolved load however, can not be estimated from sediment reservoirs, as it stays normally in dissolution.

Erosion rates from cosmogenic nuclide analysis

Erosion fluxes representative for longer time scales ($10^3 - 10^5$ years) can be derived from the analysis of cosmogenic nuclides, produced from cosmic rays in mineral grains [e.g. *Bierman and Steig*, 1996; *Granger et al.*, 1996; *von Blanckenburg*, 2005]. This methodology integrates erosion over the time span that it takes to remove approximately one attenuation length of the cosmic rays, ~ 60 *cm* in bedrock [*Granger et al.*, 1996]. The concentration of cosmogenic nuclides in river sands is inversely proportional to the mean catchment denudation rate [e.g. *Bierman and Steig*, 1996]. The production of cosmogenic nuclides depends on the location, elevation and latitude and has to be incorporated in the production rate calculation [*Stone*, 2000]. The crux of this method is the basic underlying assumption that the studied basin is in an isotopic steady state, in-going production equals the out-going flux, which is not always valid in areas where glacial and masswasting processes are dominant [e.g. *Binnie et al.*, 2006]. Glaciers and landslides can provide considerable volumes of juvenile material and thus bias the calculated erosion rates [*Heimsath and McGlynn*, 2008; *Yanites et al.*, 2009]. Nevertheless, the method provides a powerful tool to quantify mean catchments erosion rates and has closed the temporal gap between short term measurements and those representative of millions of years [*Kirchner et al.*, 2001].

With respect to fluvial sediment analysis, this methodology does not allow to compare erosion rates on the event-scale. However, it integrates the erosion processes long enough to study the influence of large-scale patterns of landscape, i.e. tectonic and precipitationn, which is difficult to study on shorter time-scales.

Erosion (cooling) rates from low-temperature thermochronology

Low-temperature thermochronology, namely fission track and $(U-Th)/He$ analysis, is a useful tool to quantify the cooling history of rocks as they pass through the upper few kilometers of the Earth crust [e.g. *Wagner and Reimer*, 1972; *Mancktelow*, 1997; *Farley*, 2002; *Ehlers and Farley*, 2003]. As rocks move closer to the surface, as a result of tectonic uplift or erosion, they pass through the isotherms, from high temperatures to lower ones. This cooling history is preserved by mineral closure ages, based on the principle that each mineral and method has its particular closing temperature [*Mancktelow*, 1997]. If the age of closure of the mineral and the geothermal gradient are known, it is possible to calculate the time it took for the particular rock sample to reach the surface. Strictly, these are exhumation rates rather than erosion rates. To turn exhumation rates into erosion rates, either topographic/elevation steady state has to be assumed (during the exhumation history) or the relative surface elevation change, with respect to the isotherm, must be know [e.g. *Brandon et al.*, 1998; *Ehlers and Farley*, 2003]. The limitation of this method is that the geothermal gradient has to be extrapolated back in time in order to model the cooling pathway of the samples. Furthermore, topography, heat advection (vertical and transversal) and also water circulation have the potential to locally adulterate the thermal gradient, leading to relative misinterpretation of the results [e.g. *Ehlers and Farley*, 2003; *Whipp and Ehlers*, 2007].

Despite the possible uncertainties, low-temperature thermochronology provides a powerful tool to estimate tectonic uplift, exhumation and denudation rates for very long time spans (Myr) and thus, to reconstruct the long term evolution of landscapes [e.g. *Jolivet et al.*, 2010].

1.3.2 Temporal scale: Modern vs. long term erosion

Comparing erosion processes derived from measurements representative of different time scales, one has to take into account the recurrence interval of events and their impact on the evolution of landscapes. Large events, triggered by rainstorms or earthquakes can dominate erosion patterns according to their frequency of occurrence. For example the 2008 Wenchuan earthquake (M_w 7.9), in the eastern margin of the Tibetan Plateau produced $5 - 15\ km^3$ of erodible material by extensive landsliding [*Parker et al.*, 2011]. In this case the mobilized material is larger than the net volume added to the orogen by coseismic uplift. Taking this as an extreme example, one single event can offset the measured signal considerably. Dating techniques representative for long time scales, e.g. fission track ages, have a high probability to include such single events, while, dating techniques representative for shorter time scales probably do not integrate such a extreme event [*Kirchner et al.*, 2001]. Consequently, erosion rates determined from different dating techniques can differ quite considerably (Fig. 1.5). This conceptual idea holds of course only if the extreme events are large enough to control significantly the long term mean erosion rate. In other words, the extreme events must outweigh the erosion in volume representative for interim times. Secondly, timing of the measurement has to be taken into account, for example the temporal spacing of the events and the timing of sampling with respect to the last event.

On the other hand, measurements integrating over long time scales are difficult to separate into the different involved processes. Therefore, short-term erosion proxies, such as suspended sediment concentration provide more detailed information on the erosion processes. Single storm events can be directly compared, for example to the transported volumes of rivers. Hence, single storm events reveal information on the efficiency of the event-magnitude. Though, the modern erosion rates might not be representative for the long-term evolution of a mountain range. In order to understand the link between the involved processes both short-term and long-term measurements are needed to understand the system.

1.3.3 Erosion and landscape

Numerous studies are conducted to find characteristic controls, such as topography, precipitation, drainage density, vegetation and basin size, which might help to describe erosional processes [e.g. *Ahnert*, 1970; *Milliman and Syvitski*, 1992; *Summerfield and Hulton*, 1994; *Montgomery et al.*, 2001; *Aalto et al.*, 2006]. Such simplified relations have been often applied to model and predict erosional systems on a catchment scale [e.g. *Tucker and Slingerland*, 1997; *Syvitski*, 1998; *Finlayson et al.*, 2002; *Kettner and Syvitski*, 2008]. But the relations of erosion rates with few parameters is often not straightforward.

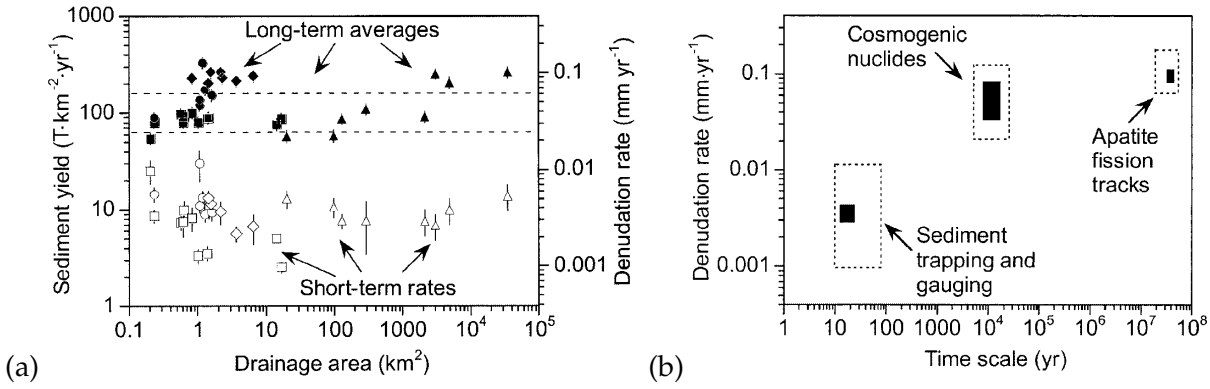

Figure 1.5: *Denudation rates over different time scales, from several catchments in central Idaho (United States). (a) Denudation rates plotted against basin size, spanning several magnitudes. Short-term erosion rates are derived from suspended sediment measurements and long-term erosion rates are derived from ^{10}Be cosmogenic nuclide concentrations. Note, that sample locations for both suspended sediments and cosmogenic nuclides are identical. (b) Denudation rates plotted against representative time scale. Suspended sediments average over several decades, cosmogenic nuclide concentrations average over several thousand years (in this kind of settings) and denudation rates from apatite fission track ages average over some million years. These denudation rates are representative for a mountain region which is tectonically inactive and heavily farmed [from Kirchner et al., 2001]*

Globally, denudation rates are negatively correlated with basin size (Fig. 1.6 d)[III] , being highest in small catchments and decrease with basin size [*Milliman and Syvitski*, 1992; *Aalto et al.*, 2006]. However, this relationship was deduced from suspended sediment concentrations and represents the increasing chance to find a less pronounced relief and intra-basin accommodation space, where sediments can be deposited.

Furthermore, denudation rates estimated from suspended sediment loads show correlations with relief, channel gradient and elevation [*Ahnert*, 1970; *Pinet and Souriau*, 1988; *Summerfield and Hulton*, 1994; *Montgomery and Brandon*, 2002; *von Blanckenburg*, 2005; *Binnie et al.*, 2007; *Ouimet et al.*, 2009, and Fig. 1.7, 1.8]. Relief exerts a very strong control on denudation rates, which seems to be a robust relationship over very contrasting climate regimes (e.g. Fig. 1.7). Similarly, these authors and others [e.g. *Ahnert*, 1970; *Montgomery and Brandon*, 2002; *von Blanckenburg*, 2005; *Binnie et al.*, 2007; *Ouimet et al.*, 2009] found a well defined relationship between denudation rates and slope. *Ouimet et al.* [2009] for

[III]Sediment yield is the mean mass yield per unit area. If the density of the mass is known, yield can be transformed into a volume, and hence denudation. Note that, the calculation of denudation rates from mass transport involves assumptions of density changes during weathering prior to physical mobilisation. For example if the a mean mean rock density (2.65 g/cm^3) is applied, steady state soil thickness is assumed [*Summerfield and Hulton*, 1994].

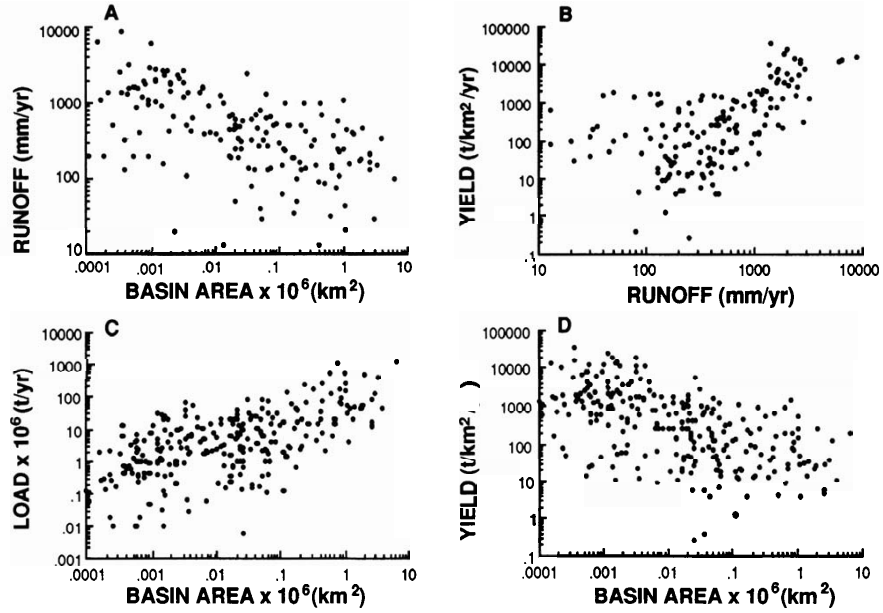

Figure 1.6: *Sediment flux vs. basin area and discharge plots. A) annual specific discharge (runoff) vs. area, B) annual suspended sediment denudation rate (yield) vs. specific discharge (runoff), C) total annual sediment flux vs. area and D) annual suspended sediment denudation rate (yield) vs. area. Note that basin denudation rate and specific discharge decrease with increasing drainage basin area. Denudation rate and specific discharge seam to be positively related as well as the absolute sediment flux with basin area [from Milliman and Syvitski, 1992].*

example, analysed cosmogenic nuclide samples from 65 small catchments ($25 - 200\ km^2$) of the eastern margin of the Tibetan Plateau (Yunnan). They show that erosion increases with mean basin slope up to a characteristic slope angle ($\sim 25 - 30°$). Erosion rates in basins with a mean slope larger than this threshold value are uncorrelated with slope (Fig. 1.8). The same relationship has been also described by *Montgomery and Brandon* [2002] and *Binnie et al.* [2007] for the Olympic Mountains and the San Bernardino Mountains, both in the western United States, using thermochronological and cosmogenic data respectively. On a global scale erosion and slope (or relief) are linearly related in low-gradient landscapes, whereas in rugged mountain terrains a small change in relief can modify significantly erosion rates [*Montgomery and Brandon*, 2002]. These findings show that actively uplifting landscapes with extreme topography, with hillslopes close to failure, are controlled by river channel incision [*Ouimet et al.*, 2009]. Landscapes having low slopes and consequently low denudations rates are typically transport limited, while landscape with steep slopes and high denudation rates are supply limited systems [*Binnie et al.*, 2007][IV]. In this sense, river incision keeps pace with uplift rates and the adjacent hillslopes

[IV] In a transported limited system, transport of material depends on the available energy, leading to a net accumulation of material. Supply limited systems depend on the supply of eroded material, the energy to transport is higher than the available material [e.g. *Fuller et al.*, 2003].

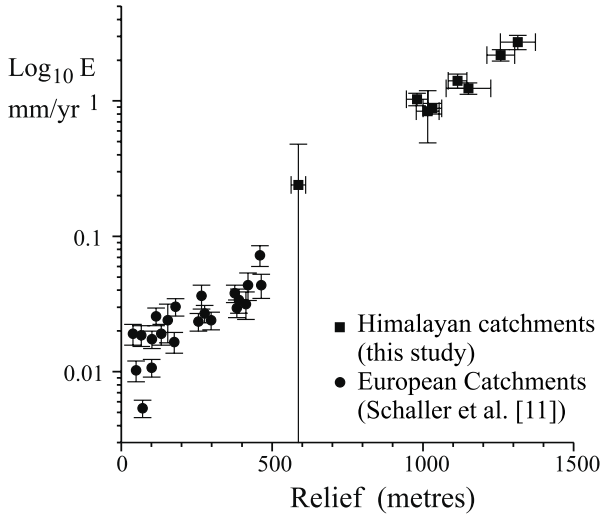

Figure 1.7: *Log-linear relationship between cosmogenic nuclide denudation rates and relief. Here, relief is calculated from a 9 by 9 km moving square window and expresses the half of the elevation range under the window. The circles show data from European catchments [Schaller et al., 2001] and the squares represent data from the upper Ganges basin in the Himalayas [Vance et al., 2003]. The clear relationship over three orders of magnitude relief and very different climate regimes is remarkable [from Vance et al., 2003].*

lag behind [*Whipple et al.*, 1999], and consequently the signal of erosion and topography is decoupled. Naturally, the question arises: What controls erosion beyond the critical threshold slope? Or is it only a stochastic effect? In Taiwan, erosion rates do not show any correlation with topography [*Dadson et al.*, 2003]. Earthquakes and typhoons which are relatively frequent in Taiwan, mobilize large quantities of material at ones and thus, flush all available sediments out of the mountain belt. Topography exerts a control on erosion over long time-scales and sets possible conditions. In the case of Taiwan, probably the intermittent recurrence of very large storm and earthquake events outweighs the effect of topography.

Topography has clearly a strong impact on erosion, e.g. very high erosion rates are detected when hillslopes are beyond threshold steepness. Steep landscapes are also more vulnerable to the impact of external forcing by earthquakes and rainstorms. However, the topography does not seem to be the sole controlling factor and the importance of its contribution might change accordingly to climatic and tectonic settings.

1.3.4 Erosion and climate

One of the most controversial parameter controlling erosion is precipitation [e.g. *Burbank et al.*, 2003; *Reiners et al.*, 2003]. As already raised before, climate can change considerably over short distances and

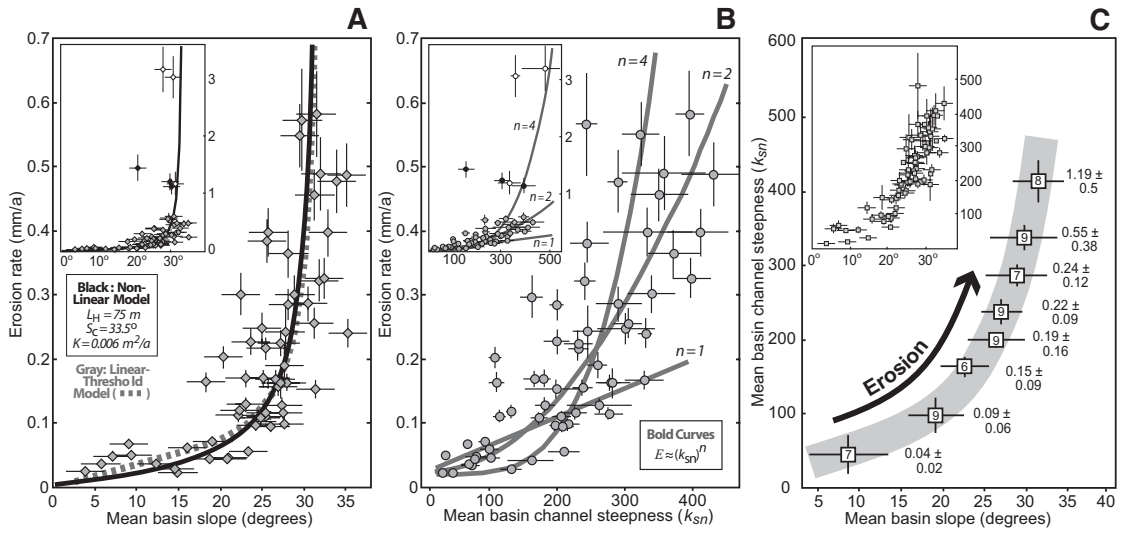

Figure 1.8: *Topographic controls on erosion rates. Mean basin erosion rates are plotted against mean basin topography. Basins are small tributary catchemnts (*$25 - 200\ km^2$*) of major streams in the eastern Tibetan Plateau margin (Yunnan). A) Plot of the mean basin slope against erosion rate, exhibiting a nonlinear relationship with a slope threshold between* $25 - 30°$*. B) Normalized channel steepness index versus erosion. Despite the general high erosion rates for high channel steepness the relationship is less well defined. C) Summarizes figure A with binned mean values. The insets of A, B and C illustrate full dataset range. [from Ouimet et al., 2009]*

depends highly on topographic patterns and the proximity of moisture sources [*Roe*, 2005; *Bookhagen and Burbank*, 2006].

Surprisingly, fission-track ages in the Himalayas show higher exhumation on the arid hinterland than in the wet mountain front, suggesting that denudation and precipitation are not connected [*Burbank et al.*, 2003]. Instead, the authors suggest glacial erosion to account for the high erosion rates. However, erosional efficiency of glaciers is closely related to climatic conditions, such as temperature and precipitation [*Zech et al.*, 2009]. In this sense, glacial erosion is also an expression of climate. On the other hand, $(U - Th)/He$ exhumation rates of the Washington Cascades, reflect the present day precipitation pattern [*Reiners et al.*, 2003]. On teh opposite, a global compilation of cosmogenic nuclide erosion rates (for similar lithology), sorted by precipitation rates and temperature (Fig. 1.9a and b) does not reveal any tendency and shows that for the same precipitation regime high and low erosion rates are possible [*von Blanckenburg*, 2005].

Precipitation is largely influenced by topography and exposition (windward or leeward) of the drainage basin [e.g. *Roe*, 2005; *Anders et al.*, 2006b; *Bookhagen and Burbank*, 2006], and is thus spatially very heterogeneously distributed. Precipitation and consequently discharge, are merely correlated with erosion rates [*Summerfield and Hulton*, 1994; *von Blanckenburg*, 2005]. Given the fact that these authors

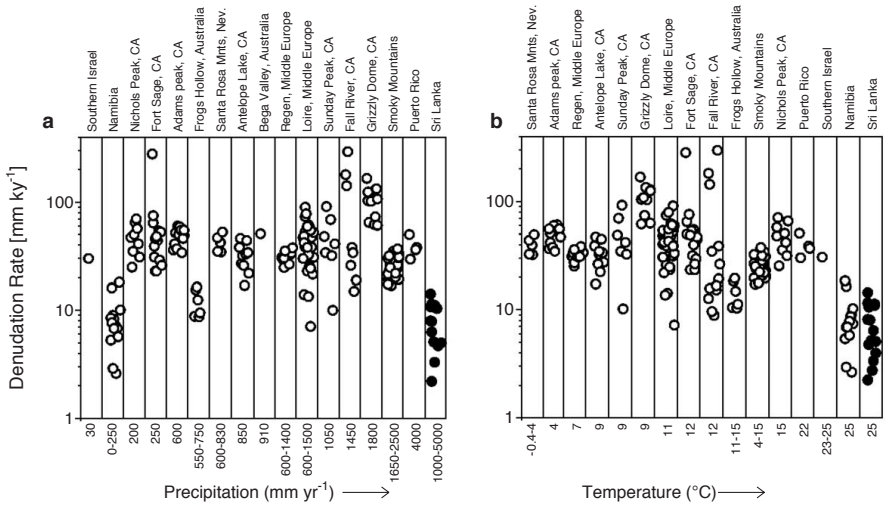

Figure 1.9: *Global compilation of denudation rates sorted by (a) mean annual precipitation and (b) temperature [Blanckenburg et al., 2004, and data sources listed therein]. The compared basins here are all for granitic settings to avoid lithology dependency. Note that in each region denudations rates vary considerably for the same mean precipitation rate [from von Blanckenburg, 2005].*

compared large scale mean basin values, the average precipitation rate gets relatively smoothed with increasing basin size, and therefore represents only to a certain degree the real local conditions which control erosion. For example, the local frequency/intensity distribution of precipitation might be more important than the accumulated annual rate. Indeed, *Bookhagen et al.* [2005a] and *Wulf et al.* [2010] demonstrated that rain storm events exert a strong control on mass movement and sediment fluxes.

From the discussion above, the question arises: Does precipitation exerts any control on erosion, and if, at which time-scale? Possibly, the temporal distribution and intensity of precipitation is a more important parameter than the amount of water precipitated

Several studies have made the link between modern erosion rates and the temporal recurrence and intensity distribution of precipitation rates [e.g. *Benda and Dunne*, 1997; *Bookhagen et al.*, 2005a,b; *Wulf et al.*, 2010]. In particular, large mass wasting events - landslides - are tightly coupled with intense rainfall [e.g. *Kirschbaum et al.*, 2009a; *Dahal and Hasegawa*, 2008; *Lin et al.*, 2008; *Gabet et al.*, 2004; *Fuller et al.*, 2003; *Iverson*, 2000]. In rapidly evolving mountain belts, mass wasting is the dominant type of erosion [*Meunier et al.*, 2008]. Intense precipitation causes saturation of the subsurface and reduces internal friction and detachments becomes more likely [*Iverson*, 2000]. On the other-hand, if precipitation intensity (or snow melt) exceeds the infiltration capacity of the surface substrate, surface runoff is generated which can cause mass movement by incision (gullys, ravins). *Hong et al.* [2006] showed for two prominent events in California and Nicaragua that the timing of failure coincides with peak intensity of the antecedent 10 day rainfall accumulation curve. Large scale mass wasting can also be triggered by high magnitude earthquakes [e.g. *Meunier et al.*, 2008; *Parker et al.*, 2011]. Erosion rates after such events (rainstorms and earthquakes) are tremendously elevated and can offset the erosion

signal significantly [*Dadson et al.*, 2003; *Hovius et al.*, 2011]. Landslides triggered by precipitation events cluster generally at the base of the slope while earthquake triggered failures tend to cluster along the mountain ridges [*Meunier et al.*, 2008]. In this work however, I concentrate on the interaction of climate and erosion. There is very little doubt that intense rainfall events have an impact on erosion. Hence, it is possible that the recurrence interval of a certain magnitude rainfall events exerts an important control on landscape formation.

As climate might have an impact on erosion, it consequently has the potential to change the shape of landscape. For example, *Montgomery et al.* [2001] proposed that the landscape of the Andes reflects the north-south distribution of precipitation. In the Buthan Himalayas, [*Grujic et al.*, 2006] illustrate the impact of climate on landscape evolution. The Bhutan Himalayas are separated in a very wet (western) and a less wet (eastern) part, because of the Shillong Plateau, an upstream mountain formation of the Himalayan range (Fig. 1.10). The plateau has been uplifted relatively rapidly, well after the Himalayan range and the monsoon system were in place. Low precipitation in the east is caused by the moister blockage of the upstream Plateau (Fig. 1.10 A), having one of the highest precipitation rates in the world on the windward site ($> 9\ m/year$). In the dryer eastern part, erosion is relatively little and the whole landscape has been passively uplifted, without changes in the topography [*Grujic et al.*, 2006]. In contrast, the western part receives the full monsoonal precipitation causing higher erosion rates and hence, a deeply incised relief. From laboratory sandbox models, [*Bonnet and Crave*, 2003] showed that relief changes with different precipitation rates under constant uplift conditions. These experiments showed that climate has the potential to change relief (range of elevation for a given reference area) under constant uplift rates. The crux is that final erosion rates, for two very different topographies and precipitation regimes, is equal.

In summary climate has the potential to leave a footprint on landscape but the process is not as straight forward as often believed. More precipitation does not necessary mean more erosion or vice versa. Nevertheless, intensity-frequency distribution of precipitation exerts a strong control on erosion processes. Futhermore, different climates can cause very different landscapes although tectonic forcing and erosion rates are very similar.

1.4 Motivation & Questions

Climate is thought to have an impact on erosion, but the processes and effects are not well described yet [*Whipple*, 2009]. The current state of the knowledge is partly inconsistent, providing arguments for and against a climate control. Especially, the mechanisms and time-scales of how climate might impact erosion is not well known. Possibly, the observed examples where climate and erosion show the same tendency are only coincidence.

The emphasis of this work is to understand more in detail the possible influence of precipitation on erosion, transport and on the formation of landscape. Therefore, it is important to investigate all

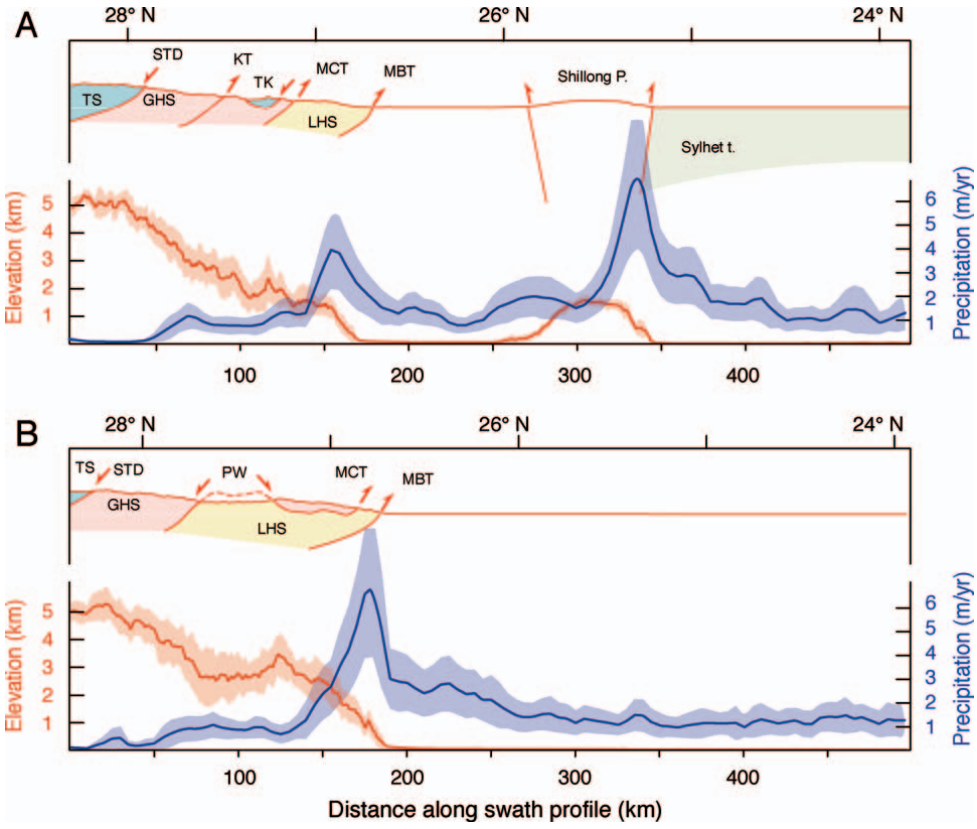

Figure 1.10: *40 km wide swath profile of topography (orange) and precipitation (blue) across the Bhutan Himalayas and the Shillong Plateau. The Shillong plateau acts as an orographic barrier* ($1.5 - 2$ *km high), blocking moisture transport from the south. A) eastern Bhutan, and B) western Bhutan. There is a strong E-W precipitation gradient: at* $\sim 1 - 1.5$ *km elevation in the east it is* ~ 4 m/yr*, while in the west it is* ~ 6 m/yr*. The eastern Himalayan topography was uplifted as a relict landscape since the formation of the Shillong Plateau, due to the blockage of moisture arrival. Main structural features are: MFT Main Frontal thrust, MBT Main Boundary thrust, MCT Main Central thrust, KT Kakhtang thrust, STD South Tibetan detachment, LHS Lesser Himalayan Sequence, GHS Greater Himalayan Sequence, TK Tethyan Klippen, PW Paro window, TSS Tethyan Sedimentary Sequence [from Grujic et al., 2006].*

successive steps involved, starting from precipitation, the transfer of precipitation to river discharge, the mobilization of material, the transport of material out of the mountain range, and the constrains over longer time-scales (up to several thousand years). In order to make this possible I will exploit multiple datasets such as precipitation, river discharge, earth observations datasets (e.g. temperature, snow and glacier cover), suspended sediment concentrations of rivers and cosmogenic nuclide analysis. In the following, I list four main points of interest which describe the thematic of each chapter of this work.

1. Precipitation data with a good resolution is needed to understand its role on both spatial and temporal scale. Today, more and more sophisticated data compilations are available but their quality has never been tested for the Himalayan region. Hence, I feel their is a strong need to evaluate the available data, in order to be able to know their limitations and strengths.

2. Precipitation impact on erosion is often stated as an hypothetical fact. In order to understand the mechanism behind this process, the fate of water after it is precipitated has to be investigated. Notably, how is precipitation transferred to river discharge and which different flow paths and reservoirs are involved.

3. Water in form of precipitation and river discharge exert a control on erosion processes. In particular the magnitude-frequency distribution of events has a huge impact on how material is mobilized and transported. To understand the erosion processes it is important to study the involved processes in parallel, in order to identify the different controls. For example, does the bulk of material comes only from few events? And what is the role of the high magnitude-low frequency monsoon climate?

4. Over a longer time period, tectonic, landscape and erosion counterbalance each other. This relation might be shifted relatively due to the climatic regime. Erosion rates determined from cosmogenic nuclide analysis, integrating over several hundreds and thousands of years are useful tools to determine the interactions. Thus, from the comparison of this rates with several landscape parameters and precipitation, some insights on the longer evolution can be gained.

1.5 Why the Himalayas?

The Himalayas are a natural place to study the climate-erosion interaction processes. The mountain range is actively uplifting and the monsoon defines a very clear cyclic seasonality, with two long-lasting seasons, one very wet and one very dry [e.g. *Lavé and Avouac*, 2001; *Hannah et al.*, 2005; *Bookhagen and Burbank*, 2006].

The very well defined cyclic climatic system of the Himalayas has a very well defined onset and end. Although the magnitude might vary between the years [*Shrestha*, 2000; *Bookhagen et al.*, 2005a; *Wulf et al.*, 2010], the average intensity has been relatively stable for at least the last few thousand

years [e.g. *Bookhagen et al.*, 2005b; *Clift et al.*, 2008b]. Furthermore, the Himalayas build a very distinct orographic barrier, separating the wet Indian Subcontinent from the arid Tibetan Plateau [*Anders et al.*, 2006a; *Bookhagen and Burbank*, 2006; *Boos and Kuang*, 2010]. The blockage of wet air masses, arriving from the Bay of Bengal and progressing along the mountain range towards the east and west, lead to an orographically enhance precipitation pattern [*Barros et al.*, 2006; *Bookhagen and Burbank*, 2010]. All of this sets a system tightly prone to precipitation-landscape interactions. Furthermore, the clear and well separated seasonality defines a cyclic system which likely allows to separate the involved processes within each season and to relate them with their exogenous forcing.

In the Nepal Himalayas, erosional processes are almost exclusively associated to monsoon. One of the main points I would like to address in this work is the question of the particularity of the Himalayan system compared to other mountain belts where climate is not characterized by such a strong seasonality. In Taiwan for example, the seasonality is less pronounced than in the Himalayas and surface processes are mainly controlled by recurrence of extreme short-term events such as typhoons and earthquakes [*Hovius et al.*, 2000; *Dadson et al.*, 2003]. Although, typhoons are clustered in the typhoon season, earthquakes are clearly random and can overlap with typhoons, which makes it difficult to separate the impact of typhoons or earthquakes on erosion. The mountain range of the Southern Alps intercepts the oceanic westerlies, resulting in a very wet north-western flank compare to a dry south-eastern flank with almost no seasonality [e.g. *Hovius et al.*, 1997; *Henderson and Thompson*, 1999].

Hence, the Himalayas are an ideal test bed to study the cyclic interactions of surface processes and the possible impact of precipitation on erosion.

Chapter 2

The Himalayas

The Himalayas are one of the youngest and the highest mountain ranges on earth. The Himalayas and the Tibetan Plateau, started to build up in the Eocene, as a result of the continent-continent collision between India and Eurasia [e.g. *Molnar and Tapponnier*, 1975; *Dupont-Nivet et al.*, 2010]. The whole Himalayan range extends over $\sim$ 2500 *km* from the west (Indus river, Nanga Parbat) to the east (Tsangpo-Brahmaputra Gauge, Namche Barwa), separating the Indian Subcontinent from central Asia (Fig. 2.1). From the south to the north, the Himalayan range rises from the low-lying Ganges Plains ($\sim$ 200 *m a.s.l.*) to the peaks of the High Himalayas ($>$ 8000 *m a.s.l.*), over less than 250 *km* horizontal distance. To the north they are bounded by the Tibetan Plateau, characterized by a low-relief and high elevations ($>$ 5000 *m asl*).

The Nepal Himalayas (Fig. 2.1) are situated in the central part of the Himalayan range, in the headwaters of the Ganges drainage system. The country extends approximately 800 *km* east-west and 200 *km* north-south and borders with Tibet/China in the north and India to the south. The three main drainage basins of Nepal are from the east to the west: the Koshi catchment, the Narayani catchment and the Karnali catchment, covering in total $\sim$ 135 km^2. All three basins have parts of their headwaters on the Tibetan Plateau (Fig. 2.1). They drain the complete Himalayan range of Nepal, amongst eight of the tallest mountains in the world ($>$ 8000 *masl*.), and outflow into the Ganges plains where they join the Ganges River. This work is constrained to the surface of these three basins, and several smaller ones in the southern most mountain front.

2.1 Geological settings and topography

Tectonics in the Himalayan range are very active as the Indian Subcontinent continues to collide with the Eurasian plate [e.g. *Lavé and Avouac*, 2001; *Bettinelli et al.*, 2006]. Uplift rates of the Himalayas are in the order of several millimeters per year [e.g. *Bilham et al.*, 1997; *Hurtrez et al.*, 1999; *Lavé and Avouac*, 2001; *Bettinelli et al.*, 2006; *Bollinger et al.*, 2006; *Blythe et al.*, 2007]. The successive underthrusting of the Indian plate underneath the Asian plate has created an orogenic wedge, underlying the Himalayan

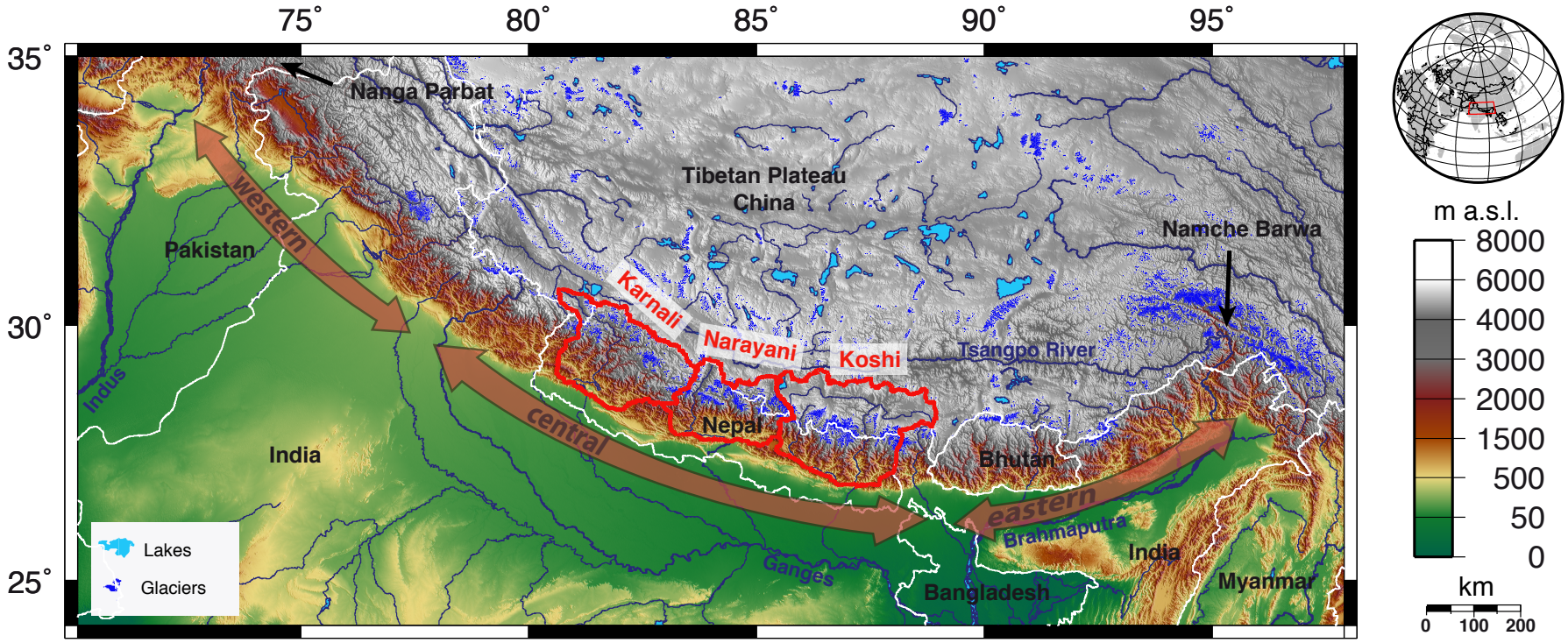

Figure 2.1: *Topographic map of the Himalayan range. Political boundaries are indicated in white. The three main drainage basins of the Nepal Himalayas are outlined in red. Glaciers are obtained from the National Snow and Ice Data Center. [1999]. Note that, the database is not complete for the western part of the Himalayas in Pakistan and India, as well as in Bhutan and eastern India.*

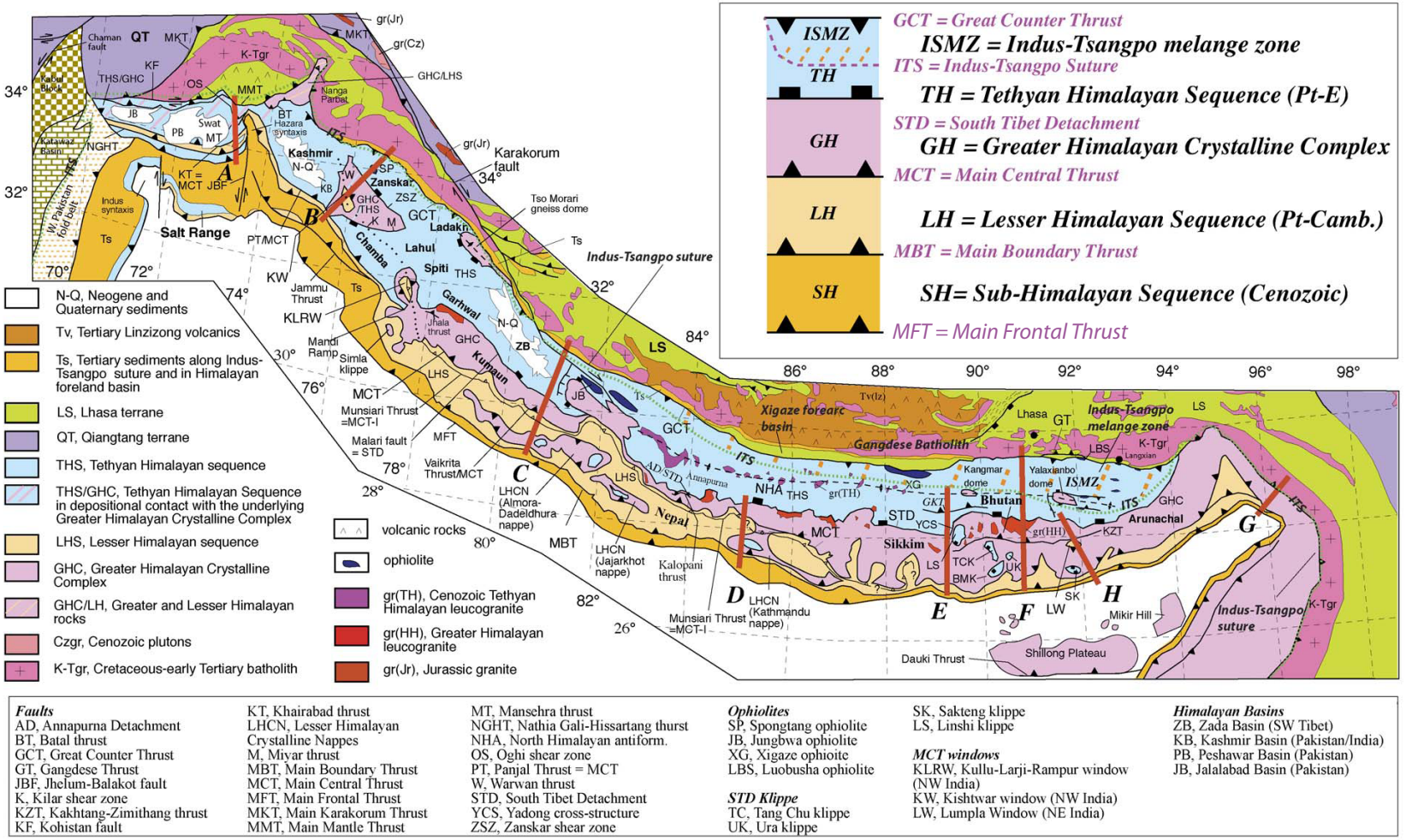

Figure 2.2: *Geological map of the Himalayan orogen. The map symbols are defined in the legend in the square box below. The major lithologic units and structures are defined in the systematic overview in the top right [from Yin, 2006, and references therein].*

range and bulging the Tibetan Plateau upwards. The Himalayas comprise four main tectonic structures [e.g. *Blythe et al.*, 2007]. From north to south, they are: 1) the South Tibetan Detachment STD, 2) the Main Central Thrust MCT, 3) the Main Boundary Thrust MBT and 4) the Main Frontal Thrust MFT (fig. 2.2). All these four structures can be traced along almost the whole Himalayan range (Fig. 2.2). Geophysical and structural studies suggest that all thrusts connect at depth to one single thrust (see Fig. 2.3 a), the Main Himalayan Thrust MHT. The MHT acts as a slide face where the Indian plate thrusts under the southern edge of the Tibetan Plateau [*Lavé and Avouac*, 2001; *Bollinger et al.*, 2006]. Horizontal shortening along the MHT are approximately $15 - 20\ mm/yr$ [*Bettinelli et al.*, 2006; *Lavé and Avouac*, 2000], consuming a large part of the modern south-north shortening between the two continental plates [*Lavé and Avouac*, 2000].

The geology of the Himalayan range comprises from north to south: 1) The Thetysian Sediment Series of the Tibetan Plateau, 2) the High Himalayan crystallines (granite and gneiss) of the High Himalayan range (or Greater Himalayas), 3) the low-grade metasediments (mainly gneiss and schist and some Thetysian Sediments) of the Lesser Himalayas, 4) the Siwaliks (Sub-Himalayas), low altitude hills and mountains ($< 1000\ m\ asl$.) composed of easily erodible Neogene Molasse (eroded material accumulated during the Himalayan formation), and 5) the southern-most Ganges plains with their Quaternary Sediments [e.g. *Lavé and Avouac*, 2001]. The lithologic contacts coincide approximately with the fault structures (Fig. 2.2). The STD separates the Tibetan Himalayas (hanging wall) from the High Himalayas (foot wall). The MCT separates the High Himalayas from the Lesser Himalayas, and together with the STD facilitated the exhumation of the High Himalayas [*Szulc et al.*, 2006].

Wobus et al. [2005, 2006] suggest the existence of a fifth out-of-sequence thrust in the Nepal Himalayas, located $\sim 30\ km$ south of the MCT. Topographic analysis show their an abrupt slope break, which coincide with very young $^{40}Ar/^{39}Ar$ cooling ages ($< Myr$) to the north of the formally undetected structure. The authors relay this thrust with high erosion rates, focused onto the Himalayan front, which favour deep exhumation rates within this zone. In contrast, *Bollinger* [2004]; *Bollinger et al.* [2006] explain the sudden drop in exhumation ages with an inverted metamorphic gradient, resulting from a combination of underplating and postmetamorphic shearing, tampering the geothermal gradient and hence the thermochronological model measurements. Both arguments are convincing and can explain the field evidences. In terms of exhumation/erosion, the one or the other have completely different consequences: The model by [*Bollinger*, 2004; *Bollinger et al.*, 2006] involves homogeneous and constant exhumation rates. The proposed out-of-sequence thrust by *Wobus et al.* [2005, 2006] however requires a localised net-input of material, provoking locally higher exhumation rates along this structure. Nevertheless, it is important to notice that topography rises abruptly from the Lesser Himalayas to the Higher Himalayas (Fig. 2.3 b).

The seismic activity within the Nepal Himalayas is closely related to the tectonic settings and however as well as by the hydrological cycle [*Pandey et al.*, 1995; *Pandey*, 1999; *Bollinger et al.*, 2007; *Bettinelli et al.*, 2008]. The background activity is very high and most seismic events are localised along

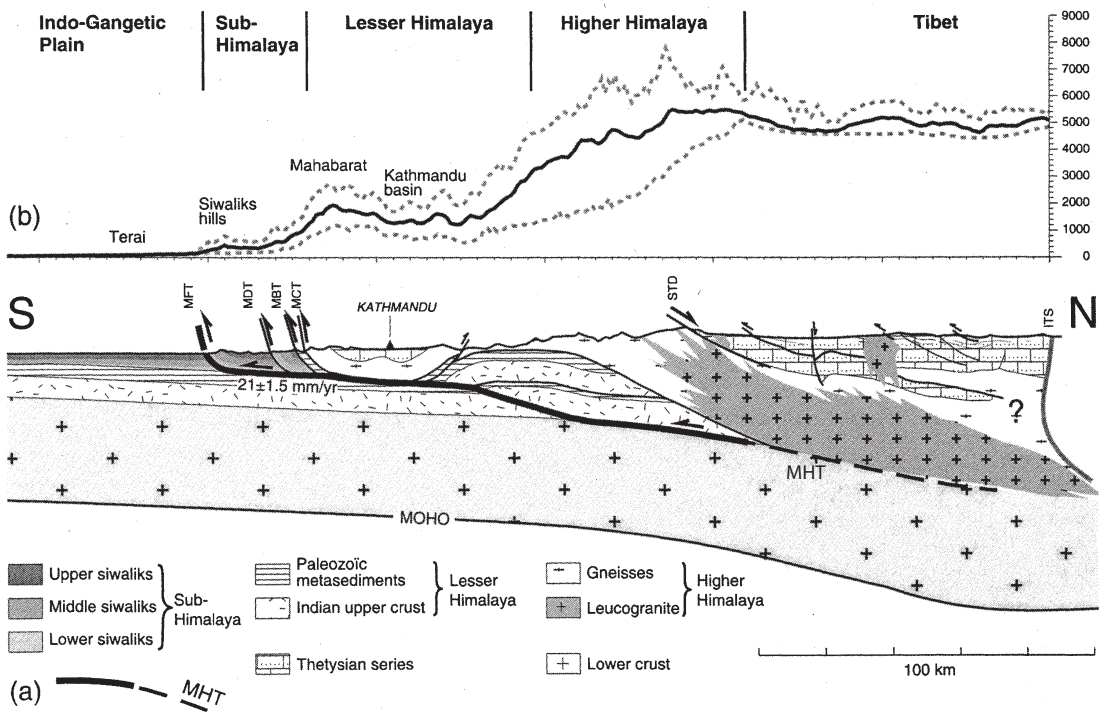

Figure 2.3: *Geological (a) and topographic (b) cross-section through the Himalayas, at the longitude of Kathmandu valley. The lines in profile b show the mean (solid) and the maximum and minimum elevation (dashed) along a 50 km long swath profile [from Lavé and Avouac, 2001, and references therein].* 21 ± 1.5 *mm/yr are slip rates according to Lavé and Avouac [2000].*

the southern front of the Higher Himalayas (Fig. 2.4 a) in an average depth of $\sim 10-20$ *km* (Fig. 2.4 b). Roughly, the concentration zone traces the surface course of the MCT [e.g. *Pandey et al.*, 1995]. Interestingly, the seismic record analyses by [*Bollinger et al.*, 2007; *Bettinelli et al.*, 2008], covering 5 years (1995-2000) of continuous measurements, show that seismic activity is clustered in the winter season and relatively little activity is recorded during monsoon time. The authors interpret this seasonality by recharge of the aquifer during monsoon time, exerting an overburden and reducing failure conditions. However, these are relatively weak seismic events (ML = 0 to 6.3) and no major earthquake ($\gtrsim 6.5$ *MW*) has occurred in the Central Himalayas since the Bihar-Nepal in 1934 [*Pandey and Molnar*, 1988; *Pandey et al.*, 1995; *Bettinelli et al.*, 2006]. The Bihar-Nepal *MW* $8.0-8.2$ earthquake, ruptured a $200-300$ *km* long segment to the east of Kathmandu [*Pandey and Molnar*, 1988; *Pandey*, 1999, and references therein]. Only two relatively strong earthquakes happened in Nepal during the time period considered for the suspended sediment and discharge analysis of this work: in 1979 (5.5 *MW*) and in 1980 (6.5 *MW*) [Global Centroid-Moment-Tensor (CMT) catalog, *www.globalcmt.org*].

As mentioned before, the topography in Nepal raises abruptly over a short distance from $<$ 200 *m asl*. to elevations $>$ 8000 *m asl*. and continues onto the Tibetan Plateau with average elevations $\sim 5000-6000$ *m asl*. (Fig. 2.3b and 2.5). Along the entire Himalayan range two different patterns

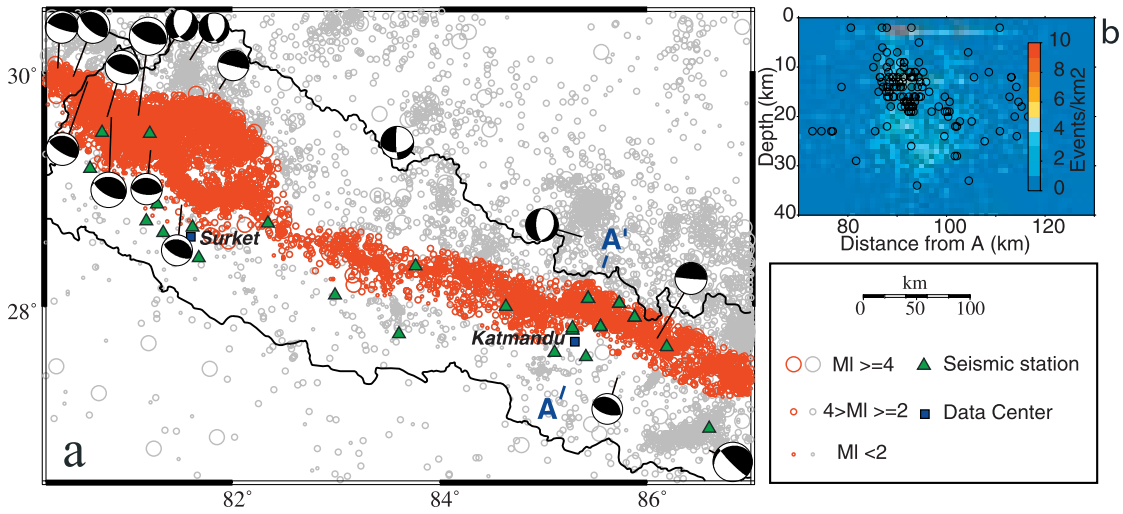

Figure 2.4: *Microseismicity recorded between 04/01/1995 and 04/11/2000 by Nepal Seismological Center [from Bollinger et al., 2007]*

of topographic rise can be observed (Fig. 2.3b and 2.5): 1) in the eastern and western Himalayas, topography rises directly in one step until the high summits, while 2) in the central Himalayan topography describes a two step pattern of successively increasing elevations, a first one at the front of the range and a second one within the Higher Himalayas [*Bookhagen and Burbank*, 2006].

2.2 Climate and hydrology

The very strong Himalayan relief marks pronounced climate differences on a very short distance [*Hannah et al.*, 2005]. The Ganges plains in the south, are characterized by a subtropical climate[I]. In the valleys of the Lesser Himalayas, climate is subtropical and gets warm to temperate with increasing elevation. The High Himalayas are marked by very strong climatic differences from partially subtropical in the very deep incised valley bottoms ($\sim$ 1000 *m asl*.), to nival, in the very high elevations ($>$ 5000 *m asl*.). Typically the horizontal distance between the valleys and the high ridges and peaks is not more than $10 - 15$ *km*, imposing very strong gradients in temperature and ecosystems. The winter snowline is $\sim$ 3000 *m asl*., while above elevations of 5000 *m asl*. all precipitation comes in form of snow [*Putkonen*, 2004]. However, the climatic regime is poorly documented within the Nepal Himalayas. Meteorological monitoring stations are sparsely distributed, mainly situated in the easily accessible valley floors, and thus climate analysis have to relay on few punctual observations. Due to the complex terrain and poor data basis climate models as well as satellite based observations perform

[I]Subtropical climate: characterized by hot, humid summers and mild to cool winters.

Temperate climate: not as hot as subtropical, but warmer than polar climate.

Nival climate: All year around below zero, above snow line. [*Koppen*, 1936]

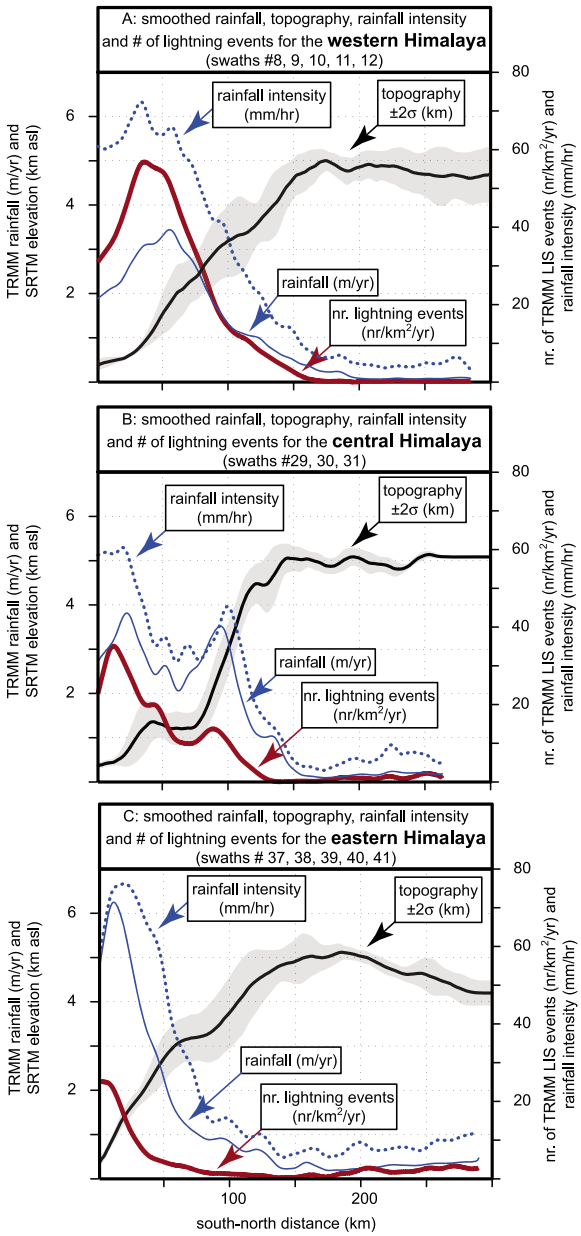

Figure 2.5: *Topographic profiles across the Himalayan range vs. annual precipitation rates, from the south (left) to the north (right). Grey shading indicates the elevation range ($\pm 2\sigma$) and the black line the respective mean, perpendicular to the* 50 *km swath width. Precipitation is derived from the TRMM-3B31 precipitation radar measurements, intensity is the maximum rainfall made over the 10 year measuring period. Red line represents the number of lightning events per km^2 TRMM-LIS, registered by the TRMM sensor and can be seen as proxy of storm intensity. A represents the western Himalayas, B the central Himalayas, typical for the Nepal Himalayas and C the eastern Himalayas [from Bookhagen and Burbank, 2010].*

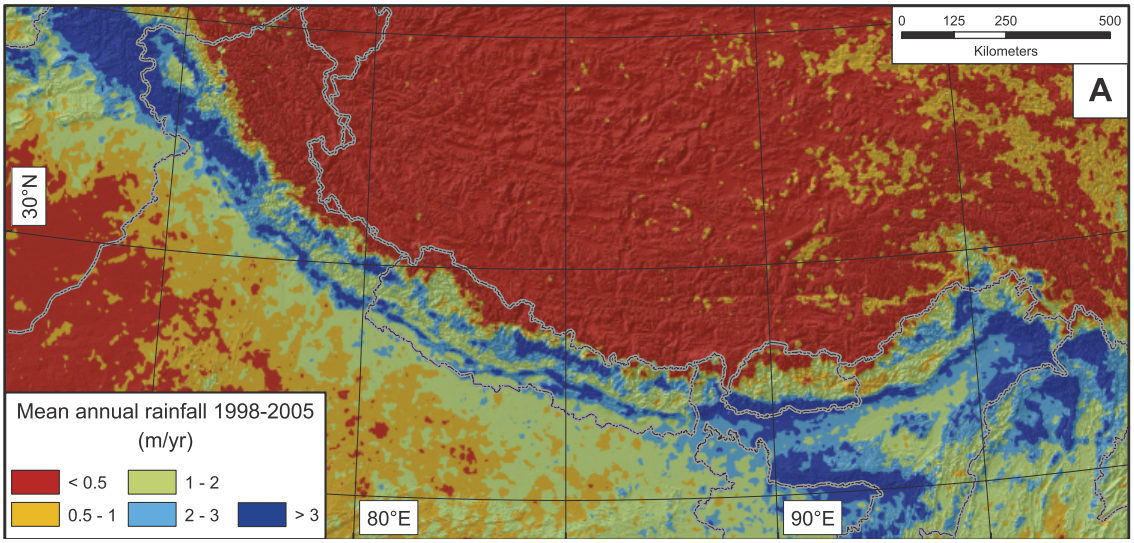

Figure 2.6: *Precipitation distribution in the Himalayas, measured from the precipitation radar, onboard of the Tropical Measuring Mission satellite TRMM. The plotted precipitation rates indicate the mean (1998-2005) annual precipitation distribution with* $\sim 5 \times 5$ *km resolution [from Bookhagen and Burbank, 2006].*

poorly in the very complex and rugged terrain of the Himalayas. The Himalayas present a prominent topographic feature, well able to influence climate on the continental or global scale [e.g. *Raymo and Ruddiman*, 1992; *Boos and Kuang*, 2010]. Hence, there is a huge need in the Earth Sciences community to get a better understanding on climate distribution (temporal and spacial) in this region.

Seasonality of the Himalayas is jointly linked with the large scale monsoon circulation, defining a very wet (monsoon) and a very dry season [e.g. *Bookhagen and Burbank*, 2010]. The dry, non-monsoon season can be subdivided in: post-monsoon (October - November), winter (December - February) and pre-monsoon (March - May). The large part ($\sim$ 80%) of the annual precipitation is associated with the Indian summer monsoon [*Anders et al.*, 2006b; *Bookhagen and Burbank*, 2006, 2010], and only a small fraction of precipitation ($\sim$ 20%) falls during winter [*Lang and Barros*, 2004]. Furthermore, the spatial precipitation distribution is strongly associated with topography (Fig. 2.5 and 2.6), due to orographic effects [*Anders et al.*, 2006b; *Bookhagen and Burbank*, 2006]. Their observations show a clear connection with the steepness and elevation of the terrain. For example, in the central Himalayas where topography describes a two step rise from the south to the north, the rainfall data reveals two discrete rainfall bands which coincide with the topographic rises (see also Fig. 2.5). The southernmost band corresponds with elevations of $\sim$ 1000 *m asl*. in the lesser Himalayas and the second one with elevations of $\sim$ 2000 *m asl*. on the foot of the High Himalayas. Annual precipitation rates exceed 3000 mm/yr at those elevation [*Bookhagen and Burbank*, 2006]. Further north precipitation decreases drastically to $\sim$ 250 mm/yr on the Tibetan Plateau (Fig. 2.6). However, this reflects only the large scale rainfall pattern, small scale variations are much more complex and change according to orientation, elevation

and proximity to moisture sources of the mountain slopes [*Barros and Lang*, 2003; *Bhatt and Nakamura*, 2005; *Barros et al.*, 2006]. Furthermore, [*Bhatt and Nakamura*, 2005] demonstrated inter-daily precipitation patterns, so called diurnal cycles, from satellite based precipitation radar analysis (TRMM-PR). Along the southern Himalayan front, precipitation is more concentrated during the midnight-early-morning hours and minimal during the late morning [*Bhatt and Nakamura*, 2005]. The existence of diurnal cycles might bias precipitation measurements as well as river discharge records.

Because precipitation and monsoon climate are so important for this work, I will use the following two chapters to explain the large scale monsoon system and how topography exerts a control (orographic effects) on the spatial distribution of rainfall pattern.

2.2.1 Monsoon

Monsoon is a global weather phenomenon caused by the unequal distribution of large ”hot” land masses, the differential heating between land-surface and oceans and the relative inclination of the earth towards the sun [e.g. *Webster and Chou*, 1980; *Molnar et al.*, 1993; *Zhisheng et al.*, 2001; *Boos and Kuang*, 2010]. The Inter Tropical Convergence zone ITC, circles the Earth near to the equator and separates the wind circulation of the southern and northern hemisphere. Depending on the exposition towards the sun, the ITC moves further north (northern hemisphere summer) or south (northern hemisphere winter), as a result of differential net heat radiation [e.g. *Webster and Chou*, 1980]. For example, the Indian Summer Monsoon ISM is formed by a summer low pressure cell over central Asia (tropospheric high), deflecting the ITC far north, and a relative high pressure cell over the Pacific and Indian Ocean. Thereby, it induces intense moisture flow from the open ocean to the Asian continent [*Bookhagen et al.*, 2005a]. In the case of the ISM (affecting the central Himalayas), the air-masses arrive from the Arabian Sea and the Indian Ocean, penetrate the Indian continent from Bay of Bengal and move westwards and eastwards along the Himalayan range (Fig. 2.7). There, they collide with the high mountain range, causing heavy monsoonal precipitation rates. Monsoonal rainfall in the Himalayas is characterized by strong upward movements and convective rainfall. Latent heating caused by moisture condensation additionally amplifies the effect [*Bookhagen et al.*, 2005a; *Barros et al.*, 2006].

Monsoon intensity can vary considerably between the years [*Shrestha*, 2000; *Gadgil et al.*, 2004; *Bookhagen et al.*, 2005a] and has also varied back in geological time [*Zhisheng et al.*, 2001; *Bookhagen et al.*, 2005b; *Clift et al.*, 2008a]. Short-term variability of the monsoon intensity are linked to global shift in climate patterns, for example El Nino/El Nina Southern Oscillation (ENSO cycles), modifying the large-scale climate circulations [*Shrestha*, 2000]. This relation is manifested in a propensity of droughts during El Nino and vice versa [*Gadgil et al.*, 2004]. During strong monsoon years the moisture laden air-masses can penetrate far deeper into the otherwise arid mountain interior (Fig. 2.7), causing catastrophic mass-wasting events [*Bookhagen et al.*, 2005a]. *Shrestha* [2000] finds a good correlation between the monsoon intensity and the monsoon Southern Oscillation Index, in the Nepal Himalayas.

The exact timing of the onset of the Asian monsoon system remains quite controversial [e.g. *Iaf-*

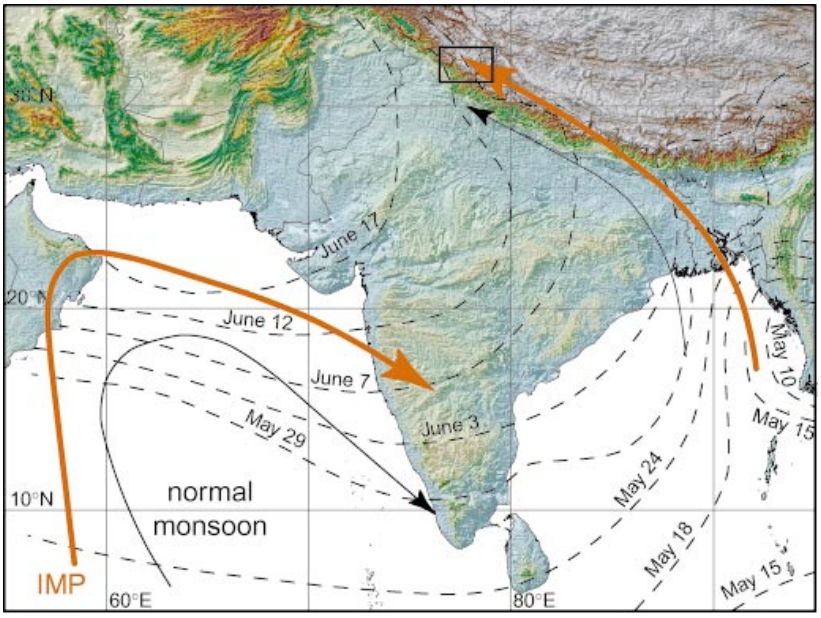

Figure 2.7: *Main Indian Summer Monsoon trajectories over the Indian subcontinent. The black arrows indicate the weak Monsoon flow directions, while the bold orange arrows show paths of strong monsoon years. The dashed lines indicate the temporal progression of the north westward propagating Indian Summer Monsoon [from Bookhagen et al., 2005b].*

faldano et al., 2011]. However, some evidences from dust deposits and sedimentary cores suggest that the monsoon system has been in place since at least the beginning of the Neogene [e.g. *Clift et al.*, 2008a]. Other authors suggest that the monsoon started only in the late Miocene [e.g. *Molnar et al.*, 1993; *Zhisheng et al.*, 2001]. Continuous research efforts have been conducted to understand the role of monsoon on a global scale and its role in atmospheric CO_2 draw-down by silica weathering [e.g. *Raymo and Ruddiman*, 1992], and to understand its role in the formation of the High Himalayas and the Tibetan Plateau [e.g. *Molnar et al.*, 1993; *Beaumont et al.*, 2001; *Zhisheng et al.*, 2001; *Clift et al.*, 2008a,b]. Most recent studies, from landslide and lake sediment dating [*Bookhagen et al.*, 2005b] and the analysis of sediment cores from the Indus River delta [*Clift et al.*, 2008b], reveal that monsoon intensity was relatively stable over the last few thousand years, approximately the integration time of this work (Chapter 6).

So far it was a common agreement that the Indian monsoon system, and eventually even the global system, is caused by the Tibetan Plateau [e.g. *Molnar et al.*, 1993]. The Plateau is a huge elevated landmass, relatively cold in winter and hot in summer. However, *Boos and Kuang* [2010] provide evidence from numerical modelling that a high Plateau is not necessarily needed but it is rather important to have a prominent east-west barrier separating the ”hot” hinterland from the moisture source.

2.2.2 Orographic effects

"Orographic effects" is a collective term for processes causing enhanced precipitation by the interaction of land surface and the atmosphere [*Roe*, 2003, 2005]. Here, I will concentrate on the particular example of the Himalayas, blocking the southward arrival of the ISM air-masses. It is the dynamic response of the airflow to the presence of orography, defining a lower boundary condition and setting the three-dimensional pattern of water condensation from which the precipitation results [*Roe*, 2005]. The fundamental ability of air to carry water in form of vapor depends on its partial pressure. The saturation pressure, when water starts to condensate, is sensitive to temperature and atmospheric pressure. For example when the moisture laden winds are forced to rise by the underlying topography, the partial pressure of the air masses increases by cooling and adiabatic expansion, leading to moisture condensation [*Roe*, 2005]. Once the gravitational forces of the condensed water droplets are larger than the buoyancy of the rising air, the droplets will fall as rain or snow. This general feedback between air flow (wind) and land surface elevation leads to distinct rainfall patterns along a mountain range such as the Himalayas (Fig. 2.8 a). Furthermore, processes such as the formation of droplets and their drift as they fall, are important to understand the rainfall patterns.

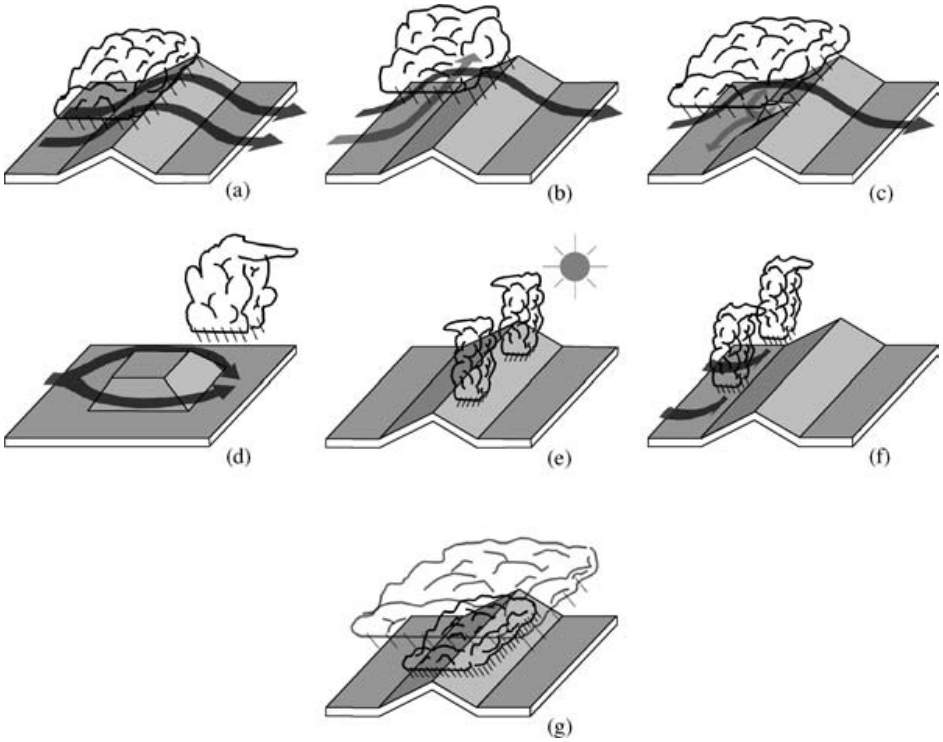

Figure 2.8: *Schematic illustration of several orographic precipitation mechanisms. (a) stable upslope ascent, (b) partial blocking of the colliding air mass, (c) down flow of air into valleys by latent heating (evaporative cooling), (d) lee-side convergence, (e) convection by solar heating, (f) upwind convection by mechanical lifting, (g) seeder-feeder mechanism case [from Roe, 2005].*

Several schematic processes of orographic rainfall mechanisms are illustrated in Figure 2.8 and will be explained partly thereafter. These processes are discussed more in detail in *Roe* [2005, and references therein]. Due to the complex and rugged topography, with deep perpendicular valleys and multiple slope expositions, all these processes can play a role in the Himalayas. The simplest form of orographic induced rainfall is the ascent of air over a broad topographic ramp which is responsible for the overall large scale precipitation pattern in the Himalayas, as described above (Fig. 2.7) It is governed by the upwind fallout of moister and the leeward decent of dry and warm air-masses. If the air flow is not strong enough, or the atmosphere too stable, parts of the airflow get blocked or diverted along the upwind mountain front (Fig. 2.8 b). One possible process is the partial cooling of the air-masses by, for example rainfall induced glacier melt, leading to a reverse of airflows down the valley (Fig. 2.8 c).

The incorporation of orographic rainfall gradients is important to evaluate water resources and landslide risks, but also to model river incision rates and tectonic uplift from river profile analysis, because in areas with a dominant rainfall gradient the surface area is not linearly related with discharge [*Roe et al.*, 2002; *Wu et al.*, 2006].

2.2.3 Himalayan hydrology

In the central Himalayas of Nepal, rivers are deeply incised and descend on a short distance ($< 300\ km$) a considerable elevation range, from several thousand meters above sea-level (High Himalayas) to around 150 meters in the Indian Lowland (Fig. 2.1). After the definition of *Turowski et al.* [2008][II], all rivers in Nepal are bedrock rivers. They are highly channelized, with little accommodation space for transient sediment deposition and with high flow rates ($> 1\ m^3/s$), inducing high transport capacities. The instant transport of material, is for example an important assumption to analyse catchment wide erosion rates from cosmogenic nuclide analysis. The annual river hydrographs (Fig. 2.9) show clearly the control of the ISM on Himalayan rivers, causing a one to two magnitude increase of discharge from non-monsoon to monsoon season [*Hannah et al.*, 2005; *Bookhagen and Burbank*, 2010]. The high elevations of the Himalayas are covered by glaciers (Fig. 2.1) and form an important water resource for the whole dwonstream region [*Immerzeel et al.*, 2010]. In contrast to the rivers of the western (e.g. Indus and Sutlej) and eastern Himalayas (e.g. Tsangpo-Brahmaputra), snow and glacier melt contribution is minor in the central Himalayas [*Bookhagen and Burbank*, 2010, and Fig. 2.9]. However, the importance of glacier melt contribution has never been evaluated on the scale of Nepal. *Alford and Armstrong* [2010, in discussion] estimate the glacier melt contribution, from an altitude based energy gradient model, to be in the range of 4% of the total stream flow. Last, the role of ground water is an important component which is merely investigated in the whole Himalayas. Geochemical analysis of river water samples show clearly the signature of an important groundwater storage volume [*Tipper et al.*, 2006].

[II] "A bedrock river can not substantially widen, lower, or shift its bed without eroding bedrock"

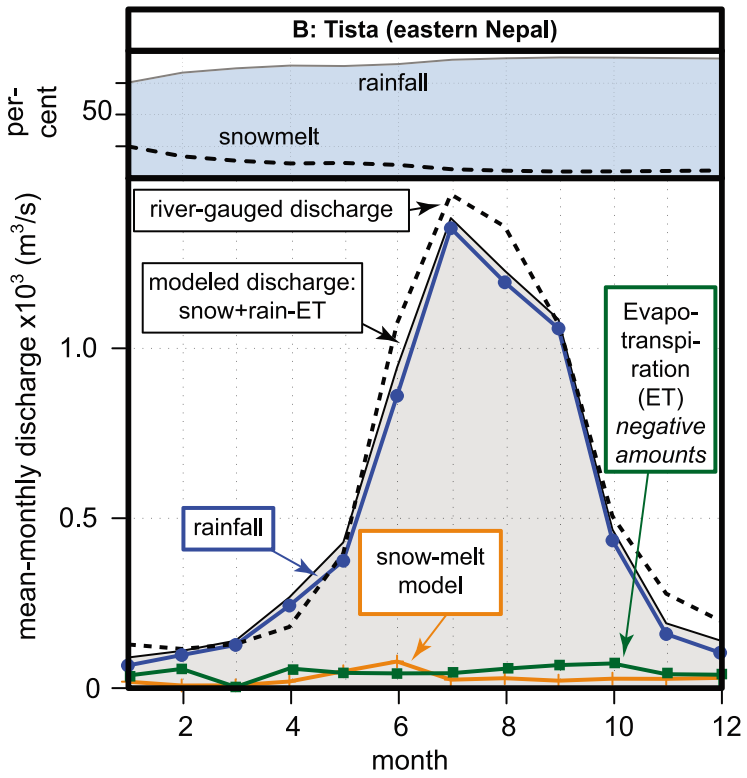

Figure 2.9: *Annual hydrograph of the Tista river, east of Nepal, Sikkim. Colored lines indicate the relative contribution of various discharge compartments, rainfall, snowmelt, evapotranspiration (groundwater and glacier melt is not included here). The drainage area is approximately* $\sim 2000\ km^2$. *The data represents modeled data from remote sensing observations, compared to gauge measurements (dashed line). The small inset on top shows the % temporal contribution of snowmelt and rainfall to the total discharge. Most important is to notice that snowmelt volumes are roughly constant through the year and contributes significantly (25%) to the total discharge only in January [from Bookhagen and Burbank, 2010].*

2.3 Erosion patterns

The spatial and temporal constrains of erosion in the central Himalayas has never been studied on a large scale, for example on the scale of Nepal. Although, several studies deal with erosion and exhumation, they focus on relatively small study areas, such as single watersheds of $< 5000\ km^2$ [e.g. *Thiede et al.*, 2004; *Wobus et al.*, 2005; *Huntington et al.*, 2006; *Garzanti et al.*, 2007; *Gabet et al.*, 2008; *Wulf et al.*, 2010].This is mainly because the availability of data (precipitation, discharge, sediment transport) in these regions is rather limited. Secondly, the terrain is very rugged and difficult to access. On the other hand, several studies attempt to evaluate the erosional behaviour over long time series and/or on a large scale from sedimentary cores [*Métivier et al.*, 1999; *Clift et al.*, 2008a, and others] and geochemical analysis [*Galy and France-Lanord*, 2001].

It is very difficult to draw a larger image from all these studies, because of the different integration time scales of the various methods. For the sake of brevity, I will concentrate here on the most important findings contributing to the discussion and conclusion of this work, in order to draw a larger image of erosion sources and the final deposition of sediments. One general observation is that today erosion rates in the Himalayas are in the range of several millimeters per year [e.g. *Galy and France-Lanord*, 2001], roughly the same as exhumation rates and uplift rates, and therefore one of the fastest erosion rates in the world.

Eroded material from the Himalayan range is transported to the south by the three main Himalayan river systems: Tsangpo-Brahmaputra, Ganges and the Indus (Fig. 2.1). Eventually it gets deposited in the foreland basins and is then passed through to their final sink, the Bay of Bengal or the Arabian Sea [*Galy et al.*, 2007; *Singh et al.*, 2007]. By studying these sedimentary reservoirs it is possible to evaluate erosion fluxes and their variability back in time [e.g. *Métivier et al.*, 1999; *Clift et al.*, 2008a]. However, to retrieve the whole Cenozoic erosion history, and possible connections with monsoonal strength, from sedimentary cores is still in debate. In particular, it seems very difficult to attribute the observed accumulation rates to real erosion and deposition rates [*Schumer and Jerolmack*, 2009]. Probably the most tricky exercise is to estimate the distance between the source and the sampling place back in time.

Geochemical analysis of the two main rivers, Tsangpo-Brahmaputra and Ganges, draining the eastern and central Himalayas, bear the signature of erosion from the upstream region [*Galy and France-Lanord*, 2001]. This approach is based on chemical budget analysis of major elements in transport, and on the idea that the composition of the source rocks (Himalayas) must equal the composition of the erosion flux (dissolved, suspended and bedload and flood plain depositions) [*Galy and France-Lanord*, 2001]. This provides a good understanding of the mean Himalayan erosion flux, which is according to *Galy and France-Lanord* [2001] in the order of 2 mm/yr for the Ganges basin and ~ 3 mm/yr for the Tsangpo-Brahmaputra basin. In total, this accounts for $\sim 2.1 \cdot 10^9$ t/yr of material transported from the Himalayan range to the Bay of Bengal. Furthermore, the ratio between dissolved load and undissolved load (bedload and suspended load) shows clearly that physical erosion processes dominate erosion in the Himalayas [*Galy and France-Lanord*, 2001]. These findings are important background information on the large scale erosion fluxes from the Himalayan range. However, they can not give any information on the local dynamics and its controls. More detailed studies with a good temporal resolution and spatial coverage are needed to provide further constraints.

In Nepal, most of the current research on erosion and exhumation has focused on the Siwaliks [e.g. *Lavé and Avouac*, 2000; *Kirby and Whipple*, 2001; *Lague and Davy*, 2003] and the Annapurna region [e.g. *Burbank et al.*, 2003; *Gabet et al.*, 2004, 2008, 2010; *Hodges et al.*, 2004; *Huntington et al.*, 2006; *Tipper et al.*, 2006; *Blythe et al.*, 2007; *Garzanti et al.*, 2007; *Pratt-Sitaula et al.*, 2007]. Drainage pattern analysis show that the very fast uplift rates in the Siwaliks [*Lavé and Avouac*, 2001] are counter balanced by erosion [*Kirby and Whipple*, 2001]. In the Siwaliks, these rates are in the range of $8 - 15$ mm/yr. Most of the data presented in this work, however, will deal with erosion processes in the High Himalayan range.

In the Higher Himalayas, erosion rates depend largely on the sampling position and the applied methodology. Suspended sediment analysis of the Marsyangdi valley, draining the north and east of the Annapurna massif, are in the order of 2 mm/yr in the Higher Himalayas and get as low as ~ 0.1 mm/yr in the hinterland, which is roughly confirmed from sand provenance analysis by *Garzanti et al.* [2007]. Outstanding is the Khudi Khola watershed, draining from the very steep southern flank of the Annapurna massif with denudation rates of ~ 3.5 mm/yr [*Gabet et al.*, 2008]. Very high erosion rates are also reported from thermochornological analysis by [*Burbank et al.*, 2003; *Huntington et al.*, 2006]. Analysis of slope and rainfall distribution suggest that erosion is mainly controlled by a combination of these two parameters[*Gabet et al.*, 2004]. Especially, intense monsoon phases (climate change) have an impact on the erosion, accelerating rates tremendously [*Pratt et al.*, 2002]. Present day observations of rainfall confirm the impact of intense rainfall on landsliding [*Gabet et al.*, 2004; *Dahal and Hasegawa*, 2008]. In summary, erosion in the Higher Himalayas is localized where relief is strong and the intense precipitation correlates well with the mobilisation of material and hence, the predominant erosion process is physical erosion. Yet, this rather complete picture, assembled from relatively short analysis and localized study areas needs to be validated on a larger scale. The challenge is to integrate measurements from different sources and representative for different processes, in order to understand the spatio-temporal constrains of erosion processes in the Himalayas.

It is important to note that erosion rates of glaciers in the Himalayas are not well studied. *Heimsath and McGlynn* [2008] determined the headwall and sidewall retreat by glacial erosion (~ 1 mm/yr), however the basal erosion rate remains an open question. Few suspended sediment analysis from glacier outlet stations report total erosion rates (headwall retreat and basal erosion) to be in the order of $1 - 6.5$ mm/yr in the central Himalayas [*Hasnain and Thayyen*, 1999, and references therein] and around $0.1 - 0.5$ mm/yr in the eastern Himalayas [*Bhutiyani*, 2000]. However, these are only some punctual short term observations. Secondly, little is known about the erosion rates of the part of the Tibetan Plateau being drained to the south. So far, *Lal et al.* [2004] has published erosion rates from cosmogenic nuclide exposure dating for the internally drained Tibetan Plateau, which are $\sim 10^3$ times lower than those of the Himalayas. *Vance et al.* [2003] has reported one mean catchment erosion rate for the southward drained Tibetan part (~ 1.2 mm/yr), however he did not correct for possible glacial erosion contribution ($\sim 20\%$ of the watershed is glaciated). It is of major importance to study more in detail the erosional capacity of glaciers and the Tibetan Plateau, because they have the potential to bias the analysis of catchment wide cosmogenic nuclide erosion rates, for example.

Chapter 3

Precipitation data evaluation

3.1 Introduction

To study the influence of temporal and spatial distribution of precipitation onto erosion processes and landscape is the central thematic of this thesis. In the Himalayas, precipitation is very difficult to measure due to the inaccessibility of the terrain and the lean rainfall gauging network. Furthermore, characterizing the highly variable spatio-temporal structure of rainfall at a single point is by no means straightforward [*Tustison et al.*, 2001]. Measuring rainfall in both space and time is much more adequate to the problematic addressed here. Today more and more sophisticated precipitation datasets exist, providing precipitation information on various temporal and spatial resolutions. Some of these datasets are based on spatial interpolations of in-situ observations, some are derived from remote sensing observations and others fuse both into one single product.

A considerable effort has been made recently to apply modern precipitation observation to the Himalayan region [e.g. *Barros et al.*, 2004; *Lang and Barros*, 2004; *Anders et al.*, 2006b; *Bookhagen and Burbank*, 2006, 2010; *Kamal-Heikman et al.*, 2007; *Yatagai and Kawamoto*, 2008] and some new outstanding observations have been possible by comparing these observations with landscape. For example *Bookhagen and Burbank* [2006] determined a very good image on the coupled distribution of precipitation and topography, and exploited these findings later to calculate the annual hydrological budget on the scale of the entire Himalayan range [*Bookhagen and Burbank*, 2010]. Similarly, *Anders et al.* [2006b] evaluated the role of orographic effects and [*Kamal-Heikman et al.*, 2007] tested a hydrological model for the eastern Himalayas. However, the quality of the data has never been really evaluated in the Nepal Himalayas.

In short, high-quality precipitation data are important for a wide community of researchers in Earth Sciences, for example people working in hydrology, short-term mass transfers, geochemical cycles and those investigating the possible influence of climate and erosion on the tectonic evolution of mountain belts. Hence, their is a strong need to evaluate the available data, in order to be able to know their limitations and strengths, and justify the choice of data for my analysis. Here, I will demonstrate that

existing precipitation datasets, particularly those derived from remote sensing techniques, show large discrepancies in the Himalayas, which I will evaluate against each other and with ground-based rain gauge data.

I will present this chapter in form of an article, published in the peer-review journal *Geochemistry, Geophysics, Geosystems*.

Geochemistry Geophysics Geosystems G3

Article
Volume 12, Number 7
28 July 2011
Q07023, doi:10.1029/2011GC003513
ISSN: 1525-2027

Published by AGU and the Geochemical Society

Evaluation of precipitation data sets along the Himalayan front

C. Andermann
Geosciences Rennes, Universite de Rennes 1, Campus de Beaulieu, F-35042 Rennes, France (christoff.andermann@univ-rennes1.fr)

Geosciences Rennes, CNRS/INSU, UMR 6118, Campus de Beaulieu, F-35042 Rennes, France

Remote Sensing Group, Geology Institute, TU Bergakademie Freiberg, Bernhard-v.-Cotta Str. 2, D-09596 Freiberg, Germany

S. Bonnet
Geosciences Rennes, Universite de Rennes 1, Campus de Beaulieu, F-35042 Rennes, France

Geosciences Rennes, CNRS/INSU, UMR 6118, Campus de Beaulieu, F-35042 Rennes, France

R. Gloaguen
Remote Sensing Group, Geology Institute, TU Bergakademie Freiberg, Bernhard-v.-Cotta Str. 2, D-09596 Freiberg, Germany

[1] Precipitation is one of the main factors which controls surface processes and landscape morphology. Large orogenic belts such as the Himalayas control precipitation distribution as a result of orographic effects due to their prominent relief. However, precipitation is difficult to monitor because mountain regions are largely inaccessible and therefore not sufficiently covered by ground-based gauge stations. The complexity of orographic effects resulting from the interaction between elevation and climatic processes and the lack of precise meteorological data thus limit our understanding of climatic influence on landscape formation. Therefore, high-quality precipitation observations with good spatiotemporal coverage are needed. Here we evaluate five gridded precipitation data sets derived from remote sensing and interpolation of rain gauge data with ground-based precipitation measurements. First, we evaluate the bulk error of each data set, then we evaluate the temporal quality of data within five watersheds, and last we compare the spatial performance along seven swath profiles across strike to the Himalayan range in Nepal. Our evaluation shows that the data sets vary significantly along the orographic front and get more consistent toward the adjacent low-relief domains, while bulk errors are largest during monsoon season. In particular, where topographic gradients are important, the resolution of gridded data sets cannot incorporate small-scale spatial changes of precipitation. We show that the data set derived from interpolation of gauge data performs best in the Himalayas. This study gives an overview on the applicability of precipitation data sets within the Himalayan orographic domains where relief has a pronounced impact on precipitation.

Components: 7500 words, 9 figures, 1 table.

Keywords: Himalaya; Nepal; climate; orography; precipitation; remote sensing.

Index Terms: 1824 Hydrology: Geomorphology: general (1625); 1843 Hydrology: Land/atmosphere interactions (1218, 1631, 3322); 1854 Hydrology: Precipitation (3354).

Received 12 January 2011; **Revised** 15 April 2011; **Accepted** 15 April 2011; **Published** 28 July 2011.

Andermann, C., S. Bonnet, and R. Gloaguen (2011), Evaluation of precipitation data sets along the Himalayan front, *Geochem. Geophys. Geosyst.*, *12*, Q07023, doi:10.1029/2011GC003513.

1. Introduction

[2] The spatial distribution and the temporal variability of precipitations governs vegetation growth, hydrology and surface mass transport on Earth [e.g., *Istanbulluoglu and Bras*, 2006], whereas precipitation is proposed to be a first-order control on landscape morphology [*Tucker and Slingerland*, 1997; *Anders et al.*, 2008; *Bonnet*, 2009] as well as on the interplay between climate, erosion and tectonics [*Willett*, 1999; *Bonnet and Crave*, 2003; *Reiners et al.*, 2003; *Whipple and Meade*, 2006; *Whipple*, 2009]. Consequently, precipitations measurements with good spatial and high temporal resolution, recorded over a long time span are crucially needed to better understand the impact of precipitation on landscape [*Barros et al.*, 2006]. This is particularly the case in mountains where local extreme events are much more frequent than in the adjacent flatlands [*Wulf et al.*, 2010].

[3] Mountain topography controls regional precipitation patterns through orographic effects [*Roe et al.*, 2003; *Roe*, 2005; *Bookhagen and Burbank*, 2006; *Bookhagen and Strecker*, 2008]. In mountainous environments, precipitation distribution can also change on short distances and within short periods of time [*Anders et al.*, 2006]. High amplitude rainfall events are often very localized [*Nesbitt and Anders*, 2009], whereas their impact on landscape forming can be enormous. Landslides, for example, are largely controlled by precipitation intensity and accumulation over time [*Gabet et al.*, 2004; *Dahal and Hasegawa*, 2008]. Such extreme precipitation events are usually localized and therefore not recorded by widely scattered ground-based meteorological stations (e.g., in Nepal).

[4] Remotely sensed precipitation data are now available at moderate to high resolution, some over long time spans to allow a reasonable comparison of local precipitation patterns with respect to landscape morphology. Several gridded data sets, with varying temporal and spatial resolution, are available (Figure 1). The measurements are derived from ground and/or satellite observations. Most remotely sensed precipitation data sets are based on multisensor algorithms, merging ground measurements, low-orbiting geostationary satellite observations, and global ground-based gauge databases [e.g., *Yatagai et al.*, 2009]. Rain gauge stations provide highly accurate local information for the point of observation but their spatial representativity is questionable [*Tustison et al.*, 2001], particularly in case of local rainfall gradients such as ridge-valley gradients [*Barros et al.*, 2004; *Bhatt and Nakamura*, 2005; *Anders et al.*, 2006]. In the Himalayas, precipitations indeed varies between ridges and valleys [*Barros et al.*, 2004], therefore a single rain gauge station does not register variability at the scale of kilometers. Rain gauge data must consequently be compared to their associated pixel value of any remotely measured rainfall information with great caution, especially at high temporal resolution. Gridded data sets (satellite observations or spatial interpolation of gauge data) provide good information on the spatial precipitation distribution, however with potentially large errors within each point of the grid space (pixel), particularly when resolution of the data is larger than the spatial variability of rainfall.

[5] Precipitation measurements from remote platforms are carried out using active precipitation radar (PR), passive microwave radiometer (MWR), such as Tropical Rainfall Measuring Mission (TRMM), Microwave Imager (TMI) and infrared radiometer (IR) sensors [*Ushio et al.*, 2009; *Huffman et al.*, 2007]. The PR sensor is an active precipitation radar, which can record the three-dimensional structure of rainfall distribution [*Kummerow et al.*, 1998]. IR observations are made at the top of the clouds and are therefore indirect measurements [*Huffman et al.*, 2007]. Microwave measurements detect the radiation emitted by the water fraction in the vertical profile of the atmosphere [*Kubota et al.*, 2007]. For all these techniques, differences between ground and remote observed quantities come from the inability to incorporate local conditions in the sensor algorithms. In particular property changes of precipitates, affecting polarization, scatter and absorption, due to slope, snow, ice and orographic effects, are not well accounted for [*Vicente et al.*, 2002]. In general, short-lasting and low precipitation rates as well as frozen precipitates are badly detected from the remote sensors. Hence, at high elevation, where precipitation comes mainly as snow, as light drizzle and during short intense storms remote measurements often underestimate the actual rates. The TRMM satellite system is so far the only platform in operation

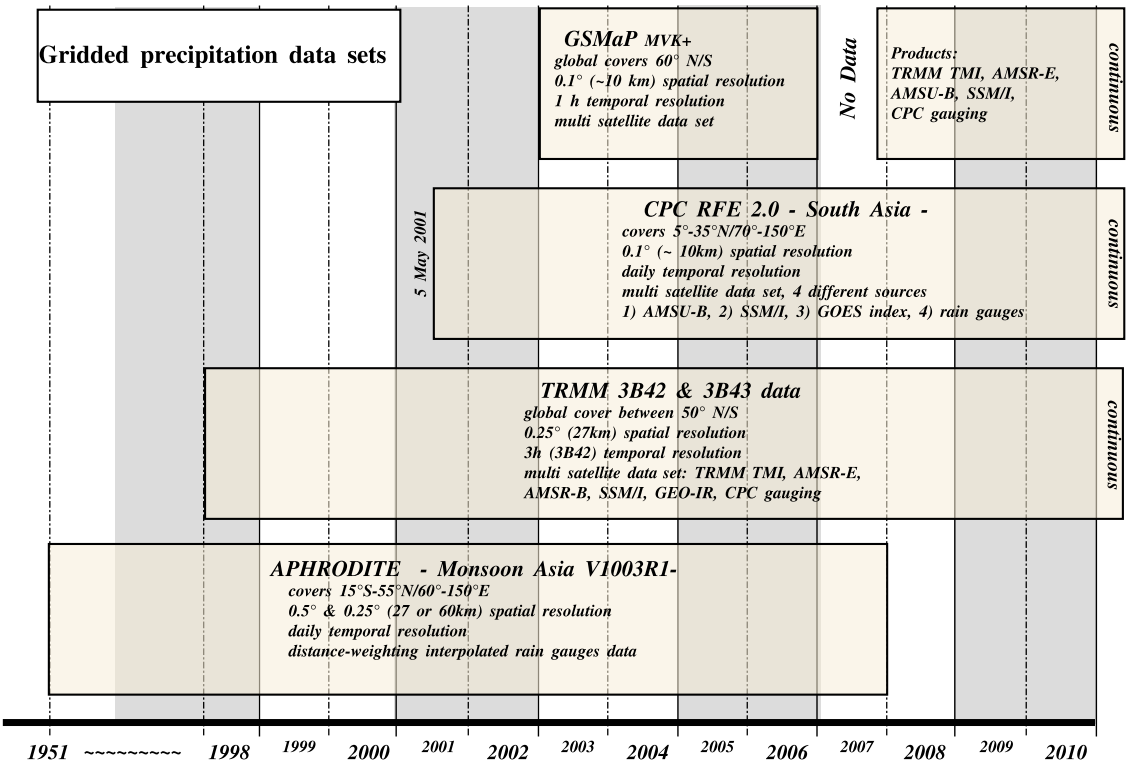

Figure 1. Schematic overview of the data sets compared in this work (APHRODITE, TRMM-3B42 (3B43), CPC-RFE, and GSMaP) and their availability timeline, spatiotemporal resolution, and data input. *Bookhagen and Burbank*'s [2006] TRMM-2B31 data are not shown here since only one mean layer for 10 years (1997–2007) is available. TRMM-2B31 has a ~4 km spatial resolution and is derived from PR and TMI sensor input.

designed specifically for rainfall monitoring from space [*Kummerow et al.*, 2000]. It will be succeeded by the Global Precipitation Measurement Mission (GPM), in 2013.

[6] In this study we compare four gridded spatio-temporal precipitation data sets (Figure 1) and one mean annual compilation of raw TRMM-2B31 data by *Bookhagen and Burbank* [2006], with ground-truth precipitation gauge data. We focus on precipitation estimates along the Himalayan front, where previous studies [*Anders et al.*, 2006; *Bookhagen and Burbank*, 2006; *Yatagai and Kawamoto*, 2008] show along-strike precipitation peaks which are strongly controlled by topography. The precipitation data sets are tested three ways (Figure 2). First, we perform a bulk comparison of gridded data set with ground station data. Second, we test the performance of each data set in five small watersheds for various temporal resolutions (daily, monthly, annual). Third, we compare precipitation distribution across the orographic barrier and its relation with elevation along seven swath profiles, orthogonal to the Himalayan range.

2. Data and Methods

2.1. Gridded Precipitation Data Sets

[7] We give here a general description of the precipitation data sets tested here (Figure 1). More technical specifications can be found in Text S1.[1]

2.1.1. APHRODITE

[8] APHRO_MA_V1003R1 (Asian Precipitation Highly Resolved Observational Data Integration Towards Evaluation of Water Resources, Monsoon Asia, Version 10, hereafter referred to as APHRODITE) data set is developed by a consortium

[1] Auxiliary materials are available with the HTML. doi:10.1029/2011gc003513.

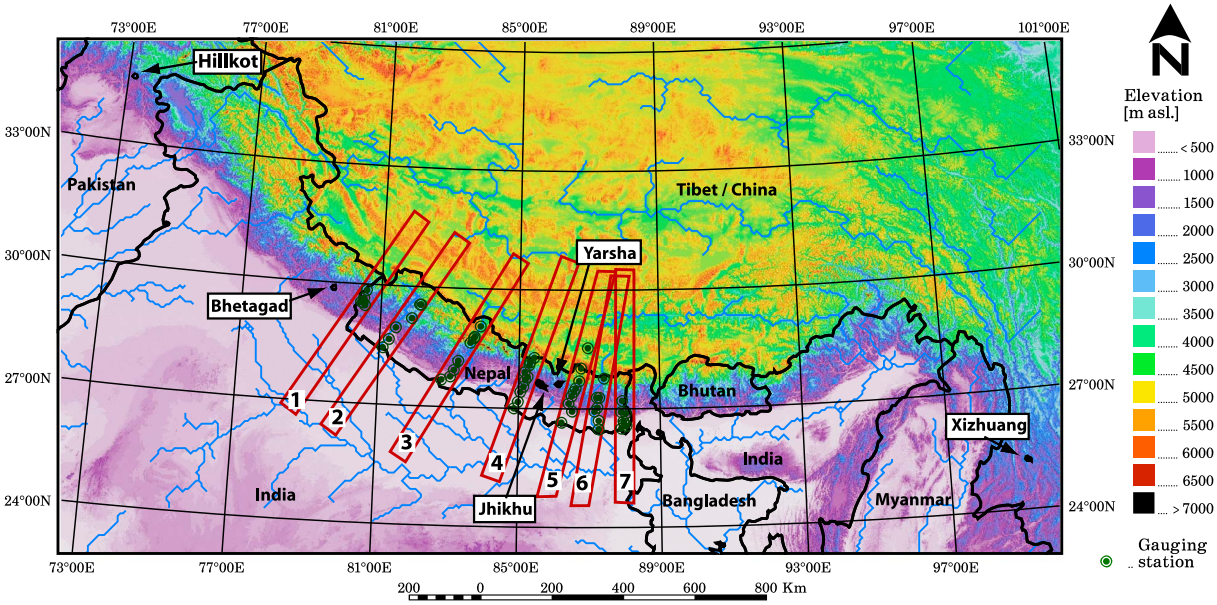

Figure 2. Topographic map of the Himalayan region. Arrows point at the location of the five PARDYP watersheds, where the data sets have been tested on a small scale for temporal accuracy. Red polygons outline the seven swath profiles across the Himalayan range, and green dots are the gauge station locations.

between the Research Institute for Humanity and Nature (RIHN) Japan and the Meteorological Research Institute of Japan Meteorological Agency (MRI/JMA). This consortium develops precipitation products with varying resolution and for several Asian subregions. We used here the latest version daily data set for monsoon Asia (60–155°E and 15°S–55°N) [*Yatagai et al.*, 2009; *Xie et al.*, 2007]. APHRODITE is a distance weighted interpolated data set from precipitation gauge stations. Depending on availability, between 5,000–12,000 stations are considered for the interpolation. Data are available for a statistically robust time span of more than 50 years, 1951–2007. This data set has daily resolution and 0.25° (~30 km) spatial resolution. The interpolation algorithm incorporates orographic correction of precipitation. *Yatagai and Kawamoto* [2008] show for the Himalayas that an earlier version of APHRODITE correlates well with monthly active TRMM-PR (2A25) measurements, however they show that TRMM-2A25 considerably underestimates precipitation with respect to APHRODITE.

2.1.2. CPC-RFE

[9] CPC-RFE 2.0 (Climate Prediction Center–Rainfall Estimates) is a precipitation product for the South Asian region published by the CPC of National Oceanic and Atmospheric Administration (NOAA), United States Agency for International Development (USAID) and United States Geological Survey (USGS). The product provides real time daily precipitation information with a good spatial resolution of 0.1° (~10 km) for the area 70–110°E and 5–35°N. Data from CPC-RFE are available since May 2001 and continuously updated. RFE2.0 combines 4 different primary products, of which, one is a rain gauge network and three are remotely sensed. The four input products are (1) GTS global gauge network (~1000 stations); (2) GOES Precipitation Index (GPI), a precipitation index derived from Geostationary Operational Environmental Satellites (GEOS) geostationary weather satellites (IR data); (3) Special Sensor Microwave/Imager (SSM/I) observations; and (4) Advanced Microwave Sounding Unit-B (AMSU-B), on board of NOAA-K, -L, -M satellites. In general all data sources have similar large-scale distribution patterns [*Xie et al.*, 2002]. The three satellite products are merged through maximum likelihood estimation methods. In comparing CPC-RFE and ground gauge stations, *Shrestha et al.* [2008] have run a hydrological model in the Bagamati basin of the middle and lower Nepal Himalayas. They show that CPC-RFE capture the occurrence of rainfall events but considerably underestimate rainfall amounts.

2.1.3. GSMaP

[10] The Global Satellite Mapping of Precipitation, passive microwave radiometer (GSMaP MVK+) data set was developed in order to provide high-

precision and high-resolution global precipitation maps from satellite observations. The project is sponsored by Core Research for Evolutional Science and Technology (CREST) of the Japan Science and Technology Agency (JST), by Japan Aerospace Exploration Agency (JAXA) and the Precipitation Measuring Mission (PMM) Science Team. GSMaP data are a global data set (60°*N/S*), available since the end of November 2002 and is provided in almost real time (with a ~10 month data gap in 2007). The data have 0.1° (~10 km) spatial resolution and 1 h temporal. The project aims to develop an advanced microwave radiometer algorithm based on a deterministic rain-retrieval algorithm and the production of precise high-resolution global precipitation maps [*Ushio et al.*, 2009; *Kubota et al.*, 2007]. The data incorporate MWR measures from TRMM-TMI, SSM/I, Advanced Microwave Scanning Radiometer–EOS on board of AQUA satellite (AMSR-E), AMSU-B and IR. Because of its high spatiotemporal resolution this data set is potentially the most interesting for analyzing climatic influence on surface processes and the links between rainfall distribution and topography. *Dinku et al.* [2009] compared GSMaP MVK+ with several other satellite derived precipitation data sets and gauge stations over the whole of Colombia. They report that GSMaP MVK+ underestimates precipitation in mountains, where the topography is complex.

2.1.4. TRMM-3B42

[11] The Tropical Rainfall Measuring Mission (TRMM) is a joint collaboration between JAXA and the United States of America National Aeronautics and Space Administration (NASA). TRMM-3B42, is a global multisatellite precipitation analysis data set. It combines several instruments, has a 0.25° (~30 km) spatial and 3 h temporal resolution, and is available within a global belt, 50°N/S latitude [*Huffman et al.*, 2007; *Kummerow et al.*, 2000]. Basically it is a set of MWR estimates from TRMM-TMI, SSM/I, AMSR-E and AMSU-B, whereas missing pixels are filled with IR observations compiled by CPC [*Huffman et al.*, 2007]. The data are corrected with the monthly field ratios between TRMM-3B43 (monthly compiled version of 3B42) and gauge stations. TRMM-3B42 has been applied successfully for measuring precipitation patterns in many studies on a global [*Tian and Peters-Lidard*, 2010] and local scale [*Kamal-Heikman et al.*, 2007; *Bookhagen and Strecker*, 2008; *Bookhagen*, 2010]. However, underestimation in mountainous regions, in particular with high snowfall contribution [*Kamal-Heikman et al.*, 2007], has been reported.

2.1.5. TRMM-2B31

[12] *Bookhagen and Burbank* [2006] have developed their own precipitation compilation from primary TRMM-2B31 orbital data (not gridded). Despite a common platform and name, TRMM-2B31 and TRMM-3B42 data set do not use the same sensor (except for TMI). TRMM-2B31 is principally derived from the active PR sensor, found only on board of the TRMM satellite [*Bookhagen and Burbank*, 2006]. Here TRMM-TMI is used to fill unobserved areas. TRMM-2B31 data have a spatial resolution of 0.05° (~4 km), one of the finest grid size available at the moment. However its temporal resolution is 1 month, averaged over several years. The PR sensor makes one or two snapshots of the Earth surface per day (depending on the latitude). Therefore, measurements are infrequent and have to be averaged over a long time span (here: 11 years, 1997–2007) to provide reliable rainfall data [*Bookhagen and Burbank*, 2006]. This data set has been successfully applied for measuring precipitation patterns in the Andes [*Bookhagen and Strecker*, 2008] and the Himalayas [*Bookhagen and Burbank*, 2006, 2010].

2.2. Rain Gauge Data

[13] We compared precipitation estimates from each product with ground measurements derived from the 55 rain gauge stations located in Nepal (54) and on the Tibetan Plateau (1): Figure 2 (see also Text S1). Most of the data are obtained from the Department of Hydrology and Meteorology Nepal DHM (~30 years data, numbers 1–51, Text S1). Three high elevation stations (3560, 4260 and 5050 m above sea level (asl), numbers 53–55) in the Khumbu-Everest region are kindly provided by the Ev-K2-CNR, Pyramid-SHARE project, while the station for the Tibetan Plateau (number 52) comes from the LocClim FAO database (http://www.fao.org/nr/climpag/pub/en0201_en.asp). We also compared the precipitation data sets with ground information from rain gauge stations in five watersheds located in Pakistan, India, Nepal (2) and Yunnan/China (Figure 2) maintained within the People and Resource Dynamics Project (PARDYP) program, realized by International Centre for Integrated Mountain Development (ICIMOD) between 1997 and 2006. Note that the 51 gauge stations provided by DHM have been used to generate the APHRODITE data set so there

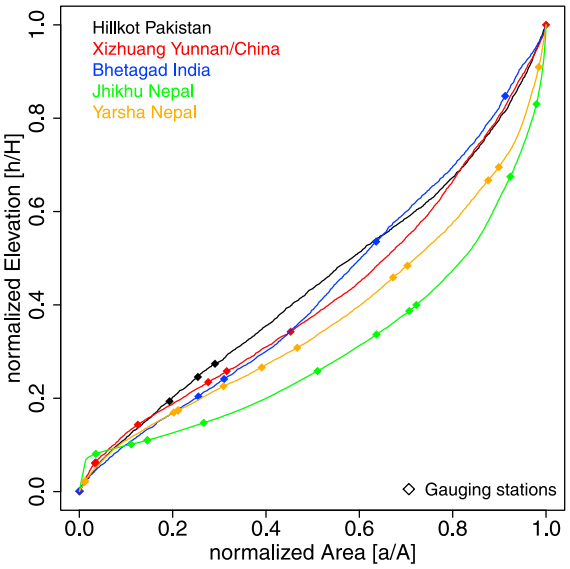

Figure 3. Hypsometric profiles of each PARDYP watershed with gauge station distribution. Gauge station elevation is plotted on the y axis as the respective cumulative normalized elevation fraction of each watershed. Area on the x axis represents the cumulative fraction of area within the watershed for each respective elevation above mean sea level.

is a dependency problem between APHRODITE and these gauge station data. They might have also served to calibrate any of the other data sets. However, this is not the case for all the precipitation gauge data of the five PARDYP watersheds, as well as the three Pyramid-SHARE stations (53–55), which provide independent data that have not been used to generate or calibrate any of these data sets. We presume the uncertainties of all precipitation gauge measurements to be ≤10%.

2.3. Bulk Validation of Data

[14] To give an overview of the bulk error of each data set at the scale of Nepal, we compared each data set with all rain gauge stations on a monthly scale. For this purpose, we subtracted the monthly accumulated ground measurements of each station from the corresponding monthly sum of each data set and average the difference considering all the stations. This comparison was carried out considering only the data for the years 2003 and 2004. Because some of the 51 DHM stations might have been used to calibrate or generate some of the products (in particular APHRODITE), we also evaluate the bulk error by considering only the stations that have not been used in the calibration or generation of products (the three Pyramid-SHARE stations and stations within the five PARDYP watersheds). Because gauge data are not always available for the same period, we sampled precipitation and rain gauge data for months of common availability between 1997 and 2006 and calculated then the monthly bulk error of each product.

2.4. Calculation of Basin-Wide Precipitation in Five Selected Watersheds

[15] We compared the precipitation data sets with ground information from rain gauge stations in the five watersheds maintained within the PARDYP program (Figure 2). The five relatively small watersheds (15–111 km^2, Table 1) have been equipped with several measuring devices to obtain meteorological, hydrological and erosional parameters. In each watershed, data are available for 4 to 12 rainfall stations (Table 1) for 5 to 10 years, providing a very good data set of ground truth information to calibrate remote sensing information [*Andermann et al.*, 2010]. The station elevation distribution is homogeneous for Bhetagad, Jhikhu Khola and Yarsha Khola basin (Figure 3), whereas in Xizhuang basin a large part between 2200 and 3000 m asl is not covered by stations. The higher part of the Hillkot basin (elevation >1800 m asl) is not covered by rain gauge stations (Figure 3). In each catchment, we interpolated (nearest neighbor interpolation technique) the available gauge data to a mean basin-wide value. The mean basin-wide value was then extracted from each data set. Since TRMM-2B31 data do not exist with high temporal resolution (daily nor monthly) it was not included in the comparison of products here.

2.5. Calculation of Precipitation Along Swath Profiles

[16] We compared the precipitation data sets during the years of common availability of all data sets, 2003 and 2004 (Figure 1), along seven swath profiles perpendicular to the Himalayan front (Figure 2). Each swath profile is 60 km wide and 650 km long. Precipitation and elevation along one profile represent the average over the swath width of the profile. Topography information is derived from the Shuttle Radar Topographic Mission (SRTM) Version 4 (A. Javis et al., Hole-filled seamless SRTM data V4, International Centre for Tropical Agriculture (CIAT), 2008, available from http://srtm.csi.cgiar.org) with a spatial resolution of

Table 1. Overview of the Selected Five PARDYP Watersheds[a]

Name	Region/Country	Area (km^2)	Elevation Range (m asl)	Catchment Orientation	Number of Stations	Literature
Bhetagad	Uttaranchal/India	24	1000–2000	north	5	*Kothyari et al.* [2004]
Hillkot	Pakistan	15	1500–2700	southwest	4	unpublished
Jhikhu Khola	Nepal	111	800–2200	southeast	11	*Merz* [2004]
Xizhuang	Yunnan/China	34	1750–3100	east	8	*Jianchu et al.* [2005]
Yarsha Khola	Nepal	53	1000–3000	southwest	12	*Merz* [2004]

[a]Area is the drainage area, and range is the elevation minima and maxima. Number of stations indicates the number of available precipitation gauge stations which have been used to interpolate mean basin-wide precipitation rates. See also Figure 2.

~90 m. Along the profiles, precipitation totals were compiled annually as well as for monsoon (June to September) and for the nonmonsoon season (October–May).

3. Results

[17] We present the results of the evaluation of precipitation data sets, first the bulk difference between fully independent and semi-independent gauge data and precipitation data sets. Second, we present results within the five PARDY catchments, allowing us to test the temporal quality of data, from annual to daily scale. Last, we present results along the swath profiles perpendicular to the Himalayan chain and examine the spatial variations of data with regard to elevation.

3.1. Bulk Error and Comparison of Products

[18] The annual bulk comparison between products and fully independent gauge data (Pyramid-SHARE and PARDYP), which have not been used to generate nor calibrate any product, including APHRODITE shows that CPC-RFE, TRMM3B42 and GSMaP underestimate rain gauge data up to 400 mm yr^{-1}, while TRMM-2B31 considerably overestimates (~600 mm/yr) the independent data set (Figure 4a). Precipitation is mainly underestimated during monsoon season (CPC-RFE 52 mm/yr, TRMM3B42 77 mm/yr, GSMaP 130 mm/yr), while APHRODITE (maximal 12 mm/yr) does not significantly differ from gauge data, whatever the season considered. Because of its temporal resolution, TRMM-2B31 cannot be compared to rain gauge

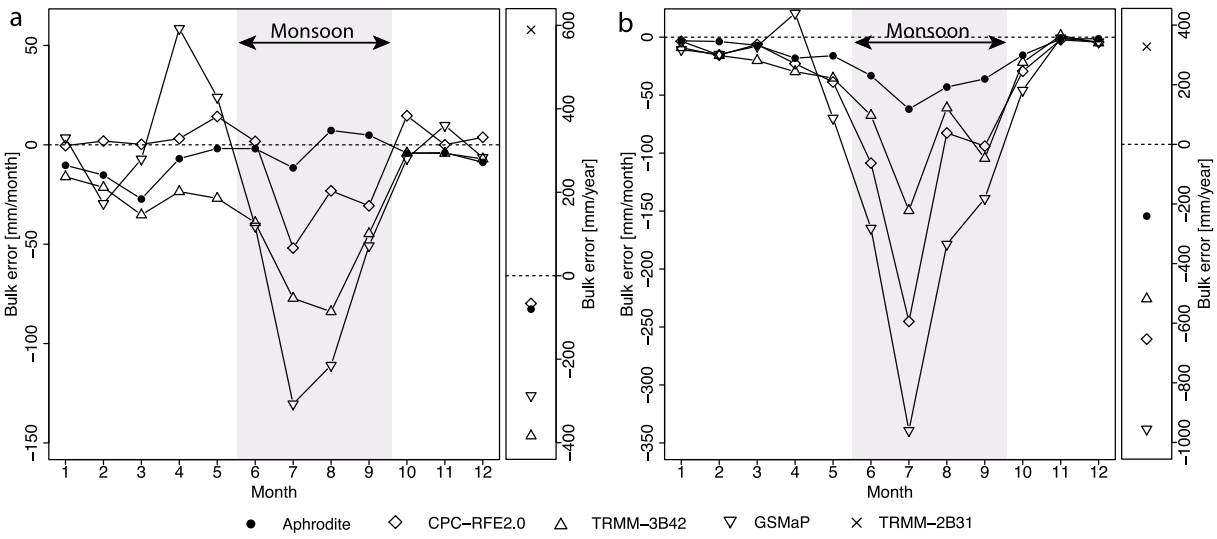

Figure 4. Monthly and annual bulk error plots of the compared precipitation data sets (APHRODITE, CPC-RFE, GSMaP, TRMM-3B31, and TRMM-2B42). Errors represent the mean accumulated sum (monthly or annual) of precipitation gauge data subtracted from the precipitation data set. (a) Bulk error derived from independent gauge stations. (b) Bulk error for all 51 DHM stations in Nepal, which have been partially used to calibrate or generate the here evaluated data sets. Stations and data represent the 2 years 2003 and 2004 (1997–2007 in case of TRMM-2B31). Because of its temporal resolution, TRMM-2B31 was not included in the monthly evaluation.

data at the monthly scale. The same conclusions could be done considering the 51 rain gauge data from DHM as a reference (Figure 4b). However, these stations have been used to generate APHRODITE, and some stations may have been used to calibrate all the other products. Despite this possible dependency problem, CPC-RFE, TRMM3B42 and GSMaP always show a significant underestimation of precipitation whereas TRMM-2B31 overestimates gauge data, but to a lesser degree than with independent data (328 mm/yr).

[19] Results from the bulk error analysis are also reflected in the intercomparison of the data sets in map view (Figure 5). The available gridded products show contrasting patterns of annual precipitation along the Himalayas. All products show high precipitation rates along the mountain chain, but with different amplitudes and patterns. Most products show the westward decrease of precipitation already described by *Bookhagen and Burbank* [2006] as well as the two along-strike rainfall peaks they also described. They are clearly expressed by TRMM-2B31 because of the higher spatial resolution of this product. The comparison of the remote products with respect to APHRODITE shows that all products differ considerably in detail (Figures 5f, 5g, 5h, and 5i). It illustrates an overestimation of precipitation by TRMM-2B31 with respect to APHRODTIE, possibly because APHRODITE cannot depict small-scale changes because of its moderate resolution (0.25°), but also because peak precipitation rates by TRMM-2B31 are likely overestimated, as the authors acknowledge themselves [*Bookhagen and Burbank*, 2010]. When compared to APHRODITE, remotely sensed products CPC-RFE, GSMaP and TRMM3B42 significantly underestimate precipitation in the eastern and central part of the Himalayas (Figures 5g, 5h, and 5i), while CPC-RFE (Figure 5g) tends to overestimate precipitation in the Western part. All data sets show similar low precipitation rates (<0.5 m/yr) on the Tibetan Plateau and moderate ones (0.5–1 m/yr) in the Indian foreland.

3.2. Comparison of Data Within the Five PARDYP Watersheds

[20] Within the five PARDYP watersheds, precipitation estimates by APHRODITE and TRMM-3B42 fit measurements derived from ground gauge stations, both at the monthly (Figures 6 and 7) and annual scales (Text S2). The correlation coefficient between monthly precipitations derived from gauge data and data sets is 0.87 for APHRODITE and 0.69 for TRMM-3B42 when one considers the five catchments all together (Figure 7). The best correlation is found in the Jhikhu Khola catchment with r^2 of 0.98 (APHRODITE) and of 0.82 (TRMM-3B42). APHRODITE always fit very well the monthly precipitation derived from gauge data (correlation coefficient between 0.83 and 0.98) except in the Hillkot catchment (Figure 6) where it gives higher estimates than the interpolated gauge data during monsoon season. This is likely the consequence of the lack of gauge stations at high elevations in this basin (Figure 3). Indeed, *Bhatt and Nakamura* [2005] and *Barros et al.* [2004] report strong ridge-valley gradients on a basin scale in the Himalayan front. If we assume an orographic gradient, with lower precipitation in the valley bottom than close to the ridges, the absence of stations at high elevation in the Hillkot catchment will result in an underestimation of mean basin-wide precipitation. Note that APHRODITE also correlates very well with precipitation derived from gauge stations at the daily scale in the Jhikhu Khola catchment (Figure 8). This correlation is not observed with the other data sets nor in the other basins. Monthly precipitation derived from TRMM-3B42 usually correlates well with gauge data (correlation coefficient between 0.78 and 0.84; Text S2) except again in the Hillkot catchment, likely for the same reason as discussed above (correlation coefficient of 0.52). Overall, CPC-RFE and GSMaP data do not match the ground information at the annual and monthly scale (Figure 6).

[21] In contrast to observations made by *Anders et al.* [2006] and *Kamal-Heikman et al.* [2007], using remote precipitation measurements (TRMM/PR and TRMM-3b42), our annual precipitation estimates from APHRODITE or from interpolated rain gauge data exceed annual water discharge recorded at the catchment outlet of the five PARDYP watersheds. In Jhikhu Khola catchment for example, annual precipitation measured by APHRODITE, TRMM-3B42 and by gauge stations (~1400 mm/yr) is roughly 3.5 times as high as the annual specific discharge (~400 mm/yr) recorded at the basin outlet [*Merz*, 2004]. As pointed out by *Bookhagen and Burbank* [2010] for the Himalayas, the hydrologic budget is only correct when evapotranspiration and snow and glacier melt processes are taken into account. High snowfall contribution on the Tibetan Plateau is difficult to detect by remote sensors and is shown to lead to considerable underestimation of basin-wide water budgets [*Kamal-Heikman et al.*, 2007].

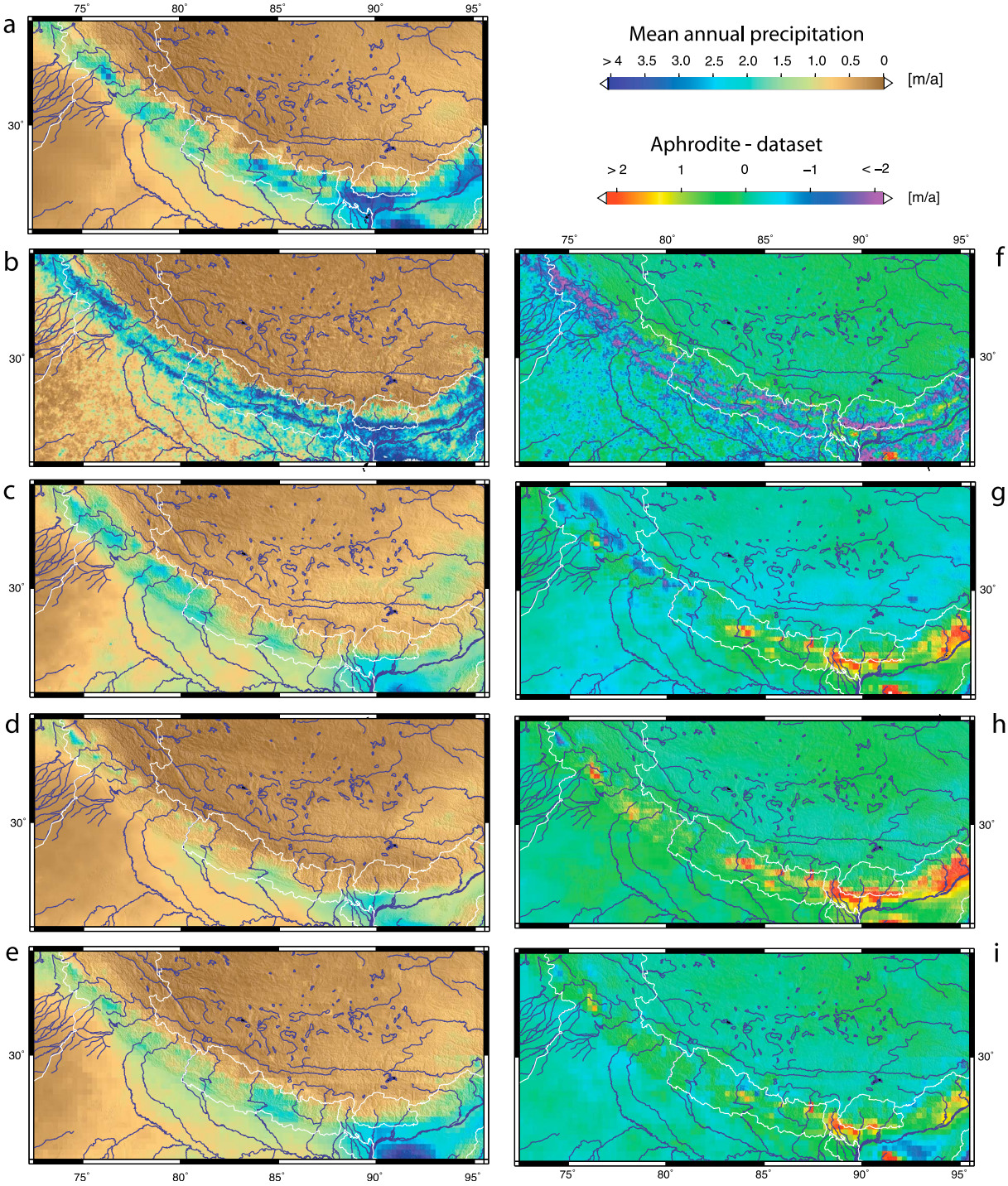

Figure 5. Mean annual precipitation distribution of the five tested precipitation data sets for their common availability (2003 and 2004, TRMM-2B31 1997–2007): (a) APHRODITE, (b) TRMM-2B31 [*Bookhagen and Burbank*, 2006], (c) CPC-RFE, (d) GSMaP, and (e) TRMM-3B42. Figures 5f–5i illustrate the differences between the data sets in respect to APHRODITE (APHRODITE - data set): (f) APHRODITE versus TRMM-2B31, (g) APHRODITE versus CPC-RFE2.0, (h) APHRODITE versus GSMaP, and (i) APHRODITE versus TRMM-3B42.

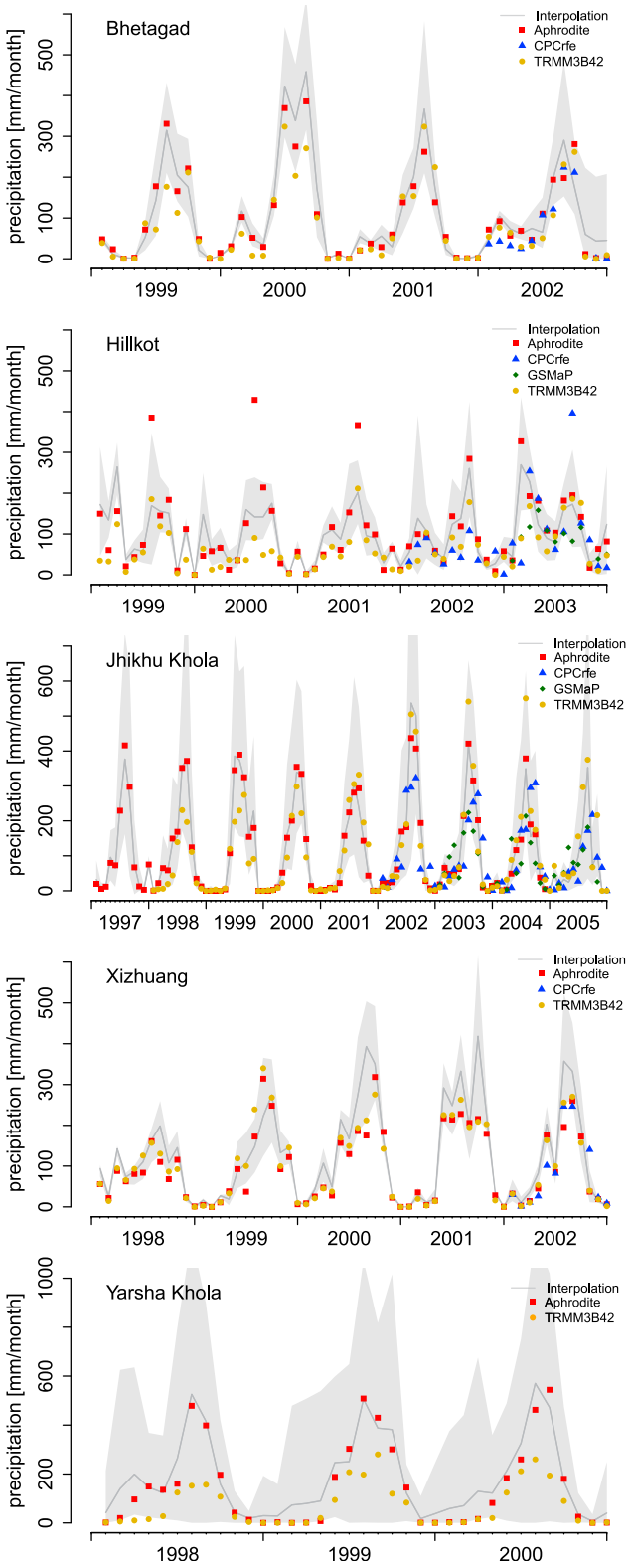

Figure 6. Monthly mean basin-wide precipitation rates from gridded precipitation data and basin-wide interpolated rain gauge stations for the five watersheds. Gray shading represents the range of interpolated gauge data. The upper and lower limits of the range represent the minimal and maximal monthly sum of precipitation rates.

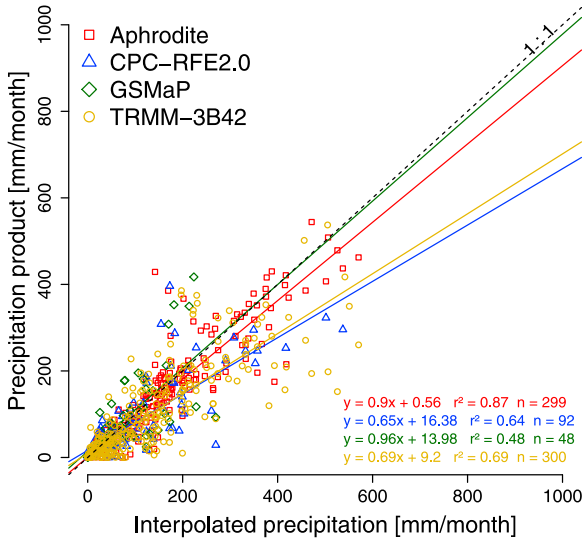

Figure 7. Correlation between monthly basin-wide precipitation rates from gridded data and basin-wide interpolation from station data. Data from all five watersheds is plotted here.

3.3. Comparison of Data Along the Seven Swath Profiles

[22] Evaluating the different data sets along swath profiles has the advantage to investigate precipitation distribution as a function of elevation. Swath profiles show mean precipitation over the swath width and average over local variations. Therefore, gridded data sets with the same resolution (e.g., TRMM-3B42 and APHRODITE) should match quantitatively. This is however not the case in our results (Figure 9).

[23] While the middle hills and the foreland are easily accessible, the High Himalayas are only sparsely covered with stations and the station elevation might not reflect the surroundings [*Bhatt and Nakamura*, 2005]. However, most existing rain gauge data indicate high precipitation rates in the Lesser Himalaya and a decrease at higher elevation, in the Higher Himalayas and on the Tibetan Plateau. Along most profiles (Figure 9 and Text S3), gauge data consequently document the orographic effect across the Himalayas, despite possible problems of point data vs. spatial data. Due to inaccessibility, gauge stations are generally situated in valleys, especially within the high Himalayan range (Text S3). Note that most stations used here are situated at mean swath elevation in the transition between the Indian Lowlands and the mountain front (e.g., stations 16, 17, 18, 19, and 20 along profile 3: Figure 9a and Text S3), whereas stations in the high mountain front are situated at minimum elevation of the swath profile (e.g., stations 12, 13, 14, and 15 along profile 3: Figure 9a and Text S3). Therefore, along profile 3 it is not clear if the decreasing trend defined by stations 18 and 14 is due to elevation or stations positioning. In contrast, thanks to the three Pyramid-SHARE stations (numbers 53–55), nearly all stations in profile 5 (Figure 9d) are situated close to mean elevation (Text S3). Here, the strong decrease in precipitation rates between stations 31 and 55, above 3000 m asl is likely the consequence of the orographic effects. Locally, the annual difference between two neighboring stations is remarkable, e.g., between stations 46 and 48 (profile 7, Text S3) or between stations 38 and 44 (profile 6, Figure 9g). In both cases the stations are almost at the same latitude but at different elevation, so they likely record different local annual precipitation variations linked to orography.

[24] For the data sets evaluated here, all seven swath profiles (Figure 9 and Text S3) illustrate the orographic effect of the Himalayan chain, on annual scale as well as during monsoon season (May–October). Depending on the data set, the amplitude of the orographically induced rainfall peak is more or less pronounced. The orographic influence during nonmonsoon season is much weaker, as already observed by *Bookhagen and Burbank* [2010]. Overall, all data sets are more or less consistent during nonmonsoon season.

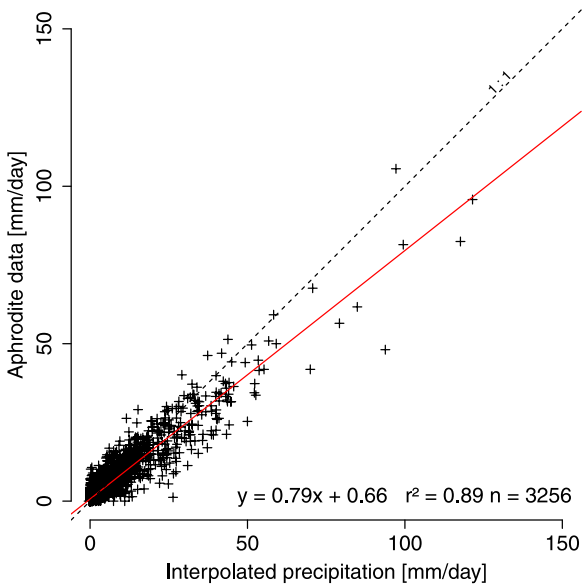

Figure 8. Daily correlation (Jhikhu Khola, Nepal) between APHRODITE data and basin-wide mean interpolated precipitation rates.

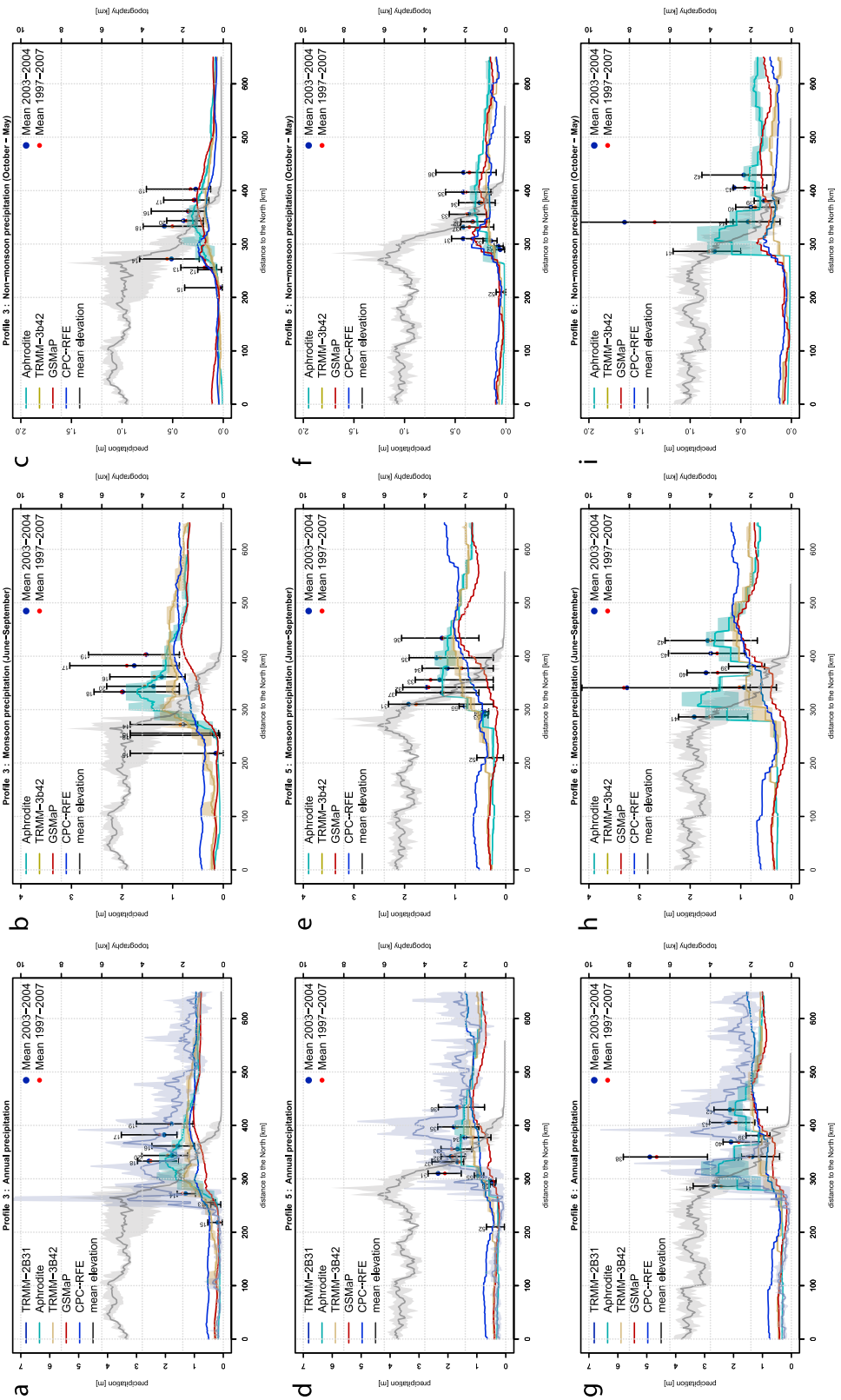

Figure 9. Precipitation swath profiles (a, b, and c) 3, (d, e, and f) 5, and (g, h, and i) 6 (further profiles are given in Text S3). Mean annual precipitation is given in Figures 9a, 9d, and 9g for each precipitation data set and swath profile, plotted against elevation from north to south. Shaded curves represent maximum, minimum, and mean values along each swath profile. The gridded data are for the years of common availability (2003 and 2004), while TRMM-2B31 [*Bookhagen and Burbank*, 2006] is for a 10 year time span (1997–2007). Gauge data are plotted as mean values for both time spans. Error bars show the long-term (~30 years) maxima and minima. Figures 9b, 9e, and 9h represent the monsoon season (June–September) only. Figures 9c, 9f, and 9i represent the nonmonsoon season (October–May).

[25] Along the Himalayan front, annual precipitation estimates at a given location along the profiles are always maximum for TRMM-2B31 data and minimum for GSMaP, the difference being often as large as two- to threefold (Figures 9a, 9d, and 9g). Between these two extreme data sets, APHRODITE usually shows higher estimates than TRMM-3B42 and CPC-RFE data, except for profiles 1 and 2 (Text S3) where the latter delivers the highest values. The three Pyramid-SHARE project stations (independent to APHRODITE) fit very well with the APHRODITE data, on an annual as well as a seasonal scale (Figures 9d–9f). A striking feature is the large difference between TRMM-2B31 data set and all the other data sets when considering mean and maximum values, as well as the high frequency spatial variations of precipitations documented. This is a direct consequence of the high spatial resolution of this data set. Overall, most of the gauge stations usually plot near the mean value of the TRMM-2B31 product, except for some local examples (e.g., stations 27 and 29 in profiles 4; stations 12 and 13 in profile 3; stations 31 and 34 in profile 5; stations 38, 39 and 41 in profile 6: see Figure 9 and Text S3). The extreme values of the TRMM-2B31 product always exceed gauge values (e.g., extremely high precipitation values (>7000 mm/yr) for few pixels on profile 3, Figure 9a), as already noticed by *Bookhagen and Burbank* [2010] and *Anders et al.* [2006]. These extreme values likely overestimate real precipitation rates. Note that *Bookhagen and Burbank* [2006] used a network of rainfall stations to calibrate their TRMM-2B31 data; however, most of the stations we used here have not been used in their work. In general the swath profiles reflect the findings of the bulk error estimation (Figure 4).

[26] *Bookhagen and Burbank* [2010, 2006] demonstrated that precipitation profiles across the Himalayas mimic the topography. When the topography steadily increases from the Indian Lowland to the Tibetan Plateau, rainfall distribution is characterized by a single high peak of rainfall at elevation ~0.9 km. Conversely, for a two-stepped increase of topography, rainfall distribution shows two peaks of lower amplitude at ~0.9 km and 2.1 km (e.g., Figures 5b and 9g). This bimodal distribution of rainfall is visible in most of the TRMM-2B31 profiles we show here (e.g., profiles 1, 4, and 6). This particular distribution is also well depicted by the APHRODITE product in most cases (e.g., profiles 1, 4, and 6) but with a lower amplitude. However, this is usually not depicted by the other products, except in profile 1 (Text S3). Overall, all the products show the increase of precipitation rates at the front of the Himalayas. TRMM-3B42, GSMaP and CPC-RFE, however, do not describe correctly the precipitation distribution at elevations higher than 1 km. This result highlights the difficulty of remote sensing techniques to capture precipitation in areas with strong orographic effects. The direct comparison of TRMM-2B31 and TRMM-3B42 in the Andes already shows that TRMM-3B42 cannot detect the local orographic precipitation maxima, due to its moderate spatial resolution [*Bookhagen and Strecker*, 2008].

4. Discussion and Conclusion

[27] We show that existing gridded precipitation data sets as well as published sources [*Bookhagen and Burbank*, 2006] display large differences along the Himalayan orographic front. With the exception of CPC-RFE, all measurements correspond in low-relief landscapes (Indian Lowlands, Tibetan Plateau) and during nonmonsoon season. On the basis of comparison with independent ground observations (Figure 4a) we show that most remote products underestimate precipitation during monsoon season at the annual and monthly scale whereas TRMM-2B31 [*Bookhagen and Burbank*, 2006] overestimates precipitation at the annual scale. These problems of precipitation estimation are likely due to remote techniques and calibration procedures. They do not concern APHRODITE data, a product processed from gauge stations, which gives the best precipitation estimates when compared to independent ground observations (Figure 4a). However, the lack of stations at high elevation limits the accuracy of this data set.

[28] Most of the rain gauges used to calibrate CPC-RFE, GSMaP and TRMM-3B42 data are derived from the GTS network with reportedly poor spatial coverage in the Himalayas [*Yatagai and Kawamoto*, 2008], which might explain the underestimation of precipitation during monsoon season. Additionally, *Yatagai and Kawamoto* [2008] report that the GTS database includes erroneous entries in the Himalayan region, where 0 mm precipitation values were reported instead of missing values, thus resulting in underestimating precipitation. In the case of APHRODITE, up to 4.5 times as many stations as GTS were considered for interpolation and erroneous gauge data sets are excluded if other information existed for the interpolation space [*Yatagai and Kawamoto*, 2008]. Many difficulties in the estimation of precipitation from space may also arise from remote techniques themselves. Remote sensors cannot determine accurately snowfall which is the major

contribution at high elevation in the Himalayas, (>5000 m asl: [*Putkonen*, 2004]) and on the Tibetan Plateau. Data sets depending on IR observations are primarily sensitive to cloud-top temperature, whose calibration for estimating precipitation is a main source of uncertainty [*Huffman et al.*, 2007]. Finally, diurnal variations and the likeliness of the satellites to miss rainfall events, may participate to the discrepancy between the remote measurements. CPC-RFE, GSMaP and TRMM-3B42 are principally derived from MVR sensors, which have an irregular return interval and therefore, likely miss precipitation events [*Huffman et al.*, 2007].

[29] Our study also highlights some of the difficulties in evaluating remote precipitation products using rainfall gauge data. In the Himalayas, precipitation varies according to a wide range of spatial scales, from small-scale ridge-valley gradients [*Barros et al.*, 2004; *Bhatt and Nakamura*, 2005; *Anders et al.*, 2006; *Craddock et al.*, 2007] to large-scale orographic effects over the whole mountain [*Anders et al.*, 2006; *Bookhagen and Burbank*, 2006]. Ideally, the validation of any remote sensed product from gauge stations is only possible if the resolution of the products is sufficient to take into account the scale of spatial variability of precipitation. Hence, the coarse resolution of all products (Figure 1) introduce an inescapable problem in the validation procedure. For example, gauge stations in valleys within the High Himalayas (e.g., profile 3; see Text S3) likely introduce a bias in the reference value of precipitation they provide. We show that several stations, covering full elevation range, are necessary to represent the climatic situation correctly and to validate remotely sensed products. We also show that basin-wide precipitation measurement deduced from gauge data are significantly altered if elevation is not sufficiently covered by gauge stations (Hillkot watershed, Figure 6). The current gauge network within the High Himalayas is generally not sufficient to characterize orographic precipitation phenomena correctly.

[30] Along the Himalayan range, several precipitation products are of potential interest depending on the problem addressed. TRMM-2B31 is a good product when one wants to investigate rainfall patterns. This is of significant interest for example to understand the topographic influence on rain distribution. The use of this product is however, limited by its temporal resolution, which is not adequate to investigate, for example, event-scale processes. As also observed by *Bookhagen and Burbank* [2006], the rainfall peaks of TRMM-2B31 data along the Himalayan front are generally overestimated. TRMM-2B31 describes correctly the large-scale orographic rainfall distribution along the Himalayan front. This distribution is poorly depicted by all other data sets based on remote sensing techniques. As in the work by *Tian and Peters-Lidard* [2010], our study shows that sensor algorithms for mountainous regions, where terrain changes on short distances and orography influences precipitation, must be improved.

[31] As observed in the five small watersheds studied here, APHRODITE (and to a lesser extent TRMM-3B42) deliver good temporal variability, both on annual and monthly scale. In some cases, for example in the Jhikhu Khola catchment, which is located in the lower middle mountains with a low relief (~1400 m), even daily precipitation estimates by APHRODITE are representative (Figure 8). Because of its long availability (>30 years), coupled with its good temporal resolution, the APHRODITE product is appropriate to track above-threshold events driven by precipitation (e.g., landslides thresholds [*Gabet et al.*, 2004; *Dahal and Hasegawa*, 2008]) as well as for hydrological budget and discharge analysis. It can be applied for hydrological budget and discharge analysis of large basins (>2000 km^2 ~ 2 pixels). If higher temporal resolution than APHRODITE is needed, then the TRMM-3B42 data, with its 3-hourly resolution, could also be exploited for relative analysis, even if not tested here. Accurate precipitation data in an active mountain belt such as the Himalayas are essential for a real understanding of the potential couplings between climate, erosion and tectonics processes as well as for hazard mitigation.

Acknowledgments

[32] We would like to thank the German academic exchange service DAAD and the French German university DFH for funding the Ph.D. thesis of C. Andermann. Pyramid Ev-K2-CNR–SHARE project for meteorological data. We would like to thank Madhav Dhakal and Isabelle Providolli from ICIMOD Kathmandu for their outstanding support, Jianchi Xu and Ma Xing for readily sharing information on Xizhuang watershed, as well as B. P. Kothyari from GBPIHED India for providing data on Bhetagad watershed. Many thanks go also to Bodo Bookhagen for providing us with a mean annual data set of TRMM-2B31. We would like to thank Jagadish Karmacharya from DHM Nepal for his great support to select and obtain gauge data. We thank Alain Crave for helpful discussions and Guillaume Dupont-Nivet for proofreading. We would also like to thank two anonymous reviewers and the Editor of G-cubed, Louis Derry, whose comments and suggestions have considerably improved this manuscript.

References

Andermann, C., S. Bonnet, and R. Gloaguen (2010), Erosion in the Himalayas on catchment scale. Integrative remote sensing assessment, in *Geoscience and Remote Sensing Symposium, 2009 IEEE International, IGARSS 2009*, vol. 3, IEEE, Washington, D. C., doi:10.1109/IGARSS.2009.5417866.

Anders, A. M., G. H. Roe, B. Hallet, D. R. Montgomery, N. J. Finnegan, and J. Putkonen (2006), Spatial patterns of precipitation and topography in the Himalaya, *GSA Spec. Pap.*, *398*, 39–53, doi:10.1130/2006.2398(03).

Anders, A. M., G. H. Roe, D. R. Montgomery, and B. Hallet (2008), Influence of precipitation phase on the form of mountain ranges, *Geology*, *36*(6), 479–482, doi:10.1130/G24821A.1.

Barros, A. P., G. Kim, E. Williams, and S. W. Nesbitt (2004), Probing orographic controls in the Himalayas during the monsoon using satellite imagery, *Nat. Hazards Earth Syst. Sci.*, *4*(1), 29–51, doi:10.5194/nhess-4-29-2004.

Barros, A. P., S. Chiao, T. J. Lang, D. Burbank, and J. Putkonen (2006), From weather to climate: Seasonal and interannual variability of storms and implications for erosion processes in the Himalaya, *GSA Spec. Pap.*, *398*, 17–38, doi:10.1130/S2006.2398(02).

Bhatt, B. C., and K. Nakamura (2005), Characteristics of monsoon rainfall around the Himalayas revealed by TRMM precipitation radar, *Mon. Weather Rev.*, *133*(1), 149–165, doi:10.1175/MWR-2846.1.

Bonnet, S. (2009), Shrinking and splitting of drainage basins in orogenic landscapes from the migration of the main drainage divide, *Nat. Geosci.*, *2*(11), 766–771, doi:10.1038/ngeo666.

Bonnet, S., and A. Crave (2003), Landscape response to climate change: Insights from experimental modeling and implications for tectonic versus climatic uplift of topography, *Geology*, *31*(2), 123–126, doi:10.1130/0091-7613(2003)031<0123:LRTCCI>2.0.CO;2.

Bookhagen, B. (2010), Appearance of extreme monsoonal rainfall events and their impact on erosion in the Himalaya, *Geomatics Nat. Hazards Risk*, *1*(1), 37–50, doi:10.1080/19475701003625737.

Bookhagen, B., and D. W. Burbank (2006), Topography, relief, and TRMM-derived rainfall variations along the Himalaya, *Geophys. Res. Lett.*, *33*, L08405, doi:10.1029/2006GL026037.

Bookhagen, B., and D. W. Burbank (2010), Toward a complete Himalayan hydrological budget: Spatiotemporal distribution of snowmelt and rainfall and their impact on river discharge, *J. Geophys. Res.*, *115*, F03019, doi:10.1029/2009JF001426.

Bookhagen, B., and M. R. Strecker (2008), Orographic barriers, high-resolution TRMM rainfall, and relief variations along the eastern Andes, *Geophys. Res. Lett.*, *35*, L06403, doi:10.1029/2007GL032011.

Craddock, W. H., D. W. Burbank, B. Bookhagen, and E. J. Gabet (2007), Bedrock channel geometry along an orographic rainfall gradient in the upper Marsyandi River valley in central Nepal, *J. Geophys. Res.*, *112*, F03007, doi:10.1029/2006JF000589.

Dahal, R. K., and S. Hasegawa (2008), Representative rainfall thresholds for landslides in the Nepal Himalaya, *Geomorphology*, *100*(3–4), 429–443, doi:10.1016/j.geomorph.2008.01.014.

Dinku, T., F. Ruiz, S. J. Connor, and P. Ceccato (2009), Validation and intercomparison of satellite rainfall estimates over Colombia, *J. Appl. Meteorol. Climatol.*, *49*(5), 1004–1014, doi:10.1175/2009JAMC2260.1.

Gabet, E. J., D. W. Burbank, J. K. Putkonen, B. A. Pratt-Sitaula, and T. Ojha (2004), Rainfall thresholds for landsliding in the Himalayas of Nepal, *Geomorphology*, *63*(3–4), 131–143, doi:10.1016/j.geomorph.2004.03.011.

Huffman, G. J., R. F. Adler, D. T. Bolvin, G. Gu, E. J. Nelkin, K. P. Bowman, Y. Hong, E. F. Stocker, and D. B. Wolff (2007), The TRMM Multisatellite Precipitation Analysis (TMPA): Quasi-global, multiyear, combined-sensor precipitation estimates at fine scales, *J. Hydrometeorol.*, *8*(1), 38–55, doi:10.1175/JHM560.1.

Istanbulluoglu, E., and R. L. Bras (2006), On the dynamics of soil moisture, vegetation, and erosion: Implications of climate variability and change, *Water Resour. Res.*, *42*, W06418, doi:10.1029/2005WR004113.

Jianchu, X., A. Xihui, and D. Xiqing (2005), Exploring the spatial and temporal dynamics of land use in Xizhuang watershed of Yunnan, southwest China, *Int. J. Appl. Earth Obs. Geoinf.*, *7*(4), 299–309, doi:10.1016/j.jag.2005.06.008.

Kamal-Heikman, S., L. A. Derry, J. R. Stedinger, and C. C. Duncan (2007), A simple predictive tool for lower Brahmaputra River basin monsoon flooding, *Earth Interact.*, *11*(21), 1–11, doi:10.1175/EI226.1.

Kothyari, B. P., P. K. Verma, B. K. Joshi, and U. C. Kothyari (2004), Rainfall-runoff-soil and nutrient loss relationships for plot size areas of Bhetagad watershed in central Himalaya, India, *J. Hydrol.*, *293*(1–4), 137–150, doi:10.1016/j.jhydrol.2004.01.011.

Kubota, T., et al. (2007), Global Precipitation map using satellite-borne microwave radiometers by the GSMaP project: Production and validation, *IEEE Trans. Geosci. Remote Sens.*, *45*(7), 2259–2275, doi:10.1109/TGRS.2007.895337.

Kummerow, C., W. Barnes, T. Kozu, J. Shiue, and J. Simpson (1998), The Tropical Rainfall Measuring Mission (TRMM) sensor package, *J. Atmos. Oceanic Technol.*, *15*(3), 809–817, doi:10.1175/1520-0426(1998)015<0809:TTRMMT>2.0.CO;2.

Kummerow, C., et al. (2000), The status of the Tropical Rainfall Measuring Mission (TRMM) after two years in orbit, *J. Appl. Meteorol.*, *39*(12), 1965–1982, doi:10.1175/1520-0450(2001)040<1965:TSOTTR>2.0.CO;2.

Merz, J. (2004), Water balances, floods and sediment transport in the Hindu Kush-Himalayas, Ph.D. thesis, Inst. of Geogr., Univ. of Bern, Bern, Switzerland.

Nesbitt, S. W., and A. M. Anders (2009), Very high resolution precipitation climatologies from the Tropical Rainfall Measuring Mission precipitation radar, *Geophys. Res. Lett.*, *36*, L15815, doi:10.1029/2009GL038026.

Putkonen, J. (2004), Continuous snow and rain data at 500 to 4400 m altitude near Annapurna, Nepal, 1999–2001, *Arct. Antarct. Alp. Res.*, *36*(2), 244–248, doi:10.1657/1523-0430(2004)036[0244:CSARDA]2.0.CO;2.

Reiners, P. W., T. A. Ehlers, S. G. Mitchell, and D. R. Montgomery (2003), Coupled spatial variations in precipitation and long-term erosion rates across the Washington Cascades, *Nature*, *426*(6967), 645–647, doi:10.1038/nature02111.

Roe, G. H. (2005), Orographic precipitation, *Ann. Rev. Earth Planet. Sci.*, *33*(1), 645–671, doi:10.1146/annurev.earth.33.092203.122541.

Roe, G. H., D. R. Montgomery, and B. Hallet (2003), Orographic precipitation and the relief of mountain ranges, *J. Geophys. Res.*, *108*(B6), 2315, doi:10.1029/2001JB001521.

Shrestha, M., G. Artan, S. Bajracharya, and R. Sharma (2008), Using satellite-based rainfall estimates for streamflow modelling: Bagmati Basin, *J. Flood Risk Manage.*, *1*(2), 89–99, doi:10.1111/j.1753-318X.2008.00011.x.

Tian, Y., and C. D. Peters-Lidard (2010), A global map of uncertainties in satellite-based precipitation measurements, *Geophys. Res. Lett.*, *37*, L24407, doi:10.1029/2010GL046008.

Tucker, G. E., and R. Slingerland (1997), Drainage basin responses to climate change, *Water Resour. Res.*, *33*(8), 2031–2047, doi:10.1029/97WR00409.

Tustison, B., D. Harris, and E. Foufoula-Georgiou (2001), Scale issues in verification of precipitation forecasts, *J. Geophys. Res.*, *106*(D11), 11,775–11,784, doi:10.1029/2001JD900066.

Ushio, T., K. Sasashige, T. Kubota, S. Shige, K. Okamoto, K. Aonashi, T. Inoue, N. Takahashi, and T. Iguchi (2009), A Kalman filter approach to the Global Satellite Mapping of Precipitation (GSMaP) from combined passive microwave and infrared radiometric data, *J. Meteorol. Soc. Jpn.*, *87A*(9), 3084–3097, doi:10.2151/jmsj.87A.137.

Vicente, G. A., J. C. Davenport, and R. A. Scofield (2002), The role of orographic and parallax corrections on real time high resolution satellite rainfall rate distribution, *Int. J. Remote Sens.*, *23*(2), 221–230, doi:10.1080/01431160010006935.

Whipple, K. X. (2009), The influence of climate on the tectonic evolution of mountain belts, *Nat. Geosci.*, *2*(2), 97–104, doi:10.1038/ngeo413.

Whipple, K. X., and B. J. Meade (2006), Orogen response to changes in climatic and tectonic forcing, *Earth Planet. Sci. Lett.*, *243*(1–2), 218–228, doi:10.1016/j.epsl.2005.12.022.

Willett, S. D. (1999), Orogeny and orography: The effects of erosion on the structure of mountain belts, *J. Geophys. Res.*, *104*(B12), 28,957–28,981, doi:10.1029/1999JB900248.

Wulf, H., B. Bookhagen, and D. Scherler (2010), Seasonal precipitation gradients and their impact on fluvial sediment flux in the northwest Himalaya, *Geomorphology*, *118*(1–2), 13–21, doi:10.1016/j.geomorph.2009.12.003.

Xie, P., Y. Yarosh, T. Love, J. E. Janowiak, and P. A. Arkin (2002), A real-time daily precipitation analysis over South Asia, paper presented at the 16th Conference of Hydrology, Am. Meteorol. Soc., Orlando, Fla., 12–17 Jan. (Available at http://www.cpc.ncep.noaa.gov/products/fews/sasia_r fe.pdf)

Xie, P., M. Chen, S. Yang, A. Yatagai, T. Hayasaka, Y. Fukushima, and C. Liu (2007), A gauge-based analysis of daily precipitation over East Asia, *J. Hydrometeorol.*, *8*(3), 607–626, doi:10.1175/JHM583.1.

Yatagai, A., and H. Kawamoto (2008), Quantitative estimation of orographic precipitation over the Himalayas by using TRMM/PR and a dense network of rain gauges, in *Proc. SPIE*, *7148-11*, doi:10.1117/12.811943.

Yatagai, A., O. Arakawa, K. Kamiguchi, H. Kawamoto, M. I. Nodzu, and A. Hamada (2009), A 44-year daily gridded precipitation data set for Asia based on a dense network of rain gauges, *SOLA*, *5*, 137–140, doi:10.2151/sola.2009-035.

3.2 General discussion

In this paper, I demonstrated that remotely sensed precipitation datasets are very discrepant in the Himalayas. It appears in particular very difficult to apply the remotely sensed measurements on a high temporal resolution, for example on a daily time-scale. Although, time series with a good temporal resolution are needed to understand the erosional processes.

From the comparison with ground based rain gauge stations, both on the spatial basin scale and with single station observations, I identified the AHRODITE (Asian Precipitation Highly Resolved Observational Data Integration Towards Evaluation of Water Resources, Monsoon Asia, Version 10) dataset as the best performing one available at the moment. This dataset has several advantages: 1) It has a daily temporal resolution, the same resolution as the river discharge and suspended sediment concentration data that I will analyse in the following chapters. 2) It integrates over more than 50 years (1951-2007) covering the whole time span of all the other datasets analysed here. 3) It has a reasonable spatial resolution of $\sim$ 30 km, and 4) It performs exceptionally well, with respect to the available ground measurements, both on a spatial and temporal time scale.

From the evaluation of the precipitation datasets, I have set the basis to further evaluate erosion processes in the Nepal Himalayas and their possible control by precipitation.

Chapter 4

Hydro-climatology

4.1 Introduction

The hydrological compartments of mountains are key issues to understand the erosion processes there. Water is the principle media to eroded and transport materials out of the mountain range. Rivers incise valley bottoms and thus create actively landscapes by bring slopes to critical inclination. The capacity of a river to incise bedrock depends directly on the amount of water and its slope [e.g. *Tucker and Slingerland*, 1997; *Whipple and Tucker*, 1999; *Kirby and Whipple*, 2001]. Hence, it is very important to have a full comprehensive knowledge on the role of different hydrological compartments. In particular, the storage and release of water from reservoirs, such as groundwater and glaciers, are crucial parameters for erosion and transport processes. The repartition of precipitation in surface runoff, snow, ice and groundwater (and evapotranspiration) controls primarily the amount of water available on the surface to erode and the amount of water available in the rivers to transport and incise. Furthermore, this has direct implication on the availability of water resources, flood hazard mitigation and the occurrence landslides [*Oki and Kanae*, 2006; *Immerzeel et al.*, 2010]. Last, a good knowledge on the flow-paths is important to understand geochemical cycles as well as climate-erosion interactions and the consumption of atmospheric CO_2 by Si-weathering [e.g. *Raymo and Ruddiman*, 1992].

In the Himalayas the role of the different hydrological compartments is practically unknown. *Bookhagen and Burbank* [2010] has published recently a hydrological budget analysis from remote sensing data for the whole Himalayas, providing a good idea of variation of snowmelt and rainfall contribution in different regions of the Himalayas. For example, the snow melt component is much more important in the eastern and the western Himalayas. Similarly, *Immerzeel et al.* [2009] has modelled snow and glacier melt river discharge contributions and under the effect of climate change for the Indus basin in the western Himalayas. However, groundwater, as an important transient storage has so far been neglected.

The following manuscript is published in the journal *Nature Geosciences*.

nature geoscience

LETTERS

PUBLISHED ONLINE: 10 JANUARY 2012 | DOI: 10.1038/NGEO1356

Impact of transient groundwater storage on the discharge of Himalayan rivers

Christoff Andermann[1,2]*, Laurent Longuevergne[1], Stéphane Bonnet[3], Alain Crave[1], Philippe Davy[1] and Richard Gloaguen[2]

In the course of the transfer of precipitation into rivers, water is temporarily stored in reservoirs with different residence times[1,2] such as soils, groundwater, snow and glaciers. In the central Himalaya, the water budget is thought to be primarily controlled by monsoon rainfall, snow and glacier melt[3,4], and secondarily by evapotranspiration[3]. An additional contribution from deep groundwater[5–7] has been deduced from the chemistry of Himalayan rivers[6], but its importance in the annual water budget remains to be evaluated. Here we analyse records of daily precipitation and discharge within twelve catchments in Nepal over about 30 years. We observe annual hysteresis loops—that is, a time lag between precipitation and discharge—in both glaciated and unglaciated catchments and independent of the geological setting. We infer that water is stored temporarily in a reservoir with characteristic response time of about 45 days, suggesting a diffusivity typical of fractured basement aquifers[8]. We estimate this transient storage capacity at about 28 km^3 for the three main Nepal catchments; snow and glacier melt contribute around 14 km^3 yr^{-1}, about 10% of the annual river discharge. We conclude that groundwater storage in a fractured basement influences significantly the Himalayan river discharge cycle.

The discharge of the central Himalayan rivers is governed by a strong precipitation seasonality[3,6,9,10] (Fig. 1) with up to 80% of the annual rainfall occurring during the Indian Summer Monsoon (ISM) season[3]. The ISM precipitation is the main source for glacier mass accumulation[9] and its spatial distribution is strongly influenced by orographic effects[3]. Variations in intensity and duration of the ISM, linked to El Nino/Southern Oscillation (ENSO; ref. 11), enhance the annual amount of precipitation by ~25–50% with respect to the annual mean at low to moderate elevation (>3 km), and up to 200% at high elevation[12]. Snow melt contributes to a significant fraction of river discharge in the western and eastern Himalayas and on the Tibetan plateau[3,13], but only to a minor fraction (~10%) in the central Himalayas, mainly in the early ISM (May–July)[3]. It has been suggested that rainfall-derived discharge, ice and snow melt are the primary factors controlling Himalayan river discharge, with evapotranspiration forming a secondary minor component[3]. Notwithstanding, this hydrological budget model neglects transient water storage in soils, floodplains and groundwater. However, geochemical data indicate that a non-negligible part of surface runoff originates from deep groundwater reservoirs[6].

We investigate the transfer of water within the main catchments of the Nepal Himalayas (Fig. 1a) using a daily meteorological and hydrological dataset spanning ~30 years (Table 1). We consider the three main catchments of Nepal (Sapta Koshi, Narayani and Karnali basins), some of their tributaries, and three unglaciated small catchments at the front of the Himalayan range (Fig. 1a and Table 1). The main catchments drain the entire Himalayan range of Nepal, from the Tibetan Plateau to the Lesser Himalayas. Most of their headwaters are located on the arid Plateau (Fig. 1a), characterized by a weaker influence of the ISM. The rivers incise bedrock comprising, from north to south, the low-grade Paleozoic–Mesozoic Tethyan Sediment Series, high-grade metamorphic gneisses and migmatites of the High Himalayan Crystalline series and low-grade Proterozoic sediments of the Lesser Himalayas (Fig. 1c). Most of the data considered here come from outlet stations located to the north of the Siwalik foreland. The annual specific discharge of the studied basins is typically on the order of ~10^3 mm yr^{-1} (Table 1) and their annual hydrograph clearly shows the seasonal impact of the ISM on river discharge, generally peaking in July/August[3,14] (Fig. 1b). Mean annual basin precipitation is 920, 1,396 and 920 mm yr^{-1} in the Sapta Koshi, Narayani and Karnali catchments, respectively. However, precipitation is spatially heterogeneous (Fig. 1a) and is strongly controlled by orography, reaching a maximum between elevations of 2–3 km (refs 15,16). The upper parts of the catchments are glaciated (Fig. 1a), covering between 4 and 15% of the catchment area (Table 1).

We calculated mean basin-wide daily precipitation rate and use daily discharge measurements to compute specific water discharge for all the studied drainage basins (see Methods). Plots of daily precipitation versus specific discharge highlight a considerable scatter within the ~30-year datasets (Fig. 2a). However, the chronology of the data exhibits a well-defined annual cycle, showing an increase of discharge with increasing precipitation during the pre-ISM (March–May) to the ISM (June–September) and a decrease during the post-ISM (October–November). The systematic higher discharge for a given precipitation rate during the post-ISM compared with the pre-ISM is striking. The data consequently shows an annual anticlockwise hysteresis loop (Fig. 2a). A 30-day moving average highlights the temporal consistency of the loop from year to year (Fig. 2a, inset). Data scattering results from inter-annual variability, particularly during the post-ISM, as illustrated by comparing the data during a strong or a weak ISM year (see Supplementary Fig. S1). The annual anticlockwise hysteresis loop is observed in all studied basins (Fig. 2b), regardless of the geological units, the presence of glaciers or snow cover (Table 1).

Anticlockwise hysteresis loops imply that precipitation is temporarily stored within the catchments and not transferred directly to the river during the pre-ISM and ISM seasons, whereas the storage compartment is drained during the post-ISM. Glaciers

[1]Géosciences Rennes, Université de Rennes 1, CNRS, Campus de Beaulieu, 35042 Rennes, France, [2]Remote Sensing Group, Geology Institute, TU Bergakademie Freiberg, B.-von-Cotta-Str. 2, 09599 Freiberg, Germany, [3]Géosciences Environnement Toulouse, Université de Toulouse, CNRS-UPS-IRD, Observatoire Midi-Pyrénées, 14 Av. Edouard Belin, 31400 Toulouse, France. *e-mail: christoff.andermann@univ-rennes1.fr.

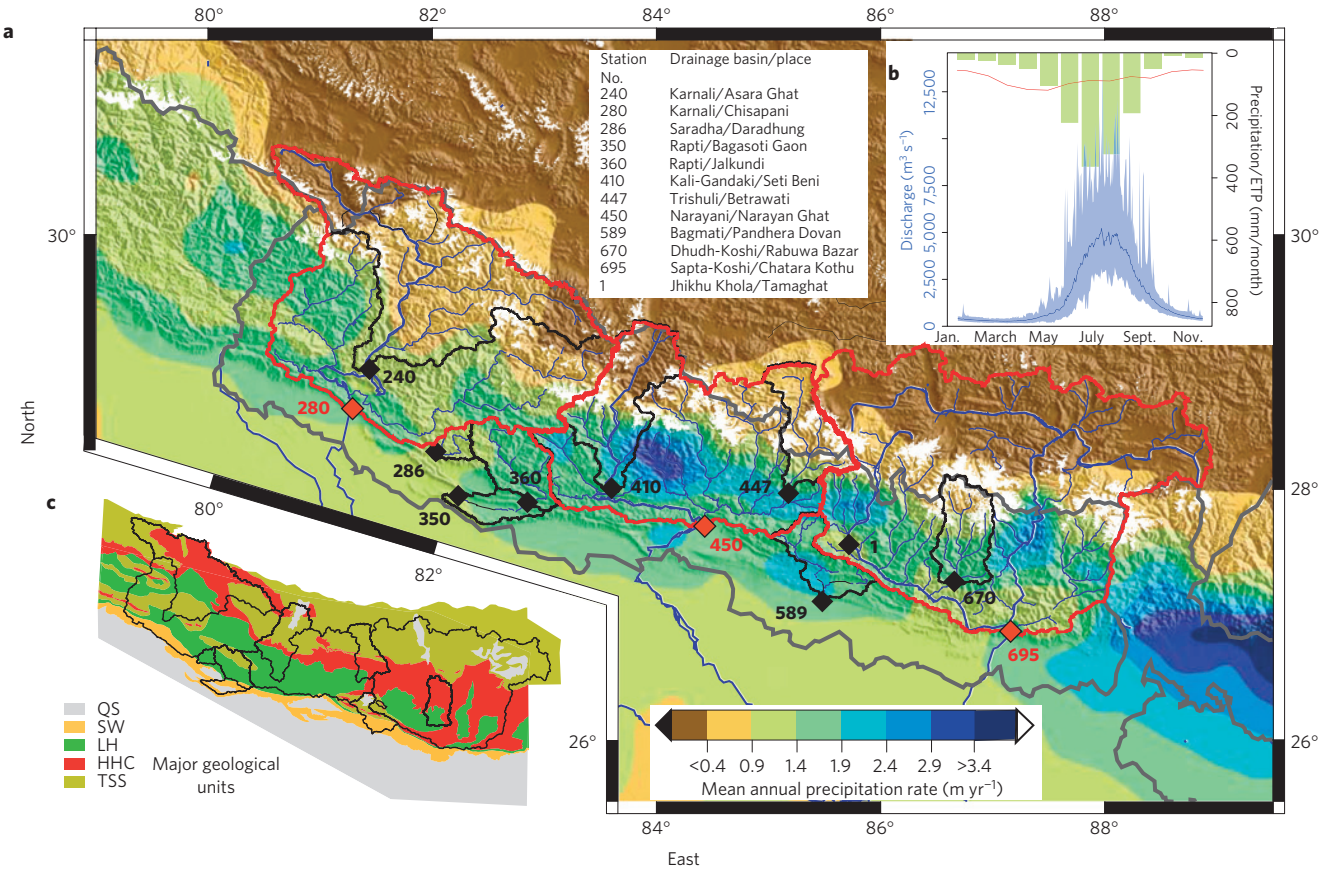

Figure 1 | Hydrological setting of the Nepal Himalayas. a, Precipitation distribution map; hydrological discharge stations used in this study (diamonds) and contours (red lines) of the studied drainage basins. Grey lines mark political boundaries. Mean annual precipitation rates (see Methods), representing 50 years of data, are draped over shaded relief. River network is shown in blue and glaciers in white (after ref. 29). **b**, Mean basin-wide precipitation (1951–2006, in green) and potential evapotranspiration (red) for the Narayani drainage basin. The bold blue line with blue shading represents the mean, maximum and minimum daily discharge over 34 years (station 450). **c**, Simplified geological map of Nepal[30]: QS; Quaternary Sediments; SW, Siwaliks Formation; LH, metasediments of the Lesser Himalayas; HHC, High Himalayan Crystalline; TSS, Tethyan Sediment Series.

can be directly ruled out as the main contributor to the observed hysteresis effect because the release of water by glacier or snow melt occurs principally during the pre-ISM to ISM season[3,13] (Fig. 3b and Supplementary Fig. S2), which is not consistent with the anticlockwise nature of the hysteresis. Moreover, hysteresis effects are observed in both glaciated and unglaciated catchments (Fig. 2b). As the potential evapotranspiration in the Himalayas reaches a maximum during the pre-ISM, in April–May[17] (Fig. 1b), this could qualitatively explain the anticlockwise hysteresis loop. However, it is estimated to account for less than 10% of the overall hydrological budget[3], so this effect probably plays a minor role, mainly because the magnitude of evapotranspiration rapidly decreases with elevation[17]. Consequently, the main mechanism explaining the hysteresis effect is probably a transient storage of water in a groundwater unit during the rising ISM and its post-ISM release.

To more precisely determine the role of groundwater storage on the Himalayan hydrological cycle, we solved the water balance at catchment scale to discriminate time response distribution in discharge data and relate it to storage compartments through hydrological modelling. We used a modified version of the conceptual hydrological model GR2M (see Methods), which addresses several physical processes in a simplified, but proven robust, way in a wide range of climatological settings[18]. Because the observed hysteresis effect is a seasonal process, daily modelling of hydrological processes is not the pertinent scale for our purpose (see ref. 19). The great diversity of the involved processes, within a wide range of environmental settings, limits the reliability of short-term modelling, so we modelled the data at a monthly rather than at a daily scale. Note that we nevertheless tested daily-scale modelling (see Methods and Supplementary Table S1). Modelled daily results are generally similar to monthly ones (Table 1), but the efficiency, however, is less well described (Table 1 and Supplementary Table S1). The model simulates the catchment response to rainfall in terms of river discharge and incorporates three components (see Supplementary Fig. S3): (1) a snow module based on the Hydrologiska Byråns Vattenbalansavdelning (HBV) approach[20] (see Methods), (2) a fast rain-to-discharge flow related to quick runoff processes, and (3) a slow-flow component representing groundwater contribution. This third reservoir retards the rain-discharge response and yields baseflow during dry periods. It is characterized by a response time t_c, defined as the time for a hydrological system to reach equilibrium after the hydraulic head has changed[1]. The model is forced by precipitation, temperature and potential evapotranspiration (see Methods). We calibrated on the logarithm of all the observed daily water discharge to account for the large range of discharges, that is to apply identical weights to both high- and low-water stages, and under the constraint that total observed and modelled discharge volumes are identical. The modelling is robust in most catchments: hysteresis loops are confidently reproduced for all catchments (for example Supplementary Fig. S4) with Nash–Sutcliffe coefficients of 0.89, 0.91 and 0.92 for Sapta Koshi, Narayani and Karnali basins, respectively (Table 1).

Table 1 | Properties of the studied drainage basins and summary of results (monthly modelling).

Station no.	240	280*	410	447	450*	670	695*
Basin	Karnali	Karnali	Kali Gandaki	Trishuli	Narayani	Dudh Koshi	Sapta Koshi
Lat (°) N	28.95	28.64	28.01	27.97	27.71	27.27	26.87
Long (°) E	81.44	81.29	83.60	85.18	84.43	86.66	87.16
Size (km^2)	21,121	45,967	7,169	4,428	32,002	3,880	57,719
Precipitation ($mm\ yr^{-1}$)	558	920	1,030	692	1,396	1,295	920
Discharge ($mm\ yr^{-1}$)	650	789	1,145	1,513	1,145	1,598	1,039
ETR ($mm\ yr^{-1}$)	176	234	178	121	367	178	179
Availability of discharge	1975–2006	1973–2006	1979–1995	1977–2006	1973–2006	1987–2006	1977–2006
% Area glaciated	5.9	4.7	10.3	6.5	9.9	14.7	7.3
Max elevation (m asl.)	7,549	7,697	8,147	7,352	8,147	8,848	8,848
Nash–Sutcliffe coef.	0.93	0.92	0.91	0.79	0.91	0.94	0.89
Recession exp. b ($Q = aS^b$) †	1.01	1.11	1.01	1.02	1.16	1.17	1.01
Storage capacity (km^3)	3.1±1.2	8.1±3.3	1.3±0.6	0.9±0.4	9.9±3	1.2±0.4	10.3±6
Storage capacity (mm)	150±60	175±70	180±80	200±80	310±125	300±105	180±100
t_c GR2M (days)†	46±5	50±5	45±4	38±4	50±5	53±11	47±4
t_c recession curve (days)†	40±10	46±15	41±15	44±11	40±13	45±9	41±11
Ice + snow melt ($km^3\ yr^{-1}$)	1.2	4.1	0.7	0.8	5.3	0.6	4.1
% snow melt	12	7	3	13	2	6	5
Geology units % coverage QS/SW/LH/HHC/TSS	0/0/17/44/39	0/5/33/25/37	10/0/32/15/43	0/0/8/ 37/55	2/0/42/23/33	0/0/26/73/1	6/0/16/40/38

Station no.	286	350	360	589	1
Basin	Saradha	Rapti	Rapti	Bagmati	Jhikhu Khola
Lat (°) N	28.64	27.90	27.95	27.11	27.59
Long (°) E	82.03	82.85	82.23	85.48	85.67
Size (km^2)	808	3,648	5,198	2,849	111
Precipitation ($mm\ yr^{-1}$)	1,107	1,522	1,470	1,932	1,285
Discharge ($mm\ yr^{-1}$)	460	903	787	1,205	374
ETR ($mm\ yr^{-1}$)	656	720	654	839	171
Availability of discharge	1976–2006	1978–2006	1985–2006	2001–2006	1998–2006
% Area glaciated	0.0	0.0	0.0	0.0	0.0
Max elevation (m asl.)	2,800	3,623	3,623	2,795	2,200
Nash–Sutcliffe coef.	0.79	0.88	0.95	0.88	0.29
Recession exp. b ($Q = aS^b$)	1.16	1.01	1.18	1.12	1.18
Storage capacity (km^3)	0.21±0.08	1.6±0.7	1.8±0.8	1.2±0.5	0.03±0.01
Storage capacity (mm)	260±90	430±180	350±150	440±180	300±120
t_c GR2M (days)	37±3	36±8	41±8	30±5	120±35
t_c recession curve (days)	37±13	44±17	42±15	41±19	77±24
Ice + snow melt ($km^3\ yr^{-1}$)	n.a.	n.a.	n.a.	n.a.	n.a.
% snow melt	n.a.	n.a.	n.a.	n.a.	n.a.
Geology units % coverage QS/SW/LH/HHC/TSS	0/3/96/0/1	0/5/62/0/33	8/24/45/0/23	13/42/2/11/32	0/0/11/17/72

Maximum elevation is used as a proxy for snow occurrence during winter (considering winter snowline at ~3,000 m asl.; ref. 16). Precipitation rate is computed as a mean basin value. Specific discharge is computed from daily river gauge data. Real evapotranspiration (ETR) is computed from our modelling (see Methods). Storage represents the mean annual amplitude of storage variation, expressed in both km^3 and mm, and its uncertainty(Supplementary Fig. S2). t_c is the characteristic basin response time, derived from hydrological modelling or from the recession curve of hydrographs (see Methods). The % glaciated values are calculated using data from ref. 29. Ice melt is the annual volumetric glacier ice melt contribution to the rivers, estimated from the relative baseflow shift in the precipitation–discharge plot (Fig. 2b). % snow melt is the contribution of snow to discharge (both directly and via the aquifer). QS: Quaternary Sediments, SW: Siwaliks Formation, LH: metasediments of the Lesser Himalayas, HHC: High Himalayan Crystalline, TSS: Tethyan Sediment Series. *Three main basins of the Nepal Himalayas outlined in red in Fig. 1. †See Methods.

The modelling implies a significant storage of water within the slow-flow reservoir, with calculated t_c longer than one month (Table 1). Modelled data are in agreement with t_c values derived directly from the fit of baseflow recession curves[21] (see Methods and Table 1). This delay between precipitation and discharge yields baseflow during dry periods and is responsible for the existence of the hysteresis loops. Shorter t_c, associated with a low storage capacity (for example ten days, equivalent to twenty times smaller storage capacity), do not allow one to reproduce the observed hysteresis loops analytically (see Methods and Supplementary Fig. S5c).

The nature of the groundwater system controlling the hysteresis effect is provided by its response time t_c. For groundwater systems, t_c is inversely proportional to the hydraulic diffusivity D (transmissivity divided by storage coefficient) and is proportional to the square of the characteristic aquifer scale L_c: $t_c \sim L_c^2 D^{-1}$ (ref. 1). L_c is the characteristic distance between the aquifer and streams, which is approximately the hillslope length if aquifers are spread homogeneously over the drainage basin. Considering L_c in the range 0.5–5 km and t_c of ~45 days, equivalent diffusivity values are about ~1 $m^2\ s^{-1}$, a typical value for aquifers in fractured rocks[8] (0.01–10 $m^2\ s^{-1}$). Recession curve exponents calculated on the falling limb of the post-ISM hydrograph (see Methods) are close to 1, and suggest the contribution of a confined aquifer to discharge[21]. The estimated aquifer storage capacity is ~180 mm per unit area, representing ~28 km^3 for the three main catchments of

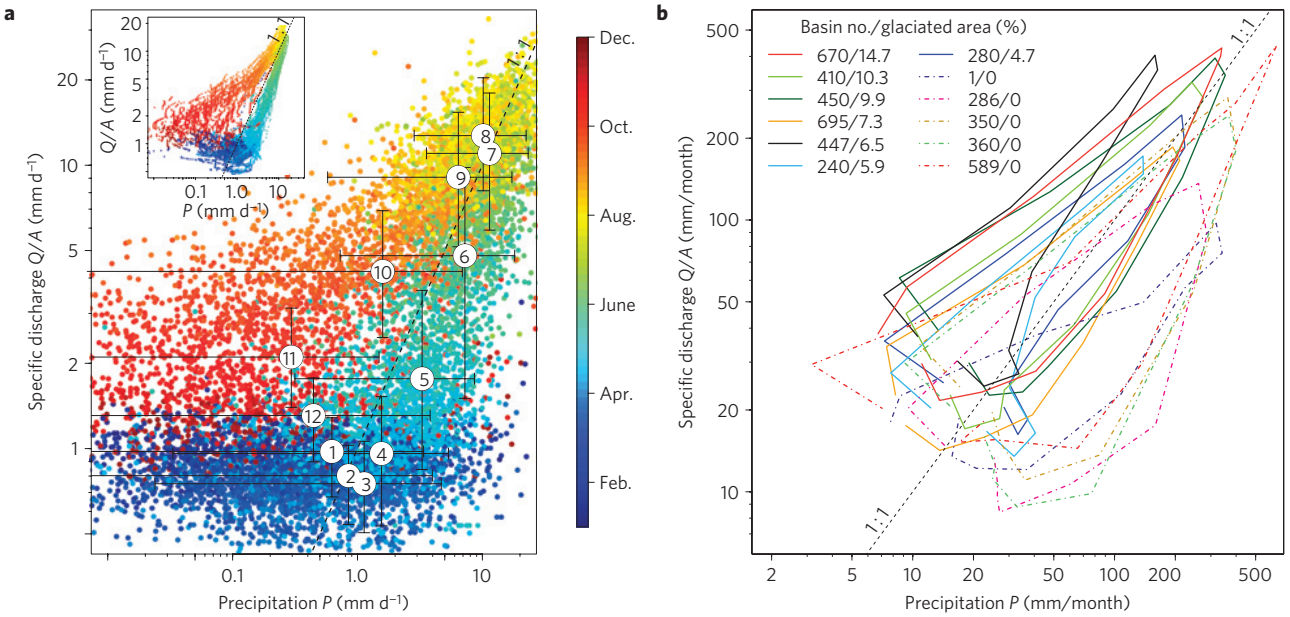

Figure 2 | Precipitation–discharge (*P*–*Q*) anticlockwise hysteresis plot. a, Bi-logarithmic *P*–*Q* plot of daily data for the Narayani basin over 34 years at station 450 (~12,300 data points). Data plotted are specific discharges (discharges normalized by drainage area) and mean basin precipitation rates. Note that discharge is not plotted when precipitation is zero. Colour bar is scaled for a calendar year. White filled circles represent the mean monthly values over 34 years, the months being indicated by numbers. The error bars represent the 5% and 95% quantiles of the daily data distribution of each month. Inset shows the data filtered with a 30-day moving average. **b**, Mean annual hysteresis loops plotted from monthly mean data for all the drainage basins. Solid lines represent partially glaciated basins and dashed lines unglaciated ones (percentage of glacial coverage from ref. 29).

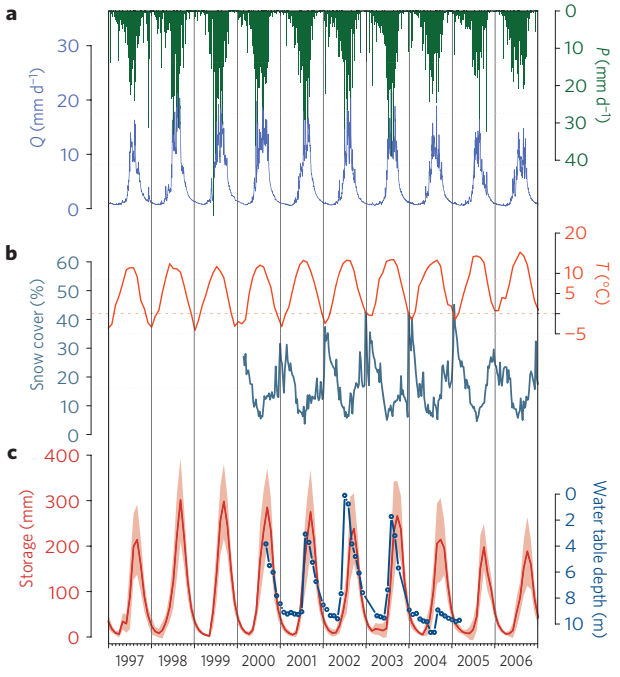

Figure 3 | 10-year (1997–2006) temporal variability of several hydrological compartments, Narayani basin. a, Daily precipitation (green) and daily specific river discharge (blue). **b**, Temperature (orange) as a glacier melt proxy (from CRU; ref. 26) and percentage of basin-wide snow cover (dark green, data from MODIS MOD10C2 v.5 (ref. 25) with an 8-day temporal resolution). **c**, Calculated groundwater storage (red), shading illustrating model uncertainty (Supplementary Fig. S2). Ground water table variation (dark blue) observed in a dug-well in Jhikhu Khola Basin[22] (station no. 1) from ref. 22 and unpublished data provided by these authors. The abnormal low water table in 2004 probably results from exhaustive exploitation.

Nepal (Table 1). Modelling also indicates that the annual volume of water flowing through this groundwater system represents ~2/3 of the annual river discharge (Supplementary Table S1). The modelled storage dynamics matches the groundwater table variations observed in dug-wells, for example in Jhikhu Khola catchment[22] (Fig. 3c). The ratio between calculated water storage variations (Table 1) and water-table depth observed here indicates low porosity values of a few per cent. We conclude from low porosity values[23], confined behaviour[21] and characteristic diffusivity values[8], that the aquifer is predominantly fractured basement. Average water-table variation (total annual storage capacity divided by rock porosity, considering low porosity value) is estimated to a few tens of metres in the studied catchments.

We show that the very specific climatic regime of Nepal, characterized by distinct long-lasting wet and dry seasons and a major increase of precipitation during the ISM (Figs 1b and 3a), is responsible for the recharge of fractured basement aquifers. The aquifers are refilled during the ISM and purged in the post-ISM, leading to the annual hysteresis effect that we observed. This behaviour is observed in all the studied drainage basins, independent of their size, physiographic location or main basement geology (Fig. 1, Table 1 and Supplementary Fig. S6). Very little is known in Nepal about the actual aquifer, its physical properties and the relationship with tectonic structures. These critical unknowns limit the further understanding of deep groundwater in the Himalayas, including water resources, flood hazard, landslide risk due to pore-pressure saturation as well as deep weathering and dissolution processes. Finally, it is noticeable that during winter (December–February) the precipitation–discharge graphs (Fig. 2b) show a systematic higher baseflow for glaciated catchments compared with unglaciated ones. Because glaciers represent an additional water storage component in some catchments, this vertical shift of the hysteresis loops of glaciated catchments reveals the contribution of glacial melt (and snow in spring) to river discharge and can be used to quantify it. From this approach (see Methods), the snow and glacier melt contribution to river discharge

is estimated to be $\sim 14 \pm 7\,km^3\,yr^{-1}$ considering the three main catchments in Nepal (Table 1), which accounts for ~10% of annual river discharge. In Nepal, the volume of water flowing through fractured basement aquifer is approximately six times higher than the contribution of glacial and snow melt to river discharge.

Methods

Data and data processing. Precipitation is calculated using APHRODITE (Asian Precipitation Highly Resolved Observational Data Integration Towards Evaluation of Water Resources) data (http://www.chikyu.ac.jp/precip/). Here, we use the daily version for monsoon Asia APHRO_MA_V1003R1, with a spatial resolution of 0.25° (ref. 24). It is currently the best available dataset for Nepal[10]. We use raw river discharge data provided by the Department of Hydrology and Meteorology of Nepal (DHM; see for example ref. 14), derived from daily stage readings and calibrated rating curves (no interpolated data are used). Potential evapotranspiration is estimated using an elevation-based model developed for Nepal[17]. Basin-wide snow cover is obtained from MOD10C2 version 5 (http://nsidc.org/data/mod10c2v5.html), with an 8-day temporal and 500 m spatial resolution[25]. We used the monthly temperature dataset CRU TS3.0 (ref. 26), with 0.5° gridded resolution. Daily temperature is obtained from linear interpolation.

Baseflow recession analysis. Recession curves have been analysed for time-series of at least 60 days, where daily rainfall is below potential evapotranspiration and cumulated rainfall <25 mm for each recession curve. The first 15 days of each recession are not considered when fitting the recession model. Both linear and nonlinear models are fitted to the relationship between river discharge Q and storage S: $Q = aS^b$. Analytically, exponent b changes from 1 when transmissivity is constant over time (most likely for confined or very deep unconfined aquifers) to 2 for unconfined flow[21]. Coefficient a is the inverse of the response time when $b \sim 1$.

The annual snow and glacier melt contribution is estimated from the baseflow offset between glaciated and unglaciated basins along the discharge axis of the hysteresis plots (Fig. 2b). The scatter of baseflow within unglaciated basins (~5 mm/month) is considered as uncertainty. For the Mount Everest region (here, Dudh Koshi, station 670), our estimated melt volume ($0.6\,km^3\,yr^{-1}$, Table 1) is consistent with independent glacier mass-loss estimates, measured on ~10% of the glaciated area using satellite altimetry[27].

Hydrological modelling. We consider parsimonious conceptual models at daily and monthly timescales, GR4J and GR2M (http://www.cemagref.fr/webgr/IndexGB.htm). The initial versions have been built up on four and two parameters respectively. We added a distributed snow module based on the HBV conceptual approach[20]. Data scarcity and the requirement of a parsimonious model structure prevented application of a more complex approach. Rainfall and temperature data are redistributed on the ETOPO2v2 (2″ resolution) elevation grid. The parameter Tsep separates rainfall and snowfall (Supplementary Fig. S3). The fusion temperature (T_f) is set to 0 °C. Snow melt (S_m) is driven by a degree-day approach with a constant melting factor M, $S_m = M(T - T_f)$. The snow module adds two parameters to the initial GR2M and GR4J models for the whole basin. Modelled snow cover fractions are validated on MODIS snow cover[25] extent ($r^2 = 0.8$).

The modified GR2M is based on three storage compartments; the snow storage, soil store and routing store, interpreted as 'groundwater storage' (Supplementary Fig. S3). Liquid rainfall and snow melt are partitioned into excess rainfall, actual evapotranspiration, slow percolation and water remaining in the soil store based on a single parameter. Actual evaporotranspiration is driven by potential evaporotranspiration and reservoir water availability. At monthly timescales, the routing store gathers all water and computes discharge. The model discharge calculation was modified on a physical basis to include a priori linear behaviour from recession curve analysis with a variable time response X5, $Q = R/X5$. GR models allow water exchanges with outside the basin (for example subsurface flow) computed with the parameter $X2$. A first order estimate of the groundwater flux contribution to river discharge is computed by tracking water flow from the routing store of GR4J model.

Modulation of hysteresis effect. The shape of the hysteresis curve is used to deduce catchment groundwater storage capacity. Forward modelling studies allow stepwise interpretation of the hysteresis shape with respect to hydrological processes or observation errors, which might have the potential to explain the hysteresis effect. The Rapti catchment (station 360 unglaciated, with no snow) is considered as a reference to test the cumulative impact of several contributions.

We tested four factors, the first being the effect of a systematic underestimation of precipitation and snow on the shape of the hysteresis loop. Applying 30% of excess rainfall[10] shrinks the hysteresis along the precipitation axis (Supplementary Fig. S5a). The second was the impact of snow storage and a delayed melting contribution to discharge, using GLDAS-NOAH model output[28] as a realistic a priori estimate ($100\,mm\,snow\,yr^{-1}$). The snow melt contribution drags the baseflow upward (in March, April and June) but does not change the general shape of the hysteresis loop (Supplementary Fig. S5a). The third was the effect of t_c on the shape of hysteresis loops, where the decrease of t_c from ~45 to 10 days and the associated decrease of the storage capacity does not allow the reproduction of the hysteresis loops observed (Supplementary Fig. S5c). The last was the effect of glacier melt on the shape of the hysteresis loops, where we considered a glacier melt contribution at a constant rate and following a seasonal temperature cycle. This induces a year-long vertical shift of the hysteresis curve (increased baseflow), keeping its shape intact (Supplementary Fig. S5b).

Received 15 April 2011; accepted 25 November 2011; published online 10 January 2012

References

1. Alley, W. M., Healy, R. W., LaBaugh, J. W. & Reilly, T. E. Flow and storage in groundwater systems. *Science* **296,** 1985–1990 (2002).
2. Oki, T. & Kanae, S. Global hydrological cycles and world water resources. *Science* **313,** 1068–1072 (2006).
3. Bookhagen, B. & Burbank, D. W. Toward a complete Himalayan hydrological budget: Spatiotemporal distribution of snowmelt and rainfall and their impact on river discharge. *J. Geophys. Res.* **115,** 1–25 (2010).
4. Scherler, D., Bookhagen, B. & Strecker, M. R. Spatially variable response of Himalayan glaciers to climate change affected by debris cover. *Nature Geosci.* **4,** 156–159 (2011).
5. Anderson, S. P., Dietrich, W. E. & Brimhall, G. H. Weathering profiles, mass-balance analysis, and rates of solute loss: Linkages between weathering and erosion in a small, steep catchment. *Geol. Soc. Am. Bull.* **114,** 1143–1158 (2002).
6. Tipper, E. *et al.* The short term climatic sensitivity of carbonate and silicate weathering fluxes: Insight from seasonal variations in river chemistry. *Geochim. Cosmochim. Acta* **70,** 2737–2754 (2006).
7. Calmels, D. *et al.* Contribution of deep groundwater to the weathering budget in a rapidly eroding mountain belt, Taiwan. *Earth Planet. Sci. Lett.* **303,** 48–58 (2011).
8. Montgomery, D. R. & Manga, M. Streamflow and water well responses to earthquakes. *Science* **300,** 2047–2049 (2003).
9. Barros, A. P., Chiao, S., Lang, T. J., Burbank, D. & Putkonen, J. From weather to climate—Seasonal and interannual variability of storms and implications for erosion processes in the Himalaya. *Geol. Soc. Am. Spec. Pap.* **398,** 17–38 (2006).
10. Andermann, C., Bonnet, S. & Gloaguen, R. Evaluation of precipitation data sets along the Himalayan front. *Geochem. Geophys. Geosys.* **12,** Q07023 (2011).
11. Shrestha, M. L. Interannual variation of summer monsoon rainfall over Nepal and its relation to Southern Oscillation Index. *Meteorol. Atmos. Phys.* **75,** 21–28 (2000).
12. Bookhagen, B., Thiede, R. & Strecker, M. Abnormal monsoon years and their control on erosion and sediment flux in the high, arid northwest Himalaya. *Earth Planet. Sci. Let.* **231,** 131–146 (2005).
13. Immerzeel, W., Droogers, P., Dejong, S. & Bierkens, M. Large-scale monitoring of snow cover and runoff simulation in Himalayan river basins using remote sensing. *Remote Sens. Environ.* **113,** 40–49 (2009).
14. Hannah, D., Kansakar, S., Gerrard, A. & Rees, G. Flow regimes of Himalayan rivers of Nepal: Nature and spatial patterns. *J. Hydrol.* **308,** 18–32 (2005).
15. Bookhagen, B. & Burbank, D. W. Topography, relief, and TRMM-derived rainfall variations along the Himalaya. *Geophys. Res. Lett.* **33,** L084505 (2006).
16. Putkonen, J. K. Continuous snow and rain data at 500 to 4400 m altitude near Annapurna, Nepal, 1999–2001. *Arct. Antarct. Alpine Res.* **36,** 244–248 (2004).
17. Lambert, L. & Chitrakar, B. Variation of potential evapotranspiration with elevation in Nepal. *Mountain Res. Dev.* **9,** 145–152 (1989).
18. Mouelhi, S., Michel, C., Perrin, C. & Andreassian, V. Stepwise development of a two-parameter monthly water balance model. *J. Hydrol.* **318,** 200–214 (2006).
19. Wang, Q. J. *et al.* Monthly versus daily water balance models in simulating monthly runoff. *J. Hydrol.* **404,** 166–175 (2011).
20. Bergström, S. in *The HBV Model. Computer Models in Watershed Hydrology* (ed. Singh, V. P.) 443–476 (Water Resources Publ., 1995).
21. Wittenberg, H. Baseflow recession and recharge as nonlinear storage processes. *Hydrol. Process.* **13,** 715–726 (1999).
22. Dongol, B. S. *et al.* Shallow groundwater in a middle mountain catchment of Nepal: Quantity and quality issues. *Environ. Geol.* **49,** 219–229 (2005).
23. De Marsily, G. *Quantitative Hydrogeology: Groundwater Hydrology for Engineering* (Academic, 1986).
24. Yatagai, A. *et al.* A 44-year daily gridded precipitation dataset for Asia based on a dense network of rain gauges. *Sola* **5,** 137–140 (2009).
25. Hall, D. K., Riggs, A. G. & Salomonson, V. V. MODIS/Terra Snow Cover 8-Day L3 Global 0.05deg CMG V005, MOD10C2. National Snow and Ice Data Center. Digital media (2006 updated daily).
26. Mitchell, T. D. & Jones, P. D. An improved method of constructing a database of monthly climate observations and associated high-resolution grids. *Int. J. Clim.* **25,** 693–712 (2005).

27. Bolch, T., Pieczonka, T. & Benn, D. I. Multi-decadal mass loss of glaciers in the Everest area (Nepal Himalaya) derived from stereo imagery. *Cryosphere* **5,** 349–358 (2011).
28. Rodell, M. *et al.* The global land data assimilation system. *Bull. Am. Meteorol. Soc.* **85,** 381–394 (2004).
29. National Snow and Ice Data Center. World glacier inventory. World Glacier Monitoring Service and National Snow and Ice Data Center/World Data Center for Glaciology. Digital media. (1999 updated 2009).
30. Department of Mines and Geology Nepal. Geological Map of Nepal. 1:1.000.000 (1994).

Acknowledgements

C.A. benefited from a three-year PhD scholarship awarded by the German Academic Exchange Service (DAAD, D/08/42538) and from the double PhD program of the French–German University Saarbrücken (DFH/UFA). The authors would like to thank K. P. Sharma and his team from the Department of Hydrology and Meteorology of Nepal (DHM) for providing hydrological data and M. Dhakal from ICIMOD Nepal for sharing their additional information on dug-well measurements.

Author contributions

C.A. acquired and analysed the data. L.L. and C.A. performed the hydrological modelling. All authors discussed the results and wrote the manuscript.

Additional information

The authors declare no competing financial interests. Supplementary information accompanies this paper on www.nature.com/naturegeoscience. Reprints and permissions information is available online at http://www.nature.com/reprints. Correspondence and requests for materials should be addressed to C.A.

4.2 General discussion

In this manuscript, I presented for the first time an annual anticlockwise hysteresis loop between precipitation and river discharge. This effect provides the unique chance to highlight the existence of an important hydrological compartment of the Himalayan discharge cycle, the fractured basement aquifer. The aquifer contributes a transient storage volume to the Himalayan discharge cycle, where water is temporally stored and retarded, yielding river discharge in the dry seasons. From the application of a conceptual hydrological model it is actually possible to quantify the transient storage volume. These findings have very important implications with regards to flood hazard management, landslide suggestibility and water resources. However, the calculated storage volume represents only a mean basin value, and it is difficult to distribute it within the basin. This is mainly because the subsurface properties in the studied basins are not well known and because of large intra-basin heterogeneities. The results provide a first order estimation of how water is transferred to river discharge, and of the response-time of the aquifer storage capacity.

In contrast to *Bookhagen and Burbank* [2010], I show that the transient storage of groundwater plays an important role in the Himalayan discharge cycle and has to be taken into account for hydrological modelling and/or stream flow predictions, for example for hydropower purposes. For annual budget analysis however, it is less important since the storage volume fluctuates always around the same mean. This is due to the very repetitive occurrence of the Indian Summer Monsoon, imposing a well defined annual cycle.

A second important observation is the similarity in the recharge-discharge behaviour between all studied basins. Regardless if the basins are situated in the front of the Himalayan range or in the glaciated High Himalayas, all basins describe the same hysteresis effect, independently of the basin lithology. Only, those basins with considerable glaciated areas and seasonal snow cover yield relatively more baseflow contribution to the river discharge. This highlights one more hydrological component, the snow and ice melt contribution to the river discharge, which can be actually quantified from the baseflow difference between glaciated and unglaciated basins. The contribution of ice and snow melt to the annual river discharge is $\sim$ 10%, confirming the importance of ice and snowmelt as a water resource [*Immerzeel et al.*, 2010]. This results are significantly higher than the $\sim$ 4% reported by *Alford and Armstrong* [2010]. First, this might be because *Alford and Armstrong* [2010] did not include snowmelt in their analysis and second, their temperature driven energy gradient model might be restrain by the temperature extrapolation technique ($1^{\circ}C/160$ m and 5400 m asl. set to 0°). Indeed, my estimations show that ice melt accounts for approximately 5% of the annual river discharge.

In summary, the ISM exerts a very clear and well defined control on the Himalayan discharge cycle. The very prominent transient groundwater storage volume leads to a 1 to 2 month phase shift in the transfer of rain to river discharge, retarding discharge in the early ISM season and yielding discharge in the dry seasons. Glacier and snow melt volumes are significant and maintain the baseflow of the rivers all year around. This three findings: 1) seasonal cyclicity, 2) groundwater storage and 3)

melt contribution, are fundamental to understand erosion and transport processes on a sub-seasonal resolution.

Chapter 5

Source, mobilization and transport of sediments

5.1 Introduction

In the two previous chapters I have presented two important properties: precipitation and river discharge, to evaluate the erosion processes of mobilisation and transport in the Nepal Himalayas. Intense rainfall can trigger the mobilisation of material [e.g. *Pratt et al.*, 2002; *Dadson et al.*, 2003; *Bookhagen et al.*, 2005a; *Wulf et al.*, 2010], rivers then transport the eroded materials out of the mountain range and deposit them in the foreland or the oceans [e.g. *Métivier et al.*, 1999; *Galy and France-Lanord*, 2001; *Clift et al.*, 2008a]. Therefore it is important to have a good knowledge on 1) the spatio-temporal distribution of rainfall, 2) the transfer of precipitation to river discharge, and finally 3) the availability of water to mobilize and transport material. In this chapter, I will investigate precipitation, river discharge and suspended sediment concentration measurements of several larger drainage basins in the Nepal Himalayas. As the precipitation and the discharge measurements, all suspended sediment concentrations are daily measurements.

The suspended sediment concentration data was collected from several places in Nepal. The largest part of the data has been obtained from the Department of Hydrology and Meteorology Nepal. Some data are published in feasibility reports of hydropower projects. Unlike the other datasets, suspended sediment concentration data was available only on hard-cover and had to be digitalized beforehand. Most of the data has never been published before and provides a new long-term and high resolution dataset to the Earth Sciences community. As such, it is the largest and most complete suspended sediment dataset for the whole Himalayas.

The following manuscript, which is submitted to *Earth Planetary Sciences Letters* has the motivation to provide suspended sediment erosion rates (denudation rates) for the three major basins of the Nepal Himalayas and several of their tributaries, and to explain the relations of mass fluxes with discharge

and precipitation throughout the seasons.

Connecting source and transport: suspended sediments in the Nepal Himalayas

Christoff Andermann[1,2,3], Alain Crave[1,2], Richard Gloaguen[3], Philippe Davy[1,2], Stephane Bonnet[4]

[1] Geosciences Rennes, CNRS/INSU, UMR 6118, Campus de Beaulieu, 35042 Rennes, France

[2] Université de Rennes 1, Campus de Beaulieu, 35042 Rennes, France

[3] Remote Sensing Group, Geology Institute, TU Bergakademie Freiberg, B.-von-Cotta-Str. 2, 09599 Freiberg, Germany

[4] Université de Toulouse, UPS (SVT-OMP), Géosciences Environnement Toulouse, UMR 5563, 14 Av. Edouard Belin, 31400 Toulouse, France

Corresponding author:

Christoff Andermann,

Tel (+33) 2 23 23 66 24

christoff.andermann@univ-rennes1.fr

Abstract:

Understanding the dynamics of sediment flux is a key issue to constrain modern erosion rates in mountain belts and the still debated level of control exerted by precipitation, topography and tectonics. In the Himalayas, the well defined monsoon seasonality, together with active tectonics and strong relief provide an ideal environment to assess these possible interactions. For this purpose, we present here a new compilation of daily suspended sediment data for 13 stations of the major rivers of the Nepal Himalayas. We analyze the relationships of sediment transport with daily river discharge and precipitation data as well as with morphometric parameters. We show that suspended sediment concentrations vary systematically through the seasons, displaying an annual clockwise hysteresis

effect when plotted against river discharge. This hysteresis effect disappears when suspended sediment fluxes are directly compared with direct storm discharge. Therefore we attribute the hysteresis effect to a dilution effect by groundwater rather than a supply effect. We infer a rating model to calculate erosion rates directly from long river discharge chronicles. We show that, when normalized by drainage area and mean sediment flux, all rivers exhibit the same trend. This implies that all river basins have the same erosion behavior, independent of location, size and catchment characteristics. Erosion rates calculated from suspended sediment fluxes range between 0.1 and 3.5 mm/yr. The highest erosion rates are calculated for stations situated at the mountain front and in the Annapurna region, while suspended sediment erosion rates in the Higher Himalayas are relatively low. We propose that material transport in the rivers depends on the supply from hillslopes, which is controlled by the occurrence of rainfall producing direct runoff. In other words, the rivers in the Nepal Himalayas are supply-limited and the hillsopes as a contributing source are transport-limited. We also show that erosion processes are not as much controlled by infrequently occurring extreme events, than by moderate ones with a high recurrence interval.

1. Introduction

Suspended sediment load in rivers is the primary proxy for present-day mean catchment denudation rates [Dadson et al., 2003; Summerfield and Hulton, 1994]. As such, these data are of first order importance to quantify the dependencies between denudation rates and their controlling factors [Dadson et al., 2003; Summerfield and Hulton, 1994; Milliman and Syvitski, 1992; Pinet and Souriau, 1988; Ahnert, 1970]. However, the use of bulk sediment load measurements to derive erosion rates is not straightforward [Fuller et al., 2003] and needs to take into account the sediment transfer mechanisms from hillslopes to the rivers, as well as within the rivers themselves [e.g. Benda and Dunne, 1997]. Discrete landslide events represent a major supply of material from hillslopes to rivers in rapidly evolving mountain settings, [Korup, 2009; Fuller et al., 2003; Hovius et al., 2000], their occurrence being tightly coupled to the spatio-temporal distribution of earthquakes [Hovius et al., 2011, 2000; Lin et al., 2008; Meunier et al., 2008] and of extreme precipitation events [Lin et al., 2008; Bookhagen et al., 2005b; Hovius et al., 2000; Iverson, 2000].

The capacity of rivers to transport sediments in suspension is proportional to their discharge and

then to rainfall and to the hydrologic properties of their drainage basin [e.g. Tucker and Slingerland, 1997]. Most of the parameters controlling sediment fluxes in mountain belts such as precipitation, floods, earthquakes, landslides among others, are consequently characterized by large intrinsic variabilities. Additionally, suspended sediment data themselves show a large variability [e.g. Kirchner et al., 2001]. Fuller et al. [2003] demonstrated that the interpretation of suspended sediment records in Taiwan needs at least to distinguish between transport-limited (sediments are available and variations in sediment flux depends only on the transport capacity of the river) and supply-limited (variations in sediment flux depend on the supply of sediments to the river from the hillslopes) conditions. Numerous studies also document discrepancies between short-term erosion rates derived from suspended sediment data and millennial to geological scale ones [Palumbo et al., 2011; Meyer et al., 2010; Dadson et al., 2003; Kirchner et al., 2001; Schaller et al., 2001]. Several reasons are invoked for the diminished relevance of the sediment flux calculation, such as the quality of the suspended sediment record itself, sampling frequency, length of record, characteristic timescale of occurrence of events, internal storage within drainage basins, or anthropogenic influences.

In the Himalayas, the spatial distribution of erosion is thought to scale with tectonics [e.g. Burbank et al., 2003], topography [e.g. Ouimet et al., 2009; Vance et al., 2003] and/or rainfall [e.g. Deeken et al., 2011; Gabet et al., 2008]. The quantification of erosion rates and a better understanding of actual impact of potential controlling factors have fundamental implications regarding the interactions and feedbacks between climate and tectonics [Wobus et al., 2005; Burbank et al., 2003; Beaumont et al., 2001; France-lanord and Derry, 1997; Raymo and Ruddiman, 1992;]. In the Himalayas, long-term changes in exhumation rates and patterns, deduced from thermochronology, have been attributed to climatic variations [Grujic et al., 2006; Huntington et al., 2006]. The possible coupling between erosion and precipitation in the Himalayas is inferred from the coincidence between spatial variations of long-term exhumation rates, also determined by thermochronology, and the present-day spatial distribution of rainfall [Deeken et al., 2011; Thiede et al., 2004; Zeitler et al., 2001]. The coincidence of spatial variations of erosion rates with present-day precipitation gradient is also documented at a shorter time-scale, for example, by Garzanti et al. [2007] using provenance analysis or by Gabet et al. [2008] using suspended sediment load data. However this coincidence is not always observed, particularly in thermochronological data [Thiede et al., 2009; Burbank et al., 2003]. To better understand the impact of

climate on erosion in the Himalayas, some authors focused their study on a millennial time scale and looked at relationships between erosion and Indian Summer Monsoon (ISM) intensity [Clift et al., 2008; Bookhagen et al., 2005a; Goodbred and Kuehl, 2000]. These studies show that Himalayan erosion is coupled to ISM intensity variations over the last thousands years, a finding also supported at the annual or event scale [e.g. Wulf et al. 2010, Bookhagen et al. 2005b]. Bookhagen et al. [2005b] observed enhanced hillslope erosion and increased suspended sediment flux in the Sutlej catchment during the 2002 abnormal monsoon year and Wulf et al. [2010] shows that fluvial sediment fluxes are largely controlled by episodic heavy monsoon rainstorms. The existence of rainfall thresholds for the triggering of landslides was proposed by Dahal and Hasegawa [2008], Gabet et al. [2004] and Froehlich et al., [1990], illustrating any coupling between precipitation and erosional processes is complex in detail.

This paper focuses on the analysis of daily sediment flux measurements covering several years, based on a new suspended sediment concentration compilation available for the whole Nepal Himalayas. Our data covers the three major drainage basins of Nepal and several tributaries. We characterize the underlying mechanisms of suspended sediment vs. discharge hysteresis phenomena. We present the temporal magnitude-frequency distribution of suspended sediment fluxes. On the basis of the clear relationship between direct river discharge and sediment fluxes we propose a new sediment transport rating model, allowing us to deduce basin wide denudation rates from long (~30 yr) river discharge chronicles. Finally, we discuss these basin-wide denudation rates in the context of basin characteristics and propose a conceptual model of mobilization and transportation of material within the monsoonal discharge cycle and its possible implications. The goal of this study is: 1) to better understand the impact of ISM on erosion fluxes, 2) to deduce basin-wide erosion rates from suspended sediments, and 3) to contribute to the understanding of the spatio-temporal relation between erosion, precipitation, river discharge and topography.

2. Local settings

The southern front of the central Himalayas has two very distinct climatic periods [Hannah et al., 2005] an extremely wet (June-September) ISM season and the very dry (October-May) season. The dry season can be subdivided into post-ISM (October - November), winter (December – February) and pre-

ISM (March – May). Up to 80% of the annual amount of precipitation falls during ISM season and only a small fraction (20%) in non-ISM season [Andermann et al., 2011; Bookhagen and Burbank, 2006; Shrestha, 2000]. The precipitation distribution across the mountain front is strongly influenced by orographic effects, resulting in a tenfold increase from the southern lowlands to elevations of ~4000 m asl. dropping to a minimum of ~250 mm/yr on the Tibetan plateau [Andermann et al., 2011; Anders et al., 2006; Bookhagen and Burbank, 2006]. Annual precipitation rates are >1500 mm/yr and locally more than 4000 mm/yr along the Himalayan front of Nepal [Andermann et al., 2011; Shrestha, 2000]. The stupendous differences between the wet and dry seasons exert a control on the environment, (e.g. water availability, soil saturation, vegetation cover, pore pressure, landslide vulnerability). The ISM may even inhibit seismic activity due to a water storage overburden in the subsurface [Bollinger et al., 2007]. In particular, the volume of groundwater water storage and consequently the availability of water is tightly coupled to the ISM [Andermann et al., in press]. The strong variability, intensity and duration of ISM precipitation can be linked to the El Nino/Southern Oscillation (ENSO cycles) [Shrestha, 2000]. Intense ISM years enhance the annual precipitation amount by 25 – 50% at elevations below 3 km asl. and up to 200% at higher elevations [Bookhagen et al., 2005b]. During these abnormal years, moisture can be transported deep into the mountain front, into the usually arid mountain interior and the Tibetan Plateau [Wulf et al., 2010].

The entire Himalayan chain in Nepal is drained through three major watersheds (Fig. 1 and Fig. 2), (1) Sapta-Koshi in the east, (2) Narayani in the center and (3) Karnali Basin in the west. These three basins differ considerably with respect to annual rainfall rate, size, elevation distribution and contributing area of the Tibetan Plateau (Table 1). Remarkable is the Sapta-Koshi basin, where the Arun River cuts through the Himalayan chain (Fig. 1), with ~55% of its total drainage area (Sapta-Koshi Basin) on the Tibetan Plateau. The part of Sapta-Koshi Basin within the Himalayan front is very humid and characterized by high precipitation intensities (Fig. 2). The Narayani Basin is the most humid basin in Nepal (Table 1). In particular, very high precipitation intensities are recorded in front of the Annapurna massif (Fig. 2). Glacier cover is relatively high (14%) and the contribution from the plateau is relatively small. In the Karnali Basin, the Himalayan front is less pronounced and the mountains are not as high (max. ~7700 m asl.) and thus, the orographic rainfall gradient is more gentle. Rainfall intensities in the upper Karnali Basin are comparably low (Fig. 2) and proportionally the

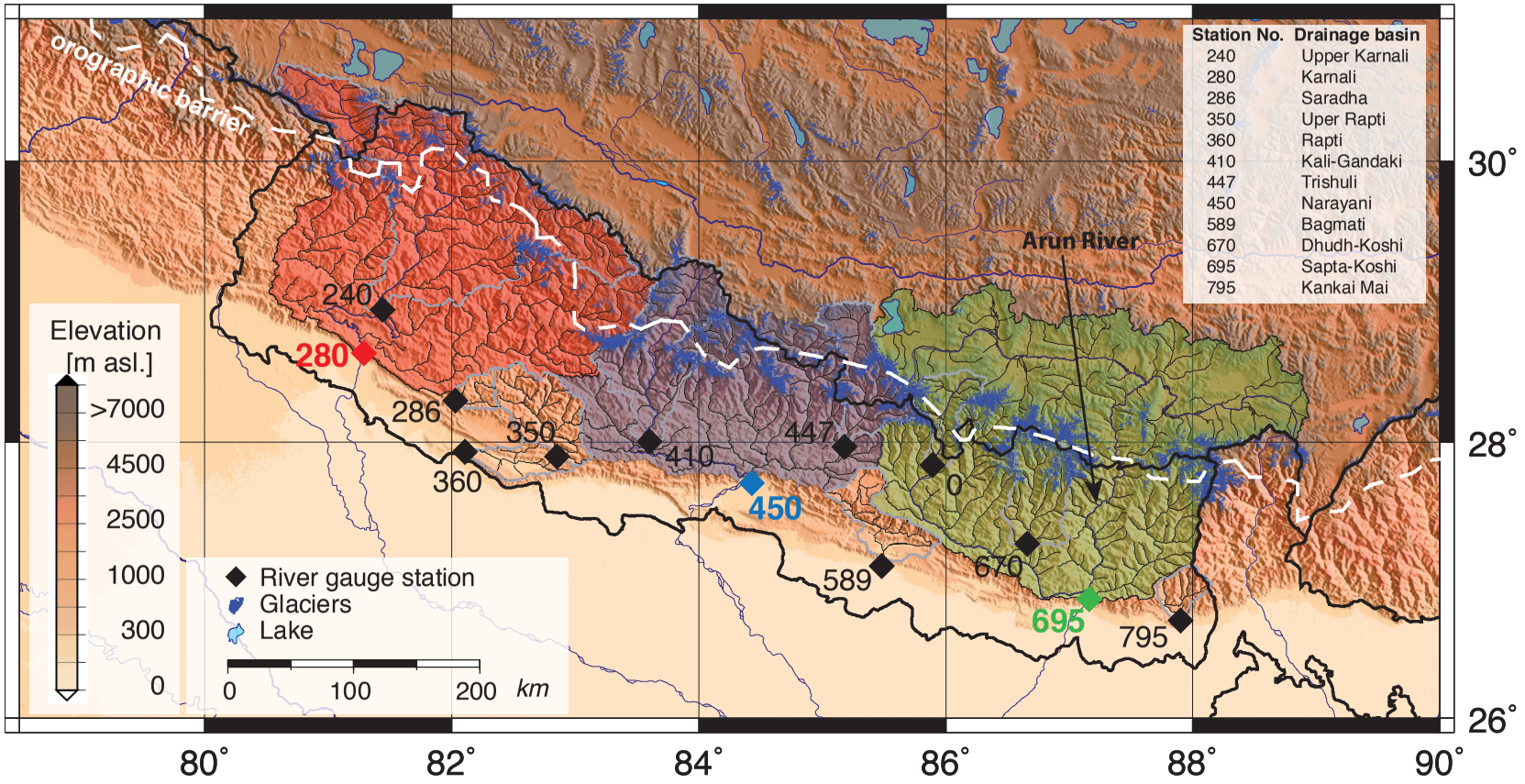

Figure 1: *Map of the three main drainage basins of the central Himalayas in Nepal, from the east to the west: Karnali (red), Narayani (blue) and Sapta Koshi Basin (green). Color coding is carried through the entire manuscript. Hydrological stations, from where we analyzed data in this work, are indicated with diamonds and their respective station number. Grey boundaries mark the outlines of sub-catchments. color coding corresponds to elevation, draped over shaded relief. Glaciers are indicated in dark blue.*

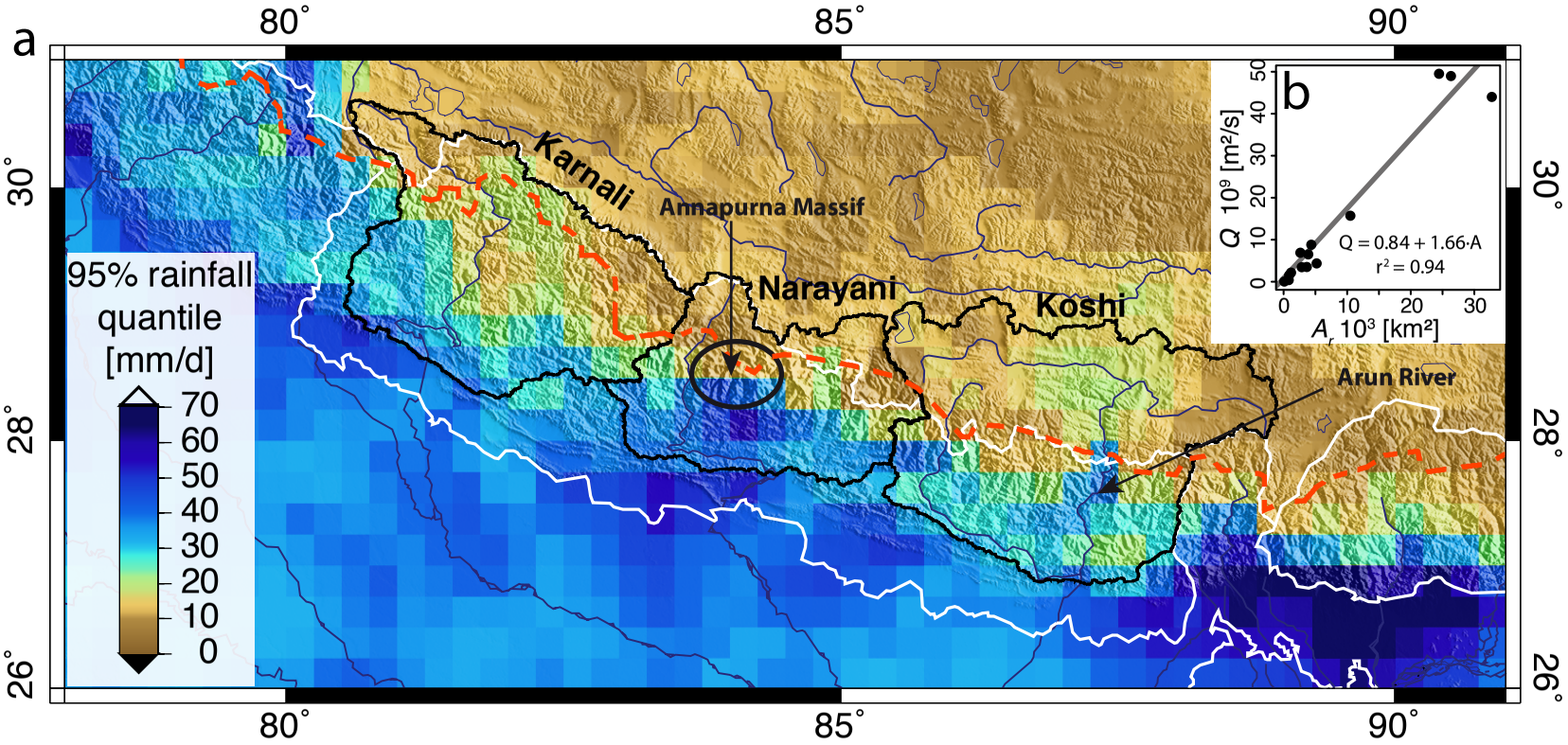

Figure 2: *a) Map of precipitation quantiles distribution, illustrating the 95% quantile of daily precipitation rates, calculated on the cumulative probability of 30 years of daily precipitation rates of each pixel. Precipitation information is derived from APHRODITE dataset. b) Regression mean annual basin discharge vs. basin area A_r (only Himalayan front). Red dotted line represents the Himalayan ridge crest extracted from precipitation gradient.*

Table 1: *Table of basin parameters of the drainage basins considered here. Geographic coordinates are the station location at basin outlet. The % contribution of Plateau is calculated from the area of the basin on the plateau in relation to the total drainage area. Slope represents the mean slope of the fraction of the watershed located at the mountain front. C_s stands suspended sediment concentration and number represents the days of available data. Discharge Q, is measured at the same location as concentrations. Precipitation R, is the mean basin-wide annual rainfall rate extracted from APHRODITE data.*

Basin No.	0	240	**280**	286	350	360	410	447	**450**	589	670	**695**	795
Basin name	Bhote Koshi	Upper Karnali	**Karnali**	Saradha	Upper Rapti	Rapti	Kali Gandaki	Trishuli	**Narayani**	Bagmati	Dudh Koshi	**Sapta Koshi**	Kankai Mai
Lat/Long [°]	27.75/85.26	28.95/81.44	**28.64/81.29**	27.64/82.02	27.90/82.85	27.95/82.23	28.01/83.60	27.97/85.18	**27.71/84.43**	27.11/85.48	27.27/86.66	**28.87/87.16**	26.70/87.88
Drainage area *A* [km²]	2308	21121	**45967**	808	3648	5197	7170	4428	**32002**	2849	3880	**57719**	1172
% contribution Plateau	62	50	**29**	0	0	0	39	40	**24**	0	0	**55**	0
Mean slope mountain front [°]	27.4	25.7	**27.9**	22.2	25.7	21.5	29.3	30.3	**26.7**	17.2	27.3	**26.1**	19.0
Mean basin relief [km]	2.7	2.3	**2.1**	1.2	1.4	1.2	2.8	2.9	**2.3**	1.2	2.6	**2.2**	1.4
% area glaciated	12.4	5.9	**4.7**	0	0	0	10.3	6.5	**9.9**	0	14.7	**7.3**	0
Number of C_s values	635	1034	**767**	1953	1391	804	1299	665	**1677**	373	365	**1185**	445
Years of availability	2004-2008	1975-1979	**1973, 1974, 1977-1979**	1976-1978, 1985-1987	1978, 1985-1988	1985, 1987, 1988	1979, 1980, 1987, 1988, 1990	1973- 1977, 1979	**1976, 1977, 1979, 1985, 1986, 1993, 2001-2003**	2001-2003	1987	**1987- 1999, 2001-2003**	2001-2003
Data source *	*3*	*1*	***1***	*1*	*1*	*1*	*1*	*1*	***1 & 2***	*2*	*4*	***1 & 2***	*2*
Availability *Q*	2004-2006	1975-2006	**1973-2006**	1976-2006	1978-2006	1985-2006	1979-1995	1977-2006	**1973-2006**	2001-2006	1987-2006	**1977-2006**	2001-2006
Annual *Q* [km³]	1.5	15.7	**44**	0.4	3.5	4.4	8.8	6.9	**49.5**	3.47	6.5	**49**	2.2
Annual *R* [mm]	797	558	**920**	1107	1522	1470	1030	692	**1396**	1932	1295	**920**	1288

** Data sources: 1) (DHM, 2003), 2) (DHM/FFS, 2004), 3) Bothe Koshi Power company Ltd., 4) (NEP, 1998)*

contributing area of the plateau is important. Rainfall intensities and specific discharge are the lowest of the three basins (Table 1).

Rivers valleys are deeply incised in the central Himalayas of Nepal, and descend a considerable elevation range over a relatively short distance (~ 300km), from several thousand meters above sea-level (High Himalayas) to around 150 meters in the Indian Lowland (Fig. 1). All rivers in the Nepal Himalayas are bedrock rivers incising actively into Himalayan basement rock. Rivers are highly channelized, with little accommodation space for temporal sediment deposition and with high transport capacities (flow rates >1 m^3/s). The annual river hydrographs (Fig. 3) highlight clearly the control of the ISM on Himalayan rivers in Nepal, causing a one to two order of magnitude increase of discharge. In contrast to the rivers of the western (e.g. Indus and Sutlej) and eastern Himalayas (e.g. Tsangpo-Brahmaputra), snow and glacier melt contribution is minor in the central Himalayas [Bookhagen and Burbank, 2010]. A large volume of the river discharge in the Nepal Himalayas passes through the deep fractured basement aquifer, representative of ~2/3 of the annual river discharge volume [Andermann et al., in press].

The retrieval of suspended sediment measurements is routine in many regions of the world but in the Himalayas measurements are limited to few stations and published detailed studies are limited to small regions over short periods of time [e.g. Haritashya et al., 2010; Wulf et al., 2010; Gabet et al., 2008; Craddock et al., 2007; Singh et al., 2005; Hasnain and Thayyen, 1999]. The fact that sediment concentrations vs. river discharge displays a hysteresis behavior through the seasons [Wulf et al., 2010; Gabet et al., 2008; Hasnain and Thayyen, 1999] suggest that the supply of material and/or water sources vary temporally between the seasons. Due to the rugged and deeply incised landscape of the Himalayas slope failure and mass-wasting are common, mobilizing considerable volumes of material [Fort et al., 2010; Burtin et al., 2009; Dortch et al., 2009]. Earthquakes can be excluded as pivotal factor of sediment mobilization in the region of interest and during the time span of available records. No large earthquake ($M > 6.5$) occurred (Global Centroid-Moment tensor (CMT) catalog, www.globalcmt.org), and moreover, seismic activity is less during monsoon season [Bollinger et al., 2007] when the highest suspended sediment concentrations are observed.

To calculate absolute erosion rates from river load, the bedload and solute transport fractions have to be considered [e.g. Turowski et al., 2010]. While the solute fraction is often only minor in terms of

volume (1 - 4 % [see e.g. Gabet et al., 2008; Summerfield and Hulton, 1994], *< 10%* [Gal and France-

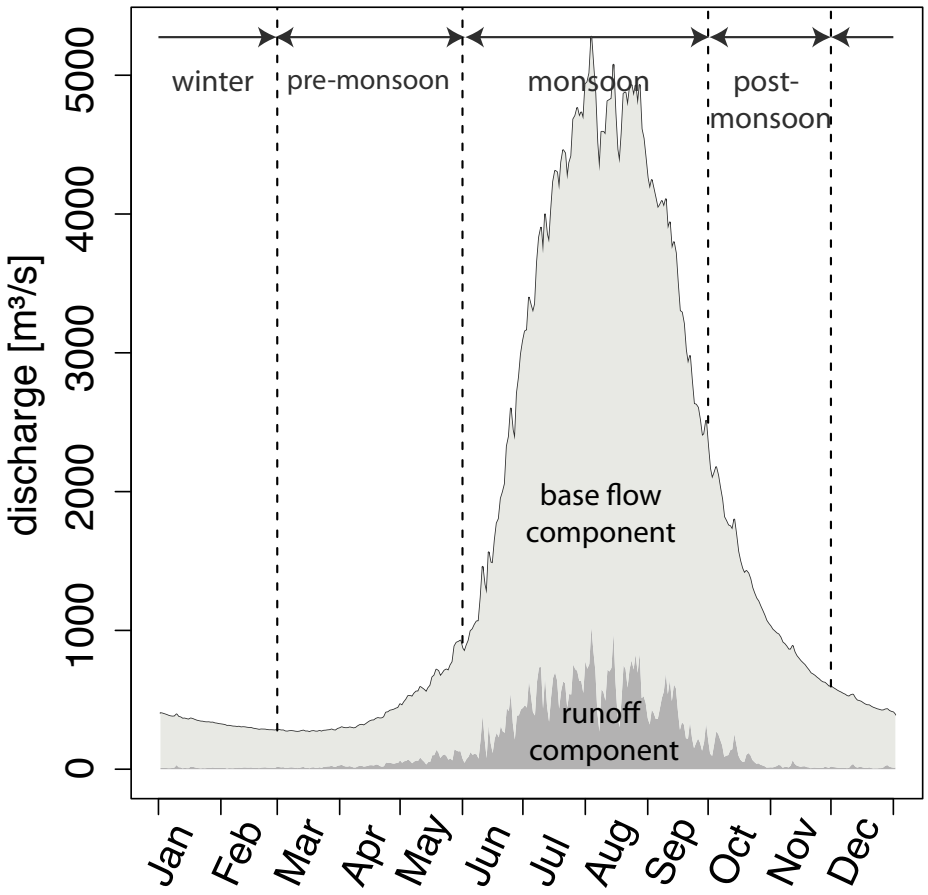

Figure 3: *Mean annual river discharge hydrograph of station 450, Narayani basin (~34 years). The four seasons are indicated with dashed lines. Runoff component is the mean daily discharge contribution by direct runoff Q_d. Base flow represents the slow flow component. Discharge was separated using the local minimum method.*

Lanord 2001]), bedload has the potential to account for large quantities of total transport [Galy and France-Lanord, 2001; Pratt-Sitaula et al., 2007; Wulf et al., 2010]. Bedload is certainly the most difficult fraction to measure and is essentially the unknown fraction [Galy and France-Lanord, 2001]. Turowski et al. [2010] show from the analysis of a large empirical dataset from the European Alps that the contribution of bedload is not constant over time and varies significantly between different settings. Pratt-Sitaula et al. [2007] report bedload fractions of ~25% of the total erosion rate, from dam-infill,

trapping sediments from the mainly arid upper Marsyandi River Basin in Nepal. Wulf et al. [2010] also analyzed a basin north of the orographic barrier and found that bedload is one third of erosion rate. Galy and France-Lanord [2001] deduced from geochemical analyzes that suspended sediments count only for the half of the erosion rate in the Himalayas. Finally, Burtin et al. [2009] suggest that bedload transport is minor on the Tibetan Plateau and in the Lesser Himalayan range.

3. Data and Methods

We use daily suspended sediment concentration, river discharge, and precipitation data to analyse the sediment transport behavior (Fig. 4). Daily suspended sediment concentrations, $C_s(i)$ (with i for daily indices), are available for 13 stations (Fig. 1) and are obtained from various sources (listed in Table 1). The majority of the data is derived from the Department of Hydrology and Meteorology Nepal DHM [DHM/FFS, 2004; DHM and His Majesty's Government, 2003]. Bhote Khoshi data (station 0) were kindly provided by the local hydropower operation company "BK Power", measured upstream of the intake. Data on Dudh Koshi (station 670) are taken from a hydro-power feasibility report [NEP, 1998]. All data are continuous daily measurements, spanning several years (i.e. ~4-6 years) between 1973 and 2006, but are not always continuous (Fig. 4 and Table 1). Years with available data are not necessarily coincident between the river basins (Table 1). Days of missing data are randomly distributed over the available time series and do not cluster preferentially in one season (e.g. monsoon season). All statistical analyses are conducted on the raw - not interpolated - data. C_s measurements are usually depth integrated measurements, "following the USGS Method" [DHM and His Majesty's Government, 2003]. However data quality might vary and representativeness between the stations might be biased. It should be noted that these data are the only available for the major hydrological units of Nepal. We used raw daily river discharge data $Q(i)$ (chronicles of ~30 years in most cases, see Table 1) provided by the DHM for all 13 stations (Fig. 1). Data are derived from daily stage readings and calibrated rating curves. We estimate discharge measuring accuracy to be ±10%. Daily precipitation (R) is extracted from the APHRODITE (Asian Precipitation Highly Resolved Observational Data Integration Towards Evaluation of Water Resources) precipitation dataset [Yatagai et al., 2009]. The data are an interpolated rain gauge product, comprising orographic corrections. In terms of temporal resolution and absolute accuracy it is presently the best available dataset for the Himalayan region [Andermann et al., 2011] APHRODITE data are available from 1951 until 2007, in

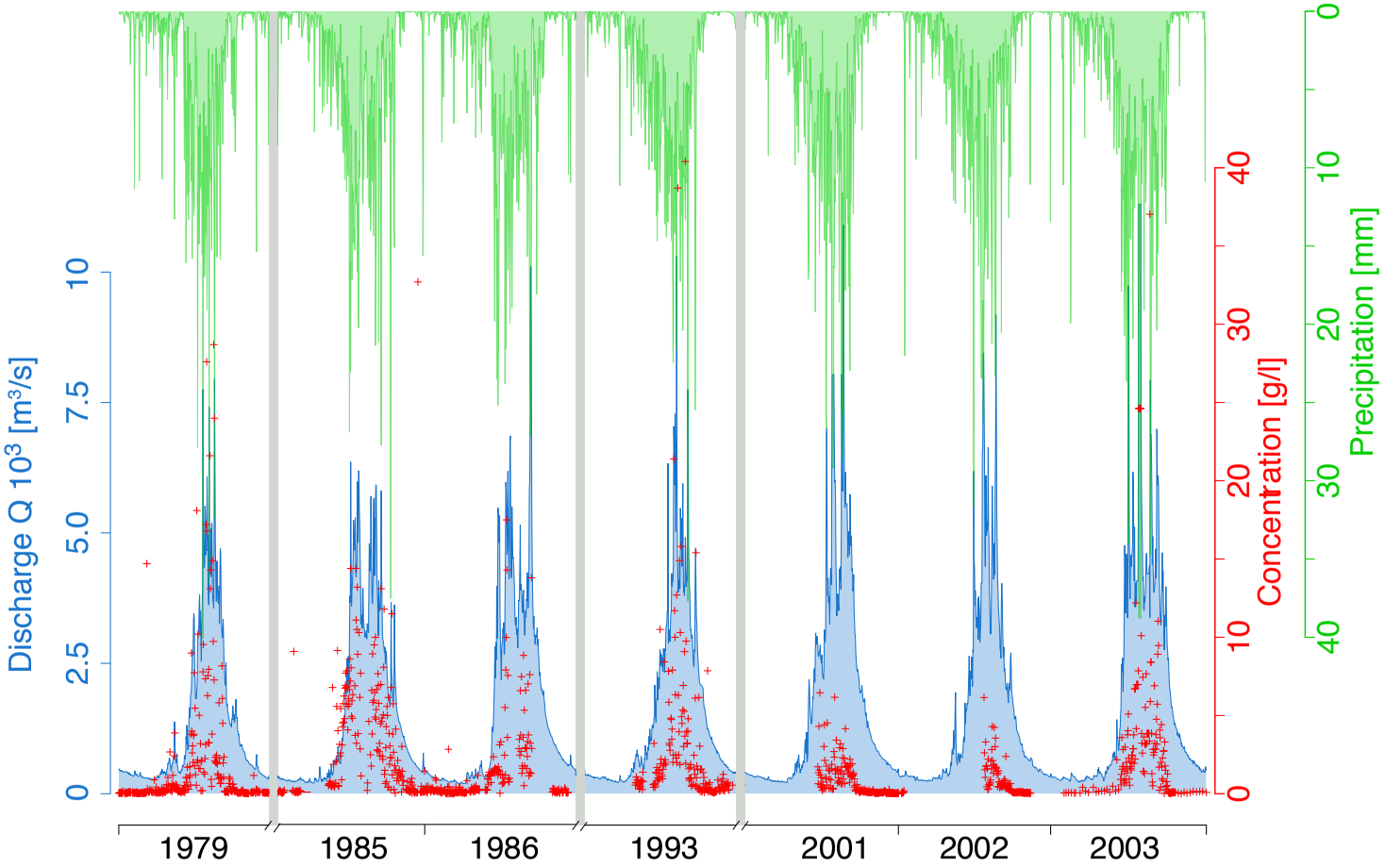

Figure 4: *Demonstration of the data used in this study at the station 450 (Narayani basin) over 7 years as an example. Daily discharge data Q, and daily suspended sediment concentrations C_s measured at the same position. Both data are derived from the Department of Hydrology and Meteorology Nepal (DHM). Mean daily basin-wide precipitation volume, extracted from APHRODITE data.*

daily temporal resolution and 0.25° (~30 km) spatial resolution. Elevation information is extracted from SRTM-4 DEM [Javis et al., 2008; http://srtm.csi.cgiar.org].

Frequency distribution analyses are commonly used to describe natural systems, e.g. distribution of fault lengths [Davy, 1993], landslide area [Malamud et al., 2004], floods [Malamud and Turcotte, 2006], hazardous events [Korup and Clague, 2009] and sediment fluxes [Hovius et al., 2000]. In this paper we calculate the density distribution as a function of probability of the total mass flux Q_s (C_s*Q), to describe their characteristic magnitude-frequency distribution. By definition, the probability density distribution function $p(x)$ is defined as the probability P of an event to fall into a certain range of magnitude between x and $x+dx$ (if: $dx>0$),

$$P[x \leqslant X \leqslant x+dx] = \int_{x}^{x+dx} p(x)\,dx \qquad (1)$$

where the probability of a certain magnitude $p(x_i)$, is a function of the number of events $n(x_i)$ within a range of magnitudes Δx_i, given by:

$$\log\left(x_j\right) = \frac{j}{N}\log\left(x_m\right) \qquad (2)$$

Here, the range Δx_i increases equally spaced on a logarithmic scale, using:

$$\log\left(x_j\right) = \frac{j}{N}\log\left(x_m\right) \qquad (3)$$

where j is the number of ranges, N is the total number of samples and x_m is the maximum value observed. Increasing spacing with magnitude has the advantage to integrate also for large magnitudes over a representative number of events [Davy, 1993]. Here we normalize with the respective mean, $\bar{x}$, $X/\bar{x}=X^*$ in order to compare over a large range of system sizes (drainage area).

We define direct runoff, or storm runoff Q_d *as* the fraction of river discharge characterized by a short transfer time, resulting in a short response (< 1 day) of the discharge hydrograph to a corresponding rainfall event. Hydrograph separation analysis are usually applied to separate river discharge into a low-frequency baseflow Q_b component and a high-frequency Q_d component [Lim et al., 2010]. Here,

we used the local minimum method implemented in the Web-based Hydrograph Analysis Tool WHAT [WHAT, 2011; Lim et al., 2010]. This method connects the local minimum points by comparing the slope of the hydrographs. Since several events might overlap within the sequence, producing local minimum points within the duration of Q_d, the Q_b component can be overestimated [WHAT, 2011]. Q_{ds} is the daily total mass flux Qs [t/day] where $Q_d \neq 0$, and $\bar{q_{ds}}$ its respective annual mean in t/day.

In order to separate regions which we assign as arid plateau or humid mountain range, we extracted the 500 mm/yr isohyet. For this purpose, we classified the high resolution TRMM-3B31 precipitation dataset of Bookhagen and Burbank [2006] in <500 mm/yr and >500 mm/yr precipitation and extracted the resulting boundary (Fig. 1 and Fig. 2). We choose this criteria as a significant precipitation boundary and hereafter referred to as the orographic barrier. The basins analyzed here are subset along the orographic barrier into the part draining the arid plateau and the part draining the wet mountain front. The total drainage area A and the respective drainage area within the wet mountain range A_r are listed in Table 1.

Because concentration measurements are not complete and only available for several years (Tab. 1), we calculated sediment fluxes on the basis of the more comprehensive and longer water discharge chronicles. Empirical power law relations are commonly used to express Q_s as function of Q in form of a rating curve [e.g. Morehead, 2003]. In this study, we define rating curves between the discharge component Q_d and the transported mass Q_s:

$$Q_s = aQ_d^b \qquad (4)$$

where a and b are rating parameters. Both Q_d and Q_s are normalized with the drainage area A_r of the Himalayan front ($Q_s^* = Q_s/A_r$). To avoid erroneous estimation of parameters a and b, rating curves (Eq. 4) are fitted to the data on a logarithmic scale applying standard maximum likelihood regression method [Goldstein et al., 2004]. The fitting procedure was carried out for the best fit as well as for the $\pm 1\sigma$ (2σ) confidence interval determination. From this general law we calculated mean basin wide denudation rates D for all basins. We calculated the annual denudation rates [mm] from the transported mass assuming a density typical for quartz, 2.65 g/cm^3.

4. Results

C_s vs. Q plots reveal a clockwise hysteresis effect on an annual scale for all the Himalayan rivers analyzed here, as illustrated by the example of Narayani outlet station (st. 450): Figure 5a. C_s and Q are low in winter season and rise with increasing ISM. Both C_s and Q are at their maxima during ISM and decrease during post-ISM, C_s is systematically lower for the same amount of Q during post-ISM as during pre-ISM. Monthly mean values confirm the annual hysteresis behavior. In general, C_s variability is high all year around, but the variability of Q increases with rising ISM, with larger variability in pre-ISM and smaller in post-ISM (Fig. 5a). Several concentrations exceed 5000 ppm (5 g/ l), mostly during pre- and ISM season. Plotting C_s against Q_d the hysteresis effect disappears (Fig. 5b), and reveals a linear relationship, with a slope of one between the two variables. Low concentrations cluster during post-ISM and winter season and high to very high concentrations cluster in pre-ISM and ISM. Variability, both for C_s and Q_d are high all year around.

The Probability density distribution of the specific direct runoff fluxes Q_{ds}^* (normalized by the mean $\bar{q_{ds}}$ [t/day]), reveals that all rivers display the same statistical distribution with respect to their means (Fig. 6). Mean C_s fluxes are listed in Table 2 and vary over a large range, from 1953 t/day in Saradha basin to ~1 million t/day in Karnali basin. Remarkable is the threshold for $Q_{ds}^* \approx 2$, which is similar for all rivers (Fig. 6). Events with $Q_{ds}^* < 1$ align along a power law distribution with a slope ~ -1. The larger events describe a different distribution trend with a slope ~ -2. Except for very small events, the scatter between different rivers is minimal. In terms of mass, the total transport of each river is dominated by events larger than the respective mean flux $\bar{q_{ds}}$. In bulk, 71% of all the transported mass, considering all rivers, fall within the specific discharge range of $1< Q_{ds}^* < 8$ (Fig. 6).

Sediment mass fluxes increase with Q_d (Fig. 7). Plotting the normalized values Q_d against the volume transported Q_{ds} during Q_d events reveals a well defined minimum threshold, above which Q_{ds} increases linearly with increasing Q_d, with a slope of >1 (Table 2). Striking is the threshold, $Q_d \approx 0.04$ mm/day, identical for all rivers. However, their corresponding base flux volumes Q_{ds} vary between the basins over one magnitude (Fig. 7 and Table 2). The fact that all Q_d and Q_s of all rivers are normalized with their respective drainage area A_r (only Himalayan front) demonstrates their similar behavior in terms of erosion and sediment fluxes. We observe more similarity between the basins when normalizing with A_r than using the total drainage area A.

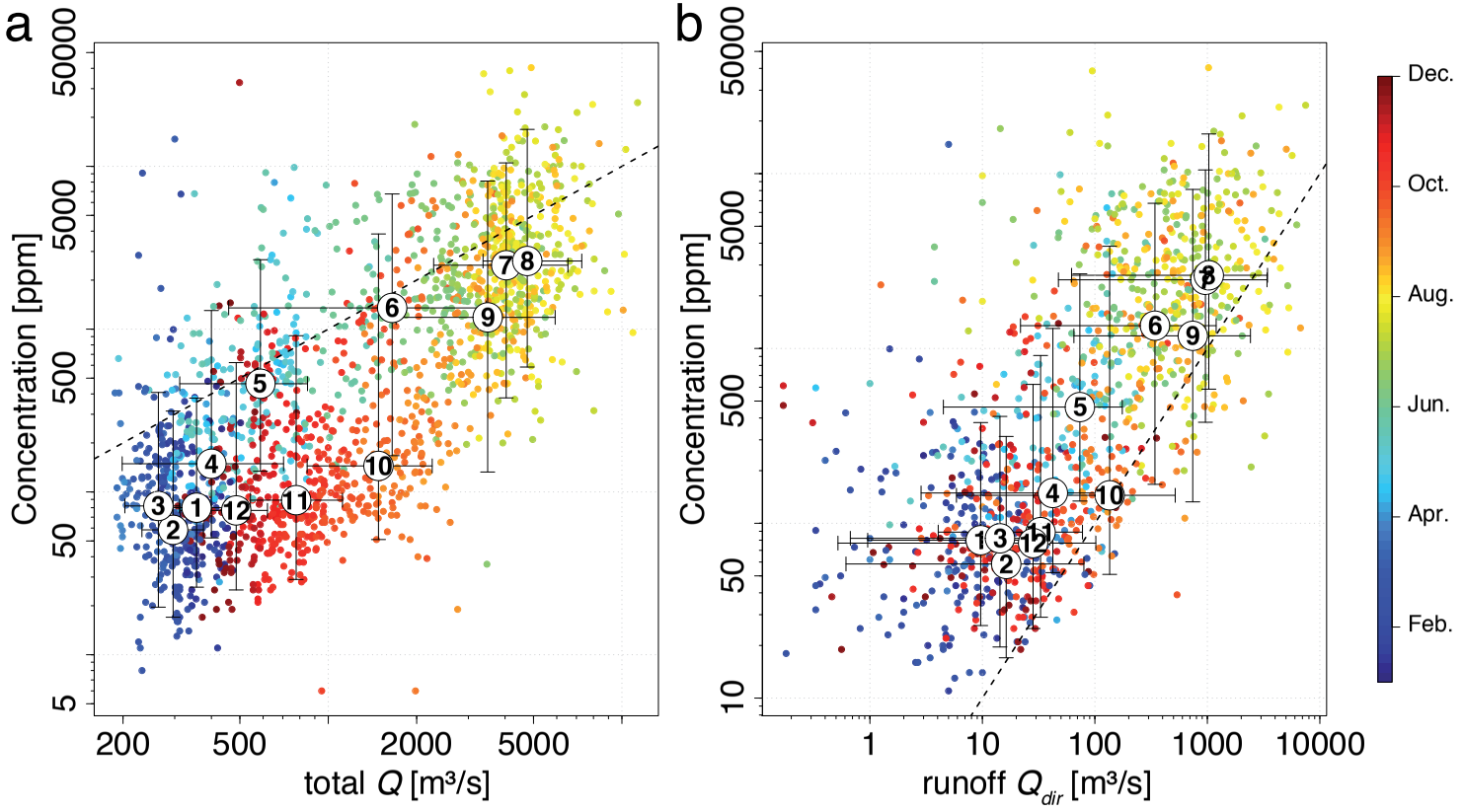

Figure 5: *Bi-logarithmic plots, suspended sediment concentration C_s vs. discharge Q component. Data points are color coded by annual sequence. White filled circles represent the mean monthly values, month are indicated by numbers. Error bars represent the quantiles (5%, 95%) of the monthly data distribution. a) Daily suspended sediment concentration C_s and daily river discharge Q hysteresis plot. Q represents the total daily discharge. b) Daily suspended sediment concentration C_s plotted against corresponding surface storm runoff fraction Q_d of the total river discharge Q. Q_d is separated from Q using the local minimum method.*

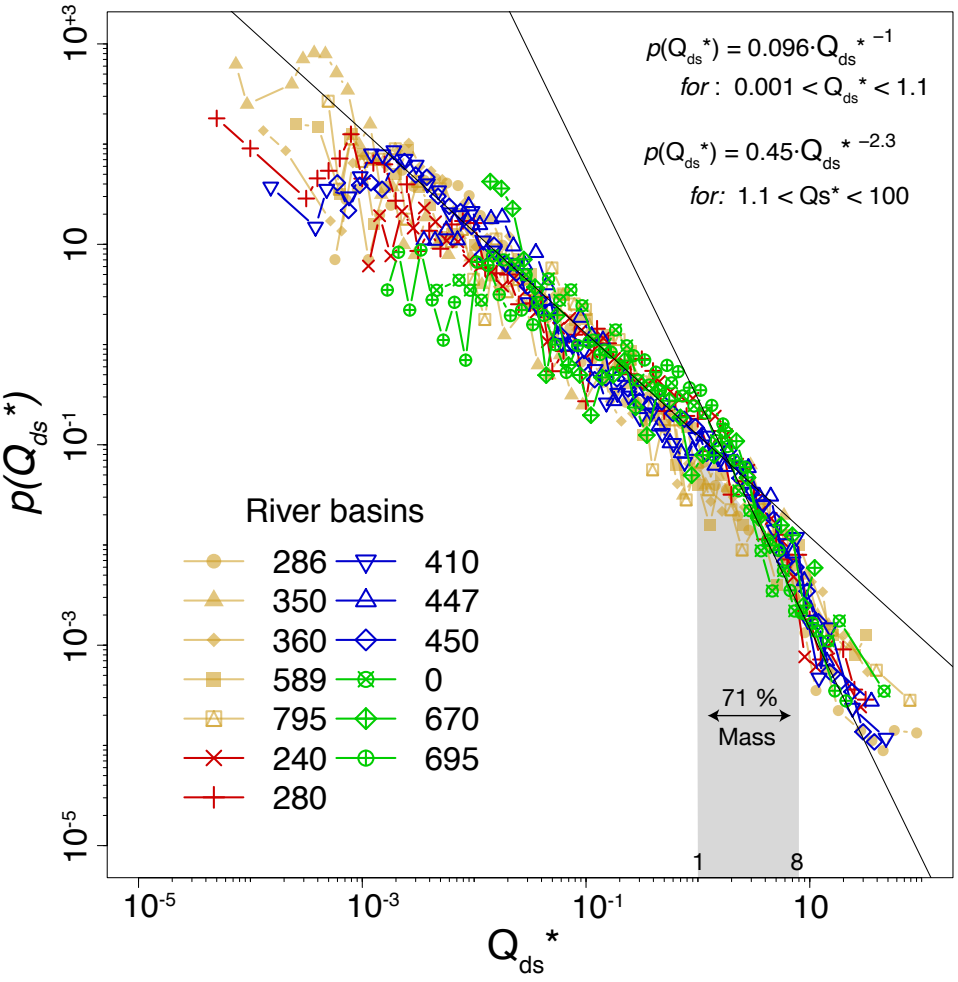

Figure 6: *Probability density distribution function plot of normalized Q_{ds}*. Q_{ds} [t/day] is the sediment flux on days where direct runoff Q_d exists. Data has been normalized by respective mean $\bar{q}_{ds}$ [t/day] of each basin. Events plotting between between Q_{ds}* 1 and 8 account for ~71% of the transported mass plotted here.*

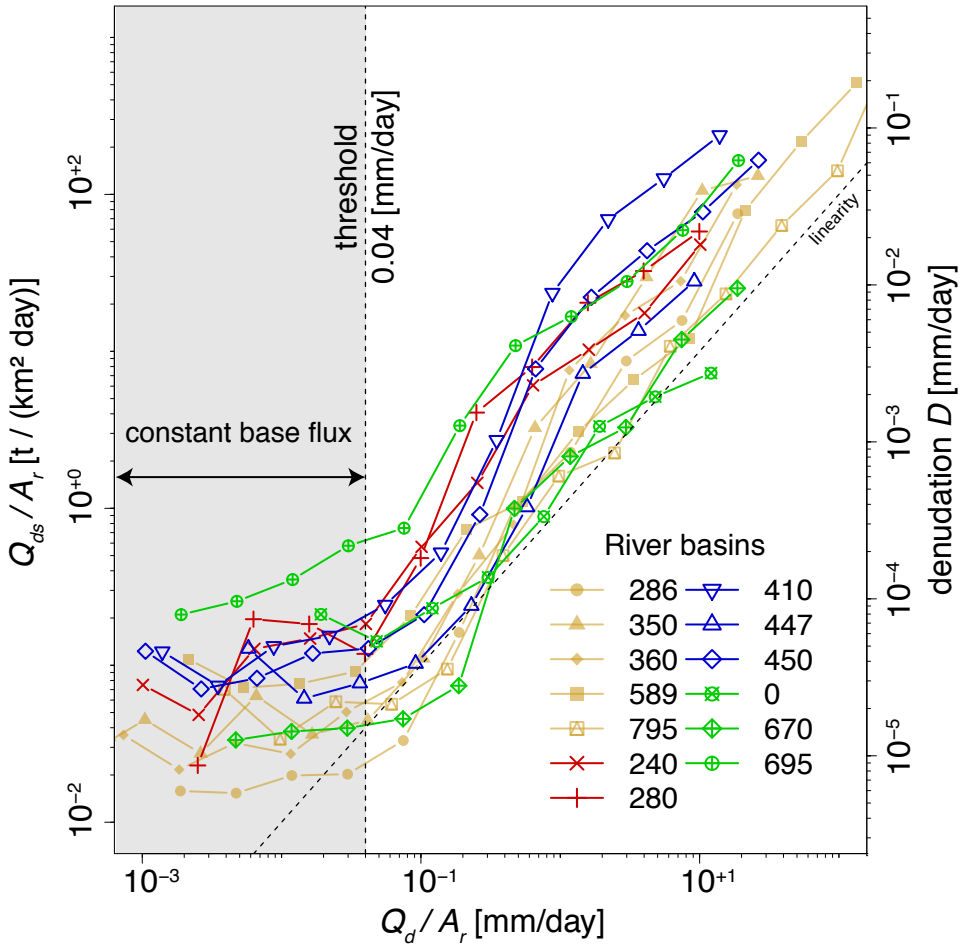

Figure 7: *Bi-logarithmic plot of suspended sediment fluxes Q_{ds} and direct runoff Q_d, binned median of logarithmic equally spaced ranges . Both Q_{ds} and Q_d are normalized with the respective basin size (Himalayan front only). Q_{ds} is the total suspended sediment flux for days where $Q_d > 0$. Denudation rates D are calculated from Q_{ds} presuming a density of 2.65 g/m³. The threshold (0.04 mm/day) indicates the limit below which suspended fluxes are constant. The gray dashed line indicates linear relationship.*

Table 2: *Main results. $\bar{q}_{sd}$ is the mean daily sediment flux calculated for each basin from the entire dataset available. $\bar{q}_{sd}$ was used to to normalize each basin dataset in the probability density function plot (Fig. 6). The % contribution Q_d represents contribution of direct runoff to the total river discharge. Rating parameters are derived from Q_d vs. Q_{sd} plot. Annual mass flux Q_s and denudation rates D are calculated from rating curves on direct storm runoff Q_d. D is calculated on the basis of the drainage area at the Himalayan front. Sigma represents the confidence interval of the fit.*

Basin No.	0	240	**280**	286	350	360	410	447	**450**	589	670	**695**	795
Basin name	Bhote Koshi	Upper Karnali	**Karnali**	Saradha	Upper Rapti	Rapti	Kali Gandaki	Trishuli	**Narayani**	Bagmati	Dudh Koshi	**Sapta Koshi**	Kankai Mai
Mean C_s flux [t/day]	3753	100635	**967683**	1953	85108	43972	117651	12399	**818240**	95255	8737	**664269**	24909
% contribution Q_d	7	8	**10**	25	22	26	12	9	**11**	46	15	**9**	38
Constant base flux [t/(km² day)]	0.15	0.12	**0.12**	0.005	0.04	0.03	0.1	0.08	**0.15**	0.08	0.03	**0.35**	0.04
Rating parameter a [t/(km² day)]	1.6	7.7	**12.4**	2.4	6.0	3.5	16.4	3.0	**9.1**	2.1	1.5	**14.2**	1.5
Rating parameter b	1.2	1.2	**1.6**	1.5	1.6	1.3	1.4	1.2	**1.3**	1.1	1.1	**0.9**	1.1
Annual mass flux Q_s 10^6 [t/yr]	0.2	13.7	**137.0**	0.7	22.5	10.2	40.0	3.1	**108.0**	6.9	2.4	**71.0**	2.0
Denudation rate D [mm/yr]	**0.1**	**0.5**	**1.6**	**0.3**	**2.3**	**0.7**	**3.5**	**0.4**	**1.7**	**0.9**	**0.2**	**1.0**	**0.6**
Uncertainties [mm/yr] +σ	0.3	1.0	**5.1**	1.0	8.0	3.0	7.8	1.1	**3.2**	3.7	1.0	**1.6**	2.3
-σ	0.04	0.3	**0.5**	0.1	0.7	0.2	1.5	0.2	**0.9**	0.2	0.06	**0.7**	0.2

4.1 Denudation rate estimation

The well defined relationship between Q_d and Q_{ds} permits us to define for each river a rating curve as defined in equation 4, in order to model basin wide denudation rates from Q_d. We fitted (maximum likelihood method) to all data with Q_d higher than the threshold (0.04 mm/day). For all Q_d inferior than this threshold, we assigned the respective constant flux Q_{ds} of each river, corresponding to the Q_d threshold (Fig. 7). All specific rating parameters and constant flux values are listed in Table 2.

At the annual scale, a part of the total sediment flux might be transported on days with $Q_d = 0$ because of a retardation effect on sediment transport, e.g. Q_s might be temporally offset compared to Q_d. The Q_d events are the results of rainfall events, landsliding and consequently the supply of material to the river might occur after the flood peak has passed the gauging station. This can introduce a bias in our model causing systematic underestimation of annual D. Therefore, in order to evaluate the relative volume of material included in the ΣQ_{ds} calculation, we compared the observed ΣQ_s and the observed ΣQ_{ds} for the whole length of each dataset. We found that ΣQ_{ds} accounts systematically for ~80% of the ΣQ_s, in all rivers. Hence, we added 20% onto modeled ΣQ_s^{mod}. We validated the calculated mass in four basins (stations 286, 360, 447 and 450) for which one year fully continuous data exist (no or nearly no day missing data). For all four basins our modeled Q_s^{mod} (best fit) are within the confidence interval of error (Tab. 3). Discrepancy between the annual reference value and the rating curve modeled is due the fit over the whole available C_s dataset.

Applying the resulting rating parameters, we calculated basin wide suspended sediment denudation rates D (Table 2). For the major drainage basins in Nepal, these are 1 mm/yr in the eastern Koshi Basin (station 695), 1.7 mm/yr in the central Narayani Basin (station 450) and 1.6 mm/yr in the western Karnali Basin (station 280). D in the upper part of the Karnali Basin (station 240) is with 0.5 mm/yr much lower than for the total basin. The largest D, 3.5 mm/yr, can be found in the Kali Gandaki Basin (station 410). The smallest one, 0.1 mm/yr, is calculated for the Bhote Koshi basin (station 0). Overall, D in the small basins at the mountain front are around 1 mm/yr, except for Saradha Basin with only 0.3 mm/yr and upper Rapti with 2.3 mm/yr. Uncertainties of D, calculated from 2σ confidence limits on the Q_d vs. Q_s fit range from 25 to 300% (Table 2).

Basin No.		**450**	**447**	**286**	**360**
Refernce	Q_s 10^6 [t/yr]	169.9	3.4	0.2	8.9
Best fit	Q_s 10^6 [t/yr]	73	1.6	0.1	7.3
	% of references	43	48	59	82
	Q_s incl. 20%	91	2.1	0.2	9.1
	% of references	**53**	**60**	**74**	**102**
Upper limit	Q_s 10^6 [t/yr]	140	4.0	0.3	29
	% of references	82	117	157	324
	Q_s incl. 20%	175	5	0.4	36
	% of references	103	146	197	406
Lower limit	Q_s 10^6 [t/yr]	38	0.7	0.1	1.9
	% of references	22	20	23	21
	Q_s incl. 20%	47	0.9	0.1	2.3
	% of references	28	25	28	26

Table 3: *Validation of suspended sediment denudation rates. The sediment rating model was validated on four stations, one year datasets. Q_s is the annual sediment flux calculated from measurements (reference), the best, lower and upper fit (5 % and 95% quantile respectively). The results are listed with systematic 20% underestimation and corrected (incl. 20%) and is used in this manuscript for further discussion.*

5. Discussion

5.1 Hysteresis effect and storm runoff

We show that C_s varies seasonally and displays an annual hysteresis behavior with respect to Q (Fig. 5a). It could be argued that the sediment supply in the contributing areas is exhausted during the course of monsoon, leading to higher concentrations in pre-ISM in comparison to post-ISM. Actually, Gabet et al. [2008] proposed that the seasonal hysteresis loop in the mainly glaciated hinterland of the Annapurna massif is driven by variations in glacial sediment supply. Similarly, Hasnain and Thayyen [1999] observed increased concentrations during the onset of monsoon in an almost exclusively glaciated catchment of the upper Ganges headwaters in India. The most obvious explanation for this phenomenon is the depletion of a sediment stock within the glacier and at its ablation front. However, we observe the annual hysteresis behavior for both glaciated and unglaciated basins (see Tab. 1 and Fig. 1 for basin wide glacier cover), suggesting that glaciers as sediment source are not solely, or perhaps even not at all, accountable for this observation. A second explanation for the hysteresis behavior is a shift in the relative contribution of Q_b (from groundwater and/or glaciers) to the river discharge. Indeed, a temporally increased contribution of groundwater and melt would cause dilution of suspended concentrations over the annual monsoonal cycle. We have shown [Andermann et al., in press] that ground water contribution to the discharge hydrographs in Nepal is not negligible. As a consequence total river discharge and/or glacial melting are not appropriate proxies to determine suspended sediment fluxes.

Separating the discharge hydrographs in its flow components - Q_d and Q_b - has the advantage of allowing us to consider their respective relation with the transport of erosional products separately. Q_d integrates all precipitation events over the whole basin and is therefore a good indicator of event magnitude. Q_d preserves the precipitation intensity signal, especially if high intensity events are very localized or temporally concentrated, while daily precipitation measurements smooth the information of the rainfall intensity distributions. Plotting the Q_d component against C_s compensates the seasonal hysteresis effect and reveals a direct proportional relationship (Fig. 5b). This observation demonstrates that C_s is not dependent on the amount of water in the river but on the contribution of water draining from the near surface into the river, and characterized by a very short residence time. This illustrates also that C_s is not limited by the sediment stock within the river itself, but is supplied proportionally to

Q_d from the hillslopes. The different apportionment of Q_d and Q_b before and after ISM explains the hysteresis effect and furthermore identifies it as a dilution effect rather than a sediment supply effect. This is the direct consequence of groundwater dominated river discharge during the falling limb of the ISM [Andermann et al., in press]. It implies that Q_d is a better proxy to estimate suspended sediment fluxes in rivers than the commonly used total discharge.

5.2 Comparability of Himalayan rivers

Whatever their size and location, all Himalayan rivers describe a strikingly consistent probability distribution of Q_d in terms of trends and characteristic threshold (Fig. 6). The threshold marks two statistical trends between small and large transport events with exponents ~-1 and ~-2 respectively. Exponents demonstrate that large events do not control the statistical mean. Indeed, most of the mass transport is carried out by events of $1 < Q_{ds}^* < 8$ (Fig. 6). The steep distribution of high magnitude events also means that return intervals of extreme events ($> 10\ Q_{ds}^*$) are too rare to contribute significantly to the bulk sediment transport.

5.3 Load-discharge rating model Nepal

Because Q_d resolves seasonal dilution effects of C_s, it is a good measure to estimate suspended sediment fluxes in the Himalayan rivers of Nepal (Fig. 5). However, because C_s represents the concentration flux of the total daily river discharge Q, it cannot be compared directly to Q_d. Therefore, a rigorous analysis was carried out on the mass flux between Q_s and Q_d (Fig. 7). The comparison of specific Q_d with specific Q_{ds} allows us to develop a rating curve model (Eq. 5) and to calculate annual mean basin erosion rates. This implies that annual sediment fluxes and consequently the mobilization of material is, to first order, controlled by the quantity and intensity of Q_d producing rainfall events.

The rating model proposed here is the very first of its kind. This model is highly reproducible and based solely on empirical data. It is constructed on Q_d, which represents a small fraction of the total river discharge, and on a specific threshold of Q_d. So far, previous studies have mainly concentrated on rating curve models [Ferguson, 1986; Morehead, 2003; Wulf et al., 2010] mostly to fill incomplete C_s datasets with the more complete discharge datasets [Fuller et al., 2003]. Strictly, this rather classical rating model is only valid for transport limited systems [Dadson et al., 2003], where C_s is only dependent on the available transport energy e.g. [Dadson et al., 2003; Fuller et al., 2003; Turowski et

al., 2008]. This implies that sufficient material is always available and that the drainage network is saturated with sediments. This might be true for large braided or alluvial systems but not in the deeply incised bed rock rivers as in the Himalayas. To avoid a bias introduced by seasonal sediment supply to the channel and with it accompanied seasonal changes in C_s, various rating models have been proposed. Dadson et al. [2003] for example propose a time dependent average, Fuller et al. [2003] propose a dual transport and supply limited model on the basis of supply by landslides and Kettner and Syvitski [2008] present a numerical model based on five different river discharge components (from ice/snow melt, ground water, rain and evaporation). Our model integrates supply and transport processes by relating the supply component Q_d, with Q_s (Fig. 7) and the introduction of a specific base flux threshold, which accounts for material which is always available for transport within the river.

The rating model exponent b (Eq. 5), for $Q_d >$ threshold, ranges from 1 to 1.6 (Tab. 2). Uncertainties of b have little impact on the resulting erosion rates. Nevertheless, the level of constant sediment base flux (for $Q_d <$ threshold) differs considerably between the single basins. It sets the intercept a of the rating curve (Eq. 5) and therefore it controls significantly the calculation of suspended sediment erosion rates. This level of constant base flux might result from basin characteristics such as topography, rainfall amount or human activity (Tab. 1). These factors could explain the observed relative shift of Q_b fluxes, although they are difficult to quantify. Processes such as road construction, agriculture or mining can provide considerable volumes of material to the river. For example, road construction is commonly associated with landsliding in Nepal [e.g. Fort et al., 2010]. However, the occurrence of such temporal activity is difficult to constrain at our scales of investigation.

5.4. Denudation fluxes in Nepal

We interpret the denudation rates presented here as modern rates, representative for a relatively stable period of climate vs. erosion interaction. No major earthquake event has destabilized the system during the study period. However, these denudation rates (Tab. 2) represent only the suspended sediment fraction of the total transport rate because bedload and dissolved load are not taken into account. From our own experiences we know that large pebbles (> 10 cm) can be found on the downstream river banks of Narayani station (450). Hence, absolute erosion rates are likely higher than the suspended fraction analyzed here. Due to the lack of quantitative constraints on the bedload and solute

contribution we restrict our analysis to C_s.

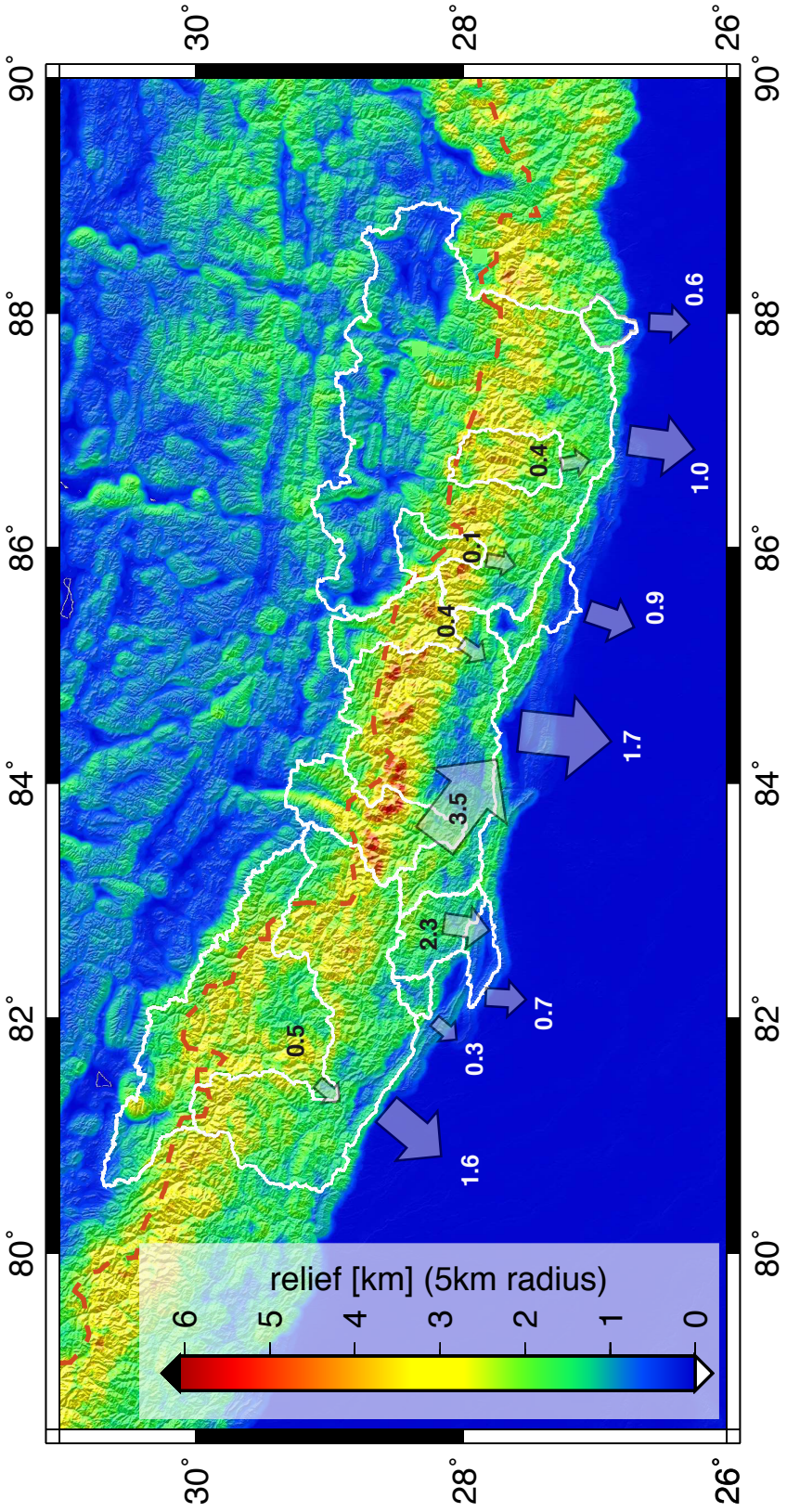

Figure 8: *Map of erosion fluxes in Nepal vs. relief. Denudation rates in mm/yr for all the basins studied here. Arrows are quasi scaled with denudation rates. Denudation rates are calculated from a rating curve modeled based on daily storm runoff Q_d. Uncertainties are listed in Table 2. Relief is calculated from a circular moving window with ~5 km radius. Shaded relief in the background represents the real topography.*

The denudation rates we deduced from C_s and the rates infered from geochronological analysis in the Himalayas agree. Our results (0.1-5.9 mm/yr, Fig. 8 and Tab. 2) fall in the same range of magnitude as the 0.2 - 0.7 mm/yr determined in Bhudi Gandaki, Nepal [Wobus et al., 2005], and the ~2 mm/yr in the upper Ganges, India [Vance et al., 2003], both deduced from cosmogenic nuclide analysis. Our results also agree with the rates of ~ 5 mm/yr determined from apatite fission-track dates in front of the Annapurna massif [Burbank et al., 2003]. Previous published data on C_s denudation rates are consistent with our findings. For example, Gabet et al. [2008] found rates of ~1 – 2 mm/yr in the Marsyandi (Nepal) and Wulf et al. [2010] found rates of ~1 mm/yr in the Indian Sutlej region. Cosmogenic erosion rates from the three major outlet stations (station 280, 450, 695) of Nepal, analyzed by Maarten Lupker (CRPG, Nancy, France, manuscript in preparation) agree within the range of error with our measurements. The agreement between independently determined erosion rates and our findings support the validity of our calculations. Furthermore, it supports the findings of Lupker et al. [2011], Burtin et al. [2009] and Attal and Lavé [2006] that bedload at the outlet stations of of the major Himalayan basins is minimal.

In a spatial context, the denudation rates we determined are heterogeneously distributed (Fig. 8). D are around 1 mm/yr in the catchments at the front of the Himalayan range. The major basins have higher D from 1 to 1.7 mm/yr. Basins draining from the High Himalayan range and the Tibetan Plateau have lower D (0.1-0.5 mm/yr). With a value of ~3.5 mm/yr the very high D in the Kali Gandaki basin (station 410) is noticeable, slightly lower than the ~5 mm/yr reported by Burbank et al. [2003]. This coincides with the strongest relief of the Annapurna range, which is partially drained by basin 410 (Fig. 8). However, we do not observe a clear relationship between all D and mean basin relief as reported for example by Vance et al. [2003] and Finnegan et al. [2008] from cosmogenic nuclide analysis. Intuitively, we would expect D in the High Himalayas to be higher than in the low relief mountain front. We can partly explain the relatively low D in the high relief basins by a locally higher bedload contribution on the total sediment flux in the High Himalayas. Indeed, high frequency seismic noise analyzes in the Trisuhli Basin (here station 447) suggest considerable bedload movements during

monsoon in the High Himalayas, while in the Lesser Himalayas bedload is a minor fraction [Burtin et al., 2009]. Nonetheless, minor bedload contribution in the Lesser Himalayas also means that our estimates from suspended sediments represent close to total *D* for the stations at the front (including the three major basins 280,450 and 695).

Precipitation rates and intensities in the upwind side of the Annapurna range are the highest in Nepal (Fig. 2), with locally > 5000 mm/yr [Putkonen, 2004]. Together with the high relief energy (Fig. 8) and several closely spaced tectonic structures such as the Thakkhola-Mustang graben, make the region tectonically complex and prone to erosional instability [Fort et al., 2010; Fort, 2000; Hodges et al., 1996]. The mean basin slope is at the failure threshold of 30° (Tab. 1), the river are deeply incised into bedrock, creating one of the world deepest gorges [Fort et al., 2010] and uplift rates are around 5 mm/yr [Blythe et al., 2007]. This results into a system which is highly controlled by relief. As the rivers are incised and highly channelized, flood concentration times are very short and therefore, transport capacities are very high. This also implies that transport times of material are prompt, resulting in highly concentrated sediment pulses. These observations support our inference of high values of *D* in the Kali Gandaki basin.

5.7. Annual Himalayan erosion cycle

The strong relation between Q_d and *D* and the highly repetitive ISM leads us to propose a conceptual cyclic surface dynamics model for the Himalayas (Fig. 9 a-d). In this representation, the low-frequency high-magnitude ISM signal of Q_b has minor impact on the annual erosion mass balances. 1) During pre-ISM water availability is at its minimum. Soils are generally dry but a few rainfall events can occur, mobilizing available sediments. Groundwater storage is being purged and starts to refill at the end. 2) During ISM, precipitation intensity and frequency are very high, providing large amounts of hillslope material to the river. This amount is evacuated directly out of the mountain range by the high river transport capacity. High transport capacity is maintained by the high Q_b (groundwater) input into the river. Water storage is replenished and pore pressure in the subsurface is high, inducing landslides. Most of the erosion takes place at that time. 3) During post-ISM, only a few precipitation events are recorded. Erosion fluxes decrease drastically and are diluted by the increase groundwater contribution, depleting the aquifer storage. 4) In winter, a few isolated precipitation events take place, mainly as

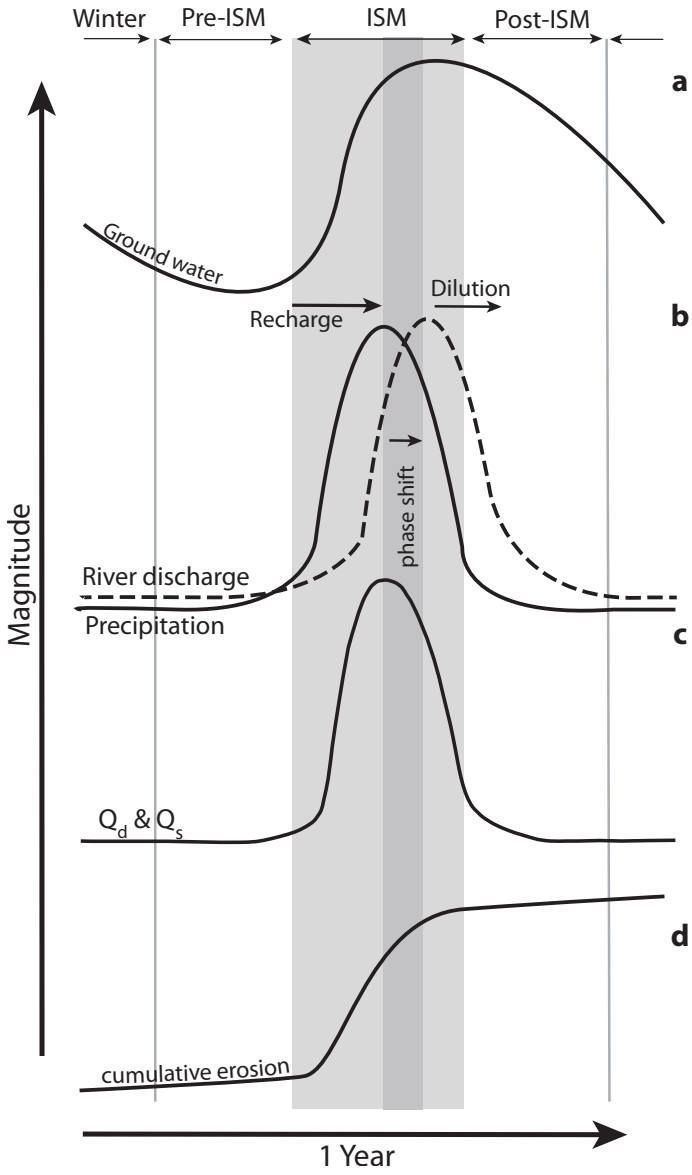

Figure 9: *Schematic model for the cyclic surface dynamics in the Nepal Himalayas. (a) illustrates how the groundwater storage volume is recharged during ISM and depleted in the dry seasons. It causes a phase shift between the peak of R and the peak of Q (b and a) leading to relatively high Q during post-ISM. (c)* Q_s *and* Q_d *are linearly related and consequently follow the same pattern. During the onset of ISM,* Q_s *and* Q_d *are slightly retarded with respect to precipitation, because groundwater has to be refilled before* Q_d *can be produced. However, the falling limb of* Q_s *and* Q_d *during post-ISM follows the rainfall curve. Hence, the relatively high river discharge in post-ISM, is maintained by* Q_b *, generating a dilution effect on* C_s*. The cumulative erosion curve (d) shows that most erosion takes place during ISM,* and strongly increases *with the onset of* Q_d*.*

snow in high elevations. Water availability is close to its minimum. Frost cracking and shattering at the higher elevations weakens material and makes it prone to failure in the subsequent monsoon season.

6 Conclusions

We show that erosion in the Himalayas is strongly coupled with the magnitude-frequency distribution of precipitation expressed in the fast Q_d fraction of river discharge. Total river discharge can not explain temporal variations of C_s. The observed annual hysteresis effect between Q and C_s disappears when comparing C_s only to Q_d, and reveals a reproducible relationship, with a threshold of minimum Q_d. All 13 studied rivers show the same relationship with an universal threshold revealing a homogeneous character of all rivers in Nepal. The high magnitude base frequency of the ISM does not control erosion dynamics, but contributes significantly to the river discharge, which is important to evacuate the erosional material from the mountain range. From these observations we propose a empirical model which relies on the high frequency signal of precipitation events (producing Q_d) to predict erosional mass fluxes. The supply of material from the hillsopes to the river depends on the occurrence of rainfall producing Q_d. This implies that the rivers in the Nepal Himalayas are supply-limited and that the hillsopes as contributing source are transport-limited. We calculate denudation rates for the Himalayan front in Nepal. The calculated erosion rates are consistent with long term erosion rates, derived from geochronological measurements. This is the direct consequence of a system which is not controlled by infrequently occurring extreme events, but rather by moderate ones with a high recurrence interval. To gain more insights on erosion dynamic in Nepal, three points need further investigation: (1) what are the spatial and temporal dynamics of bedload, (2) what controls the baseflow concentration of each basins, and (3) what controls the hillslope production processes e.g. landslide triggering?

Appendix A. Table of notations

A and A_r	*drainage area and drainage area in the Himalayan front*
C_s	*suspended sediment concentrations in river discharge [ppm] or [mg/l]*
D	*Suspended sediment flux denudation rate (employing 2.65 g/cm³ density) [mm/yr]*
ISM	*Indian Summer Monsoon*
Q	*Total river discharge over time*
Q_s	*Suspended sediment flux over time*
Q_d	*Direct river discharge fraction of Q, short response and residence time*
Q_b	*Baseflow river discharge fraction of Q, originates from groundwater*
Q_{ds}	*Suspended sediment flux where $Q_d > 0$*
Q_{ds}*	*Suspended sediment flux where $Q_d > 0$, normalized by the annual mean of Q_{ds}*
ΣQ_s^{mod}	*Suspended sediment flux, modeled from rating model*
$\bar{q_{ds}}$	*Mean annual direct suspended sediment flux*

References:

Ahnert, F. (1970), Functional relationships between denudation, relief, and uplift in large, mid-latitude drainage basins, *Am. J. Sci.*, *268*(3), 243-263, doi:10.2475/ajs.268.3.243.

Andermann, C et al. (in press), Impact of transient groundwater storage on the discharge of Himalayan rivers, *Nat. Geosci.,* advanced online publications, doi:10.1038/NGEO1356.

Andermann, C., S. Bonnet, and R. Gloaguen (2011), Evaluation of precipitation data sets along the Himalayan front, *Geochem. Geophys. Geosyst.*, *12*(7), doi:10.1029/2011GC003513.

Anders, A. M., G. H. Roe, B. Hallet, D. R. Montgomery, N. J. Finnegan, and J. Putkonen (2006), Spatial patterns of precipitation and topography in the Himalaya, *GSA Special Paper*, *398*(03), 39–53, doi:10.1130/2006.2398(03).

Attal, M., and J. Lavé, 2006, Changes of bedload characteristics along the Marsyandi River (central Nepal): Implications for understanding hillslope sediment supply, sediment load evolution along fluvial networks, and denudation in active orogenic belts, GSA *Special Paper*, *398*(03), 143–171, doi: 10.1130/2006.2398(09).

Beaumont, C., R. Jamieson, M. Nguyen, and B. Lee (2001), Himalayan tectonics explained by extrusion of a low-viscosity crustal channel coupled to focused surface denudation, *Nature*, *414* (6865), 738–742.

Benda, L., and T. Dunne (1997), Stochastic forcing of sediment routing and storage in channel networks, *Water Resour. Res.*, *33*(12), 2865, doi:10.1029/97WR02387.

Blythe, A. E., D. W. Burbank, A. Carter, K. Schmidt, and J. Putkonen (2007), Plio-Quaternary exhumation history of the central Nepalese Himalaya: 1. Apatite and zircon fission track and apatite [U-Th]/He analyses, *Tectonics*, *26*(3), 1-16, doi:10.1029/2006TC001990.

Bollinger, L., F. Perrier, J.-P. Avouac, S. Sapkota, U. Gautam, and D. R. Tiwari (2007), Seasonal modulation of seismicity in the Himalaya of Nepal, *Geophys Res. Lett.*, *34*(8), 1-5, doi: 10.1029/2006GL029192.

Bookhagen, B., R. C. Thiede, and M. R. Strecker (2005a), Late Quaternary intensified monsoon phases control landscape evolution in the northwest Himalaya, *Geology*, *33*(2), 149, doi:10.1130/ G20982.1.

Bookhagen, B., R. Thiede, and M. Strecker (2005b), Abnormal monsoon years and their control on erosion and sediment flux in the high, arid northwest Himalaya, *Earth and Planet. Sci. Lett.*, *231* (1-2), 131-146, doi:10.1016/j.epsl.2004.11.014.

Bookhagen, B., and D. W. Burbank (2006), Topography, relief, and TRMM-derived rainfall variations along the Himalaya, *Geophys Res. Lett.*, *33*(8), 1-5, doi:10.1029/2006GL026037.

Bookhagen, B., and D. W. Burbank (2010), Toward a complete Himalayan hydrological budget: Spatiotemporal distribution of snowmelt and rainfall and their impact on river discharge, *J. Geophy. Res.*, *115*(F3), 1-25, doi:10.1029/2009JF001426.

Burbank, D. W., a E. Blythe, J. Putkonen, B. Pratt-Sitaula, E. Gabet, M. Oskin, A. Barros, and T. P. Ojha (2003), Decoupling of erosion and precipitation in the Himalayas., *Nature*, *426*(6967), 652-5, doi:10.1038/nature02187.

Burtin, A., L. Bollinger, R. Cattin, J. Vergne, and J. L. Nábělek (2009), Spatiotemporal sequence of Himalayan debris flow from analysis of high-frequency seismic noise, *J. Geophy. Res.*, *114*(F4), 1-15, doi:10.1029/2008JF001198.

Clift, P. D. et al. (2008), Holocene erosion of the Lesser Himalaya triggered by intensified summer monsoon, *Geology*, *36*(1), 79, doi:10.1130/G24315A.1.

Craddock, W. H., D. W. Burbank, B. Bookhagen, and E. J. Gabet (2007), Bedrock channel geometry along an orographic rainfall gradient in the upper Marsyandi River valley in central Nepal, *J. Geophy. Res.*, *112*(F3), 1-17, doi:10.1029/2006JF000589.

DHM, and His Majesty's Government (2003), *Suspended Sediment Concentration Records*, Department of Hydrology and Meteorology, Kathmandu, Nepal.

DHM/FFS (2004), *Hydrological Data (2002-2003)*, Department of Hydrology and Meteorology, Flood Forecasting Section, Kathmandu, Nepal.

Dadson, S. J. et al. (2003), Links between erosion, runoff variability and seismicity in the Taiwan orogen., *Nature*, *426*(6967), 648-51, doi:10.1038/nature02150.

Dahal, R., and S. Hasegawa (2008), Representative rainfall thresholds for landslides in the Nepal Himalaya, *Geomorphology*, *100*(3-4), 429-443, doi:10.1016/j.geomorph.2008.01.014.

Davy, P. (1993), On the Frequency-Length Distribution of the San Andreas Fault System, *J. Geophy. Res.*, *98*(B7), 12141-12151, doi:10.1029/93JB00372.

Deeken, A., R. C. Thiede, E. R. Sobel, J. K. Hourigan, and M. R. Strecker (2011), Exhumational variability within the Himalaya of northwest India, *Earth and Planet. Sci. Lett.*, *305*(1-2), 103-114, doi:10.1016/j.epsl.2011.02.045.

Dortch, J. M., L. a Owen, W. C. Haneberg, M. W. Caffee, C. Dietsch, and U. Kamp (2009), Nature and timing of large landslides in the Himalaya and Transhimalaya of northern India, *Quat. Sci. Rev.*, *28*(11-12), 1037-1054, doi:10.1016/j.quascirev.2008.05.002.

Ferguson, R. I. (1986), River Loads Underestimated by Rating Curves, *Water Resour. Res.*, *22*(1), 74, doi:10.1029/WR022i001p00074.

Finnegan, N. J., B. Hallet, D. R. Montgomery, P. K. Zeitler, J. O. Stone, a M. Anders, and L. Yuping (2008), Coupling of rock uplift and river incision in the Namche Barwa-Gyala Peri massif, Tibet, *GSA Bulletin*, *120*(1-2), 142-155, doi:10.1130/B26224.1.

Fort, M. (2000), Glaciers and mass wasting processes: their influence on the shaping of the Kali Gandaki valley (higher Himalaya of Nepal), *Quat. Inter.*, *65-66*(1), 101-119, doi:10.1016/S1040-6182(99)00039-7.

Fort, M., E. Cossart, and G. Arnaud-Fassetta (2010), Hillslope-channel coupling in the Nepal Himalayas and threat to man-made structures: The middle Kali Gandaki valley, *Geomorphology*,

124(3-4), 178-199, doi:10.1016/j.geomorph.2010.09.010.

France-lanord, C., and L. A. L. A. Derry (1997), Organic carbon burial forcing of the carbon cycle from Himalayan erosion, *Nature*, *390*(6655), 65–66, doi:10.1038/36324.

Froehlich, W., E. Gil, I. Kasza, and L. Starkel (1990), Thresholds in the transformation of slopes and river channels in the Darjeeling Himalaya, India, *Mt. Res. and Dev.*, *10*(4), 301–312.

Fuller, C. W., S. D. Willett, N. Hovius, and R. Slingerland (2003), Erosion Rates for Taiwan Mountain Basins: New Determinations from Suspended Sediment Records and a Stochastic Model of Their Temporal Variation, *J. Geol.*, *111*(1), 71-87, doi:10.1086/344665.

Gabet, E., D. W. Burbank, J. K. Putkonen, B. A. Pratt-Sitaula, and T. Ojha (2004), Rainfall thresholds for landsliding in the Himalayas of Nepal, *Geomorphology*, *63*(3-4), 131-143, doi:10.1016/j.geomorph.2004.03.011.

Gabet, E., D. Burbank, B. Prattsitaula, J. Putkonen, and B. Bookhagen (2008), Modern erosion rates in the High Himalayas of Nepal, *Earth and Planet. Sci. Lett.*, *267*(3-4), 482-494, doi:10.1016/j.epsl.2007.11.059.

Galy, A., and C. France-Lanord (2001), Higher erosion rates in the Himalaya: Geochemical constraints on riverine fluxes, *Geology*, *29*(1), 23, doi:10.1130/0091-7613(2001)029<0023:HERITH>2.0.CO;2.

Garzanti, E., G. Vezzoli, S. Ando, J. Lave, M. Attal, C. Francelanord, and P. Decelles (2007), Quantifying sand provenance and erosion (Marsyandi River, Nepal Himalaya), *Earth and Planet. Sci. Lett.*, *258*(3-4), 500-515, doi:10.1016/j.epsl.2007.04.010.

Goldstein, M. L., S. A. Morris, G. G. Yen (2004), Problems with fitting to the power-law distribution, *Eur. Phys. J. B*, 41, 255–258 , doi:10.1140/epjb/e2004-00316-5 .

Goodbred, S. L., and S. a Kuehl (2000), Enormous Ganges-Brahmaputra sediment discharge during strengthened early Holocene monsoon, *Geology*, *28*(12), 1083-1086, doi:10.1130/0091-7613(2000)028<1083:EGBSDD>2.3.CO;2.

Grujic, D., I. Coutand, B. Bookhagen, S. Bonnet, A. Blythe, and C. Duncan (2006), Climatic forcing of erosion, landscape, and tectonics in the Bhutan Himalayas, *Geology*, *34*(10), 801, doi:10.1130/G22648.1.

Hannah, D., S. Kansakar, A. Gerrard, and G. Rees (2005), Flow regimes of Himalayan rivers of Nepal: nature and spatial patterns, *J. Hydrol.*, *308*(1-4), 18-32, doi:10.1016/j.jhydrol.2004.10.018.

Haritashya, U. K., A. Kumar, and P. Singh (2010), Particle size characteristics of suspended sediment transported in meltwater from the Gangotri Glacier, central Himalaya — An indicator of subglacial sediment evacuation, *Geomorphology*, *122*(1-2), 140-152, doi:10.1016/j.geomorph.2010.06.006.

Hasnain, S., and R. Thayyen (1999), Discharge and suspended-sediment concentration of meltwaters, draining from the Dokriani glacier, Garhwal Himalaya, India, *J Hydrol.*, *218*(3-4), 191-198, doi:10.1016/S0022-1694(99)00033-5.

Hodges, K. V., R. R. Parrish, and M. P. Searle (1996), Tectonic evolution of the central Annapurna Range, Nepalese Himalayas, *Tectonics*, *15*(6), 1264, doi:10.1029/96TC01791.

Hovius, N., P. Meunier, C.-W. Lin, H. Chen, Y.-G. Chen, S. Dadson, M.-J. Horng, and M. Lines (2011), Prolonged seismically induced erosion and the mass balance of a large earthquake, *Earth and Planet. Sci. Lett.*, *304*(3-4), 347-355, doi:10.1016/j.epsl.2011.02.005.

Hovius, N., C. Stark, C. Hao-Tsu, and L. Jiun-Chuan (2000), Supply and Removal of Sediment in a Landslide-Dominated Mountain Belt: Central Range, Taiwan., *J. Geol.*, *108*(1), 73-89.

Huntington, K. W., A. E. Blythe, and K. V. Hodges (2006), Climate change and Late Pliocene acceleration of erosion in the Himalaya, *Earth and Planet. Sci. Lett.*, *252*(1-2), 107-118, doi: 10.1016/j.epsl.2006.09.031.

Iverson, R. M. (2000), Landslide triggering by rain infiltration, *Water Resour. Res.*, *36*(7), 1897–1910.

Javis, A. et al., Hole filled seamless SRTM data V4, International Centre for Tropical Agriculture (CIAT), 2008, available from http://srtm.csi.cgiar.org

Kettner, A. J., and J. P. M. Syvitski (2008), HydroTrend v.3.0: A climate-driven hydrological transport model that simulates discharge and sediment load leaving a river system, *Comput. & Geosci.*, *34* (10), 1170-1183, doi:10.1016/j.cageo.2008.02.008.

Kirchner, J. W., R. C. Finkel, C. S. Riebe, D. E. Granger, J. L. Clayton, J. G. King, and W. F. Megahan (2001), Mountain erosion over 10 yr, 10 k.y., and 10 m.y. time scales, *Geology*, *29*(7), 591, doi: 10.1130/0091-7613(2001)029<0591:MEOYKY>2.0.CO;2.

Korup, O. (2009), Linking landslides, hillslope erosion, and landscape evolution, *Earth Surf. Process. Land.*, *34*(9), 1315-1317, doi:10.1002/esp.1830.

Korup, O., and J. J. Clague (2009), Natural hazards, extreme events, and mountain topography, *Quat. Sci. Rev.*, *28*(11-12), 977-990, doi:10.1016/j.quascirev.2009.02.021.

Lim, K. J., Y. S. Park, J. Kim, Y.-C. Shin, N. W. Kim, S. J. Kim, J.-H. Jeon, and B. A. Engel (2010), Development of genetic algorithm-based optimization module in WHAT system for hydrograph analysis and model application, *Comput. & Geosci., 36*(7), 936-944, doi:10.1016/j.cageo. 2010.01.004.

Lin, G.-W., H. Chen, N. Hovius, M.-J. Horng, S. Dadson, P. Meunier, and M. Lines (2008), Effects of earthquake and cyclone sequencing on landsliding and fluvial sediment transfer in a mountain catchment, *Earth Surf. Process. Land.*, *33*(9), 1354-1373, doi:10.1002/esp.1716.

Lupker, M., C. France-Lanord, J. Lavé, J. Bouchez, V. Galy, F. Métivier, J. Gaillardet, B. Lartiges, and J.-L. Mugnier (2011), A Rouse-based method to integrate the chemical composition of river sediments: application to the Ganga basin, *J. Geophy. Res.*, in press, doi:10.1029/2010JF001947.

Malamud, B. D., D. L. Turcotte, F. Guzzetti, and P. Reichenbach (2004), Landslides, earthquakes, and erosion, *Earth and Planet. Sci. Lett.*, *229*(1-2), 45-59, doi:10.1016/j.epsl.2004.10.018.

Malamud, B. D., and D. L. Turcotte (2006), The applicability of power-law frequency statistics to floods, *J. Hydrol.*, *322*(1-4), 168-180, doi:10.1016/j.jhydrol.2005.02.032.

Meunier, P., N. Hovius, and J. Haines (2008), Topographic site effects and the location of earthquake induced landslides, *Earth and Planet. Sci. Lett.*, *275*(3-4), 221-232, doi:10.1016/j.epsl. 2008.07.020.

Meyer, H., R. Hetzel, and H. Strauss (2010), Erosion rates on different timescales derived from cosmogenic 10Be and river loads: implications for landscape evolution in the Rhenish Massif, Germany, *Int. J. Earth Sci.*, *99*(2), 395-412, doi:10.1007/s00531-008-0388-y.

Milliman, J. D., and J. P. M. Syvitski (1992), Geomorphic/Tectonic Control of Sediment Discharge to the Ocean: The Importance of Small Mountainous Rivers, *J. Geol.*, *100*(5), 525-544, doi: 10.1086/629606.

Morehead, M. (2003), Modeling the temporal variability in the flux of sediment from ungauged river basins, *Glob. Planet. Change*, *39*(1-2), 95-110, doi:10.1016/S0921-8181(03)00019-5.

NEP (1998), *Dudh Koshi Hydroelectric Project, Feasibility Study, Volume 4 of 8*, Nepal Electricity Authority NEA, conducted by Canadian International water and Energy Consultants CIWEC, Kathmandu, Nepal.

Ouimet, W. B., K. X. Whipple, and D. E. Granger (2009), Beyond threshold hillslopes: Channel adjustment to base-level fall in tectonically active mountain ranges, *Geology*, *37*(7), 579-582, doi: 10.1130/G30013A.1.

Palumbo, L., R. Hetzel, M. Tao, and X. Li (2011), Catchment-wide denudation rates at the margin of NE Tibet from in situ-produced cosmogenic 10Be, *Terra Nova*, *23*(1), 42-48, doi:10.1111/j. 1365-3121.2010.00982.x.

Pinet, P., and M. Souriau (1988), Continental erosion and large-scale relief, *Tectonics*, *7*(3), 563, doi: 10.1029/TC007i003p00563.

Pratt-Sitaula, B., M. Garde, D. W. Burbank, M. Oskin, A. Heimsath, and E. Gabet (2007), Bedload-to-suspended load ratio and rapid bedrock incision from Himalayan landslide-dam lake record, *Quat. Res.*, *68*(1), 111-120, doi:10.1016/j.yqres.2007.03.005.

Putkonen, J. K. (2004), Continuous Snow and Rain Data at 500 to 4400 m Altitude near Annapurna, Nepal, 1999 - 2001, *Arct. Antarct. Alp. Res.*, *36*(2), 244-248, doi:10.1657/1523-0430(2004)036 [0244:CSARDA]2.0.CO;2.

Raymo, M. E., and W. F. Ruddiman (1992), Tectonic forcing of late Cenozoic climate, *Nature*, *359* (6391), 117-122, doi:10.1038/359117a0.

Schaller, M., F. von Blanckenburg, N. Hovius, and P. W. Kubik (2001), Large-scale erosion rates from in situ-produced cosmogenic nuclides in European river sediments, *Earth and Planet. Sci. Lett.*, *188*(3-4), 441-458, doi:10.1016/S0012-821X(01)00320-X.

Shrestha, M. L. (2000), Interannual variation of summer monsoon rainfall over Nepal and its relation to Southern Oscillation Index, *Meteorol. Atmo. Phy.*, *75*(1-2), 21-28, doi:10.1007/s007030070012.

Singh, P., U. K. Haritashya, K. S. Ramasastri, and N. Kumar (2005), Diurnal variations in discharge and suspended sediment concentration, including runoff-delaying characteristics, of the Gangotri Glacier in the Garhwal Himalayas, *Hydrol. Process.*, *19*(7), 1445-1457, doi:10.1002/hyp.5583.

Summerfield, M. a, and N. J. Hulton (1994), Natural controls of fluvial denudation rates in major world drainage basins, *J. Geophy. Res.*, *99*(B7), 13871-13883, doi:10.1029/94JB00715.

Thiede, R. C., B. Bookhagen, J. R. Arrowsmith, E. R. Sobel, and M. R. Strecker (2004), Climatic control on rapid exhumation along the Southern Himalayan Front, *Earth and Planet. Sci. Lett.*, *222*(3-4), 791-806, doi:10.1016/j.epsl.2004.03.015.

Thiede, R. C., T. a Ehlers, B. Bookhagen, and M. R. Strecker (2009), Erosional variability along the northwest Himalaya, *J. Geophy. Res.*, *114*(F1), doi:10.1029/2008JF001010.

Tucker, G. E., and R. Slingerland (1997), Drainage basin responses to climate change, *Water Resour. Res.*, *33*(8), 2031, doi:10.1029/97WR00409.

Turowski, J. M., N. Hovius, A. Wilson, and M.-J. Horng (2008), Hydraulic geometry, river sediment and the definition of bedrock channels, *Geomorphology*, *99*(1-4), 26-38, doi:10.1016/j.geomorph.2007.10.001.

Turowski, J. M., D. Rickenmann, and S. J. Dadson (2010), The partitioning of the total sediment load of a river into suspended load and bedload: a review of empirical data, *Sedimentology*, *57*(4), 1126-1146, doi:10.1111/j.1365-3091.2009.01140.x.

Vance, D., M. Bickle, S. Ivy-Ochs, and P. W. Kubik (2003), Erosion and exhumation in the Himalaya from cosmogenic isotope inventories of river sediments, *Earth and Planet. Sci. Lett.*, *206*(3-4), 273-288, doi:10.1016/S0012-821X(02)01102-0.

WHAT (2011), Web-based Hydrograph Analysis Tool, [online] Available from: http://cobweb.ecn.purdue.edu/~what/

Wobus, C., A. Heimsath, K. Whipple, and K. Hodges (2005), Active out-of-sequence thrust faulting in the central Nepalese Himalaya., *Nature*, *434*(7036), 1008-11, doi:10.1038/nature03499.

Wulf, H., B. Bookhagen, and D. Scherler (2010), Seasonal precipitation gradients and their impact on fluvial sediment flux in the Northwest Himalaya, *Geomorphology*, *118*(1-2), 13-21, doi:10.1016/j.geomorph.2009.12.003.

Yatagai, A., O. Arakawa, K. Kamiguchi, H. Kawamoto, M. I. Nodzu, and A. Hamada (2009), A 44-year daily gridded precipitation dataset for Asia based on a dense network of rain gauges, *Sola*, *5*, 137–140, doi:10.2151/sola.2009–035.

Zeitler, P. K. et al. (2001), Crustal reworking at Nanga Parbat, Pakistan: Metamorphic consequences of thermal-mechanical coupling facilitated by erosion, *Tectonics*, *20*(5), 712, doi:10.1029/2000TC001243.

5.2 General discussion

From the multi-data analysis of precipitation, river discharge and suspended sediment analysis, I presented some new results and proposed a conceptual image of the seasonal erosion cycle. Erosion in the Nepal Himalayas is clearly controlled by hillslope processes limiting the transport of material in the rivers. In return, hillslope processes are closely connected with the occurrence and intensity of precipitation.

With respect to erosion analysis using different methods (suspended sediments or cosmogenic nuclides) I like to underline again that the occurrence of large erosion events follows a different probability distribution than moderate and small events and the large events do not control the volume of the total erosion flux. This has important implications concerning the inter-comparability of modern erosion fluxes with for example, catchment wide erosion rates from cosmogenic nuclide analysis. Although I studied data chronicles of only few years, the data shows a robust distribution which is identical for all rivers. However, these results are representative for a relatively stable period of roughly constant monsoon intensity [e.g. *Clift et al.*, 2008b] and the absence of any major seismic events. One large earthquake might offset the erosion model [e.g. *Hovius et al.*, 2011], but due to the extremely high transport capacity of the rivers, the excess material of such an event will be most likely fast evacuated. Furthermore, to statistically bias the already very high erosion rates, the mass wasting event would have to be significantly larger than the mean annual erosion rate. An intensification of monsoon [e.g. *Bookhagen et al.*, 2005b] might eventually have the potential to bring the erosion processes to a different state, for example to a temporary transport limited one [*Pratt et al.*, 2002]. Nevertheless, over the last couple of thousand years climate was relatively constant [e.g. *Clift et al.*, 2008b] and therefore, the demonstrated relatively little impact of extreme events onto the total erosion rate persists for this timespan.

I showed that direct discharge is linearly related with the mass fluxes. This suggests that precipitation (direct discharge as a function of precipitation intensity and infiltration capacity) controls the mobilisation of material. However, on an intra basin scale these processes need to be evaluated in more detail. For example, I did not manage to explain the rating threshold differences (and therefore the intercept) amongst the basins. Some suggestions can be made towards landuse, road construction or lithology, but without any further investigations those possibilities are rather hypothetical. A second problematic is the limited number of documented mass-wasting events. Figure 5.1 illustrates a short time series where some documented landslides could be obtained from the two databases of *Dahal and Hasegawa* [2008] and *Kirschbaum et al.* [2009b]. However, the landslide occurrence does not necessarily fall together with the peak of direct discharge. At the same time sediment fluxes do not increase automatically when landslide occur. For example, before the 28^{th} of August, landsliding coincides with high precipitation and direct discharge and consequently increased sediment fluxes. In contrast, after the 29^{th} of August precipitation rates and direct discharge are relatively low, along with decreasing sediment fluxes, but several consecutive landslides happened. Note, sediment fluxes in this time series are very high, in the range of $\sim 10^5 - 10^6\ t/day$. The second series of landslides is possibly triggered by

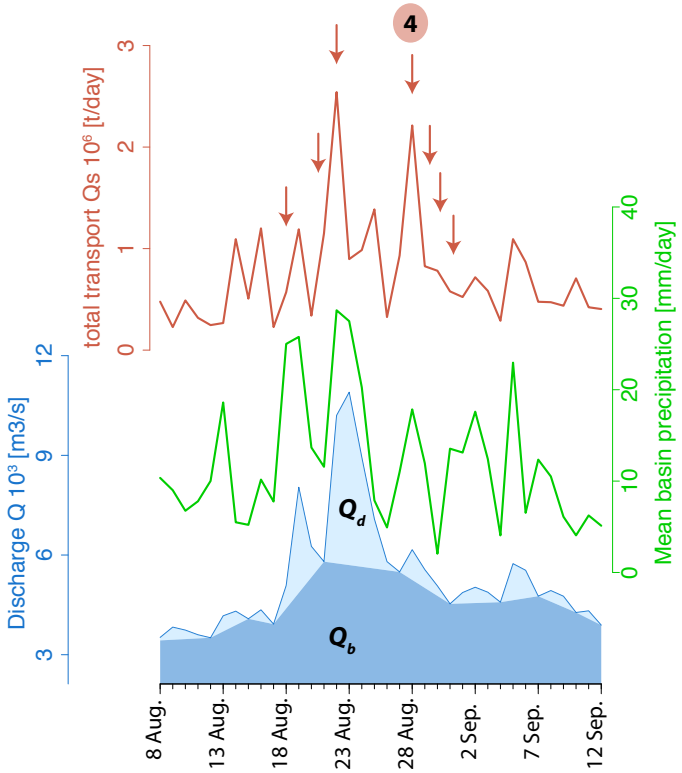

Figure 5.1: *Example time series of 36 days during the 2001 monsoon. Discharge is separated in direct Q_d (light blue) and baseflow Q_b (dark blue). The sum of Q_d and Q_b represents the total measured river discharge at the Narayani outlet station (450). Mean catchment precipitation (APHRODITE) is plotted in green. The total sediment discharge Q_s is plotted in brown. For comparison landslides are indicated with brown arrows. The landslide information was derived from the landslide catalogues of Dahal and Hasegawa [2008] and Kirschbaum et al. [2009b]. On the 29^{th} of August 2001, four landslides have been documented within the drainage Narayani drainage basin.*

elevated pore pressure saturation processes [*Iverson*, 2000], while the early series of landslides is triggered by intense rainfall rates, exceeding the infiltration capacities of surface material. This example demonstrates the huge need to document landslides and quantify their volumes in order to evaluate the involved erosion processes in the Nepal Himalayas.

Another remarkable result is the similarity of the sediment flux probability distribution between the basins with respect to its mean flux. The same observation can be also made for river discharge and precipitation, as illustrated in Figure 5.2. The data (sediment flux, river discharge and precipitation) shows a well defined threshold, with a steeper relation for high magnitude events. Some further research has to be done to evaluate these distributions and to interpret the graphs in terms of return intervals. A second highly reproducible threshold was observed in the sediment rating model, when normalized by the drainage area. The existence of these very reproducible thresholds illustrates the

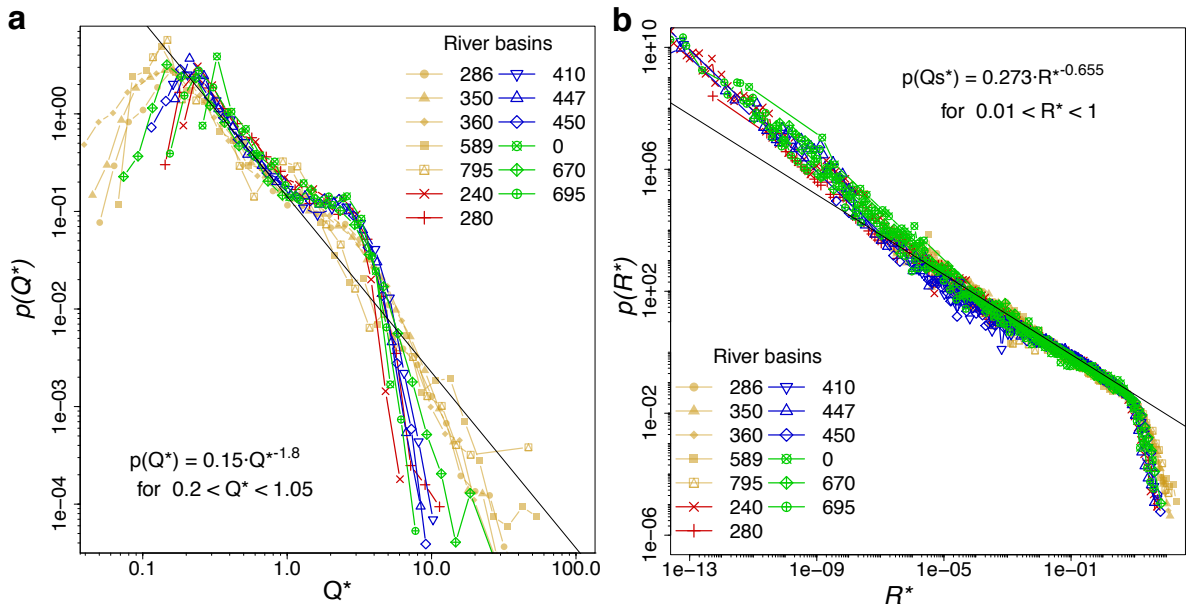

Figure 5.2: *Normalized probability density distribution plots of a) river discharge Q [m^2/s] and b) precipitation R [mm/yr]. The data of each basins is normalized by the mean, river discharge and precipitation respectively.*

similarity of different regions in the Nepal Himalayas in terms of erosion, discharge and precipitation, and highlights the predominant control of precipitation and river discharge onto the system, rather than local catchment characteristics, such as landuse and lithology. Furthermore, the results highlight the often-over-looked importance of geomorphic thresholds in landscape analysis as for example discussed by [*Lague and Davy*, 2003], which seems to be important in the study of surface processes in the Himalayas.

The results confirm that in the Himalayas sediment fluxes are mainly controlled by supply from the hillslopes, while the rivers are supply limited [e.g. *Gabet et al.*, 2008]. The transported sediment volumes in the rivers of the three watersheds in Nepal are hardly ever close to their transport capacity, which I interpret as the consequence of the large groundwater contribution to the river discharge. Depending on the season the relative contribution of surface runoff and groundwater discharge shifts. This relative shift of surface verses groundwater contribution generates an annual clockwise hysteresis effect between suspended sediment concentrations and river discharge. I showed in the manuscript that this effect is not, as usually interpreted, a supply effect, but rather the dilution effect of the retarded groundwater contribution to the river discharge.

Chapter 6

Millennial scale erosion rates

^{10}Be erosion rates, precipitation and topography in the Nepal Himalayas

6.1 Introduction

Spatial erosion distribution patterns are first-order controlled by driving boundary conditions of precipitation and tectonic uplift rate [*Molnar and England*, 1990; *Willett*, 1999; *Beaumont et al.*, 2001; *Whipple*, 2009], yet the role of climate is controversially debated [e.g. *Molnar*, 2003]. Short-time scale erosion depends clearly on the transport capacity, hence on mobilisation and availability of water [*Bookhagen et al.*, 2005a; *Gabet et al.*, 2008; *Wulf et al.*, 2010]. *Burbank et al.* [2003]; *Dadson et al.* [2003]; *von Blanckenburg* [2005]; *Thiede et al.* [2009] argue that on a millennial time scale, tectonic forcing sets the pace of erosion, while *Reiners et al.* [2003]; *Thiede et al.* [2004]; *Deeken et al.* [2011] report a spatial coherence of modern rainfall distribution and long-time exhumation rates. The latter studies suggest that climate has a profound impact on exhumation over a long time span. However, it is tricky to compare modern climate with dynamical processes integrating over several thousands to millions of years and the observed coherence might be only coincidence.

Numerous studies have recently attempted to quantify erosion in the Himalayas, applying a variety of determination techniques. *Gabet et al.* [2008] and *Wulf et al.* [2010] analysed suspended sediment load chronicles to determine modern erosion rates. *Vance et al.* [2003] and *Wobus et al.* [2005] applied cosmogenic nuclide analysis on river sands to determine catchment-wide erosion rates and relay them to tectonic and topographic features. *Thiede et al.* [2004]; *Wobus et al.* [2006]; *Deeken et al.* [2011] applied low-temperature geochronology to quantify long-term erosion rates. All studies report typical erosion rates for the Himalayas in the range of $0.1 - 5\ mm/yr$. However, these studies are difficult to compare since result is representative of different time-scales and contribution by beadload, glaciers, mass wasting, geology, or temporal changes in geothermal gradients. For example, *Binnie et al.* [2006] and

Yanites et al. [2009] documented with numerical models how landsliding and incomplete mixing of the sediments can change the calculated cosmogenic-derived erosion rates. Finally, these studies do not attempt to differentiate between glacial- and hillslope erosion [*Heimsath and McGlynn*, 2008].

In this work I present an integrated comparison of mean catchment erosion rates, calculated from in-situ (not atmospheric) produced ^{10}Be cosmogenic isotope concentration in river sands, and precipitation-landscape features of the Nepal Himalayas. These erosion rates integrate the erosional processes of the whole drainage basin over several thousand years. It can be confidently assumed that the integration time of this approach is sufficiently long to level out short-term variations, such as strong or weak monsoon years [*Bookhagen et al.*, 2005a]. Furthermore it is long enough to represent the impact of relief and long-term precipitation patterns. Emphasis of this study is to document the spatial pattern of erosion rates in the Nepal Himalayas and to constrain its links with rainfall distribution and topography. In particular I compare ^{10}Be erosion rates with: 1) topographic features, such as mean basin relief and slope, 2) precipitation, both volume and frequency-intensity distribution, and 3) possible bias effects by glacial coverage and basement lithology. Finally, cosmogenic derived erosion rates are also compared with rates derived from suspended loads by [Andermann et al. to be submitted].

6.2 Study area

6.2.1 Tectonic and geological settings

The Himalayas are built by the continuous underthrusting of the Indian crust underneath Asia [e.g. *Blythe et al.*, 2007]. The range comprises several east-west running tectonic faults (Fig. 6.1). From the north to the south the main tectonic structures are: 1) the South Tibetan Detachment STD, 2) the Main Central Thrust MCT, 3) the Main Boundary Thrust MBT, 4) and the southernmost Main Frontal Thrust MFT [*Yin*, 2006]. *Wobus et al.* [2003, 2005, 2006] have detected from thermochronological, cosmogenic nuclide and topographic analysis an out-of-sequence thrust, south of the MCT. The authors interpret this formally undetected structure as a consequence of high precipitation rates concentrated along strike of this feature. However, the existence of this structure is still debated [*Bollinger et al.*, 2006].

The major geological units are from north to south: 1) the low-grade Paleozoic-Mesozoic Tethyan Sediment Series of the Tibetan Plateau, 2) the high-grade metamorphic gneisses and migmatites of the High Himalayan Crystalline Series, 3) the low-grade Proterozoic sediments of the Lesser Himalayas, 4) the fine to coarse grained Siwalik Sediment Series, and 5) finally the quaternary deposits of the Indian Foreland [*Yin*, 2006, and references therein] (see Fig. 6.1).

6.2.2 Climate and topography

The climate of the Himalayan front is controlled by the Indian Summer Monsoon ISM, imposing a very well defined wet and dry seasonality [*Hannah et al.*, 2005; *Bookhagen and Burbank*, 2006, , Andermann et

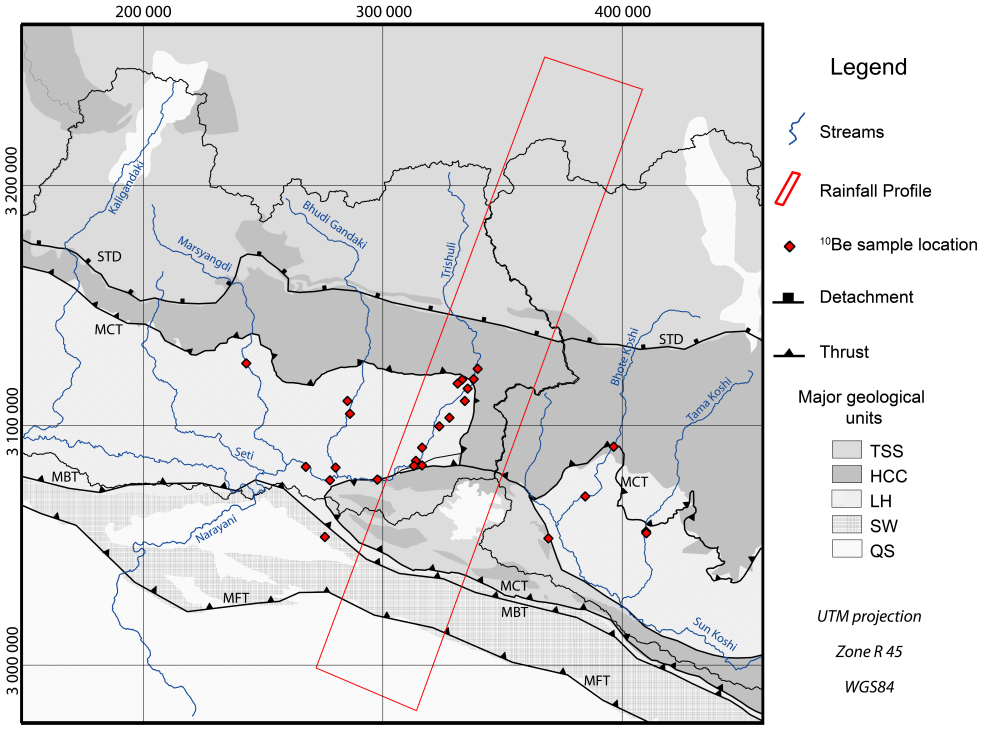

Figure 6.1: *Simplified map of tectonic structures and major geological units of the study area. Major geological units are: TSS: Tethyan Sediment Series, HCC: High Himalayan Cristalline, LH: metasediments of the Lesser Himalayas, SW: Siwaliks formation, QS: Quaternary Sediments.* ^{10}*Be sampling locations are market with diamonds. The red swath profile marks the precipitation and topography swath profile plotted in the inset. Inset: North-south swath profile of mean elevation (grey shading illustrates elevation range along the profile) and precipitation (shading illustrates the precipitation range).*

al. in review, NG and Andermann et al. to be submitted]. The ISM penetrates the Indian sub-continent from the Bay of Bengal and propagates westward along the Himalayan front, generating a east-to-west decreasing rainfall gradient [*Bookhagen and Burbank*, 2006]. In addition, a $\sim$ 10-fold (over $\sim$ 200 *km*) south-to-north increasing rainfall gradient exists due to orographic effects [*Bookhagen and Burbank*, 2006, 2010; *Andermann et al.*, 2011, and inset Fig. 6.1]. On the leeward side of the Himalayan range, on the Tibetean Plateau, annual precipitation rates drop abruptly to $\sim 250 mm/yr$. The intensity and duration of ISM varies from year to year by $25-50\%$ [*Bookhagen et al.*, 2005b] and is thought to be linked to El Nino/Southern Oscillation (ENSO) [*Shrestha*, 2000]. During winter precipitation occurs mainly in form of snowfall under the influence of the westerlies [*Lang and Barros*, 2004]. Considerable long-lasting snow cover is minimal and only significant in elevations $>$ 5000 *m asl.*, where all precipitation comes in form of snow [*Putkonen*, 2004], and on the Tibetan Plateau [*Immerzeel et al.*, 2009]. Glacial coverage for all major basins is around $\sim 10-20\%$ [Andermann et al. in review, NG].

The topography of the Himalayan range in Nepal raises from south to north, from $<$ 200 *m asl.* to

the high summits of > 8000 *m asl*. over a distance of only ~ 200 *km* (inset Fig. 6.1). On a south-north profile the topography describes a two step rise, first to ~ 2000 *m asl*. and secondly up to the mean elevation of the Tibetan Plateau, ~ 6000 *m asl*. (Fig. 6.1). Especially, over the second rise spanning a horizontal distance of only $\sim 20 - 40$ *km*, rivers are very deeply incised and elevation differences between the ridges and the valleys are ~ 3000 *m*. This results in a landscape constantly close to critical slope angle of $\sim 30°$. The rivers are all bedrock rivers and erosional material entering the streams from the adjacent hillslopes usually stays in transport and is not redeposited [Andermann et al. to be submitted].

6.2.3 Sampling locations

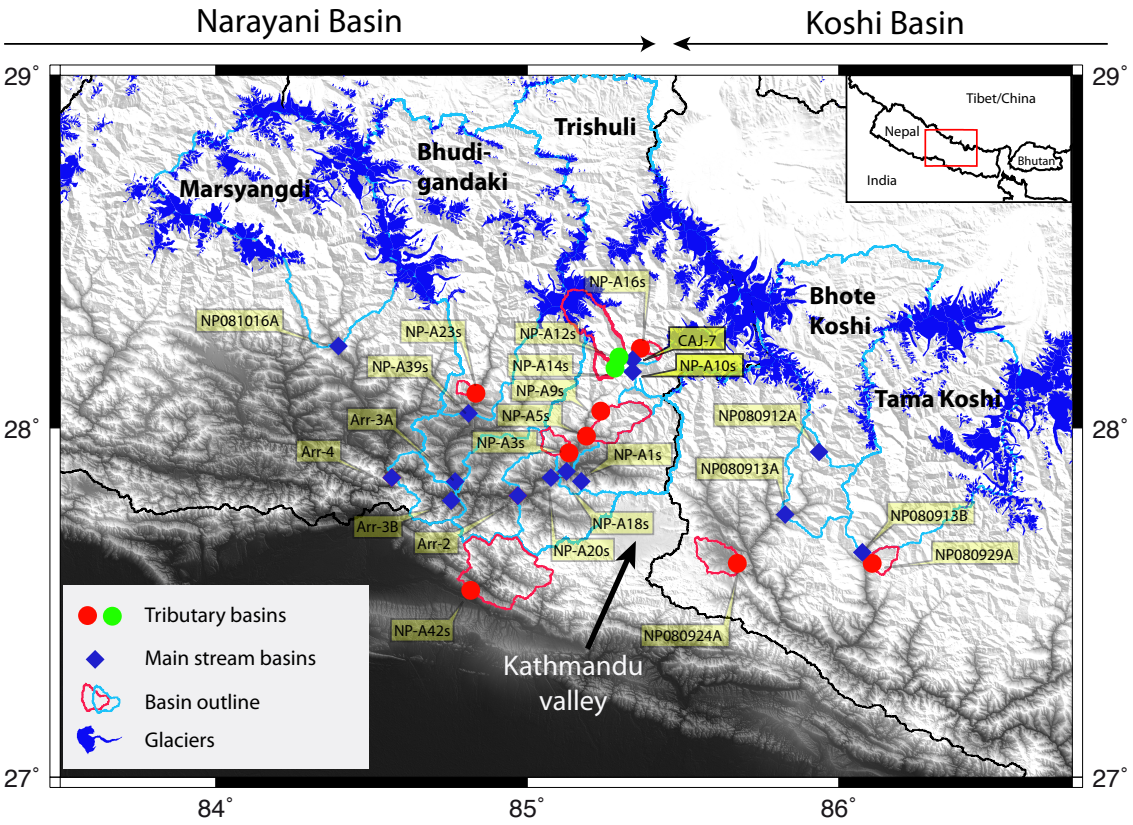

Figure 6.2: *Shaded relief map of the studied drainage basins.* ^{10}*Be sample locations are indicated with diamonds (main streams) and dots (tributary basins). Basin outlines are given in blue for major basins and in red for tributaries. Tributary basins are in general* < 250 km^2*. Glaciers are plotted in dark blue. Inset gives the location of the map subset.*

In this study I present samples from three major watersheds of the Narayani Basin (central Nepal) and from two watersheds of the Koshi Basin (eastern Nepal) and from several of their small tributaries (Fig 6.2). In particular I sampled the following rivers: Tama Koshi and Bhote Koshi (further down-

stream Sunkoshi) in the Koshi Basin, and Trishuli, Bhudigandaki and Marsyangdi in the Narayani Basin. In the Trishuli watershed I have eight samples along the main stream, spanning from the mainly arid Himalayan hinterland close to the border with Tibet, to the very wet mountain front just upstream of the confluence with Marsyangdi and Kali Gandaki river. Most of the tributary basins are within the Trishuli watershed and are in general $< 250\ km^2$. So far no large scale study based on cosmogenic nuclide erosion rates has been published in this area. [*Wobus et al.*, 2003] has analysed eight tributary basins in Bhudigandaki basins, of which I sampled one (01WBS7, in my study: NP-23s, Table 6.1), in order to test the reproducibility of the measurements between the two studies. However, direct comparison is difficult since earlier results are calculated with a different ^{10}Be half-life, analysing techniques and production rates. After personal communication with C. Wobus, it was not possible to obtain these parameters to make direct comparison possible.

These samples cover most of the Himalayan physiographic and geological units. All sample locations are between the MBT and the STD, mainly south of the MCT (Fig. 6.1).

6.3 Methods

6.3.1 Theory of cosmogenic nuclide erosion rates

Cosmogenic nuclide concentration measurements offer the possibility to estimate catchment-wide erosion rates from the isotopic nuclide concentration of river sands [e.g. *Granger et al.*, 1996; *Schaller et al.*, 2001; *Vance et al.*, 2003; *von Blanckenburg*, 2005]. The basic idea of this method is to determine the cosmogenic nuclide concentration in mineral grains (here quartz), in this case of ^{10}Be, inherited over the average exposure time by cosmogenic radiation (neutrons, fast- and slow muons). The ratio between the nuclide concentration $C_{(0)}$ and the catchment-wide production rate $P_{(0)}$ is proportional to the catchment erosion rate ε [e.g. *Granger et al.*, 1996].

$$C_{(0)} = P_{(0)}/(\lambda + \rho\varepsilon/\Lambda) \tag{6.1}$$

Where λ (yr^{-1}) is the decay constant of the nuclide, ρ is the mineral density (g/cm^3) and Λ the attenuation coefficient (g/cm^2) [*Lal*, 1991; *Granger et al.*, 1996; *von Blanckenburg*, 2005; *Dunai*, 2010]. $P_{(0)}$ depends on the amount of cosmic rays reaching the Earth surface, varying with the latitude and elevation [*Stone*, 2000; *Gosse and Phillips*, 2001]. The $P_{(0)}$ increases with altitude as a function of decreasing atmospheric attenuation by $\sim 1\%$ with each 10 m of elevation [*Lal*, 1991; *Stone*, 2000]. Due to the earth magnetic field cosmic rays are deflected towards the poles and consequently $P_{(0)}$ increases with latitude [*Lal*, 1991; *Gosse and Phillips*, 2001]. Last, the heterogeneous irradiation of the catchment surface due to shielding effects has to be corrected [see *Dunne*, 1999]. Two different types of cosmic rays can produce ^{10}Be isotopes in minerals: 1) high energy neutrons produce ^{10}Be by spallation in the top few meters of the Earth surface, 2) a second production path is by capture of slow muons and stopping of

fast muons. Although muon reaction is only minor in terms of production, they are less apt to react with matter and penetrate much deeper into the surface, producing a significant amount of ^{10}Be over long periods. Hence $P_{(0)}$ is the sum off all these productions paths [*Ivy-Ochs and Schaller*, 2009]:

$$P_{tot} = P_{(0)neut.}e^{-(x\rho/\Lambda_{neut.})} + P_{(0)\mu stopped}e^{-(x\rho/\Lambda_{\mu stopped})} + P_{(0)\mu fast}e^{-(x\rho/\Lambda_{\mu fast})} \tag{6.2}$$

where x (cm) is the depth to the surface and $\Lambda_{neut.}$, $\Lambda_{\mu stopped}$ and $\Lambda_{\mu fast}$ are the respective attenuation length of each production path (150, 1300 and 5300 g/cm^2) [*Braucher et al.*, 2003, 2011]. In particular in regions with high erosion rates, muon induced production is important.

The cosmic ray flux, received on a specific surface, also depends on the field of view of each single point within the catchment. Thick topographic features such as mountains and cliffs partially shield the incoming radiation and therefore lower $P_{(0)}$ [*Dunne*, 1999; *Dunai*, 2010]. The fraction of the cosmic ray flux which can reach the surface at one point depends on the inclination θ of the horizon over a certain azimuthal length $\triangle\varphi$ and can be expressed in form of a shielding factor:

$$S_{topo} = 1 - \frac{1}{360^\circ}\sum_{i=1}^{n} \triangle\phi_i \sin^{m+1}\theta_i \tag{6.3}$$

Where $\triangle\phi_i$ is the baseline of the horizon triangulation and θ_i the inclination over the i^{th} azimuthal length fraction. The exponent m (typically 2.3) describes the angular dependency of the cosmic rays [*Dunne*, 1999] and n is the number of azimuthal computing steps ($n = 1 - (360^\circ / \triangle\varphi_i)$). The influence of the topography can be corrected by multiplying the production rate with the shielding factor.

The averaging time-scale T_{eff} (approximately the time to remove one attenuation path length), for which the calculated erosion rates are representative, depends directly on the respective erosion rate: the faster the erosion processes the shorter T_{eff} [*Lal*, 1991; *von Blanckenburg*, 2005]. After *Lal* [1991] T_{eff} can be calculated as follows:

$$T_{eff} = \frac{\Lambda}{\rho\varepsilon} \tag{6.4}$$

The following six hypothesis have to be fulfilled to calculate catchment-wide erosion rates from the in-situ produced ^{10}Be concentration [*Dunai*, 2010, and references therein]:

1. Erosion in the catchment is constant over T_{eff}. This might be biased when landsliding and/or glacial erosion contributes dominantly to the erosion processes. In this case, fresh un-radiated material enters the system.
2. The target material (here quartz) must be homogeneously concentrated in all catchment lithologies and each lithology must contribute equally to the erosion rate.
3. The grainsize of the quartz minerals must be similar over the whole catchment.
4. Erosion must take place by dominantly surface lowering and not by subsurface dissolution processes.

5. The transport of eroded material must be instantaneous or very short with respect to T_{eff}. In other words, the measured sand sample must not be deposited during transport.

6. T_{eff} must be shorter than the half-life $T_{1/2}$ of ^{10}Be isotope (1.36 ± 0.07 *Ma* [*Nishiizumi et al.*, 2007]).

The main limitations for this method in the Himalayas are: 1) In-homogeneous distribution of quartz concentration between the major geological units, 2) undefined glacial erosion contribution, 3) possibility of landslide dominated erosion processes, and 4) partial shielding by temporary snow coverage. The first might bias the calculation of the production rate inducing a relative miss-estimation of the production rate. The second and third can provide partially juvenile (un-radiated) material to the sediment budget, altering the results towards higher erosion rates. The latter one, leads to a lower isotope concentration inducing likewise higher erosion rates.

6.3.2 Sample preparation and analysis

To estimate erosion rates from cosmogenic nuclides elaborated mechanical/chemical cleaning and separation techniques are necessary to segregate the respective isotope [*Brown et al.*, 1991; *Merchel and Herpers*, 1999]. All samples were collected on fresh sandbars within the river channel itself. Sampling locations were chosen according to clearly fresh deposits of the previous monsoon season. The samples were dried and sieved to $250 - 1000$ μm grain size fraction. For each sample, ~ 100 g of quartz were separated by standard magnetics separation techniques. The remaining feldspars and some minor fraction of undefined non-magnetic mineral were chemically dissolved. Because of the possible contamination by atmospheric produced ^{10}Be the remaining pure-quartz sample were etched in three leaching steps with hydrofluoric acid (48%). In each step $\sim 10\%$ of the remaining mass was dissolved. Following the cleaning, the samples were spiked with ^{9}Be carrier (Phenakite DD - MER08, [*Merchel et al.*, 2008]). The total Be inventory (^{10}Be and ^{9}Be) was then extracted by classical exchange column chemistry following the protocol of *Merchel and Herpers* [1999], and prepared for accelerator mass spectrometry AMS. All samples were measured at the AMS facility ASTER (Accelerateur pour les Sciences de la Terre, Environnement, Risques), Aix-en-Provence, France [*Arnold et al.*, 2010], except for two samples which were analysed at the AMS facility in Dresden/Rossendorf DREAMS (DREsden-AMS facility), Germany.

$P_{(0)}$ of each sample are calculated spatially (not only mean catchment values). All calculations are conducted within a GRASS GIS environment [*GRASS Development Team*, 2010]. $P_{(0)}$ and S_{topo} are calculated on the basis of a ~ 90 m SRTM-4 digital elevation model (A. Javis et al., Hole filled seamless SRTM data V4, International Centre for Tropical Agriculture (CIAT), 2008, available from $http://srtm.csi.cgiar.org$). The elevation scaling scheme of $P_{(0)}$ was calculated after *Stone* [2000] for a constant latitude of 30° and a sea-level high-latitude production rate of 4.5 $[at/(g\ yr)]$. $\Lambda_{neut.}$, $\Lambda_{\mu stopped}$ and $\Lambda_{\mu fast}$ parameters are 150, 1500 and 5300 respectively [*Braucher et al.*, 2003, 2011; *Siame*

et al., 2004]. Topographic shielding was corrected on a pixel scale (equation 6.3) using $\triangle\phi_i$ of 30 km, which is sufficiently longer than the average ridge-to-ridge valley width ($\sim 10-20$ km). Glaciated areas are excluded of the $P_{(0)}$ calculation. The resulting production rate map is sub-sampled for each catchment to extract the respective mean $P_{(0)}$ in order to calculate mean catchment erosion rates using equation 6.1. I assumed homogeneous quartz concentration and rock erodibility. I did not correct for juvenile sediment contribution by glacial erosion which might be significant [*Burbank et al.*, 2003; *Heimsath and McGlynn*, 2008]. However, glacial erosion depends on bedrock lithology and intra-glacial dynamics (e.g. temperature, accumulation rate and glacier bed inclination) and can vary significantly from glacier to glacier [*Paterson*, 1994; *Zech et al.*, 2009; *Scherler et al.*, 2011a]. Erosion rates are calculated assuming uniform rock density of 2.65 g/cm^3.

6.3.3 Calculation of catchment characteristics

I extracted the following basin characteristics in order to compare with ^{10}Be erosion rates: 1) slope, 2) relief, 3) mean annual precipitation rate P, 4) mean precipitation intensity P_{Int}, 5) glaciated area, and 6) percent surface are within a major geological unit. All spatial calculations and procedures are conducted in a GRASS GIS environment [*GRASS Development Team*, 2010], using standard implemented routines.

1) Slope is calculated from the SRTM-4 DEM in degree of inclination to the horizontal plain, using a 3 *by* 3 neighbourhood kernel. 2) Relief, or local relief [see *Ahnert*, 1970] is calculated on a ~ 10 km circular kernel, assigning the elevation range (maximum elevation - minimum elevation) to the central pixel. 4) Annual mean basin precipitation is extracted from APHRODITE (Asian Precipitation Highly Resolved Observational Data Integration Towards Evaluation of Water Resources, Monsoon Asia, Version 10, hereafter referred to as APHRODITE [see *Yatagai et al.*, 2009; *Andermann et al.*, 2011]) precipitation dataset, compiled to a mean annual dataset ($\sim$ 50 years). 4) Rainfall intensity is calculated as the pixel based 99% rainfall quantile over the $\sim$ 50 years daily precipitation distribution. It represents a minimum intensity which is exceeded in average on $\sim$ 3.6 days per year. 5) The percent glaciated area of each catchment is extracted from the global glacier database provided online by the *National Snow and Ice Data Center.* [1999]. 6) The major geological units are sub-sampled for each basin from the simplified geological map (see Fig. 6.1) published by *Department of Mines and Geology Nepal* [1994].

6.4 Results

The calculated erosion rates range between 0.2 and 4.4 mm/yr (Table 6.1), typical for cosmogenic erosion rates reported from independent studies in the Himalayan region [*Vance et al.*, 2003; *Wobus et al.*, 2005; *Heimsath and McGlynn*, 2008, and Lupker et al., in preparation]. Sample NP-A42s sticks out from the rest with an erosion rate of 8.7 ± 8.9 mm/yr. This sample gave only one count during the

Table 6.1: *Results for ^{10}Be erosion rates in Nepal. Latitude and longitude of the sampling locations are given in WGS84 reference system. Elevation at sampling location is derived from GPS readings. Bl. corr. stands for blank correction. AMS Accelerator Mass Spectroscopy, ASTER facility at Aix-en-Provence (France), DREAMS facility at Dresden/Rossendorf (Germany). C is the ^{10}Be concentrations with (1σ) measuring uncertainty. ε is the erosion rate and T_{eff} the integration time scale. Standard: NIST-27900, ^{10}Be half live $T_{1/2}$ is 1.36 ± 0.07 Ma [Nishiizumi et al., 2007]. Scaling factors for the production rate are calculated for a constant latitude of 30° after Stone [2000]. Attenuation parameters for neutrons, slow- and fast muons are from Braucher et al. [2003, 2011] and Siame et al. [2004]. Sea-level high-latitude production rate $[at/(g\ yr)]$ is 4.5. Density ρ is assumed to be $2.65\ g/cm^3$.*

			Sampling location			Erosion results						
Sample	**River**	**Location**	**Lat.**	**Long.**	**Elevation**	**Bl. corr.**	**AMS**	**C ^{10}Be**	**uncert.**	ε	**uncert.**	**T_{eff}**
			[°]	[°]	[m asl.]	[%]		$10^3[at/g]$	$10^3[at/g]$	[mm/yr]	[mm/yr]	yr
Main streams												
NP081016A	Marshyangdi	Beshishar	82.42	28.23	698	10.07	ASTER	7.56	1.55	4.42	0.90	136.7
NP080912A	Bhote Koshi	Power plant	85.94	27.93	1404	1.28	ASTER	51.21	2.76	0.89	0.05	674.9
NP080913A	Sunkoshi	Pangretar	85.83	27.75	720	3.79	ASTER	14.12	0.70	2.76	0.14	219.0
NP080913B	Tama Koshi	Nayapul	86.08	27.62	1084	3.89	ASTER	15.47	1.59	2.16	0.22	279.2
NP-A1s	Tati	Tandipul	85.13	27.86	485	4.11	DREAMS	20.00	2.30	0.45	0.05	1331.4
NP-A10s	Trishuli River	Shyaphru	85.34	28.16	1389	5.06	ASTER	16.25	2.30	2.38	0.34	254.0
NP-A18s	Trishuli River	Devighat	85.11	27.86	454	6.33	ASTER	12.13	1.79	2.79	0.41	216.5
NP-A20s	Trishuli River	Downstream Devighat	85.10	27.86	446	5.63	DREAMS	18.11	3.58	1.67	0.33	362.4
NP-A39s	Bhudi Gandaki	Arughat	84.81	28.04	470	71.08	ASTER	15.27	2.54	2.12	0.35	284.2
CAJ-7	Trishuli River /Botekoshi	Upstream Confluence	85.34	28.18	1502	3.40	ASTER	25.98	2.02	1.55	0.12	390.3
Arr-2	Trishuli River	Adamghat	84.97	27.81	414	4.00	ASTER	17.94	1.64	1.52	0.14	396.9
Arr-3B	Trishuli River	downstream Benighat	84.77	27.81	330	8.70	ASTER	8.56	0.81	3.05	0.29	197.9
Arr-3A	Bhudi Gandaki	Benighat	84.78	27.82	336	8.90	ASTER	9.59	1.68	2.86	0.50	211.2
Arr-4	Trishuli River	Mugling	84.56	27.86	256	4.90	ASTER	15	1.15	1.70	0.13	354.4
Tributary catchments												
NP080929A	Yarsha Khola	Gopitar	86.08	27.61	847	2.51	ASTER	38.24	1.99	0.27	0.01	2249.9
NP080924A	Jhikhu Khola	close Lekalibesi	85.67	27.95	780	4.40	ASTER	32.03	1.41	0.18	0.01	3263.5
NP-A3s	Samari Khola	Outlet	85.13	27.93	563	4.06	ASTER	13.15	0.82	0.46	0.03	1306.7
NP-A5s	Phalakhu Khola	Betrawati	85.19	27.98	615	4.01	ASTER	13.71	0.83	0.88	0.05	687.6
NP-A9s	Trishuli Khola	Dhunche	85.31	28.11	1844	0.85	ASTER	82.18	2.58	0.33	0.01	1851.8
NP-A16s-I	Phenglung Khola	Outlet	85.36	28.23	1634	4.28	ASTER	17.96	2.73	1.42	0.22	423.8
NP-A16s-II	Phenglung Khola	Outlet	85.36	28.23	1634	3.91	ASTER	18.81	2.38	1.36	0.17	443.8
NP-A23s	Arkhet Khola	Arkhet	84.83	28.10	563	5.30	ASTER	8.74	0.63	0.73	0.05	831.1
NP-A42s	Lothar Khola	Debichaur	84.73	27.59	258	7.90	ASTER	0.68	0.66	8.74	8.88	69.0
Special case												
NP-A12s	Chilime Khola	Thambuchet	85.30	28.19	1744	6.57	ASTER	10.32	1.39	2.71	0.37	222.7
NP-A14s	Bamdang Khola	Thambuchet	85.30	28.18	1777	8.99	ASTER	8.22	0.72	2.03	0.18	297.5

AMS measurement (usually > 50) and is considered as an outlier and not further considered here. I separated the samples in three different batches: 1) Samples from main streams with drainage areas $> 250\ km^2$, 2) samples from tributaries of small catchments of $< 250\ km^2$ (Table 6.2) and 3) two catchments with some special conditions (explained thereafter). Batch three is considered as tributary catchments. The highest erosion rates are measured in the main streams, all $\geq 1.5\ mm/yr$ (with exception of Bhotekoshi NP080912A and Tati NP-A1s), while the tributary catchments have in general lower erosion rates ($\leq 1.4\ mm/yr$). The highest erosion rate is measured in the Marshyangdi catchment 4.4 mm/yr (NP081016A). The lowest erosion rate is measured in the Jhikhu Khola (NP080924A) catchment, which is located south of the High Himalayan range, characterized by a lower relief ($\sim 1000\ m$). Measuring uncertainties are in the range of $\sim 3-20\%$ of the calculated erosion rate, in general higher for high erosion rates. Depending on the rates, T_{eff} is very short for high erosion rates, 137 years in Marshyangdi, and is in the order of $\sim 1000-3000$ years for catchments with erosion rates $< 1\ mm/yr$. Concerning the two samples measured at the AMS facility in Dresden DREAMS (NP-A20s and NP-A1s), I find good reproducibility between ASTER and DREAMS (identical in construction) in the order of few percent (see also Appendix). Sample NP-A16s was separated in two different batches (NP-A16s-I and NP-A16s-II) in order to test the reproducibility of the separation and AMS measurements. Both samples show the same results with $< 1\%$ difference.

6.4.1 Catchment Characteristics

The catchment characteristics are listed in Table 6.2. All main stream catchments include a glaciers, covering between 11 and 23% of the catchment area. Among the tributaries only one basin (NP-A12s) is glaciated, with an area of 34% covered by glaciers. Mean catchment slope of all three batches ranges between $\sim 20-30^{\circ}$. The mean catchment relief of all three batches ranges from 1000 to 3400 m. Both P and P_{Int} are much smaller for the main stream catchments than for the tributary catchments. Large rivers originate on the arid Tibetan Plateau and drain through the wet Himalayan front. The tributaries are situated in the more or less wet monsoon climate mountain front and have therefore much higher mean P and P_{Int} values. The percental surface area of the major geological units is relatively heterogeneously distributed and non of the batches is exclusively dominated by one geological unit.

The two catchments termed as special case (NP-A12s and NP-A14s) are located at the end of a larger side branch of the Trishuli River (see Fig. 6.2). As mentioned above the Chilime Khola NP-A12s is strongly glaciated which might lead to artificial higher erosion rates, therefore it is graphically set apart. Bamdang Khola NP-A14s is physiographically similar to the other tributary catchments (no glaciers, similar slope). Just before I sampled this basin, a strong flood has lowered the river bed by $\sim 1\ m$. Remains of intense mass transport where found and sediments are eventually not perfectly mixed. The sampling location is upstream of the fresh debris deposits.

Table 6.2: *Catchment characteristics for the respective drainage area of each ^{10}Be sample. Mean basin values (elevation, slope, relief, precipitation P and precipitation intensity P_{int}, glaciers) are calculated spatially in a GIS system. Relief is calculated with circular moving kernel with $\sim$ 11 km radius, as maximum-minimum elevation. Area represents the whole catchment including glaciated area. P is derived from the spatial APHRODITE dataset [Yatagai et al., 2009]. P_{int} is the 99% quantile of the pixelbased rainfall distribution of the $\sim$ 50 yr daily precipitation time series. Glacier cover is the % area of the catchment covered by glaciers [National Snow and Ice Data Center., 1999]. Major geological units in % area contribution of each catchment: TSS: Tethyan Sediment Series, HCC: High Himalayan Cristalline, LH: metasediments of the Lesser Himalayas, SW: Siwaliks formation, QS: Quaternary Sediments.*

		Mean catchment parameters							**Geological units**			
Sample	**River**	**Area**	**Elevation**	**Slope**	**Relief**	**P**	**P_{Int}**	**Glaciers**	**TSS**	**HHC**	**LH**	**SW**
		[km^2]	[m asl.]	[°]	[m]	[mm/yr]	[mm/yr]	*%cover*	*% area*	*% area*	*% area*	*% area*
Main streams												
NP081016A	Marshyangdi	3000	4408	29.3	2925.0	909.3	29.9	21	60.74	34.57	4.7	n.a.
NP080912A	Bhote Koshi	2105	4868	22.5	1925.2	453.5	30.2	13	41.49	58.51	n.a.	n.a.
NP080913A	Sunkoshi	2572	4379	23.5	1998.6	1111.9	38.0	11	33.95	52.55	13.51	n.a.
NP080913B	Tama Koshi	2962	4239	27.8	2456.5	894.9	25.5	18	n.a.	87.11	12.84	n.a.
NP-A1s	Tati	657	1653	24.4	1984.3	2195.6	56.3	no	n.a.	78.08	21.92	n.a.
NP-A10s	Trishuli River	4086	4625	26.4	2339.6	632.2	20.3	23	59.37	38.93	1.69	n.a.
NP-A18s	Trishuli River	4798	4259	26.5	2354.0	813.6	25.0	19	50.57	34.72	14.71	n.a.
NP-A20s	Trishuli River	5469	3939	26.3	2307.9	967.1	28.5	17	44.36	39.98	15.65	n.a.
NP-A39s	Bhudi Gandaki	3981	4215	30.3	2784.2	939.1	31.4	15	41	31.52	16.39	10.74
CAJ-7	Trishuli River /Botekoshi	3207	4675	25.3	2191.3	535.1	19.9	20	74.96	25.04	n.a.	n.a.
Arr-2	Trishuli River	6091	3670	25.8	2219.5	967.1	28.5	15	44.28	39.06	16.67	n.a.
Arr-3B	Trishuli River	11716	3570	27.1	2362.3	1048.2	31.7	13	43.67	34.14	22.2	n.a.
Arr-3A	Bhudi Gandaki	5048	3739	29.3	2652.4	1023.0	31.9	12	44.88	30.53	24.58	n.a.
Arr-4	Trishuli River	11997	3507	27.0	2342.0	1083.0	32.9	13	42.81	33.34	23.85	n.a.
Tributary catchments												
NP080929A	Yarsha Khola	55	1773	18.9	1803.2	1779.2	45.6	n.a.	n.a.	100	n.a.	n.a.
NP080924A	Jhikhu Khola	113	1129	14.9	1009.9	1196.4	41.8	n.a.	78.92	13.47	7.6	n.a.
NP-A3s	Samari Khola	53	1258	24.0	1644.4	2082.7	57.8	n.a.	n.a.	n.a.	100	n.a.
NP-A5s	Phalakhu Khola	148	2145	28.1	2560.4	1543.2	37.6	n.a.	n.a.	17	83	n.a.
NP-A9s	Trishuli Khola	52	3548	27.4	2730.3	1152.7	25.5	n.a.	n.a.	57.4	42.6	n.a.
NP-A16s-I	Phenglung Khola	21	3393	32.2	3676.1	1152.7	25.5	n.a.	n.a.	100	n.a.	n.a.
NP-A16s-II	Phenglung Khola	21	3393	32.2	3676.1	1152.7	25.5	n.a.	n.a.	100	n.a.	n.a.
NP-A23s	Arkhet Khola	18	1427	27.1	2565.5	1973.0	51.1	n.a.	56.92	33.23	9.85	n.a.
NP-A42s	Lothar Khola	433	1156	25.0	1541.3	1637.5	66.0	n.a.	n.a.	n.a.	100	n.a.
Special case												
NP-A12s	Chilime Khola	227	4441	31.4	3070.0	597.3	17.1	34	n.a.	95.39	4.61	n.a.
NP-A14s	Bamdang Khola	42	3003	29.3	2828.4	1526.3	30.3	n.a.	n.a.	2.22	97.78	n.a.

6.4.2 Erosion vs. precipitation

The plot of precipitation (P and P_{Int}) vs. ^{10}Be erosion rates shows overall a negative relation (Fig. 6.3). However, when separating the data in tributary catchments and main stream catchments, the data plots in two different groups and within each group no relation between erosion and precipitation can be observed. The small basins have overall the lowest erosion values and plot over a wide range of mean precipitation rates ($1200 - 2100\ mm/yr$, Fig. 6.3a). In contrast, the main stream basins cluster around mean basin precipitation rates of $500 - 1000\ mm/yr$. The plot of P_{Int} reveals a similar distribution (Fig. 6.3 b). Although, the pattern between Figure 6.3a and Figure 6.3b changes slightly I can not observe any relation between precipitation and ^{10}Be erosion rates. I have to further investigate the role of precipitation by for example only considering the Himalayan front.

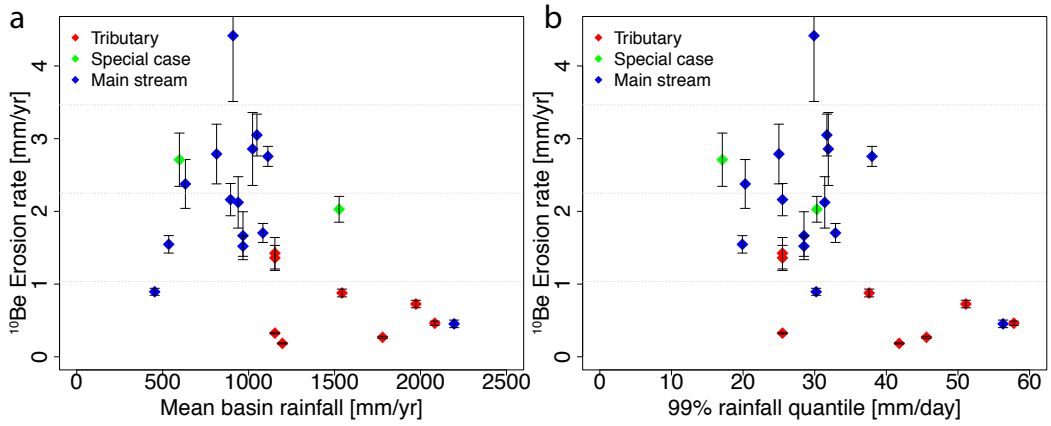

Figure 6.3: *^{10}Be erosion rate plotted against mean catchment precipitation parameters. The three different batches are indicated by color, red: tributaries, green: special case, tributaries, and blue: main streams. a) Mean annual rainfall rate (integrating 50 years) plotted against ^{10}Be erosion rate. b) 99% rainfall quantile, calculated on a pixel base over the whole 50 year time series.*

6.4.3 Erosion vs. topography

^{10}Be erosion rates compared to relief show clear positive trends, different for the main basin samples and tributaries ones. The main stream catchments show a steeper trend than the small tributaries (Fig. 6.4 a), however the two basins termed as special case plot close to the main stream basins. The comparison of my results with literature data from *Finnegan et al.* [2008] *Vance et al.* [2003] and *Schaller et al.* [2001] reveals globally similar trends. A shift between the data of *Vance et al.* [2003] and *Schaller et al.* [2001] along the relief axis is possibly induced by the methodology used to calculate relief. I calculated relief as the difference between the maximum and the minimum elevation (local relief), while *Vance et al.* [2003] and *Schaller et al.* [2001] have calculated relief, using a slightly smaller kernel, as the mean elevation minus the minimum elevation. Consequently, their respective relief values are smaller for a given erosion rate (roughly half). However, the data of *Finnegan et al.* [2008], who

calculated relief in the same way as us, plots well with my dataset. The data of *Finnegan et al.* [2008] and the main streams follow a exponential-law: $E_{St} = 0.07exp(0.0013 * Relief)$ with $r^2 = 0.61$ and the tributaries a different exponential-law: $E_{TR} = 0.1exp(0.00068 * Relief)$ with $r^2 = 0.69$.

The comparison of ^{10}Be erosion rates with mean basin slope (Fig. 6.4 b) shows a clear non-linear relation, confirming the findings of *Ouimet et al.* [2009]; *Norton et al.* [2010] and *Palumbo et al.* [2011] using cosmogenic data, as well as the findings of *Montgomery and Brandon* [2002] using thermochronological data. Erosion tends to increase with slope to a certain slope threshold ($\sim 25 - 30^\circ$) and then independently of slope. Above the threshold, erosion varies over a wide range for the same mean basin slope. However, the slope threshold in the central Himalayas seems to be smaller than the 30° reported by *Ouimet et al.* [2009] and *Norton et al.* [2010] (see Fig. 6.4) and tends to be closer to the 25° reported by *Palumbo et al.* [2011]. This threshold is usually interpreted as a threshold value for landsliding. However, the significance of a lower slope threshold for the Nepal Himalayas would need to be further evaluated.

6.4.4 Erosion vs. geology and glaciers

The majority of all catchments lays within the geological units of the TSS, HCC and LH (Fig. 6.5). No correlation can be observed when comparing the ^{10}Be erosion rates with geological % surface area of the geological units (Fig. 6.5a, b and c). I conclude that ^{10}Be erosion rates are not influenced by the contributing lithology. Or if geology plays a role, the significance of five units is not pertinent enough.

Again the contributing area of glaciers does not show any tendency (Fig. 6.6). However, this might be the result of highly heterogeneous glacier dynamics. Therefore, their surface area and eventual impact on mean catchment erosion rates is not necessarily related.

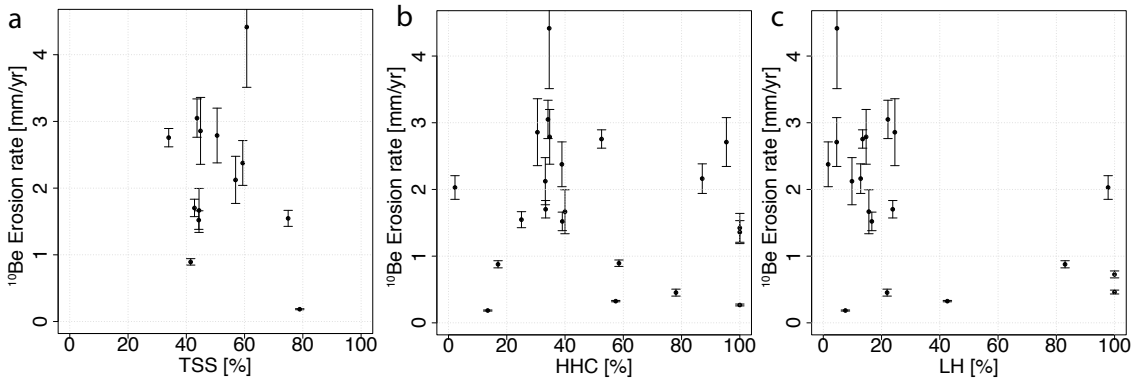

Figure 6.5: *^{10}Be erosion rates plotted against % surface area of the major geological units. a) TSS: Tethyan Sediment Series, b) HCC: High Himalayan Cristalline, c) LH: metasediments of the Lesser Himalayas.*

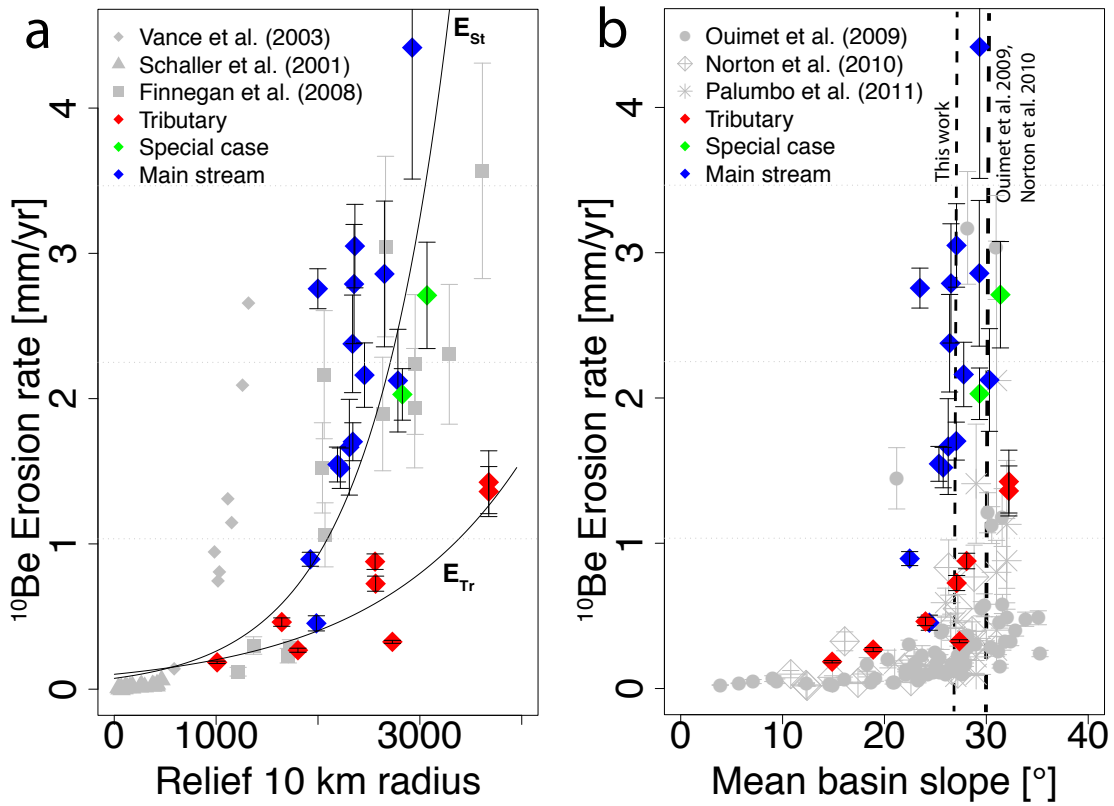

Figure 6.4: *^{10}Be erosion rates plotted against topographic parameters. The three different batches are indicated by color, red: tributaries, green: special case tributaries, and blue: main streams. a) Plot of mean basin relief (calculated over a circular moving kernel with $\sim$ 10 km radius) vs. ^{10}Be erosion rates. The data is compared to literature values from Vance et al. [2003] (Himalayas, upper Ganges catchment) , Schaller et al. [2001] (European catchments), and Finnegan et al. [2008] (eastern Himalayan syntaxis), indicated with grey triangles, diamonds and squares. Note, Vance et al. [2003] and Schaller et al. [2001] did not calculate local relief (see text). The data of the main streams catchments and the data by Finnegan et al. [2008] are fitted by a exponential law ($E_{St} = 0.07\ exp(0.0013 * Relief)$, $r^2 = 0.61$), as well as the data of tributaries catchments ($E_{Tr} = 0.1\ exp(0.00068 * Relief)$, $r^2 = 0.69$). I did not plot the data of Norton et al. [2010] and Palumbo et al. [2011] since their relief was calculated on $<$ 1 km radius. b) Mean basin slope plotted against ^{10}Be erosion rates. Data from Ouimet et al. [2009]; Norton et al. [2010] and Palumbo et al. [2011], from the eastern Himalayan margin, the European Alps and the NE Tibet respectively, are plotted in grey for comparison. The dashed lines indicate the critical slope threshold above which erosion rates are uncorrelated with slope.*

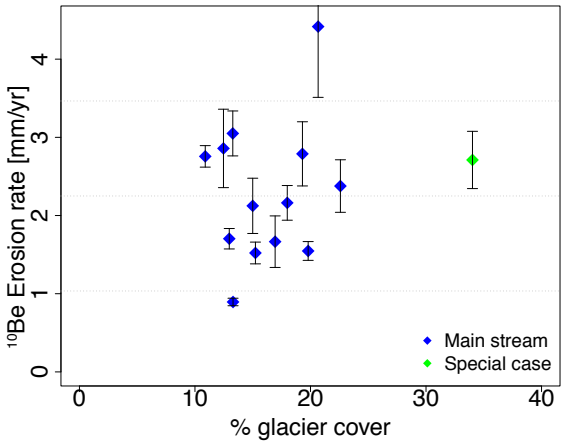

Figure 6.6: *^{10}Be erosion plotted against % glaciated surface area. Only catchments with glaciers are plotted.*

6.4.5 Erosion variations across the Himalayan range

I plotted ^{10}Be erosion rates of the tributary basins against the distance to the southern front of the Himalayan range (see Fig. 6.1), in order to test how erosion rates evolve across the mountain range (Fig. 6.7). Elevation and precipitation is plotted for orientation. As a spatial reference I defined the MFT as the Himalayan front. I did not compare the main stream catchments because the source of erosion is not well represented by the sampling location. The tributary samples show a clear increase with the increasing distance to the Himalayan front. Roughly the erosion rates mimic the relief (grey shading) across the Himalayan range. Unfortunately I miss tributary samples from the arid Tibetan Plateau, in order to see if erosion decreases beyond the Himalayan range.

6.5 Discussion

Erosion rates calculated from ^{10}Be concentration in river sand are all in the typical range $\sim 0.2 - 4.5 mm/yr$ of published erosion rates for Himalayas [e.g. *Vance et al.*, 2003; *Wobus et al.*, 2005; *Finnegan et al.*, 2008; *Gabet et al.*, 2008; *Wulf et al.*, 2010; *Ouimet et al.*, 2009]. One striking result is the general difference between erosion rates from the main rivers and the tributary catchments.

6.5.1 Erosion vs. precipitation

As I showed in a previous manuscript [Andermann et al. to be submitted] from analyses of suspended sediment concentrations, precipitation plays an important role in mobilizing and transporting material. Though, published erosion rates derived from cosmogenic nuclide analysis, integrating over several hundreds to thousands of years do not show any correlation with precipitation [e.g. *von Blanckenburg*, 2005]. My data shows overall a weak negative correlation between erosion and precipitation (Fig. 6.3).

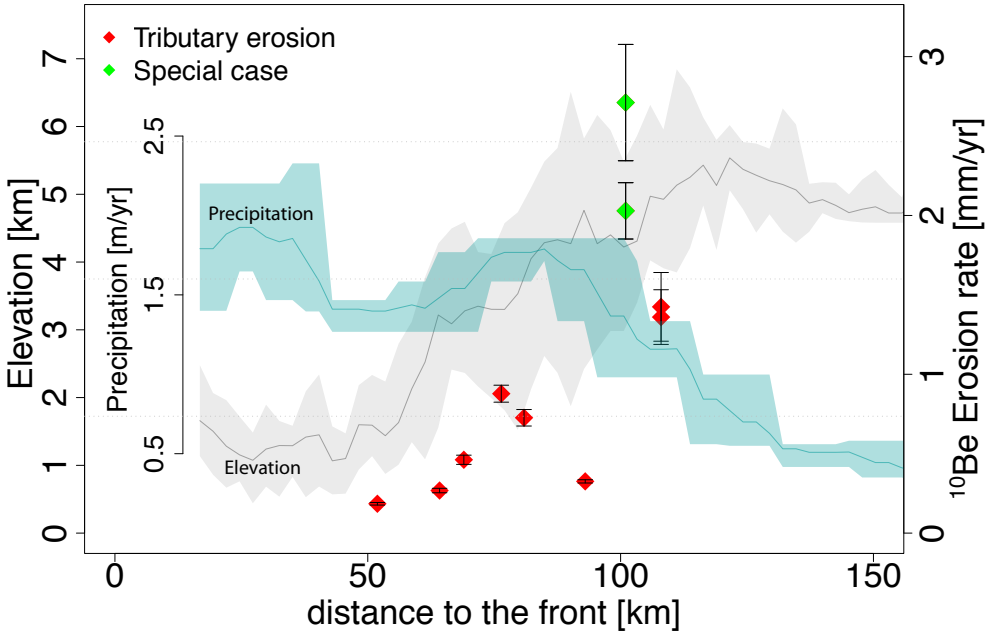

Figure 6.7: *^{10}Be erosion rates of tributary basins plotted against their shortest distance to the Himalayan front (see Fig. 6.1). Zoom of the elevation and precipitation swath profile of the inset of Figure 6.1. Here the Himalayan front is the Main Frontal Thrust MFT (Fig. 6.1).*

However, the negative correlation vanishes when separating between tributary basin and main stream basin samples and no trend can be documented when considering the batches separately. The main stream basins have generally lower mean precipitation rates and higher erosion rates than the tributary ones and it is likely that the overall observed negative relation is only an artifact. Note that, their is no physical meaningful reason why erosion rates should increase with decreasing precipitation rate. In order to explain the artifact two possibilities could be discussed: 1) a general overestimation of erosion rates in the main stream basins, and/or 2) a methodological underestimation of the precipitation rates in the main stream basins.

Overestimation of the catchment wide erosion rates of the main stream catchments can arise from the contribution of glacial erosion to the river sediments. Depending on the erosion efficiency of the glacier, considerable volumes of juvenile material can be brought to the river, which would decrease the ^{10}Be concentration and hence the erosion rate. However, glacial erosion behaviour is very complex, depending on climate variations and topographic conditions [e.g. *Zech et al.*, 2009; *Scherler et al.*, 2011b] and is therefore difficult to quantify. As illustrated in Figure 6.6 I do not observe a relation between the glaciated surface area and erosion rates, suggesting that either glaciers do not bias the calculations or that strong inter-glacier variabilities do not allow to define a trend between the surface area of the glacier and their erosion capacity.

Intuitively I would expect that the bulk of the eroded material comes from the Himalayan range

and only a small fraction from the Tibetean Plateau. Indeed, *Lal et al.* [2004] show that erosion rates across the Tibetan Plateau, determined from comsogenic exposure dating, are in average $\sim 6.3\ mm/kyr$, roughly 2 to 3 magnitudes lower than typical Himalayan ones [e.g. *Vance et al.*, 2003]. Since the large catchments integrate partially the Plateau, the mean catchment erosion rates should be lower then the ones determined from small catchments, draining exclusively the Himalayan range. This rises the question of where does the material comes from? On the other hand the results of *Lal et al.* [2004] represent only the internally drained Tibetan Plateau, north of the Tsangpo Sature and thus the base level of erosion for the analysed rivers is very high. The base level of erosion for the rivers draining south, through the Himalayan range, however is controlled by the Himalayan forland [*Lavé and Avouac*, 2001], $\sim$ 6000 m lower than the Plateau. Hence, the erosive capacity of the south draining Tibetan Plateau is much higher than the one of the interior.

One other possible reason why the erosion rates in the main catchments could be overestimated comes from my sampling strategy. Before the sampling field-campaign I selected catchments from satellite image interpretation, where no massif landsliding could be observed. Hence, the large catchments integrate both, the large landslides and areas with erosion processes by surface lowering. This can explain overall higher erosion rates in the large catchments.

Another reason for a possible overestimation in the main stream basins lays in the heterogeneous quartz concentration of the basement geology. For example *Vance et al.* [2003] report that modal quartz concentrations of the TSS ($\sim$ 38%) are about 15% lower as those from the HHC. As a consequence, the production rate of the Tibetan Plateau, being very high because of the elevation, is leading to an overestimation of the mean catchment production rate and hence, of the erosion rate. The same affect could be caused by a very low erosion contribution from the Tibetan Plateau. Considering for example the very low erosion rates reported by *Lal et al.* [2004], the considered mean production rate would be disproportional high with respect to the actual erosional contribution from the Plateau. Furthermore, large parts of the Tibetan Plateau and the High Himalayas are temporally snow covered, which leads to a partial shielding of the snow covered areas and thus decreases the production rate of ^{10}Be, and thus leads to an overestimation of the erosion rates. However, shielding by snow is very difficult to evaluate, because the shielding efficiency depends on the properties (thickness and density) of the snow cover which is highly variable in time [e.g. *Stewart*, 2009].

The two northernmost samples (CAJ-7 and NP080912A) from the upper Trishuli River and Bhote Koshi River (Arniko Highway), both north of the MCT yield erosion rates of $1.5 \pm 0.12\ mm/yr$ and $0.9 \pm 0.05\ mm/yr$ respectively, approximately three magnitudes higher than those erosion rates reported by *Lal et al.* [2004] for the Plateau. Thoroughly, comparable with those erosion rates reported for the southern edge of the Plateau by *Vance et al.* [2003], $1.2 \pm 0.1\ mm/yr$. Although, *Vance et al.* [2003] corrected their calculations for variable quartz concentrations but they did not correct for possible glacial contribution and therefore their results might be incorrectly high.

Secondly, the apparent negative relation between erosion rates and precipitation (Fig. 6.3) could

arise from my method to extract mean basin precipitation rates. The main stream basins average precipitation over a large range of precipitation regimes, from the wet mountain front to the overall arid Tibetan Plateau. The tributary basins are all relatively small and are situated in the south facing mountain front, and consequently each basin averages over a relative homogeneous precipitation regime. Hence, mean precipitation rates for large basins are lower than for the small basins characterized by a very wet climate. However, without any a-priori information on the spatial distribution of the erosion processes I did not calculated the precipitation rate for only one region.

Considering the reasons discussed above, it is most likely that the erosion rates of the main streams are overestimated to a certain degree. Probably the highest uncertainty comes from the difficulty to quantify glacier erosion rates and from the inaccurate consideration of the production rates of the Tibetan Plateau. In order to quantify the effect of these uncertainties further sensitivity analysis have to be carried out.

Due to the lack of necessary information, in particular the glacier contribution and shielding by snow, I did not corrected the calculations for these parameters.

6.5.2 Erosion vs. topography

Comparing the ^{10}Be erosion rates with relief (Fig. 6.4 a) reveals overall an exponential relationship. The observation of an exponential relation is different from earlier observations made by *Ahnert* [1970] and *Schaller et al.* [2001], who reported a linear relation between these two parameters, but in good agreement with for example the observations of *Vance et al.* [2003] in the Himalayas and *Palumbo et al.* [2011] in the northern margin of the Tibetan Plateau. The latter ones show the same tendency, although relief was calculated using a different technique (Fig. 6.4 a). This, however, fits well into the conclusions by *Montgomery and Brandon* [2002], that the linear relation shown by *Ahnert* [1970] provides only a lower limit for tectonic active landscapes, while erosion rates in landscapes with a relief $\gtrsim 1000$ m behave in a non-linear fashion.

In comparison with mean basin slope, my data show the same effect than the data from the eastern margin of the Tibetan Plateau [*Ouimet et al.*, 2009], data from the Transverse Ranges of Southern California [*Binnie et al.*, 2007], the Swiss Alps [*Norton et al.*, 2010] and the north-eastern Tibet [*Palumbo et al.*, 2011]. The plot of mean basin slope vs. ^{10}Be erosion rates reveals a non-linear increase with slope and a decorrelation between erosion and slope for mean basin slopes larger than the critical angle (Fig. 6.4 b). Although, my erosion rates are higher for a given slope as those of *Ouimet et al.* [2009] and the critical slope angle seems to be lower ($\sim 25 - 30°$) than theirs ($30 - 35°$). It is possible that the lower critical slope angle detected in the Himalayas might be due to overall higher precipitation rates in the Nepal Himalayas. For example, more water in the landscape can increase pore saturation and hence decreases internal friction, bringing slopes faster to collapse [e.g. *Iverson*, 2000].

A striking feature is that I observe two different exponential relations (Fig. 6.4 a), one for the main streams and one for the tributaries, indicating that for the same relief, erosion rates are systematically

lower in tributaries than along the main streams. Indeed, the exponential increase of erosion with relief for the small tributary basins is less strong than in the large main stream basins. Note that, I am going to consider here that this systematic difference in erosion rates between tributaries and mains stream samples is real, however one has to keep in mind that this could be an atrifact, for the reasons explained before.

Since I observe the same range of mean basin relief for both types of basins I can assume that the hillslope angle distribution is similar and indeed all basins have comparable mean basins slopes, close to the critical hillslope angle (Fig. 6.4 b). Consequently, in the tributary basins erosion is not as strongly coupled with relief as in the larger basins, suggesting that relief alone is not a good proxy to estimate erosion rates. I interpret this as the direct result of very faster stream incision rates in the main stream basins and hence, a stronger coupling with hillslopes. The nonlinear increase of erosion rates with slope and relief indicates that slope angles have reached a threshold value in the steep catchments [*Binnie et al.*, 2007; *Palumbo et al.*, 2011]. Probably the different incision rates between the two types of basins induce a different landslide frequency, hence in the large basins landslides are more frequent causing faster erosion rates. If this is the case, the small basins erode more slowly than the main stream basins which would indicate that the landscape is in a disequilibrium state. Indeed, from field observations I know that the tributaries are disconnected from the main stream by knick-points, indicating that these rivers incise more slowly than the main streams. However, the significance of the two different relations has to be further investigated, as the different behaviour in erosion could also simply result from the systematic overestimation of the erosion rates along the main stream basins, as it was discussed above.

Binnie et al. [2007] interpreted the nonlinear relation between erosion and mean basin slope in terms of transport and supply (detachment) limitation. Low erosion rates in areas with less inclined slopes are typical of transport limited system, where the transport of material depends only on the available transport energy of water. The high erosion rates are typical of systems, where the amount of material transported is limited by the supply of material from the hillslopes. Amongst the data (Fig. 6.4) all basins are supply limited, or in transition between the two conditions, in agreement with the earlier findings from suspended sediment analysis [Andermann et al. to be submitted].

6.5.3 Comparison with suspended sediments

The ^{10}Be erosion rates are higher than suspended sediment erosion rates analysed earlier, and illustrated in Figure 6.8. The direct comparison shows that the erosion rates in the High Himalayas (Trishuli, Bhote Koshi and Dudh Koshi) are 4 to 9 times higher than the suspended sediment erosion rates. In the Annapurna region, erosion rates are the highest, shown by both cosmogenic nuclide (Marsyangdi basin) and suspended sediment (Kaligandaki Basin) analysis. Similar high erosion rates for this region are reported by *Burbank et al.* [e.g. 2003]; *Blythe et al.* [e.g. 2007], determined from (U-Th)/He low-temperature cooling ages. These findings are supported by sediment provenance analysis of *Garzanti*

et al. [2007], who report highest erosion rates for the hangingwall of the MCT zone (see Fig. 6.1, HHC unit) in the Annapurna region. However, suspended sediment analysis measured in the Marsyangdi valley by *Gabet et al.* [2008], few kilometers upstream from my sampling location (NP081016A), are roughly half 2.1 mm/yr. The suspended sediment erosion rates measured at the two outlet stations of the Narayani Basin and the Koshi Basin agree well, in the range of uncertainty, with cosmogenic nuclide erosion rates measured by Maarten Lupker (manuscript in preparation), CRPG Nancy, France.

Even though, the presented cosmogenic nuclide erosion rates in Figure 6.8 might be overestimated, for the reasons discussed before. Indeed, they are very significantly higher than suspended sediment ones in the High Himalayas (except Anapurna region). On the other hand, the suspended sediment erosion rates measured at stations within the High Himalayas might be underestimated, due to the lack of information on bedload transport [Andermann et al. to be submitted]. These findings are supported by high-frequency seismic noise analysis of *Burtin et al.* [2009], who detect significant bedload movements between the Tibetan Plateau and the Lesser Himalayas, where relief and river channels gradients are highest. However, both analysis agree for the three main outlet stations where bedload is considered to play a minor role. Consequently, beadload contribution in the High Himalayas is a tremendous fraction of the total sediment transport, considerably higher than the $\sim 33\%$ reported by *Pratt-Sitaula et al.* [2007] or the 50% applied by *Gabet et al.* [2008] and even more than the $60 - 350\%$ reported by[cf *Galy and France-Lanord*, 2001], if no overestimation of the ^{10}Be rates is assumed. Hence, the suspended sediment erosion rates can be interpreted as a lower limit and the ^{10}Be erosion rates as a higher limit of the High Himalayan erosion rates. I conclude that bedload contributes to a significant fraction to the sediment flux in the High Himalayas and the cosmogenic nuclide erosion rates are slightly overestimated.

6.6 Conclusions and outlook

I have compared spatial patterns of ^{10}Be erosion rates to topography, precipitation and the possible controls of glacier cover and dominant lithology. The presented data confirms high erosion rates of several millimeters per year, determined by different authors and analysing techniques [*Burbank et al.*, 2003; *Vance et al.*, 2003; *Blythe et al.*, 2007; *Garzanti et al.*, 2007; *Finnegan et al.*, 2008; *Gabet et al.*, 2008; *Ouimet et al.*, 2009; *Wulf et al.*, 2010] for the Himalayan region. My results present a first order evaluation of five large streams in Nepal and several of their tributary catchments. I have discussed in detail possible effects which might bias the reported results and show how important it is to investigate the role of glaciers and their erosion efficiency. This might not be an easy task, since each glacier behaves differently, but is desperately needed to further constrains cosmogenic nuclide analysis within the Himalayan range.

I demonstrated that in the Nepal Himalayas erosion does not correlate with precipitation, integrating over a millennial time span. However, precipitation is important as it furnishes river discharge

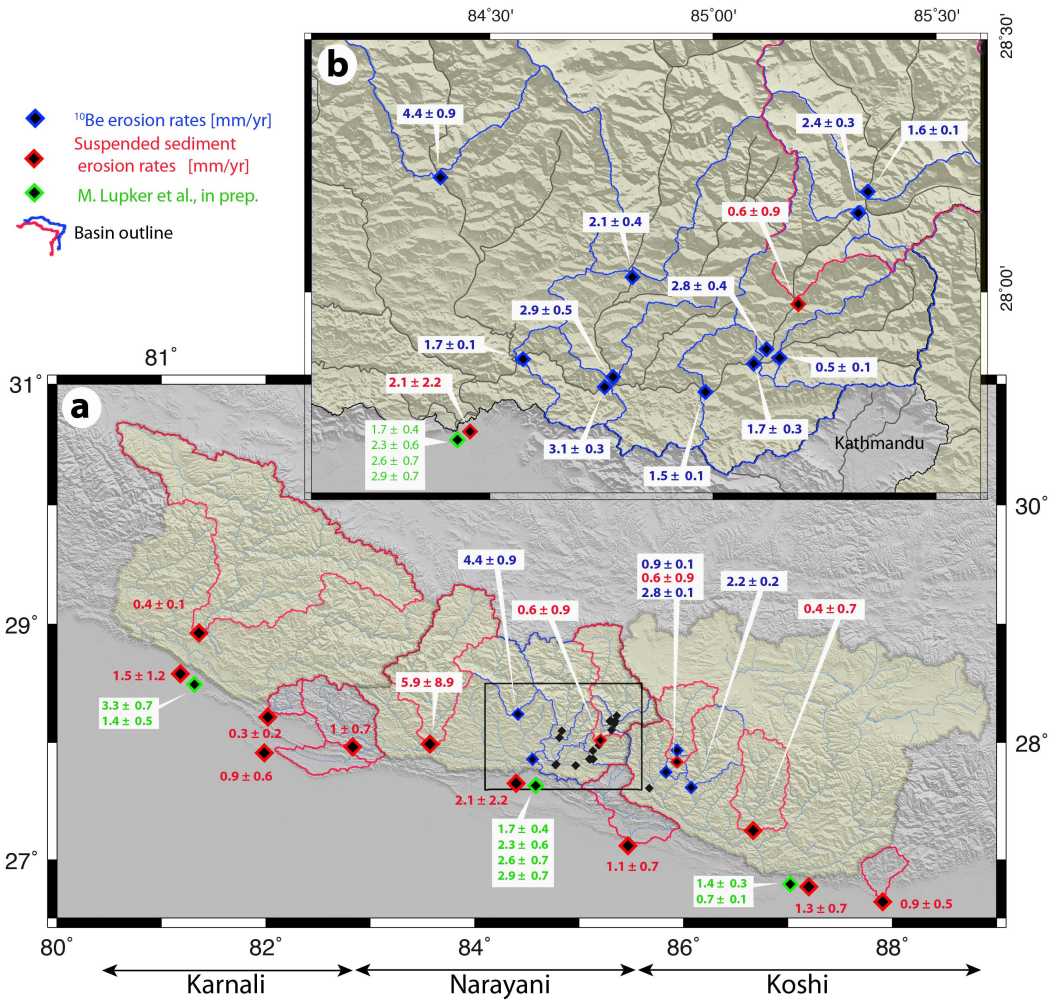

Figure 6.8: *Map of ^{10}Be erosion rates (blue) vs. suspended sediments erosion rates (red) [Andermann et al., to be submitted]. Only main stream basins are plotted. The cosmogenic nuclide erosion rates of the major outlet stations (green) of Koshi, Narayani and Karnali basin are provided by Maarten Lupker (CRPG Nancy, manuscript in preparation). The errors of cosmogenic nuclide erosion rates are measuring uncertainty (1σ). The errors of suspended sediment erosion rates are mean uncertainty of the 5% and 95% quantile fit of the rating model. a) Overview of all sampling locations. b) Zoom of the region with the highest sampling density indicated in (a) by the black outline.*

and hence, controls incision of bedrock [e.g. *Tucker and Slingerland*, 1997]. The non-linear relationship between erosion rates and topography (slope and relief) confirms the existence of a critical hillslope gradient [*Montgomery and Brandon*, 2002; *Binnie et al.*, 2006; *Finnegan et al.*, 2008; *Ouimet et al.*, 2009; *Palumbo et al.*, 2011]. The fact that the erosion rates and slope show a supply limitation is supported from suspended sediment analysis of these rivers [Andermann et al. to be submitted]. Furthermore, I show an unreported offset between tributary and main streams erosion rates, suggesting that the system is not in equilibrium. Though, to further promote the hypothesis of landscape disequilibrium I

have to evaluate if the observed difference between main stream and tributary basins is significant or if it exhibits a methodological artifact.

Chapter 7

Conclusions and outlook

Here I review the main results of each chapter and synthesise them with respect to the four principle research questions I developed in Chapter 1. I pinpoint the major conclusions and discuss their implications for the research of landscape evolution in the Nepal Himalayas. I understand this chapter as a chance to discuss in a comprehensive way the four research topics of this thesis, compare the results with respect to their temporal representativeness and develop some ideas which were not addressed before. Then I discuss the temporal distribution of erosion processes and their sequential organisation. Finally, I give some perspectives of research needs arising from the results of this thesis.

7.1 Main results and implications

Chapter 3 addresses the fundamental needs of precipitation data with a good temporal and spatial resolution. This information represents the basis for evaluating erosion processes in the Himalayas. Principally, two different datasets are available to understand precipitation: 1) ground based rain gauge measurements and 2) remotely sensed observations, and both have their pros and cons. In-situ gauge measurements have the potential to provide highly accurate measurements of a single point with almost realtime resolution, but they provide only limited information on the spatial distribution of rainfall patterns [*Tustison et al.*, 2001]. Remotely sensed measurements facilitate very good information on the spatial patterns without any need to extrapolate the information. However, the temporal resolution (and to a certain degree the spatial resolution) of remotely sensed time series are restrained by the return interval of the remote sensor. In total, I evaluated the spatio-temporal performance of four different precipitation datasets available for the Himalayas. Three are mainly remote sensing datasets and one is an interpolated rain gauge dataset. Additionally, the data was compared to the high resolution precipitation data of *Bookhagen and Burbank* [2006].

The data was tested against 53 in-situ gauge observations and rain distribution maps of 5 small watersheds. I identified the APHRODITE dataset [*Yatagai et al.*, 2009] as the best performing one for the Himalayas, both spatially and temporally. The APHRODITE dataset provides data for a very long

time-span of > 50 years, with a daily resolution. Since, all the other applied time series (river discharge, suspended sediment concentrations) in my thesis are also in daily resolution, precipitation data with a daily resolution is sufficient for my approach. I also demonstrated that remotely sensed precipitation datasets perform very poorly in mountains with important orographic effects. This is mainly because the rain retrieval algorithms are not adapted to the physical complex precipitation processes caused by orography. With respect to the importance of mountains as water resources [*Viviroli et al.*, 2007; *Immerzeel et al.*, 2010] these algorithms need to be urgently revised. Furthermore, the existence of an important rainfall gradient across the Himalayas has important implications regarding the analysis of fluvial incision models [*Roe et al.*, 2002; *Wu et al.*, 2006] and for the flood hazard mitigation. The good spatio-temporal quality of the APHRODITE dataset provides the unique possibility to study the role of precipitation, furnishing water to the landscape and being one of the fundamental parameters in landscape evolution.

In Chapter 4, I studied the fate of precipitated water. The particular emphasis was to understand the pathways to transfer precipitation into river discharge. I applied ~ 30 year time series of precipitation and river discharge of 12 watersheds, in order to compare the temporal phase-shift of peak precipitation and river discharge. The temporal plot of precipitation vs. river discharge data revealed an annual anticlockwise hysteresis effect, highlighting with respect to precipitation relatively fewer river discharge in the pre- to early monsoon season and relatively more river discharge in the late monsoon and post monsoon season. I concluded from this observation that a fraction of precipitated water is temporally stored, and thus retarded, before it is released to the river. The response time of the system, of ~ 45 days, is significant and can not yield from the retardation of water in soils and/or by a surface runoff. I identified this effect as the result of transient storage of water in a deep fractured basement aquifer. This until now neglected component of the hydrological discharge cycle in the Himalayas retards water during monsoon and maintains river discharge during the dry season. Furthermore, the recharge-discharge behaviour of all studied basins shows the same progress and the same hysteresis shape, regardless of the basin location within the Himalayan range, as well as the partial glaciation and temporal snow coverage. Only the hysteresis loops of those basins with considerable glaciated areas and seasonal snow cover are relatively shifted along the discharge axis, revealing an elevated basflow component. I used this relative shift to estimate the annual snow and ice melt contribution to the Himalayan discharge cycle. The calculated snow and ice melt volume is in the order of $\sim 14\ km^3/yr$, which is roughly 10% of the annual river discharge of the three main drainage basins in Nepal, and is consequently a significant fraction. Yet, the calculated storage variability of the three main basins, estimated through hydrological modelling, accounts for $\sim 28\ km^3/yr$. This storage variability has to be interpreted as a volume which is purged and refilled every year. The actual water volume passing through this compartment is a multiple of it and thus much more important in terms of volume than the ice and snow melt contribution. Saying this, I am not intending to neglect the importance of glaciers but rather want to point out the importance of this transient groundwater storage

compartment.

The precondition to observe such a well defined cyclic discharge behaviour is the very strong and likewise cyclic seasonality imposed by the Indian Summer Monsoon. One of the most important finding is the retardation of the groundwater contribution to the river discharge. Therefore, very high flow rates can be observed during post-monsoon, even though the climate is very dry. This has important implications with respect to the transport capacity of sediments during this time. Furthermore, as the rivers are high, precipitation events present a larger risk for flooding with respect to a similar precipitation event in pre-monsoon season.

Chapter 5 deals with the constrains of mobilization and transport of suspended sediments in space and time. I present in this work some new unpublished data on daily suspended sediment concentrations measurements from 13 hydrological stations, covering all major drainage basins of the Nepal Himalayas. These data provide a new long-term and high resolution dataset to the Earth Sciences community. It is so far the largest and most complete suspended sediment dataset for the whole Himalayas. I applied a multi-data analysis of daily precipitation, river discharge and suspended sediment concentration observations and show some new fundamental observations on the transport and mobilization of material. Here, I separated the river discharge hydrograph in a direct runoff (fast response time) and a basflow component (slow response time). Baseflow is the fraction of river discharge which passes through a reservoir before it is released to the river, and thus gets temporally retarded. The direct runoff is the fraction of river discharge characterized by a short transfer time, resulting in a short response ($\lesssim 1$ day) of the corresponding rainfall event into the discharge hydrograph. I show that suspended sediment concentrations plotted against river discharge describe an annual clockwise hysteresis effect. However, when plotting suspended sediment concentration only against the direct runoff component, the hysteresis effect disappears, revealing a linear relationship. From this observation and with the beforehand achieved knowledge of an important groundwater contribution, I identified the hysteresis effect as an dilution effect. The observation of an hysteresis effect between suspended sediment concentrations and river discharge is a common phenomena and has been usually attributed as a temporal supply effect [e.g. *Morehead*, 2003], for example, the depletion of a sediment stock in the river system during the course of a large flood [e.g. *Morehead*, 2003]. From the linear relation between sediment fluxes and river discharge, I developed a rating model, allowing me to calculate basin wide denudation rates directly from the river hydrograph for the whole of Nepal. The calculated denudation rates are in the order of $0.1 - 6\ mm/yr$ which is typical for the central Himalayas [e.g. *Gabet et al.*, 2008; *Wulf et al.*, 2010].

I also show that all river systems of the Nepal Himalayas have the same behaviour with respect to their mean flux. For example, the probability density of sediment fluxes is highly reproducible between the different basins. The data shows a well defined threshold, with a stepper relation for high magnitude events. Consequently, the occurrence of large erosion events follows a different probability distribution than moderate and small events. Furthermore, the large events do not control the erosion

flux. This has important implications concerning inter-comparability of modern erosion fluxes with, for example, catchment wide erosion rates from cosmogenic nuclide analysis. Similarly, the normalized sediment flux vs. river discharge plot reveals the same linear relation and an identical minimum threshold. One major conclusion from this observation is that precipitation and river discharge exert a predominant control on the mobilization and transport processes. Other basin characteristics, such as lithology and landuse have only a minor impact. It is possible that the threshold in the rating model is influenced by one of these parameters.

The analysis of suspended sediment fluxes reveals that erosion in the Nepal Himalayas is clearly controlled by hillslope processes, limiting the transport of material in the rivers. In return, hillslope processes are closely connected with the occurrence and intensity of precipitation. The rivers in the three watersheds of Nepal are hardly ever close to their transport capacity, which is a result of a large discharge contribution by groundwater. This implies that the rivers in the Nepal Himalayas are supply limited and the hillsopes as contributing source are transport limited.

In Chapter 6, I analysed the cosmogenic nuclide concentration of river sand samples in order to calculate the mean catchment denudation rates of 24 catchments, integrating over several hundred to thousands of years. Then, I compared these results with those calculated from the suspended sediment concentrations. For the Nepal Himalayas, no large scale study dealing with cosmogenic nuclide erosion rates has been carried out so far. In general, the results confirm erosion rates of 0.1 to $\sim$ 6 mm/yr calculated from suspended sediment concentrations and reported in the literature [*Burbank et al.*, 2003; *Vance et al.*, 2003; *Blythe et al.*, 2007; *Garzanti et al.*, 2007; *Gabet et al.*, 2008; *Wulf et al.*, 2010]. I compared the data to mean basin slope and relief, in order to see if I can establish a relationship between topography and erosion as documented in the literature [e.g *Ahnert*, 1970; *Montgomery and Brandon*, 2002; *Vance et al.*, 2003; *Binnie et al.*, 2007; *Finnegan et al.*, 2008; *Ouimet et al.*, 2009]. Secondly, I plotted the data against mean basin rainfall rate and intensity, in order to test if the short-term precipitation control can be also observed for longer time scales.

The results of the cosmogenic nuclide analyses confirm the overall established relationship between relief and slope, showing clearly that slope exerts a predominant control on spatial erosion rates. I observe non-linear relations between catchment wide erosion rates and relief, confirming that erosion in the Nepal Himalayas is supply limited. Especially, the very high erosion rates for a slope larger than the critical hillslope demonstrate that erosion takes place in form of mass-wasting.

Cosmogenic nuclide analysis suggest a different erosion behaviour of small tributary basins than large main stream basins. The small basins show in general lower erosion rates than large basins. However, further work is necessary to test whereas this finding is real or a methodology artifact. If true however, this result would imply that the landscape in the central Himalayas is not in a state of equilibrium, which might be the result of a change in climatic forcing, for example the documented monsoon intensification around 5000 years ago [*Bookhagen et al.*, 2005b; *Clift et al.*, 2008b; *Huntington et al.*, 2006]. Even if the demonstration needs to be strengthen, the observation of faster erosion rates in

the large mainstream basins than the small tributary basins is supported by field observation showing knick-points on the tributary just before the confluence with the main streams.

In summary, I provided some new data on erosion processes for the Nepal Himalayas. The results are overall consistent and demonstrate that precipitation is important to mobilize and transport eroded materials, but that on a longer time scale ($> kyr$) erosion seems to be controlled by topography. On the long time-scale erosion rates do not show an explainable correlation with precipitation. However, landscape is produced by the fast incision rate of rivers, due to their high transport energy, generated by the high precipitation rates. From the analysis of high resolution (temporal and spatial) precipitation analysis, I established the importance of the formally neglected transient groundwater storage compartment and I show that all rivers in Nepal have a similar erosion behaviour. The existence of a threshold in the probability of occurrence between large events and small events is the direct consequence of a system which is not controlled by infrequently occurring extreme events, but rather moderate ones with a high recurrence interval. Furthermore, the high magnitude base frequency of the Indian Summer Monsoon does not control erosion dynamics, but contributes significantly to the river discharge, which is important to evacuate the erosional material from the mountain range. Finally, I show that the landscape is currently not in a state of equilibrium.

7.2 The seasonal erosion cycle

The strong relation between direct runoff vs. denudation rates and the highly repetitive Indian Summer Monsoon leads me to propose a conceptual cyclic surface dynamics model (Fig. 7.1). In this representation, the low-frequency high-magnitude monsoon signal has a minor impact on the annual erosion mass balances. Erosion is mainly driven by the high-frequency low-magnitude event intensity. 1) In pre-monsoon water availability is at its minimum and soils are dry but a few rainfall events can occur, mobilizing available sediments. Groundwater storage is being refilled. 2) In monsoon, precipitation intensity and frequency are very high, providing large amounts of hillslope material to the river. This amount is evacuated directly out of the mountain range by the high river transport capacity. High transport capacity is maintained by the high groundwater input into the rivers. Water storage is replenished and pore pressure in the subsurface is high, inducing landslides. Most of the erosion takes place during monsoon, mainly in from of mass wasting. 3) In Post-monsoon, only few precipitation events are recorded. Erosion fluxes decrease drastically and are diluted by the relatively increased groundwater contribution, depleting the aquifer storage. 4) Winter, few isolated precipitation events take place, mainly as snow at high elevations. Water availability is close to its minimum. Frost cracking and shattering at higher elevations weakens material and makes it prone to failure in the subsequent monsoon season.

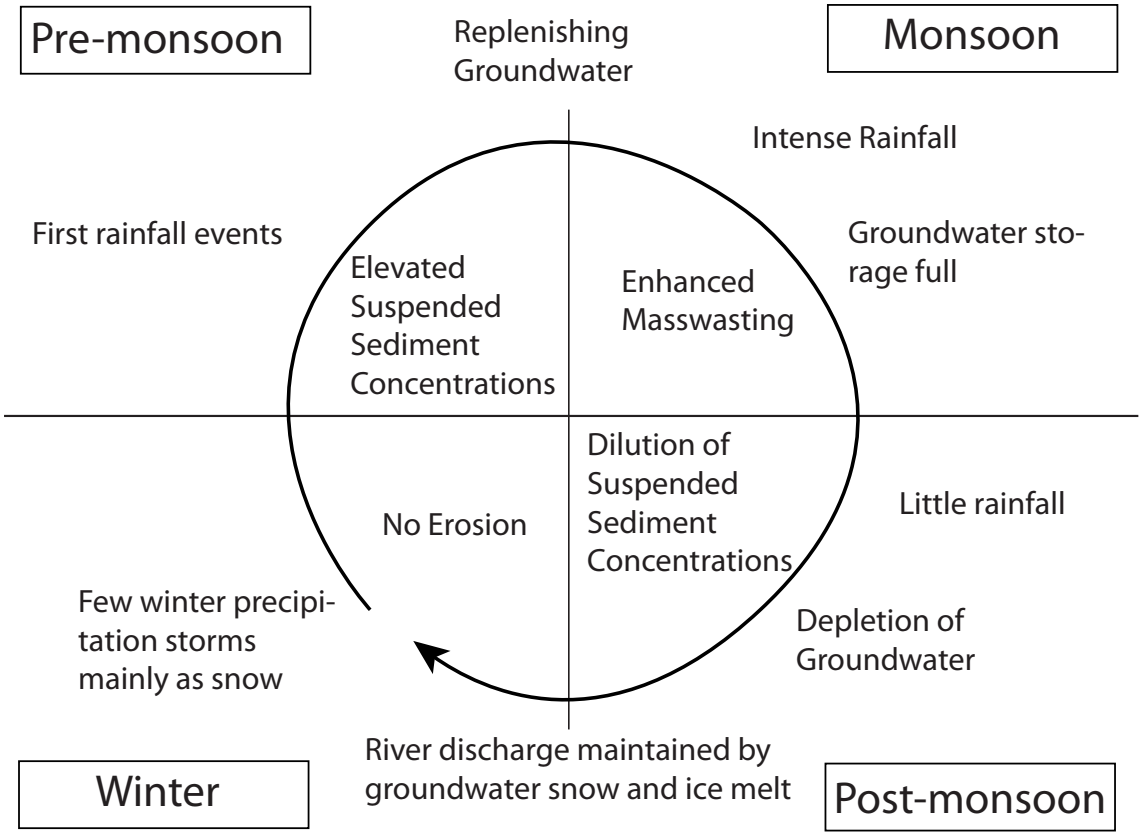

Figure 7.1: *Conceptual schema of the seasonal erosion cycle in the Nepal Himalayas. Winter: December-February, Pre-monsoon: March-May, Monsoon: June-September, Post-monsoon: October-November.*

7.3 Outlook

Precipitation data with higher spatial resolution are needed to evaluate the orographic effects on a finer scale, for example valley-bottom ridge-crest gradients within small watersheds. Remotely sensed precipitation datasets have to be urgently revised to be applicable in the Himalayas. As these datasets serve as input for global climate models, their general unsatisfying performance might also bias the quality of these models. This underlines the need to bring forward the new remote precipitation measuring system GPM (Global Precipitation Measuring mission) which promises to have a better spatial and temporal resolution as well as a higher precision of measurements [e.g. *Gruber et al.*, 2008].

I demonstrated the general importance of groundwater contribution to the Himalayan discharge cycle. Deep groundwater is a non-negligible compartment to take into account when estimating water resources in the central Himalayas, as well as flood hazard and landslide occurrence due to pore-pressure saturation processes. It requires improving our knowledge about the geometry and physical properties of the basement fracture systems [e.g. *Davy et al.*, 2010] and their relationship with relief. Furthermore, it is important to separate between snow and glacier melt contribution. These are two

crucial components of river discharge and might shift towards higher or lower contributions due to climate change and therefore can change the hydrological system of the Nepal Himalayas.

The suspended sediment concentrations, I present in this work, show a clear relation with direct river discharge. Nevertheless, the database has to be extended over longer time spans, including also measurements on smaller basins ($< 250\ km^2$), in order to resolve more robust results. Also, it is important to study the distribution of the sediment concentration fluxes within the river cross profile, in order to have a more representative image of the real suspended sediment flux. Secondly, the hydrograph separation method has to be improved. I used the local minimum technique, connecting the local minimum points of the hydrograph. Since several events might overlap within the sequence, producing local minimum points within the duration of a direct discharge event, this method might underestimate the volume of direct discharge. Furthermore, to gain more insights on erosion dynamics in the Nepal Himalayas, the following points need further investigation: 1) the spatial and temporal dynamics of bedload, 2) what controls the baseflow concentration of each basins, and 3) what controls the hillslope production processes, for example landslide triggering.

Cosmogenic nuclide analysis offer the huge potential to measure erosion rates from only one hand full of sand. However, the calculation of erosion rates might be biased by the impact of four essential unknowns: 1) glacial erosion rates, 2) the erosion contribution of the Tibetan Plateau, 3) the heterogeneous quartz distribution, and 4) the temporal shielding by snow cover. Further research has to be carried out to quantify the impact of these four parameters onto the calculation of catchment wide erosion rates from cosmogenic nuclide analysis, in order to test if the observed differences between main stream basins and tributary basins persist. Finally, more data is needed to constrain the apparent differences between tributary catchment erosion rates and main stream catchment erosion rates.

Appendix Chapter 3

Supplementary material, data sources and description

1. Aphrodite $APHRO\_V1003R1$

The APHRODITE (Asian Precipitation Highly Resolved Observational Data Integration Towards Evaluation of Water Resources) project is a consortium by the Research Institute for Humanity and Nature (RIHN) and the Meteorological Research Institute of Japan Meteorological Agency (MRI/JMA). In joint collaboration this project develops precipitation products with varying resolution and for several Asian regions. We used the latest version daily dataset for monsoon Asia ($60-155°E$, $15°S$ - $55°N$) $APHRO\_MA\_V1003R1$ [*Yatagai et al.*, 2009; *Xie et al.*, 2007] (released 25 Aug. 2010) with a spatial resolution of $0.25°$ ($\sim 30km$). $APHRO\_MA\_V1003R1$ provides data for a statistical robust time span of more than 50 years (1951-2007).

$APHRO\_MA\_V1003R1$ is a distance weighted interpolated dataset from precipitation gauging stations. Depending on availability, between 5000 - 12000 stations are considered for interpolation. The project uses a compilation of precipitation gauge stages from several sources: 1) Global Telecommunication System GTS network stations for this area, 2) historical archive data, e.g. GSOD (Global Surface Summary of the Day) by the National Climatic Data Center (NCDC)/National Oceanic and Atmospheric Administration (NOAA) and *Xie et al.* [2007], as well as 3) pre-compiled data-sets [*Yatagai et al.*, 2009, suppl. 2]. Additional the data has been bias corrected with WORLDCLIM data [*Hijmans et al.*, 2005] for gauge-sparse areas as well as for orography. Stations falling within the same $0.05°$ grid have been combined [*Yatagai et al.*, 2009].

More information is available here: $http://www.chikyu.ac.jp/precip/data/APHRO\_V1003R1\_readme.txt$
The data can be downloaded from here: $http://www.chikyu.ac.jp/precip/products/index.html$

2. $CPC-RFE2.0$

CPC-RFE 2.0 (Climate Prediction Center - Rainfall Estimates) is a precipitation product for the south Asian region published by the CPC of NOAA (National Oceanic and Atmospheric Administration), USAID (United States Agency for International Development) and USGS (United States Geological Survey). The product provides real time daily precipitation information with a spatial resolution of $0.1°$ ($\sim 10km$) for the area ($70-110°E, 5-35°N$. RFE2.0 combines 4 different primary product, including data from one rain gauging network whereas the three others are remotely sensed. Data from RFE2.0 is available since May 2001 and continuously updated.

The four input products are: 1) GTS global gauging network ($\sim$ 1000 stations), 2) GPI (GOES Precipitation Index), a precipitation index derived from GEOS (Geostationary Operational Environmental Satellites) geostationary weather satellites (IR data), 3) SSM/I (Special Sensor Microwave/Imager) observations and 4) and AMSU-B (Advanced Microwave Sounding Unit-B, on-board of NOAA-K, -L, -M satellites). In general all data sources have similar large scale distribution patterns [*Xie et al.*, 2002]. The three satellite products are merged through maximum likelihood estimation methods.

More information is available here: $http://www.cpc.ncep.noaa.gov/products/fews/SASIA/climatology.shtml$
The data can be downloaded from here: $ftp://ftp.cpc.ncep.noaa.gov/fews/S.Asia/$

3. GSMaP MVK+

The Global Satellite Mapping of Precipitation, passive microwave radiometer (GSMaP MVK+) dataset was developed in order to provide high-precision and high-resolution global precipitation maps from satellite data. The project is sponsored by CREST (Core Research for Evolutional Science and Technology) of the Japan Science and Technology Agency (JST) and by the JAXA (Japan Aerospace Exploration Agency) Precipitation Measuring Mission (PMM) Science Team.

GSMaP data is an global dataset ($60°N/S$), available since the end of November 2002 and is provided in almost real time (with an $\sim$ 10 month data gap in 2007). The data has an $0.1°$ ($\sim 10km$) spatial resolution and one hour temporal. The project aims to develop an advanced microwave radiometer algorithm based on a deterministic rain-retrieval algorithm and the production of precise high-resolution global precipitation maps [*Ushio et al.*, 2009; *Kubota et al.*, 2007]. The data incorporates MWR measures from TRMM-TMI, SSM/I,AMSR-E (Advanced Microwave Scanning Radiometer-EOS, on-board of AQUA satellite) and AMSU-B sensors and IR from geostationary satellites compiled by CPC. The algorithm is using morphing methods and Kalman filter prediction correction.

More information is available here: $http://sharaku.eorc.jaxa.jp/GSMaP\_crest/html/about\_data.html$

Data can be downloaded from: $ftp://hokusai.eorc.jaxa.jp/pub/gsmap\_crest/MWR+/$ (archive 2003-2006) and $http://sharaku.eorc.jaxa.jp/GSMaP/index.htm$ (real time >2007)

4. TRMM 3B42 and 2B31

The Tropical Rainfall Measuring Mission (TRMM) is an joint collaboration between the JAXA and the United States of America National Aeronautics and Space Administration (NASA). TRMM is an independent satellite carrying an arrangement of radar and optical sensors.

The 3B42, is a multisatellite precipitation analysis dataset. It combines several instruments and outputs gridded rainfall with and $0.25°$ ($\sim 30km$) spatial- and 3 hour temporal resolution and is available within a global belt, $50°N/S$ latitude [*Huffman et al.*, 2007]. Basically it is a set of MWR estimates from TRMM-TMI, SSM/I, AMSR-E and AMSU-B, missing pixels have been filled with IR observations compiled by CPC. The data are corrected with the monthly field ratios between 3B43 (monthly compiled version of 3B42) and gauging stations.

More information is available here: $http://trmm.gsfc.nasa.gov/3b42.html$

Bookhagen and Burbank [2006] have developed his own precipitation record from primary TRMM 3B31 orbital dataset, that is data are not yet projected and merged into global coordinate systems, but are rather provided in an orbital strip of observation. This data has a $0.05°$ ($\sim 4km$) spatial resolution (one of the finest grid size available at the moment). In contrast the temporal resolution is at its best one month. In contrast to multi satellite datasets, this observation has only one or two snapshots per day, and is likely to miss large quantities of precipitation. Analysis of a 12 year time series show that when averaged over more than 6 years, the correlation coefficient (r^2) with ground based observations (GPCC, Global Prepitation Climatology Centre, stations) is 0.82, for the whole observation circumference.

All TRMM datasets can be downloaded here: $http://trmm.gsfc.nasa.gov/data_dir/data.html$
More information is available here: $http://trmm.gsfc.nasa.gov/2b31.html$

Table 1: Table of ground truth precipitation gauging stations. All these stations have been used to validate precipitation distribution along swath profiles. The station within the five small watersheds are not included here. # is the station id, P0304 mean annual precipitation [mm/a] for 2003 and 2004 (APHRO, CPC-RFE, GSMaP and TRMM-3B42 data), P9707 mean annual precipitation [mm/a] from 1997 to 2007 (TRMM-2B31), P30a mean long term annual precipitation [mm/a] for $\sim$ 30 years.

No.	**#**	**Place**	**Elevation** [m asl.]	**Lat. N** [°]	**Long. E.** [°]	**Availability**	**Source**	**P0304** [mm/a]	**P9707** [mm/a]	**P30a** [mm/a]	**Profile**
1	101	KAKERPAKHA	842	29.65	80.50	1978-2008	DHM	1742	1518	1824	1
2	102	BAITADI	1635	29.55	80.42	1978-2008	DHM	1435	1037	1374	1
3	103	PATAN (WEST)	1266	29.47	80.53	1978-2008	DHM	1303	1622	1353	1
4	107	DARCHULA	1097	29.85	80.57	1978-2008	DHM	2491	2740	2584	1
5	108	SATBANJH	2370	29.53	80.47	1978-2008	DHM	1609	1609	1634	1
6	206	ASARA GHAT	650	28.95	81.45	1978-2008	DHM	1199	1171	1167	5
7	306	GAM SHREE NAGAR	2133	29.55	82.15	1978-2008	DHM	790	704	680	2
8	307	RARA	3048	29.55	82.12	1978-2006	DHM	882	965	789	2
9	308	NAGMA	1905	29.20	81.90	1978-2008	DHM	777	1004	769	2
10	405	CHISAPANI(KARNALI)	225	28.65	81.27	1978-2008	DHM	2238	2184	2407	2
11	411	RAJAPUR	129	28.43	81.10	1978-2008	DHM	1414	1767	1335	2
12	601	JOMSOM	2744	28.78	83.72	1978-2008	DHM	260	274	266	3
13	604	THAKMARPHA	2566	28.75	83.70	1978-2008	DHM	405	395	411	3
14	607	LETE	2384	28.63	83.60	1978-2008	DHM	1335	1305	1408	3
15	610	GHAMI (MUSTANG)	3465	29.05	83.88	1978-2008	DHM	168	187	147	3
16	715	KHANCHIKOT	1760	27.93	83.15	1978-2008	DHM	1845	1566	1712	3
17	721	PATTHARKOT (WEST)	200	27.77	83.05	1978-2008	DHM	2247	2046	2203	3
18	722	MUSIKOT	1280	28.17	83.27	1978-2008	DHM	2246	2572	2510	3
19	723	BHAGWANPUR	80	27.68	82.80	1978-2008	DHM	1811	1797	1865	3
20	725	TAMGHAS	1530	28.07	83.25	1981-2008	DHM	1906	1774	1916	3
21	904	CHISAPANI GADHI	1706	27.55	85.13	1978-2008	DHM	2201	2464	2563	4
22	906	HETAUNDA N.F.I.	474	27.42	85.05	1978-2008	DHM	2405	3050	2755	4
23	909	SIMARA AIRPORT	130	27.17	84.98	1978-2008	DHM	1920	2058	2154	4
24	918	BIRGANJ	91	27.00	84.87	1978-2008	DHM	1628	1785	1694	4
25	1001	TIMURE	1900	28.28	85.43	1978-2008	DHM	913	1175	841	4
26	1004	NUWAKOT	1680	27.92	85.17	1978-2008	DHM	1970	2112	1989	4
27	1007	KAKANI	2064	27.80	85.25	1978-2008	DHM	2863	3032	2985	4
28	1038	DHUNIBESI	1085	27.72	85.18	1978-2008	DHM	1618	1820	1807	4
29	1054	THAMACHIT	1847	28.17	85.32	1978-2008	DHM	664	298	330	4
30	1055	DHUNCHE	1982	28.10	85.30	1978-2008	DHM	1976	2228	1947	4
31	1202	CHAURIKHARK	2619	27.70	86.72	1978-2008	DHM	2082	2343	2107	5
32	1203	PAKARNAS	1982	27.43	86.57	1978-2008	DHM	1827	1892	1851	5
33	1206	OKHALDHUNGA	1720	27.32	86.50	1978-2008	DHM	1783	1667	1872	5
34	1210	KURULE GHAT	497	27.13	86.42	1978-2008	DHM	984	1413	1116	5
35	1213	UDAYAPUR GADHI	1175	26.93	86.52	1978-2008	DHM	1791	1791	1691	5

No.	**#**	**Place**	**Elevation** [m asl.]	**Lat.** [°]	**Long.** [°]	**Availability**	**Source**	**P0304** [mm/a]	**P9707** [mm/a]	**P30a** [mm/a]	**Profile**
36	1216	SIRAHA	102	26.65	86.22	1978-2008	DHM	1455	1678	1599	5
37	1220	Chyalsa	2770	27.52	86.62	1984-2008	DHM	1942	1678	1599	5
38	1301	NUM	1497	27.28	87.28	1978-2008	DHM	4411	4895	4660	6
39	1306	MUNGA	1317	27.03	87.23	1978-2008	DHM	1122	1112	1050	6
40	1309	TRIBENI	143	26.93	87.15	1978-2008	DHM	1722	2088	1818	6
41	1317	CHEPUWA	2590	27.77	87.42	1978-2008	DHM	2626	2681	2426	6
42	1319	BIRATNAGAR AIRPORT	72	26.48	87.27	1978-2008	DHM	1880	2126	2013	6
43	1320	TARAHARA	200	26.70	87.27	1978-2008	DHM	1951	2159	1925	6
44	1321	TUMLINGTAR	303	27.28	87.22	1978-2008	DHM	1288	1359	1437	6
45	1406	MEMENG JAGAT	1830	27.20	87.93	1978-2008	DHM	2260	2103	2162	7
46	1407	ILAM TEA ESTATE	1300	26.92	87.90	1978-2008	DHM	1706	2001	1698	7
47	1409	ANARMANI BIRTA	122	26.63	87.98	1978-2008	DHM	2426	2713	2641	7
48	1410	HIMALI GAUN	1654	26.88	88.03	1978-2008	DHM	2372	2429	2387	7
49	1412	CHANDRA GADHI	1220	26.57	88.05	1978-2008	DHM	2314	2337	2278	7
50	1415	SANISCHARE	168	26.68	87.97	1978-2008	DHM	2739	2938	2671	7
51	1421	GAIDA (KANKAI)	143	26.50	87.90	1984-2008	DHM	2686	2600	2517	7
52	CN87TNGR	TINGRI	4300	28.63	87.08	1959-1990	FAOCLIM	NaN	NaN	270	5
53	AWS1	PYRAMID	5050	27.96	86.81	2001-2006	Ev-K2-CNR	NaN	414	NaN	5
54	AWS2	PHERICHE	4268	27.89	86.82	2002-2006	Ev-K2-CNR	NaN	502	NaN	5
55	AWSNP	NAMCHE	3560	27.80	86.71	2002-2006	Ev-K2-CNR	NaN	954	NaN	5

DHM: Department of Hydrology and Meteorology Nepal $http://www.dhm.gov.np/$
FAOCLIM: FAO Agroclimatic database management system $http://www.fao.org/nr/climpag/pub/EN1102_en.asp$
Ev-K2-CNR: Pyramid SHARE project, Italian National Research Council and Nepal Academy of Science and Technology $http://www.evk2cnr.org/cms/en/home.html$
P30a: Mean annual longterm ($\sim 30yr$) Precipitation
P0304: Mean annual precipitation, 2 years (2003 and 2004)
P9707: Mean annual precipitation, 10 years (1997 - 2007)

References

Bookhagen, B., and D. W. Burbank (2006), Topography, relief, and trmm-derived rainfall variations along the himalaya, *Geophys. Res. Lett.*, *33*, doi:10.1029/2006GL026037.

Hijmans, R. J., S. E. Cameron, J. L. Parra, P. G. Jones, and A. Jarvis (2005), Very high resolution interpolated climate surfaces for global land areas, *International Journal of Climatology*, *25*(15), 1965–1978, doi:10.1002/joc.1276.

Huffman, G. J., R. F. Adler, D. T. Bolvin, G. Gu, E. J. Nelkin, K. P. Bowman, Y. Hong, E. F. Stocker, and D. B. Wolff (2007), The trmm multisatellite precipitation analysis (tmpa): Quasi-global, multiyear, combined-sensor precipitation estimates at fine scales, *Journal of Hydrometeorology*, *8*(1), 38–55, doi:10.1175/JHM560.1.

Kubota, T., et al. (2007), Special issue papers-precipitation-global precipitation map using satellite-borne microwave radiometers by the gsmap project: Production and validation, *IEEE Transactions on Geoscience and Remote Sensing*, *45*(7), 2259–2275.

Ushio, T., K. Sasashige, T. Kubota, S. Shige, K. Okamoto, K. Aonashi, T. Inoue, N. Takahashi, and T. Iguchi (2009), A kalman filter approach to the global satellite mapping of precipitation (gsmap) from combined passive microwave and infrared radiometric data, *J. Meteor. Soc. Japan*, *87A*(9), 3084–3097, doi:10.2151/jmsj.87A.137.

Xie, P., Y. Yarosh, T. Love, J. E. Janowiak, and P. A. Arkin (2002), A real-time daily precipitation analysis over south asia, *Paper presented at the 16th Conference. of Hydrology.*

Xie, P., M. Chen, S. Yang, A. Yatagai, T. Hayasaka, Y. Fukushima, and C. Liu (2007), A gauge-based analysis of daily precipitation over east asia, *Journal of Hydrometeorology*, *8*(3), 607–626, doi:10.1175/JHM583.1.

Yatagai, A., O. Arakawa, K. Kamiguchi, H. Kawamoto, M. I. Nodzu, and A. Hamada (2009), A 44-year daily gridded precipitation dataset for asia based on a dense network of rain gauges, *SOLA*, *5*, 137–140, doi:10.2151/sola.2009-035.

Supplementary material, PARDYP watersheds

1. Monthly regression

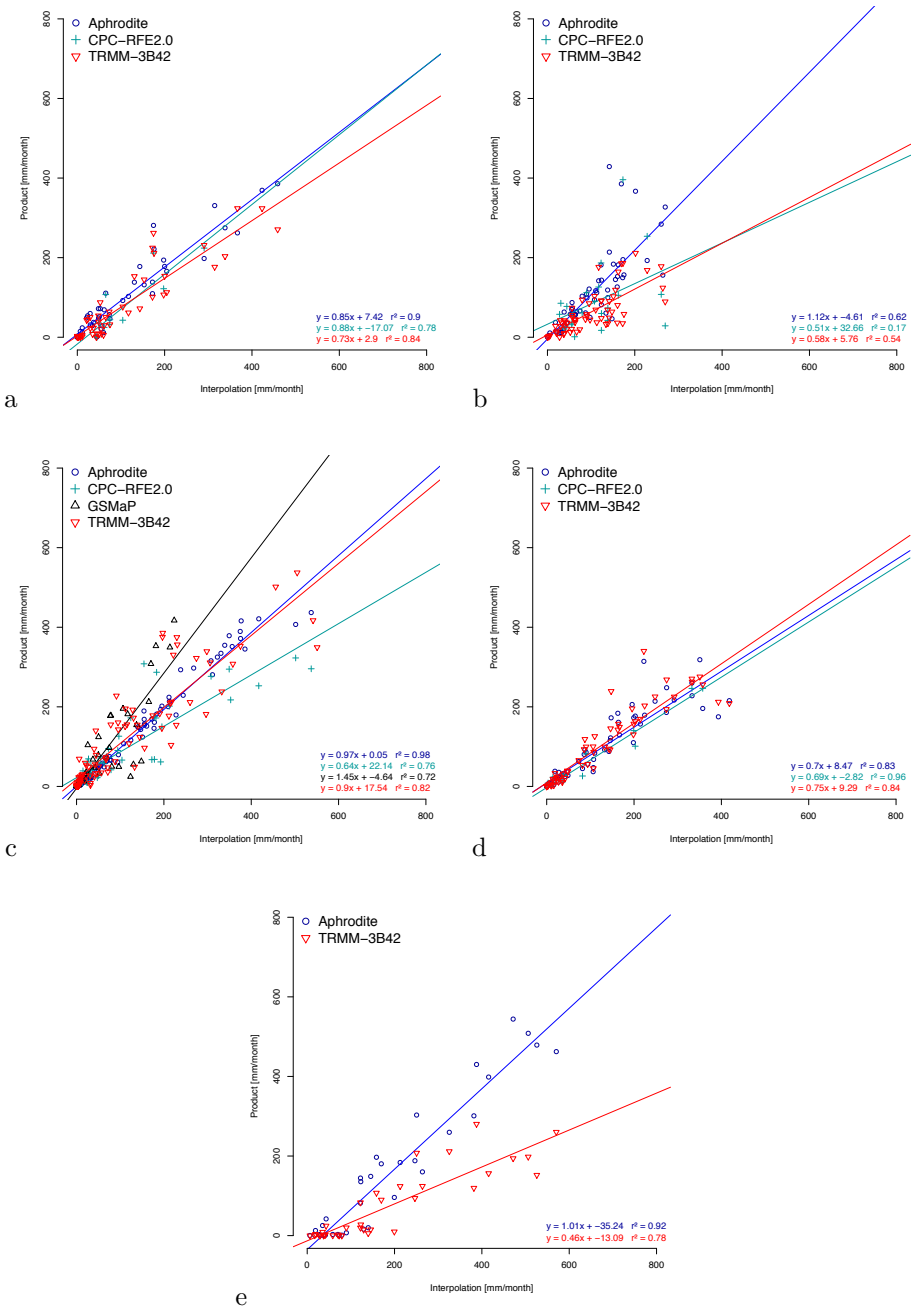

Figure 1. Regression between the interpolation of local rain gauges and each respective precipitation product for the five PARDYP watersheds (A) Bhetagad India, (B) Hillkot Pakistan, (C) Jhikhu Nepal, (D) Xizhuang Yunnan/China and (E) Yarsha Nepal.

2. Annual comparison

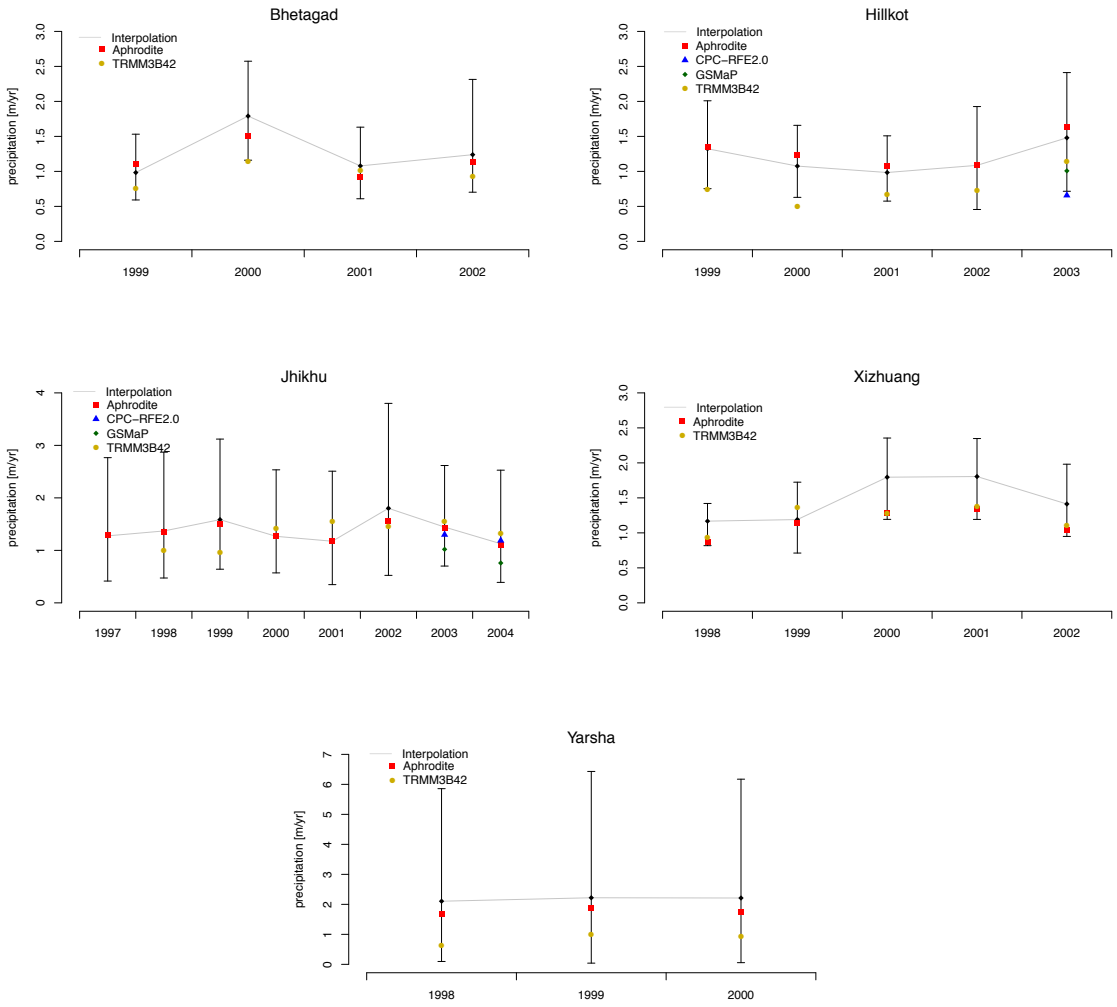

Figure 2. Annual mean basin wide precipitation rates from gridded precipitation data and basin wide interpolated rain gauging stations. Error bars represent the range of interpolated gauging data. The upper and lower limits of the error bars represent the minimal and maximal annual sum of precipitation rates.

Supplementary material, swaths profiles

1. Station elevation profiles

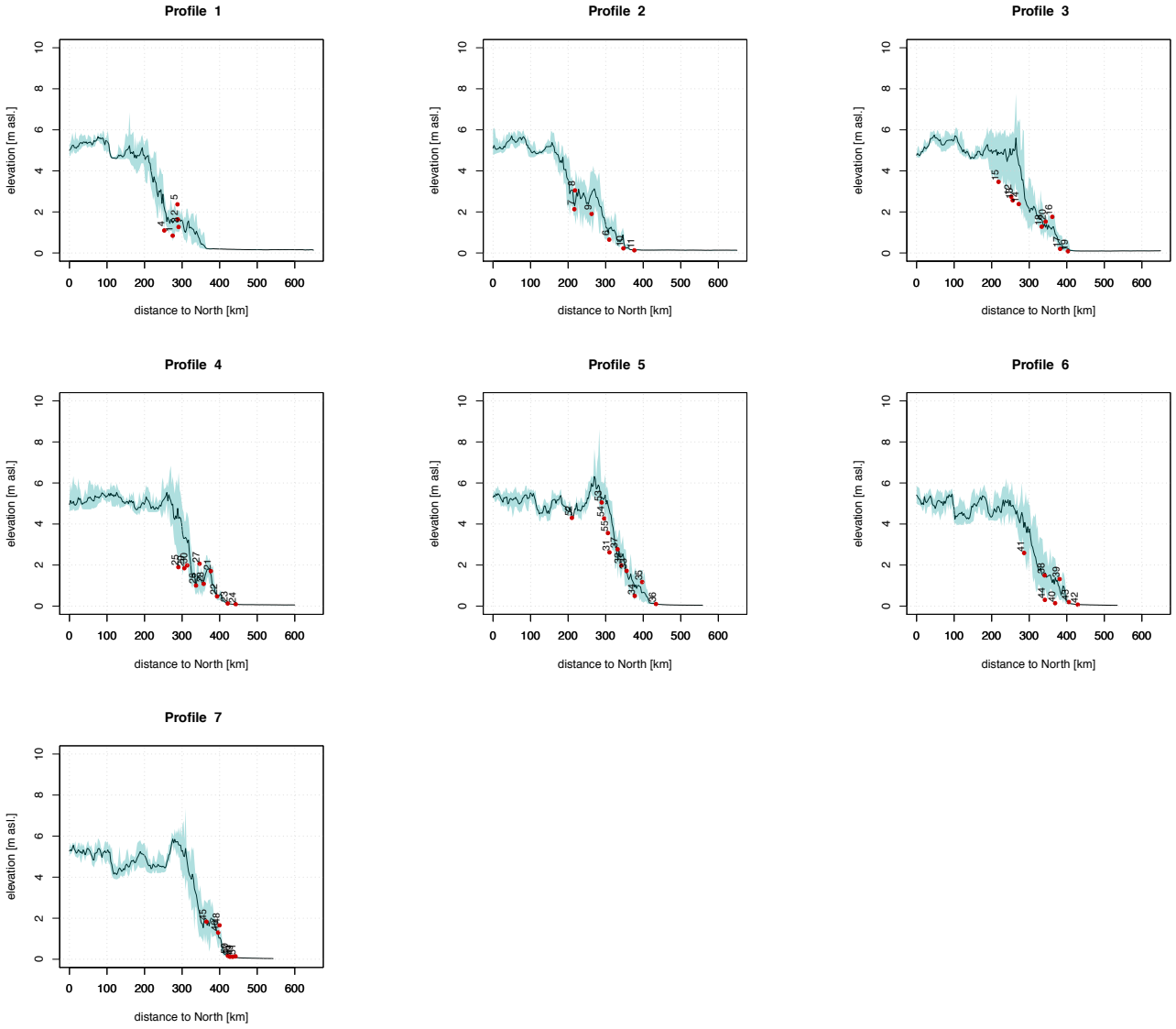

Figure 1: Elevation range along the swath profiles and stations elevation. Note that swath profiles are averaged over the whole swath width.

2. annual swath profiles

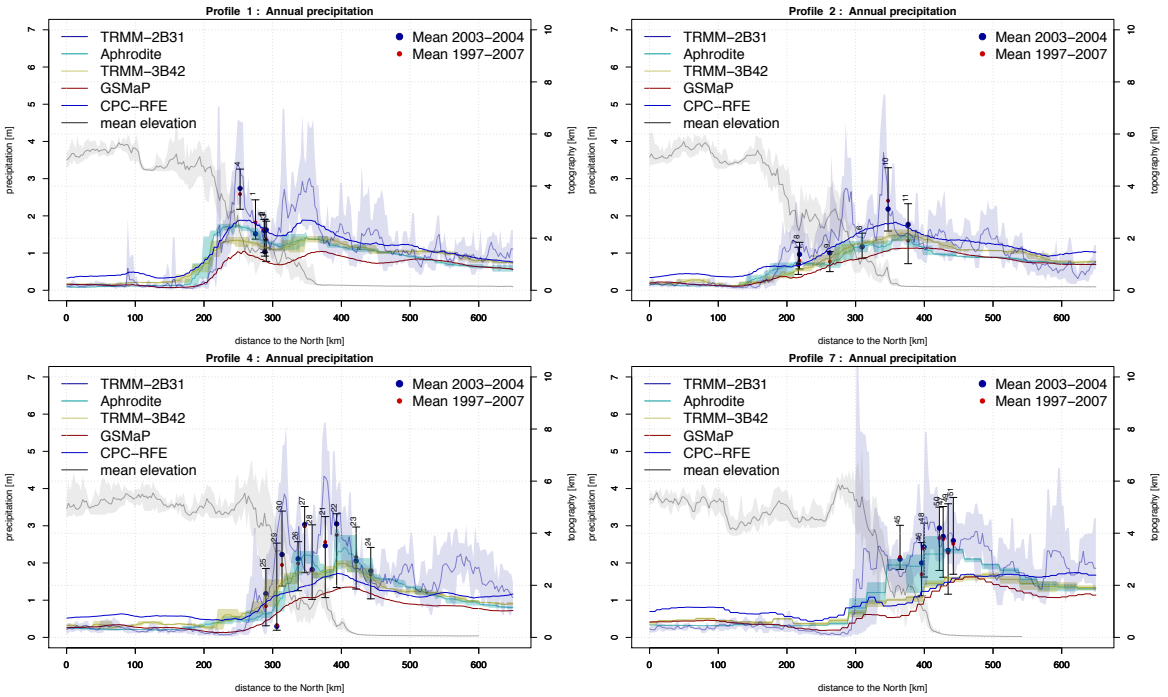

Figure 2: Annual precipitation swath profiles. Mean precipitation for each precipitation dataset, plotted against elevation from North to South. Shaded curves represent max., min. and mean values along each swath profile. The gridded data are for the years of common availability (2003 and 2004) while TRMM-2B31 [*Bookhagen and Burbank*, 2006] if for a 10 year time span (1997-2007). Gauging data is plotted as a mean value for both time spans. Error bars show the long term ($\sim$ 30 years) maxima and minima.

3. Monnsoon swath profiles

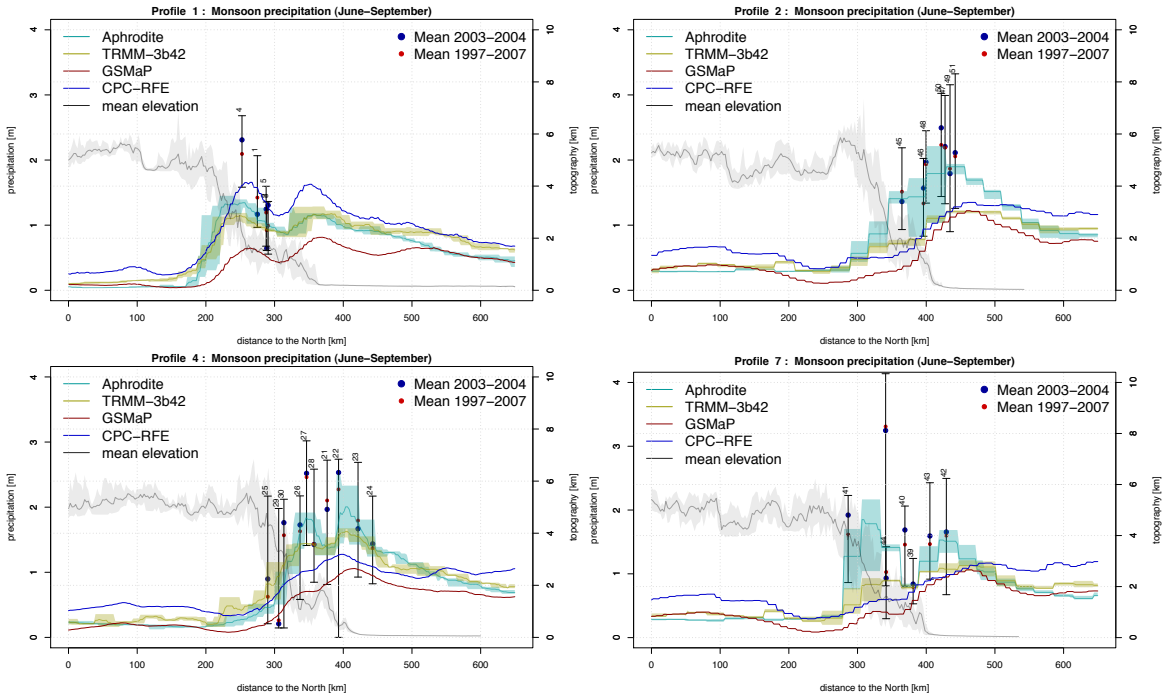

Figure 3: Precipitation swath profiles for monsoon season (June - September). Mean precipitation for each precipitation dataset, plotted against elevation from North to South. Shaded curves represent max., min. and mean values along each swath profile. The gridded data are for the years of common availability (2003 and 2004) while TRMM-2B31 [*Bookhagen and Burbank*, 2006] if for a 10 year time span (1997-2007). Gauging data is plotted as a mean value for both time spans. Error bars show the long term ($\sim$ 30 years) maxima and minima.

4. Swaths profiles out of monsoon season

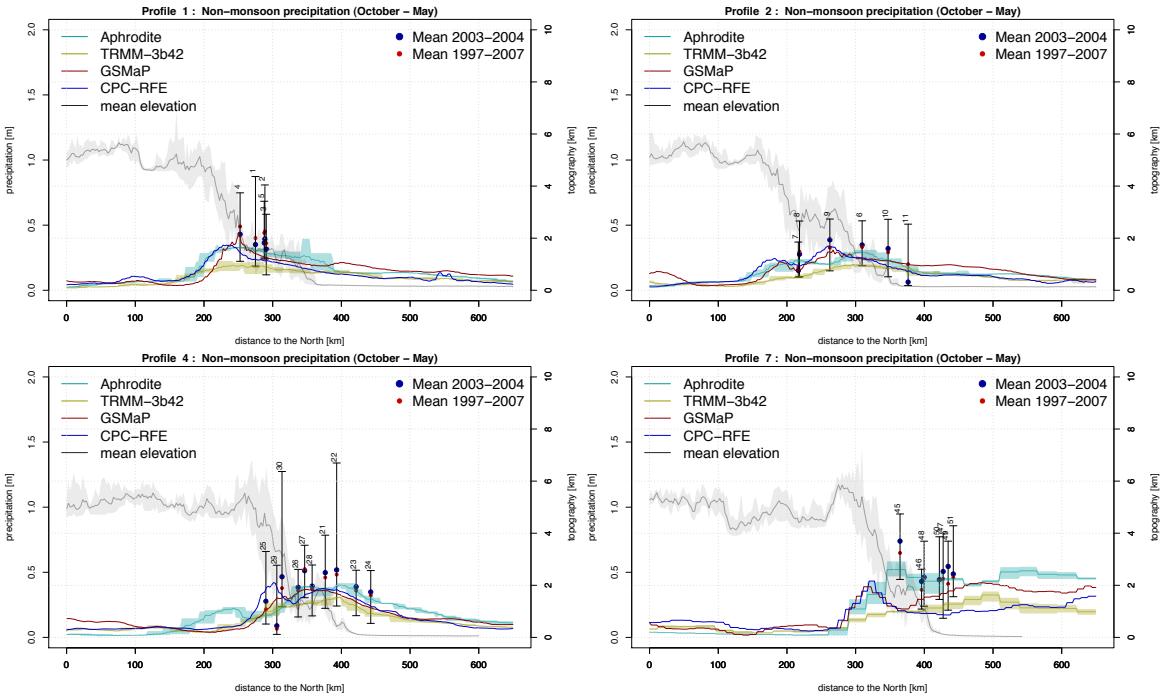

Figure 4: Precipitation swath profiles for out of monsoon season (October - May). Mean precipitation for each precipitation dataset, plotted against elevation from North to South. Shaded curves represent max., min. and mean values along each swath profile. The gridded data are for the years of common availability (2003 and 2004) while TRMM-2B31 [*Bookhagen and Burbank*, 2006] if for a 10 year time span (1997-2007). Gauging data is plotted as a mean value for both time spans. Error bars show the long term ($\sim$ 30 years) maxima and minima.

References

Bookhagen, B., and D. W. Burbank (2006), Topography, relief, and trmm-derived rainfall variations along the himalaya, *Geophys. Res. Lett.*, *33*, doi:10.1029/2006GL026037.

Appendix Chapter 4

nature geoscience

SUPPLEMENTARY INFORMATION

DOI: 10.1038/NGEO1356

Impact of transient groundwater storage on the discharge of Himalayan rivers

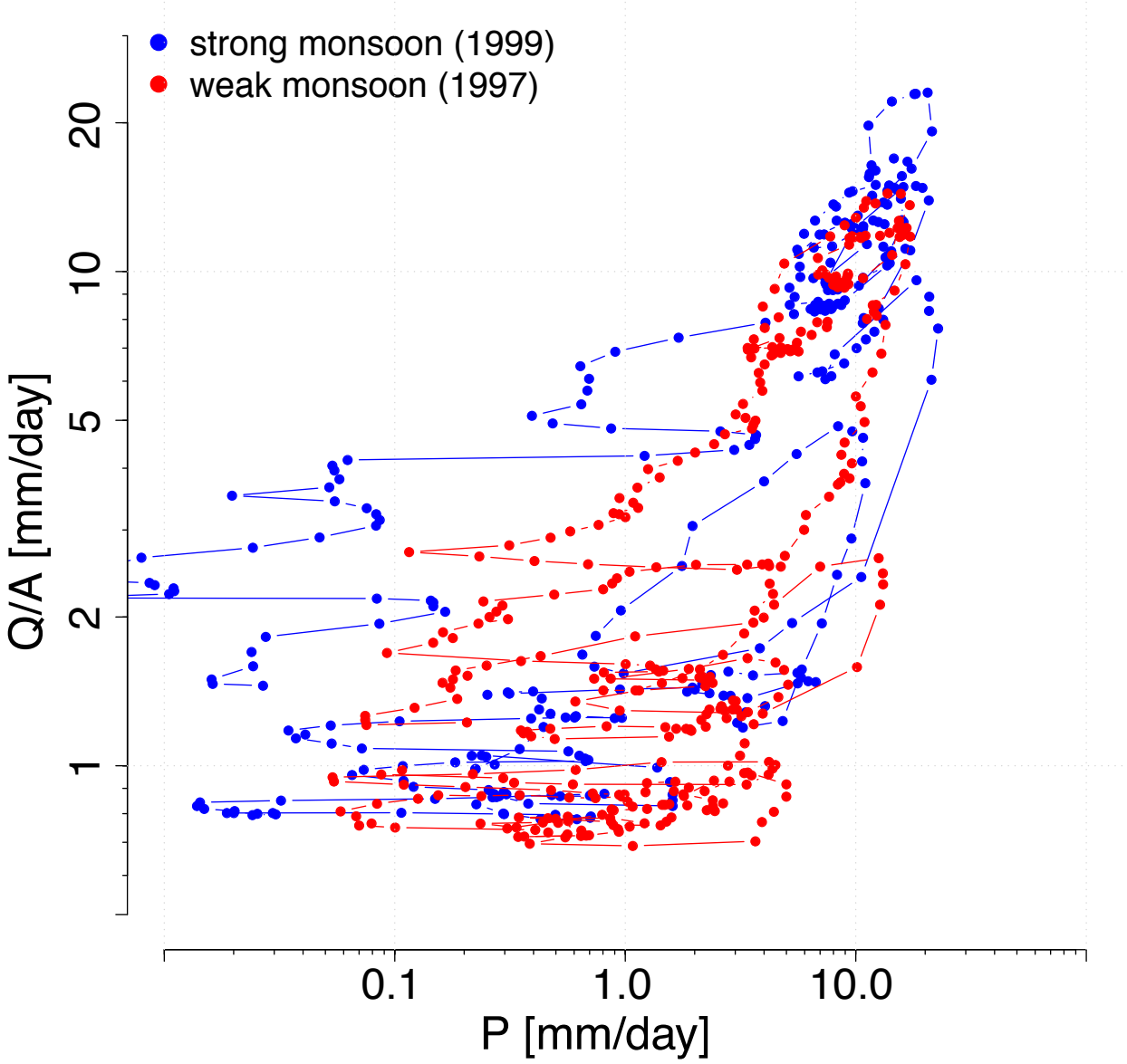

S1| Difference between strong and weak monsoon hysteresis loops. Precipitation-discharge hysteresis loop for the strong monsoon year 1999 and the weak monsoon year 1997[11] for the Narayani Basin. Data has been filtered with a 5-day moving average to avoid small-scale noise. The amplitude of the hysteresis loop is larger during strong monsoon years compared to weak ones. Q/A is the specific discharge, P is the mean basin precipitation.

DOI: 10.1038/NGEO1356

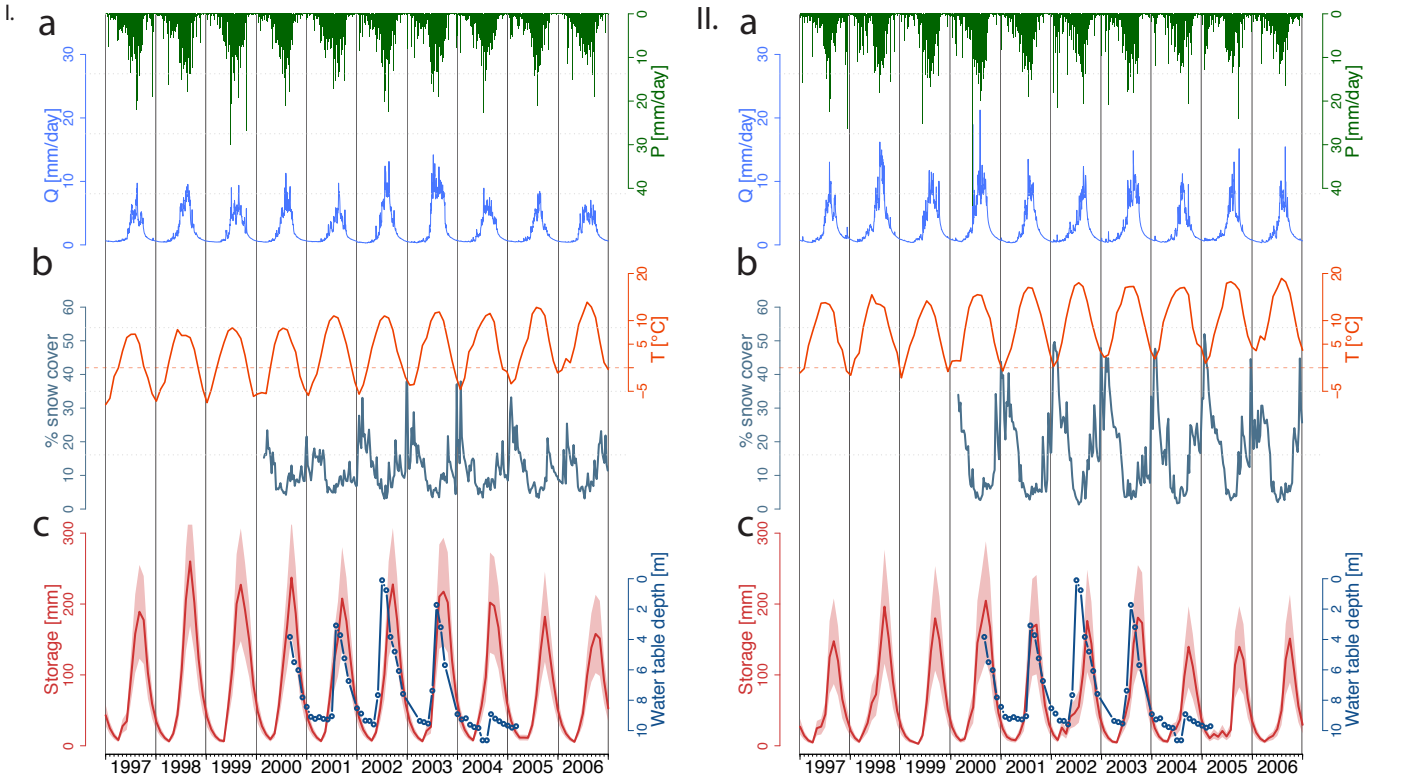

S2| 10-year (1997-2006) temporal variability of several hydrological discharge cycle compartments, Koshi Basin (I) and Karnali Basin (II), central Nepal. a, Daily precipitation (green), and daily specific river discharge (blue). b, Temperature (orange) as a glacier melt proxy (from CRU[26]) and percentage of basin-wide snow cover (dark green, data from MOD10C2 v.5[27] with an 8-day temporal resolution). c, Calculated groundwater storage evolution (red) derived from a modified version of the conceptual hydrological model GR2M[18] (see methods), shading illustrating model uncertainty, and ground water table variation (dark blue) observed in dug-wells in the Jhikhu Khola Basin[22] (station no. 1).

Uncertainty estimation:

A Monte-Carlo approach is carried out to quantify the impact of observation data uncertainties on modeled groundwater properties (storage capacity, response time, see Table 1). Multiplicative errors have been considered for rainfall and discharge. Rainfall might be systematically underestimated by 30%[10], and discharge biased by ±5%. Conversely, ET and temperature errors are taken as additive, based on differences between independent datasets. Model is then recalibrated, model structure error is therefore not considered in this uncertainty analysis. While groundwater storage capacity is highly sensitive to systematic bias in precipitation data, recession curves, and therefore time response, are rather well constrained (Table 1).

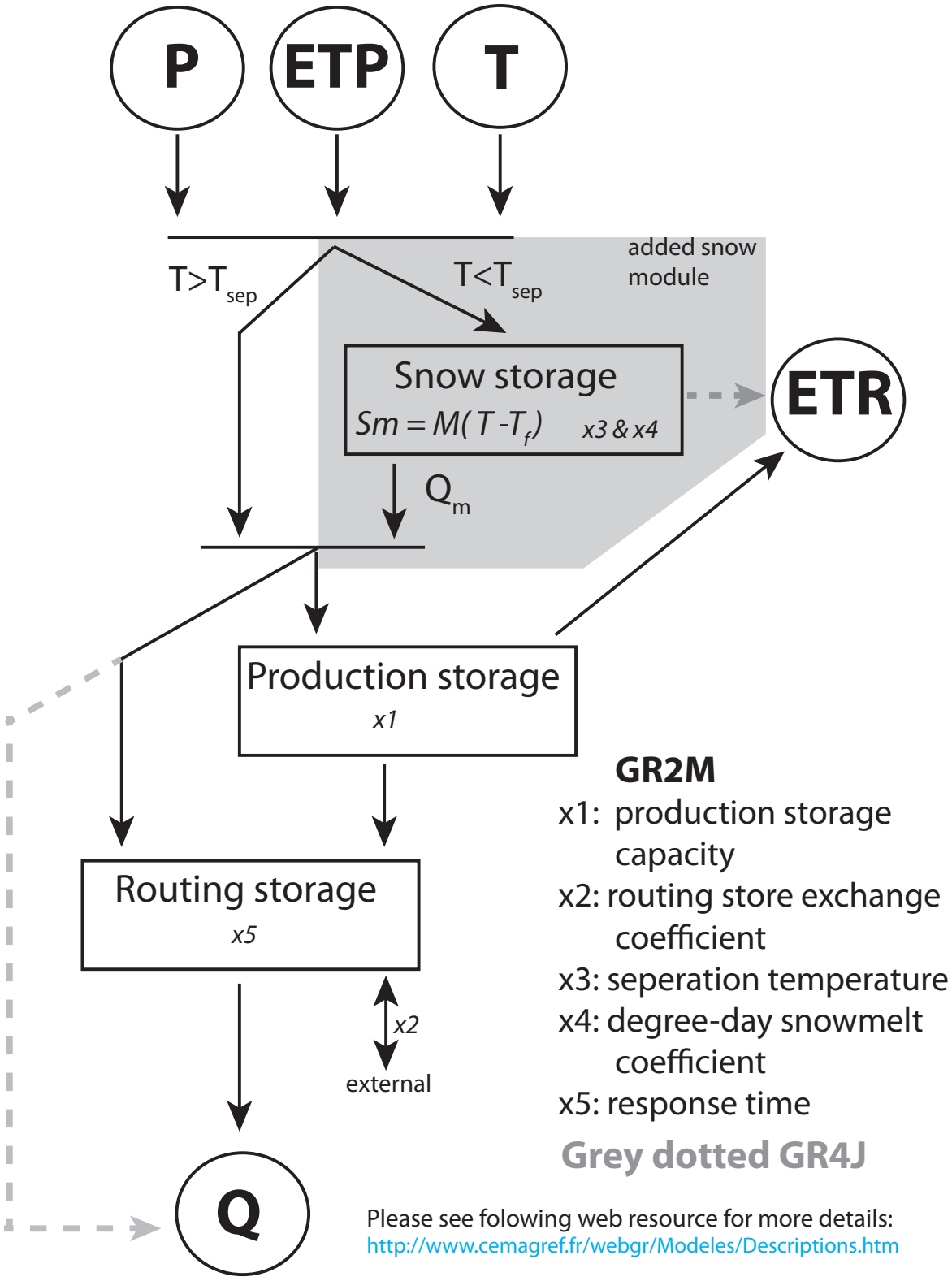

S3| Flowchart of the modified version of the conceptual hydrological model used in this study. Simplified schema of the conceptual models GR2M and GR4J[18], and the added snow module. Black lines applied for both models GR2M and GR4J whereas gray dotted lines applied only for model GR4J. Please refer to Mouelhi et al. 2006 (ref. 18), the method section and the following web resource http://www.cemagref.fr/webgr/Modelesgb/descriptionsgb.htm for more detailed information.

DOI: 10.1038/NGEO1356

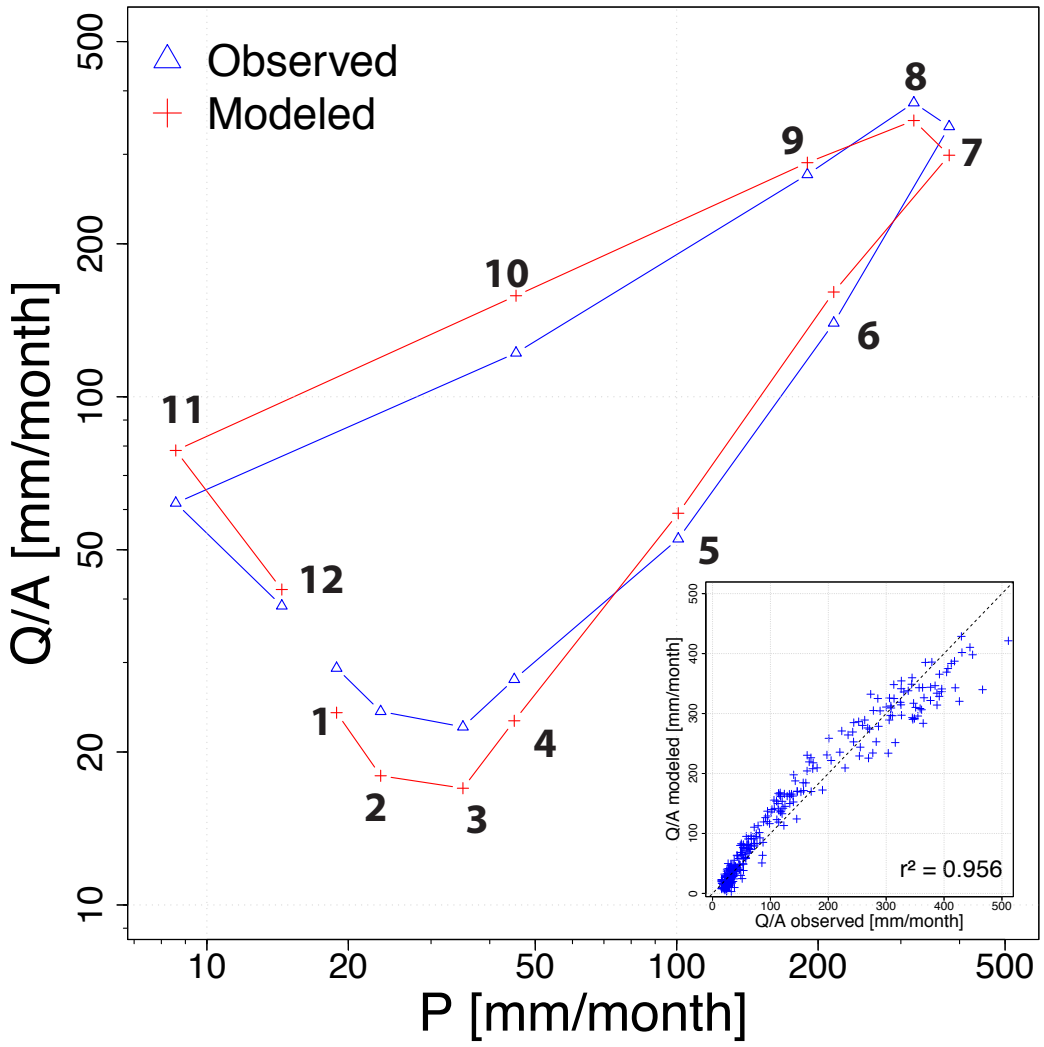

S4| Modeled vs. observed hysteresis loop for Narayani catchment (450). Data are plotted on a monthly scale. The inset shows the linear correlation between the observed and modeled discharge. Q/A is the specific discharge. P is the monthly basin-wide precipitation rate.

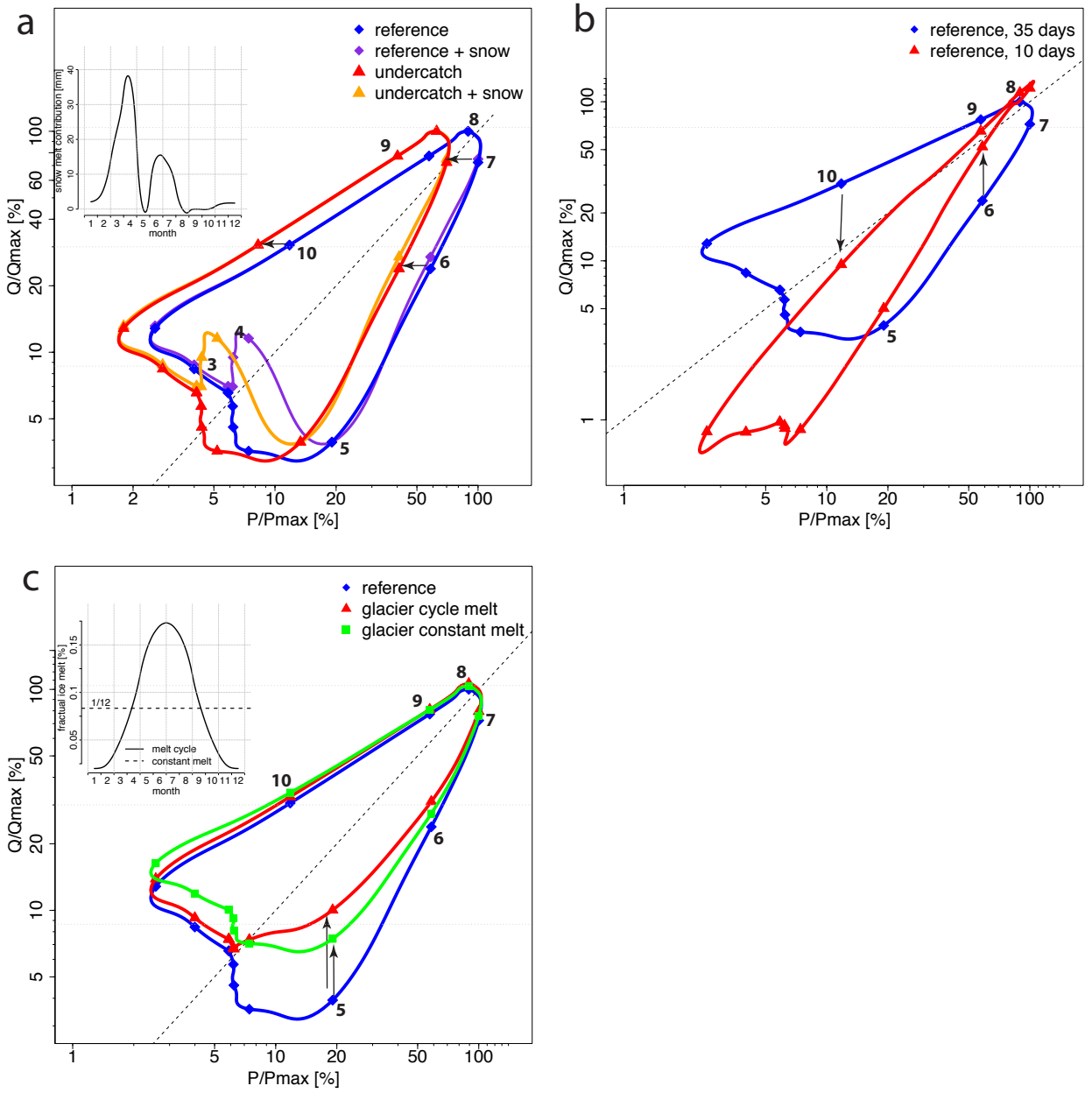

S 5| Influence of precipitation undercatch, snow melt, reservoir residence time and glacier melt on the shape of hysteresis loops. The months are indicated by numbers. In all the examples, the mean monthly precipitation-discharge values for Rapti River at station 360 are used as a reference (blue). a, Effect of a constant 30% undercatch of precipitation and impact of snowmelt contribution, considering an annual water equivalent of the snowmelt contribution after the GLDAS-NOAH model25 (inset). b, Impact of the basin-wide storage capacity on the hysteresis shape of the Rapti catchment, considering characteristic basin response times of 35 days and of only 10 days, corresponding to a 20-fold downsizing of the storage capacity (see Methods). c, Influence of a 100 mm yr-1 glacier melt contribution (or storage), considering a constant melt rate, equally distributed over the whole year or assuming a cyclic, temperature-driven ice melt contribution (both illustrated in the inset).

DOI: 10.1038/NGEO1356

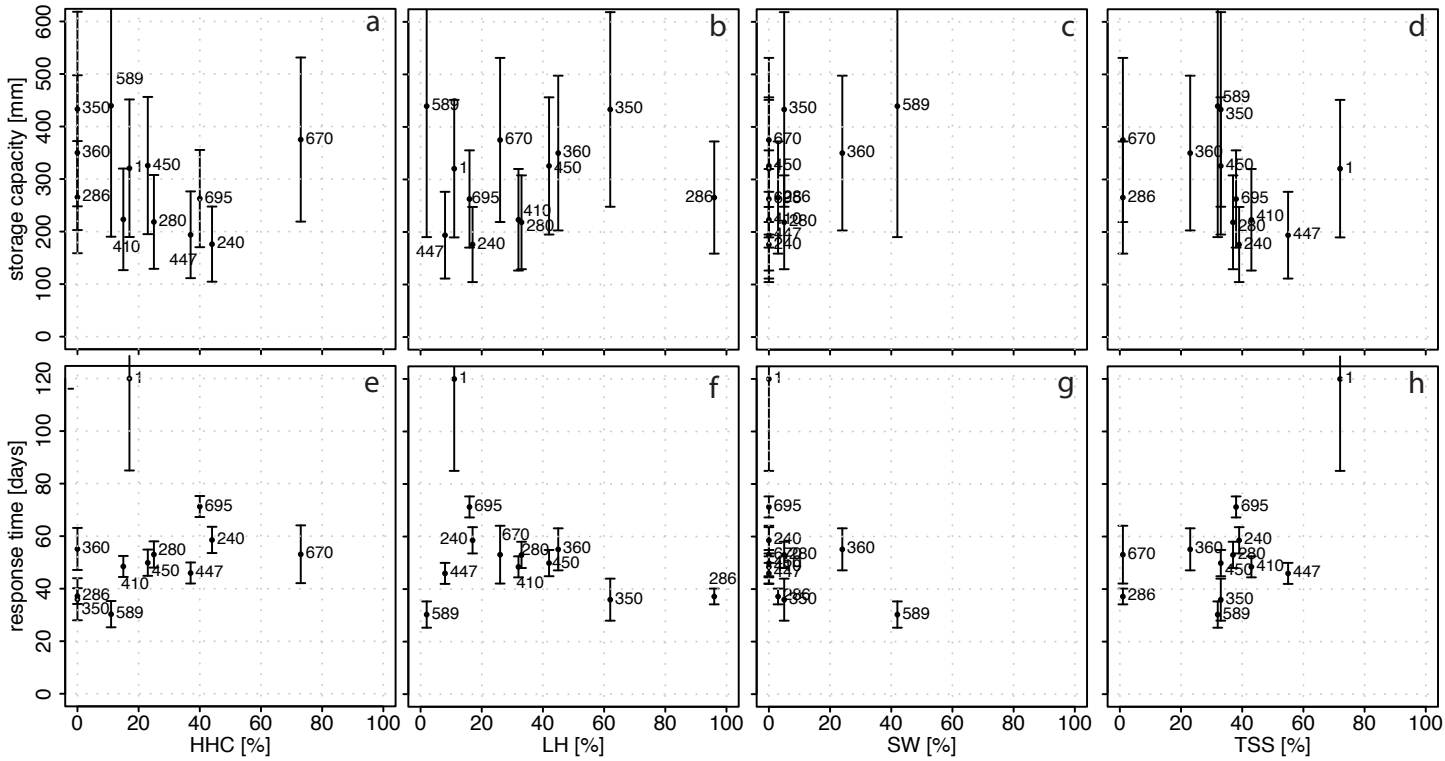

S6 | Comparison between groundwater storage properties and geological units within the studied drainage basins. Graphs illustrate storage properties (response time and storage capacity), plotted against geological unites.

Station No.	240	**280**	286	350	360	410	447	**450**	670	**695**	589	1
Basin	Karnali	**Karnali**	Saradha	Rapti	Rapti	Kali Gandaki	Trishuli	**Narayani**	Dudh Koshi	**Sapta Koshi**	Bagmati	Jhikhu Khola
ETR [mm yr^{-1}]*	304	**407**	576	630	607	359	258	**457**	643	**591**	703	617
Nash-Sutcliffe coef.	0.73	**0.78**	0.8	0.84	0.84	0.84	0.48	**0.21**	0.75	**0.61**	0.61	0.12
Storage capacity [km^3]	4.0 ±1.6	**8.9 ±3.7**	0.2 ± 0. 1	1.6 ±0.7	1.8 ±0.8	1.6±0.7	0.8±0.3	**9.9 ± 4**	1.0 ± 0.4	**9.9** ± 3.5	1.4 ± 0.7	0.02 ± 0.01
Storage capacity [mm]	200±75	200±80	240±90	425±180	340±140	220±90	190±80	310±120	250±100	170±60	490±90	210±90
Estimated surface time response [days]	0.41	0.68	0.73	0.70	0.45	0.27	0.37	0.71	0.24	0.43	0.27	0.70
Estimated soil moisture time response [days]	7	7.6	3.8	8.3	5.8	7.8	6.9	7.4	5.1	10	9.5	12
t_c GR4J [days]*	59 ± 13	47 ± 10	44±6	63±26	51±22	54±10	43±6	36±8	35±25	66±12	24±5	120±35
% snow-melt	12	**6**	n.a.	n.a.	n.a.	2	10	**2**	3	**2**	n.a.	n.a.
% discharge retarded	60	**65**	92	86	92	66	50	**68**	59	**60**	84	94

* see Methods

Appendix Chapter 6

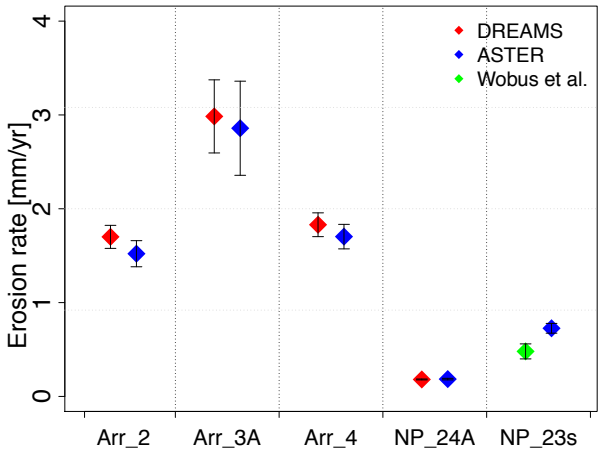

Figure 2: *Comparison of cosmogenic nuclide erosion rates measured at different AMS (Accelerated Mass Spectroscopy) facilities. Compared are identical samples measured ones at the DREAMS (DREsden AMS) facility, Dresden/Rossendorf, Germany, and ones at the ASTER (Accelerateur pour les Sciences de la Terre, Environnement, Risques) facility, Aix-en-Prenvence, France. A fourth sample was compared to the measurement of Wobus et al. [2005]. The two later ones are not the same samples but were sampled at the same location with several years time difference. Our sample NP-23s was collected in November 2009. The sample of Wobus et al. [2005] was collected in 2001 (sample ID 01WBS7).*

Bibliography

Aalto, R., T. Dunne, and J. L. Guyot (2006), Geomorphic Controls on Andean Denudation Rates, *The Journal of Geology*, *114*(1), 85–99, doi:10.1086/498101.

Ahnert, F. (1970), Functional relationships between denudation, relief, and uplift in large, mid-latitude drainage basins, *American Journal of Science*, *268*(3), 243–263, doi:10.2475/ajs.268.3.243.

Alford, D., and R. Armstrong (2010), The role of glaciers in stream flow from the Nepal Himalaya, *The Cryosphere Discussions*, *4*(2), 469–494, doi:10.5194/tcd-4-469-2010.

Andermann, C., S. Bonnet, and R. Gloaguen (2011), Evaluation of precipitation data sets along the Himalayan front, *Geochem. Geophys. Geosyst.*, *in press*, doi:10.1029/2011GC003513.

Anders, A., G. Roe, B. Hallet, D. Montgomery, N. Finnegan, and J. Putkonen (2006a), Spatial patterns of precipitation and topography in the Himalaya, *Geological Society of America Special Paper*, *398*(03), 39–53, doi:10.1130/2006.2398(03).

Anders, A. M., G. H. Roe, D. R. Montgomery, and N. J. Finnegan (2006b), Spatial patterns of precipitation and topography in the Himalaya, *Geological Society of America Special Paper*, *398*, 39–53, doi:10.1130/2006.2398(03).

Arnold, M., S. Merchel, D. L. Bourlès, R. Braucher, L. Benedetti, R. C. Finkel, G. Aumaître, A. Gottdang, and M. Klein (2010), The French accelerator mass spectrometry facility ASTER: Improved performance and developments, *Nuclear Instruments and Methods in Physics Research Section B: Beam Interactions with Materials and Atoms*, *268*(11-12), 1954–1959, doi:10.1016/j.nimb.2010.02.107.

Barros, A., S. Chiao, T. Lang, D. Burbank, and J. Putkonen (2006), From weather to climate-Seasonal and interannual variability of storms and implications for erosion processes in the Himalaya, *Geological Sociaety of America Special Papers*, *2398*(02), 17–38, doi:10.1130/2006.2398(02).

Barros, A. P., and T. J. Lang (2003), Monitoring the Monsoon in the Himalayas: Observations in Central Nepal, June 2001, *Monthly Weather Review*, *131*(7), 1408–1427, doi:10.1175/1520-0493(2003)131¡1408:MTMITH¿2.0.CO;2.

Barros, A. P., G. Kim, E. Williams, and S. W. Nesbitt (2004), Probing orographic controls in the Himalayas during the monsoon using satellite imagery, *Natural Hazards and Earth System Science*, *4*(1), 29–51, doi:10.5194/nhess-4-29-2004.

Beaumont, C., R. Jamieson, M. Nguyen, and B. Lee (2001), Himalayan tectonics explained by extrusion of a low-viscosity crustal channel coupled to focused surface denudation, *Nature*, *414*(6865), 738–742.

Benda, L., and T. Dunne (1997), Stochastic forcing of sediment supply to channel networks from landsliding and debris flow, *Water Resources Research*, *33*(12), 2849, doi:10.1029/97WR02388.

Bettinelli, P., J.-P. Avouac, M. Flouzat, F. Jouanne, L. Bollinger, P. Willis, and G. R. Chitrakar (2006), Plate Motion of India and Interseismic Strain in the Nepal Himalaya from GPS and DORIS Measurements, *Journal of Geodesy*, *80*(8-11), 567–589, doi:10.1007/s00190-006-0030-3.

Bettinelli, P., J. Avouac, M. Flouzat, L. Bollinger, G. Ramillien, S. Rajaure, and S. Sapkota (2008), Seasonal variations of seismicity and geodetic strain in the Himalaya induced by surface hydrology, *Earth and Planetary Science Letters*, *266*(3-4), 332–344, doi:10.1016/j.epsl.2007.11.021.

Bhatt, B. C., and K. Nakamura (2005), Characteristics of Monsoon Rainfall around the Himalayas Revealed by TRMM Precipitation Radar, *Monthly Weather Review*, *133*(1), 149–165, doi:10.1175/MWR-2846.1.

Bhutiyani, M. (2000), Sediment load characteristics of a proglacial stream of Siachen Glacier and the erosion rate in Nubra valley in the Karakoram Himalayas, India, *Journal of Hydrology*, *227*(1-4), 84–92, doi:10.1016/S0022-1694(99)00174-2.

Bierman, P., and E. J. Steig (1996), Estimating Rates of Denudation Using Cosmogenic Isotope Abundances in Sediment, *Earth Surface Processes and Landforms*, *21*(2), 125–139, doi:10.1002/(SICI)1096-9837(199602)21:2¡125::AID-ESP511¿3.0.CO;2-8.

Bilham, R., K. Larson, J. Freymueller, and P. I. Members (1997), GPS measurements of present-day convergence across the Nepal Himalaya, *Nature*, *386*(6), 61–63.

Binnie, S., W. Phillips, M. Summerfield, and L. Keith Fifield (2006), Sediment mixing and basin-wide cosmogenic nuclide analysis in rapidly eroding mountainous environments, *Quaternary Geochronology*, *1*(1), 4–14, doi:10.1016/j.quageo.2006.06.013.

Binnie, S. a., W. M. Phillips, M. a. Summerfield, and L. K. Fifield (2007), Tectonic uplift, threshold hillslopes, and denudation rates in a developing mountain range, *Geology*, *35*(8), 743, doi:10.1130/G23641A.1.

Bird, P. (1991), Lateral Extrusion of Lower Crust From Under High Topography in the Isostatic Limit, *Journal of Geophysical Research*, *96*(B6), 10,275–10,286, doi:10.1029/91JB00370.

Blanckenburg, F. V., P. W. Kubik, F. von Blanckenburg, and T. Hewawasam (2004), Cosmogenic nuclide evidence for low weathering and denudation in the wet, tropical highlands of Sri Lanka, *Journal of Geophysical Research*, *109*(F3), doi:10.1029/2003JF000049.

Blythe, A. E., D. W. Burbank, A. Carter, K. Schmidt, and J. Putkonen (2007), Plio-Quaternary exhumation history of the central Nepalese Himalaya: 1. Apatite and zircon fission track and apatite [U-Th]/He analyses, *Tectonics*, *26*(3), 1–16, doi:10.1029/2006TC001990.

Bollinger, L. (2004), Thermal structure and exhumation history of the Lesser Himalaya in central Nepal, *Tectonics*, *23*(5), doi:10.1029/2003TC001564.

Bollinger, L., P. Henry, and J. Avouac (2006), Mountain building in the Nepal Himalaya: Thermal and kinematic model, *Earth and Planetary Science Letters*, *244*(1-2), 58–71, doi:10.1016/j.epsl.2006.01.045.

Bollinger, L., F. Perrier, J.-P. Avouac, S. Sapkota, U. Gautam, and D. R. Tiwari (2007), Seasonal modulation of seismicity in the Himalaya of Nepal, *Geophysical Research Letters*, *34*(8), 1–5, doi:10.1029/2006GL029192.

Bonnet, S., and A. Crave (2003), Landscape response to climate change: Insights from experimental modeling and implications for tectonic versus climatic uplift of topography, *Geology*, *31*(2), 123, doi:10.1130/0091-7613(2003)031¡0123:LRTCCI¿2.0.CO;2.

Bookhagen, B., and D. W. Burbank (2006), Topography, relief, and TRMM-derived rainfall variations along the Himalaya, *Geophysical Research Letters*, *33*(8), 1–5, doi:10.1029/2006GL026037.

Bookhagen, B., and D. W. Burbank (2010), Toward a complete Himalayan hydrological budget: Spatiotemporal distribution of snowmelt and rainfall and their impact on river discharge, *Journal of Geophysical Research*, *115*(F3), 1–25, doi:10.1029/2009JF001426.

Bookhagen, B., R. Thiede, and M. Strecker (2005a), Abnormal monsoon years and their control on erosion and sediment flux in the high, arid northwest Himalaya, *Earth and Planetary Science Letters*, *231*(1-2), 131–146, doi:10.1016/j.epsl.2004.11.014.

Bookhagen, B., R. C. Thiede, and M. R. Strecker (2005b), Late Quaternary intensified monsoon phases control landscape evolution in the northwest Himalaya, *Geology*, *33*(2), 149, doi:10.1130/G20982.1.

Boos, W. R., and Z. Kuang (2010), Dominant control of the South Asian monsoon by orographic insulation versus plateau heating., *Nature*, *463*(7278), 218–22, doi:10.1038/nature08707.

Brandon, M. T., M. K. Roden-Tice, and J. I. Garver (1998), Late Cenozoic exhumation of the Cascadia accretionary wedge in the Olympic Mountains, northwest Washington State, *Geological Society of America Bulletin*, *110*(8), 985–1009, doi:10.1130/0016-7606(1998)110¡0985:LCEOTC¿2.3.CO;2.

Braucher, R., E. Brown, D. Bourlès, and F. Colin (2003), In situ produced 10Be measurements at great depths: implications for production rates by fast muons, *Earth and Planetary Science Letters*, *211*(3-4), 251–258, doi:10.1016/S0012-821X(03)00205-X.

Braucher, R., S. Merchel, J. Borgomano, and D. Bourlès (2011), Production of cosmogenic radionuclides at great depth: A multi element approach, *Earth and Planetary Science Letters*, *309*(1-2), 1–9, doi:10.1016/j.epsl.2011.06.036.

Brown, E. T., J. M. Edmond, G. M. Raisbeck, and F. Yiou (1991), Examination of surface exposure ages of Antarctic moraines using in situ produced 10Be and 26Al, *Geochimica et Cosmochimica Acta*, *55*, 2269–2283.

Burbank, D. W., a. E. Blythe, J. Putkonen, B. Pratt-Sitaula, E. Gabet, M. Oskin, A. Barros, and T. P. Ojha (2003), Decoupling of erosion and precipitation in the Himalayas., *Nature*, *426*(6967), 652–5, doi:10.1038/nature02187.

Burtin, A., L. Bollinger, R. Cattin, J. Vergne, and J. L. Nábělek (2009), Spatiotemporal sequence of Himalayan debris flow from analysis of high-frequency seismic noise, *Journal of Geophysical Research*, *114*(F4), 1–15, doi:10.1029/2008JF001198.

Clift, P. D., K. V. Hodges, D. Heslop, R. Hannigan, H. Van Long, and G. Calves (2008a), Correlation of Himalayan exhumation rates and Asian monsoon intensity, *Nature Geoscience*, *1*(12), 875–880, doi:10.1038/ngeo351.

Clift, P. D., et al. (2008b), Holocene erosion of the Lesser Himalaya triggered by intensified summer monsoon, *Geology*, *36*(1), 79, doi:10.1130/G24315A.1.

Dadson, S. J., et al. (2003), Links between erosion, runoff variability and seismicity in the Taiwan orogen., *Nature*, *426*(6967), 648–51, doi:10.1038/nature02150.

Dahal, R., and S. Hasegawa (2008), Representative rainfall thresholds for landslides in the Nepal Himalaya, *Geomorphology*, *100*(3-4), 429–443, doi:10.1016/j.geomorph.2008.01.014.

Davy, P., R. Le Goc, C. Darcel, O. Bour, J. R. de Dreuzy, and R. Munier (2010), A likely universal model of fracture scaling and its consequence for crustal hydromechanics, *Journal of Geophysical Research*, *115*(B10), 1–13, doi:10.1029/2009JB007043.

Deeken, A., R. Thiede, E. Sobel, J. Hourigan, and M. Strecker (2011), Exhumational variability within the Himalaya of northwest India, *Earth and Planetary Science Letters*, *305*(1-2), 103–114, doi:10.1016/j.epsl.2011.02.045.

Department of Mines and Geology Nepal (1994), Geological Map of Nepal, p. 1:1.000.000.

Derry, L. A., and C. France-Lanord (1996), Neogene growth of the sedimentary organic carbon reservoir, *Paleoceanography*, *11*(3), 267, doi:10.1029/95PA03839.

Dunai, T. (2010), *Cosmogenic Nuclides - Principles, Concepts and Applications in the Earth Surface Sciences*, Cambridge University Press, UK.

Dunne, J. (1999), Scaling factors for the rates of production of cosmogenic nuclides for geometric shielding and attenuation at depth on sloped surfaces, *Geomorphology*, *27*(1-2), 3–11, doi:10.1016/S0169-555X(98)00086-5.

Dupont-Nivet, G., P. C. Lippert, D. J. Van Hinsbergen, M. J. Meijers, and P. Kapp (2010), Palaeolatitude and age of the Indo-Asia collision: palaeomagnetic constraints, *Geophysical Journal International*, *182*(3), 1189–1198, doi:10.1111/j.1365-246X.2010.04697.x.

Ehlers, T. A., and K. A. Farley (2003), Apatite (UâTh)/He thermochronometry: methods and applications to problems in tectonic and surface processes, *Earth and Planetary Science Letters*, *206*(1-2), 1–14, doi:10.1016/S0012-821X(02)01069-5.

Farley, K. A. (2002), (U-Th)/He Dating: Techniques, Calibrations, and Applications, *Reviews in Mineralogy and Geochemistry*, *47*(1), 819–844, doi:10.2138/rmg.2002.47.18.

Finlayson, D. P., D. R. Montgomery, and B. Hallet (2002), Spatial coincidence of rapid inferred erosion with young metamorphic massifs in the Himalayas, *Geology*, *30*(3), 219, doi:10.1130/0091-7613(2002)030¡0219:SCORIE¿2.0.CO;2.

Finnegan, N. J., B. Hallet, D. R. Montgomery, P. K. Zeitler, J. O. Stone, a. M. Anders, and L. Yuping (2008), Coupling of rock uplift and river incision in the Namche Barwa-Gyala Peri massif, Tibet, *Geological Society of America Bulletin*, *120*(1-2), 142–155, doi:10.1130/B26224.1.

France-lanord, C., and L. L. A. Derry (1997), Organic carbon burial forcing of the carbon cycle from Himalayan erosion, *Nature*, *390*(6655), 65–66, doi:10.1038/36324.

Fuller, C. W., S. D. Willett, N. Hovius, and R. Slingerland (2003), Erosion Rates for Taiwan Mountain Basins: New Determinations from Suspended Sediment Records and a Stochastic Model of Their Temporal Variation, *The Journal of Geology*, *111*(1), 71–87, doi:10.1086/344665.

Gabet, E., D. Burbank, B. Prattsitaula, J. Putkonen, and B. Bookhagen (2008), Modern erosion rates in the High Himalayas of Nepal, *Earth and Planetary Science Letters*, *267*(3-4), 482–494, doi:10.1016/j.epsl.2007.11.059.

Gabet, E. J., B. a. Pratt-Sitaula, and D. W. Burbank (2004), Climatic controls on hillslope angle and relief in the Himalayas, *Geology*, *32*(7), 629, doi:10.1130/G20641.1.

Gabet, E. J., D. Wolff-Boenisch, H. Langner, D. W. Burbank, and J. Putkonen (2010), Geomorphic and climatic controls on chemical weathering in the High Himalayas of Nepal, *Geomorphology*, *122*(1-2), 205–210, doi:10.1016/j.geomorph.2010.06.016.

Gadgil, S., P. N. Vinayachandran, P. A. Francis, and S. Gadgil (2004), Extremes of the Indian summer monsoon rainfall, ENSO and equatorial Indian Ocean oscillation, *Geophysical Research Letters*, *31*(12), 2–5, doi:10.1029/2004GL019733.

Galy, A., and C. France-Lanord (2001), Higher erosion rates in the Himalaya: Geochemical constraints on riverine fluxes, *Geology*, *29*(1), 23, doi:10.1130/0091-7613(2001)029¡0023:HERITH¿2.0.CO;2.

Galy, V., C. France-Lanord, O. Beyssac, P. Faure, H. Kudrass, and F. Palhol (2007), Efficient organic carbon burial in the Bengal fan sustained by the Himalayan erosional system., *Nature*, *450*(7168), 407–10, doi:10.1038/nature06273.

Garzanti, E., G. Vezzoli, S. Ando, J. Lave, M. Attal, C. Francelanord, and P. Decelles (2007), Quantifying sand provenance and erosion (Marsyandi River, Nepal Himalaya), *Earth and Planetary Science Letters*, *258*(3-4), 500–515, doi:10.1016/j.epsl.2007.04.010.

Gosse, J. C., and F. M. Phillips (2001), Terrestrial in situ cosmogenic nuclides: theory and application, *Quaternary Science Reviews*, *20*(14), 1475–1560, doi:10.1016/S0277-3791(00)00171-2.

Granger, D., J. Kirchner, and R. Finkel (1996), Spatially averaged long-term erosion rates measured from in situ-produced cosmogenic nuclides in alluvial sediment, *The Journal of Geology*.

GRASS Development Team (2010), *Geographic Resources Analysis Support System (GRASS GIS) Software*, Open Source Geospatial Foundation, USA.

Gruber, A., V. Levizzani, and L. Authors (2008), Assessment of global precipitation products, *WCRP Series Report No. 128 and WMO TD-No. 1430, (available from http://cics.umd.edu/$yin/GPCP//main.html)*.

Grujic, D., I. Coutand, B. Bookhagen, S. Bonnet, A. Blythe, and C. Duncan (2006), Climatic forcing of erosion, landscape, and tectonics in the Bhutan Himalayas, *Geology*, *34*(10), 801, doi: 10.1130/G22648.1.

Hannah, D., S. Kansakar, A. Gerrard, and G. Rees (2005), Flow regimes of Himalayan rivers of Nepal: nature and spatial patterns, *Journal of Hydrology*, *308*(1-4), 18–32, doi:10.1016/j.jhydrol.2004.10.018.

Harrison, T. M. (2006), Did the Himalayan Crystallines extrude partially molten from beneath the Tibetan Plateau?, *Geological Society, London, Special Publications*, *268*(1), 237–254, doi: 10.1144/GSL.SP.2006.268.01.11.

Hasnain, S., and R. Thayyen (1999), Discharge and suspended-sediment concentration of meltwaters, draining from the Dokriani glacier, Garhwal Himalaya, India, *Journal of Hydrology*, *218*(3-4), 191–198, doi:10.1016/S0022-1694(99)00033-5.

Hays, J. D., J. Imbrie, and N. J. Shackleton (1976), Variations in the Earth's Orbit: Pacemaker of the Ice Ages., *Science (New York, N.Y.)*, *194*(4270), 1121–32, doi:10.1126/science.194.4270.1121.

Heimsath, A. M., and R. McGlynn (2008), Quantifying periglacial erosion in the Nepal high Himalaya, *Geomorphology*, *97*(1-2), 5–23, doi:10.1016/j.geomorph.2007.02.046.

Henderson, R., and S. Thompson (1999), Extreme rainfalls in the Southern Alps of New Zealand, *Journal of Hydrology (NZ)*.

Hodges, K. V., C. Wobus, K. Ruhl, T. Schildgen, and K. Whipple (2004), Quaternary deformation, river steepening, and heavy precipitation at the front of the Higher Himalayan ranges, *Earth and Planetary Science Letters*, *220*(3-4), 379–389, doi:10.1016/S0012-821X(04)00063-9.

Hong, Y., R. Adler, and G. Huffman (2006), Evaluation of the potential of NASA multi-satellite precipitation analysis in global landslide hazard assessment, *Geophysical Research Letters*, *33*(22), 1–5, doi:10.1029/2006GL028010.

Hovius, N., C. P. Stark, and P. a. Allen (1997), Sediment flux from a mountain belt derived by landslide mapping, *Geology*, *25*(3), 231, doi:10.1130/0091-7613(1997)025¡0231:SFFAMB¿2.3.CO;2.

Hovius, N., C. Stark, C. Hao-Tsu, and L. Jiun-Chuan (2000), Supply and Removal of Sediment in a Landslide-Dominated Mountain Belt: Central Range, Taiwan., *The Journal of geology*, *108*(1), 73–89.

Hovius, N., P. Meunier, C.-W. Lin, H. Chen, Y.-G. Chen, S. Dadson, M.-J. Horng, and M. Lines (2011), Prolonged seismically induced erosion and the mass balance of a large earthquake, *Earth and Planetary Science Letters*, *304*(3-4), 347–355, doi:10.1016/j.epsl.2011.02.005.

Huntington, K. W., A. E. Blythe, and K. V. Hodges (2006), Climate change and Late Pliocene acceleration of erosion in the Himalaya, *Earth and Planetary Science Letters*, *252*(1-2), 107–118, doi: 10.1016/j.epsl.2006.09.031.

Hurtrez, J.-E., F. Lucazeau, J. Lavé, and J.-P. Avouac (1999), Investigation of the relationships between basin morphology, tectonic uplift, and denudation from the study of an active fold belt in the Siwalik Hills, central Nepal, *Journal of Geophysical Research*, *104*(B6), 12,779–12,796, doi:10.1029/1998JB900098.

Iaffaldano, G., L. Husson, and H.-P. Bunge (2011), Monsoon speeds up Indian plate motion, *Earth and Planetary Science Letters*, *304*(3-4), 503–510, doi:10.1016/j.epsl.2011.02.026.

Immerzeel, W., P. Droogers, S. Dejong, and M. Bierkens (2009), Large-scale monitoring of snow cover and runoff simulation in Himalayan river basins using remote sensing, *Remote Sensing of Environment*, *113*(1), 40–49, doi:10.1016/j.rse.2008.08.010.

Immerzeel, W. W., L. P. H. van Beek, and M. F. P. Bierkens (2010), Climate change will affect the Asian water towers., *Science (New York, N.Y.)*, *328*(5984), 1382–5, doi:10.1126/science.1183188.

Iverson, R. (2000), Landslide triggering by rain infiltration, *Water Resources Research*, *36*(7), 1897–1910.

Ivy-Ochs, S., and M. Schaller (2009), Examining processes and rates of landscape change with cosmogenic radionuclides, *Radioactivity in the Environment*, *16*(09), 231–294, doi:10.1016/S1569-4860(09)01606-4.

Jolivet, M., S. Dominguez, J. Charreau, Y. Chen, Y. Li, and Q. Wang (2010), Mesozoic and Cenozoic tectonic history of the central Chinese Tian Shan: Reactivated tectonic structures and active deformation, *Tectonics*, *29*(6), 1–30, doi:10.1029/2010TC002712.

Kamal-Heikman, S., L. a. Derry, J. R. Stedinger, and C. C. Duncan (2007), A Simple Predictive Tool for Lower Brahmaputra River Basin Monsoon Flooding, *Earth Interactions*, *11*(21), 1–11, doi:10.1175/EI226.1.

Kettner, A. J., and J. P. Syvitski (2008), HydroTrend v.3.0: A climate-driven hydrological transport model that simulates discharge and sediment load leaving a river system, *Computers & Geosciences*, *34*(10), 1170–1183, doi:10.1016/j.cageo.2008.02.008.

Kirby, E., and K. Whipple (2001), Quantifying differential rock-uplift rates via stream profile analysis, *Geology*, *29*(5), 415, doi:10.1130/0091-7613(2001)029¡0415:QDRURV¿2.0.CO;2.

Kirchner, J. W., R. C. Finkel, C. S. Riebe, D. E. Granger, J. L. Clayton, J. G. King, and W. F. Megahan (2001), Mountain erosion over 10 yr, 10 k.y., and 10 m.y. time scales, *Geology*, *29*(7), 591, doi:10.1130/0091-7613(2001)029¡0591:MEOYKY¿2.0.CO;2.

Kirschbaum, D. B., R. Adler, Y. Hong, and A. Lerner-Lam (2009a), Evaluation of a preliminary satellite-based landslide hazard algorithm using global landslide inventories, *Natural Hazards and Earth System Science*, *9*(3), 673–686, doi:10.5194/nhess-9-673-2009.

Kirschbaum, D. B., R. Adler, Y. Hong, S. Hill, and A. Lerner-Lam (2009b), A global landslide catalog for hazard applications: method, results, and limitations, *Natural Hazards*, *52*(3), 561–575, doi:10.1007/s11069-009-9401-4.

Koons, P. O. (1990), The two-sided orogen: Collision and erosion from the sand box to the Southern Alps,, *Geology*, *18*(8), 679, doi:10.1130/0091-7613(1990)018¡0679:TSOCAE¿2.3.CO;2.

Koppen, W. (1936), *Das geographisca System der Klimate, in: Handbuch der Klimatologie*, 1–44 pp., Gebr, Borntraeger.

Lague, D., and P. Davy (2003), Constraints on the long-term colluvial erosion law by analyzing slope-area relationships at various tectonic uplift rates in the Siwaliks Hills (Nepal), *Journal of Geophysical Research*, *108*(B2), doi:10.1029/2002JB001893.

Lal, D. (1991), Cosmic ray labeling of erosion surfaces: in situ nuclide production rates and erosion models, *Earth and Planetary Science Letters*, *104*(2-4), 424–439, doi:10.1016/0012-821X(91)90220-C.

Lal, D., N. B. Harris, K. K. Sharma, Z. Gu, L. Ding, T. Liu, W. Dong, M. W. Caffee, and a.J.T Jull (2004), Erosion history of the Tibetan Plateau since the last interglacial: constraints from the first studies of cosmogenic 10Be from Tibetan bedrock, *Earth and Planetary Science Letters*, *217*(1-2), 33–42, doi:10.1016/S0012-821X(03)00600-9.

Lang, T. J., and A. P. Barros (2004), Winter Storms in the Central Himalayas, *Journal of the Meteorological Society of Japan*, *82*(3), 829–844, doi:10.2151/jmsj.2004.829.

Lavé, J., and J. Avouac (2001), Fluvial incision and tectonic uplift across the Himalayas of central Nepal, *Journal of Geophysical Research*, *106*(B11), 26,561–26, doi:10.1029/2001JB000359.

Lavé, J., and J. P. Avouac (2000), Active folding of fluvial terraces across the Siwaliks Hills, Himalayas of central Nepal, *Journal of Geophysical Research*, *105*(B3), 5735–5770, doi:10.1029/1999JB900292.

Lin, G.-W., H. Chen, N. Hovius, M.-J. Horng, S. Dadson, P. Meunier, and M. Lines (2008), Effects of earthquake and cyclone sequencing on landsliding and fluvial sediment transfer in a mountain catchment, *Earth Surface Processes and Landforms*, *33*(9), 1354–1373, doi:10.1002/esp.1716.

Mancktelow, N. (1997), Time-dependent effects of heat advection and topography on cooling histories during erosion, *Tectonophysics*, *270*(3-4), 167–195, doi:10.1016/S0040-1951(96)00279-X.

Merchel, S., and U. Herpers (1999), An update on radiochemical separation techniques for the determination of long-lived radionuclides via accelerator mass spectrometry, *Radiochimica acta*, *84*(4), 215–219.

Merchel, S., et al. (2008), Towards more precise 10Be and 36Cl data from measurements at the 10â14 level: Influence of sample preparation, *Nuclear Instruments and Methods in Physics Research Section B: Beam Interactions with Materials and Atoms*, *266*(22), 4921–4926, doi:10.1016/j.nimb.2008.07.031.

Métivier, F., Y. Gaudemer, P. Tapponnier, and M. Klein (1999), Mass accumulation rates in Asia during the Cenozoic, *Geophysical Journal International*, *137*(2), 280–318, doi:10.1046/j.1365-246X.1999.00802.x.

Meunier, P., N. Hovius, and J. Haines (2008), Topographic site effects and the location of earthquake induced landslides, *Earth and Planetary Science Letters*, *275*(3-4), 221–232, doi:10.1016/j.epsl.2008.07.020.

Milliman, J. D., and J. P. M. Syvitski (1992), Geomorphic/Tectonic Control of Sediment Discharge to the Ocean: The Importance of Small Mountainous Rivers, *The Journal of Geology*, *100*(5), 525–544, doi:10.1086/629606.

Molnar, P. (2003), Geomorphology: nature, nurture and landscape., *Nature*, *426*(6967), 612–4, doi:10.1038/426612a.

Molnar, P. (2004), Late Cenozoic increase in accumulation rates of terrestrial sediment: How Might Climate Change Have Affected Erosion Rates?, *Annual Review of Earth and Planetary Sciences*, *32*(1), 67–89, doi:10.1146/annurev.earth.32.091003.143456.

Molnar, P., and P. England (1990), Late Cenozoic uplift of mountain ranges and global climate change: chicken or egg?, *Nature*, *346*(6279), 29–34, doi:10.1038/346029a0.

Molnar, P., and P. Tapponnier (1975), Cenozoic Tectonics of Asia: Effects of a Continental Collision: Features of recent continental tectonics in Asia can be interpreted as results of the India-Eurasia collision., *Science*, *189*(4201), 419–26, doi:10.1126/science.189.4201.419.

Molnar, P., P. England, and J. Martinod (1993), Mantle dynamics, uplift of the Tibetan Plateau, and the Indian Monsoon, *Reviews of Geophysics*, *31*(4), 357–396, doi:10.1029/93RG02030.

Montgomery, D. R., and M. T. Brandon (2002), Topographic controls on erosion rates in tectonically active mountain ranges, *Earth and Planetary Science Letters*, *201*(3-4), 481–489, doi:10.1016/S0012-821X(02)00725-2.

Montgomery, D. R., G. Balco, and S. D. Willett (2001), Climate, tectonics, and the morphology of the Andes, *Geology*, *29*(7), 579, doi:10.1130/0091-7613(2001)029¡0579:CTATMO¿2.0.CO;2.

Morehead, M. (2003), Modeling the temporal variability in the flux of sediment from ungauged river basins, *Global and Planetary Change*, *39*(1-2), 95–110, doi:10.1016/S0921-8181(03)00019-5.

Mouelhi, S., C. Michel, C. Perrin, and V. Andreassian (2006), Stepwise development of a two-parameter monthly water balance model, *Journal of Hydrology*, *318*(1-4), 200–214, doi:10.1016/j.jhydrol.2005.06.014.

National Snow and Ice Data Center. (1999), World glacier inventory. World Glacier Monitoring Service and National Snow and Ice Data Center/World Data Center for Glaciology, Boulder, CO. Digital media.

Nishiizumi, K., M. Imamura, M. Caffee, J. Southon, R. Finkel, and J. McAninch (2007), Absolute calibration of 10Be AMS standards, *Nuclear Instruments and Methods in Physics Research Section B: Beam Interactions with Materials and Atoms*, *258*(2), 403–413, doi:10.1016/j.nimb.2007.01.297.

Norton, K. P., F. von Blanckenburg, and P. W. Kubik (2010), Cosmogenic nuclide-derived rates of diffusive and episodic erosion in the glacially sculpted upper Rhone Valley, Swiss Alps, *Earth Surface Processes and Landforms*, *662*(January), n/a–n/a, doi:10.1002/esp.1961.

Oki, T., and S. Kanae (2006), Global hydrological cycles and world water resources., *Science (New York, N.Y.)*, *313*(5790), 1068–72, doi:10.1126/science.1128845.

Ouimet, W. B., K. X. Whipple, and D. E. Granger (2009), Beyond threshold hillslopes: Channel adjustment to base-level fall in tectonically active mountain ranges, *Geology*, *37*(7), 579–582, doi:10.1130/G30013A.1.

Palumbo, L., R. Hetzel, M. Tao, and X. Li (2011), Catchment-wide denudation rates at the margin of NE Tibet from in situ-produced cosmogenic 10Be, *Terra Nova*, *23*(1), 42–48, doi:10.1111/j.1365-3121.2010.00982.x.

Pandey, M. (1999), Seismotectonics of the Nepal Himalaya from a local seismic network, *Journal of Asian Earth Sciences*, *17*(5-6), 703–712, doi:10.1016/S1367-9120(99)00034-6.

Pandey, M. R., and P. Molnar (1988), The distribution of intensity of the Bihar-Nepal earthquake of 15 January 1934 and bounds on the extent of the rupture zone, *Journal of Nepal Geological Society*, *5*(1), 22–44.

Pandey, M. R., R. P. Tandukar, J. P. Avouac, J. Lavé, and J. P. Massot (1995), Interseismic strain accumulation on the Himalayan crustal ramp (Nepal), *Geophysical Research Letters*, *22*(7), 751, doi:10.1029/94GL02971.

Parker, R. N., A. L. Densmore, N. J. Rosser, M. de Michele, Y. Li, R. Huang, S. Whadcoat, and D. N. Petley (2011), Mass wasting triggered by the 2008 Wenchuan earthquake is greater than orogenic growth, *Nature Geoscience*, *4*(5), 1–4, doi:10.1038/ngeo1154.

Paterson, W. S. B. (1994), *The Physics of Glaciers*, third ed., 494 pp., Butterworth-Heinemann, Oxford.

Pinet, P., and M. Souriau (1988), Continental erosion and large-scale relief, *Tectonics*, *7*(3), 563, doi:10.1029/TC007i003p00563.

Pratt, B., D. W. Burbank, A. Heimsath, and T. Ojha (2002), Impulsive alluviation during early Holocene strengthened monsoons, central Nepal Himalaya, *Geology*, *30*(10), 911, doi:10.1130/0091-7613(2002)030¡0911:IADEHS¿2.0.CO;2.

Pratt-Sitaula, B., M. Garde, D. W. Burbank, M. Oskin, A. Heimsath, and E. Gabet (2007), Bedload-to-suspended load ratio and rapid bedrock incision from Himalayan landslide-dam lake record, *Quaternary Research*, *68*(1), 111–120, doi:10.1016/j.yqres.2007.03.005.

Putkonen, J. K. (2004), Continuous Snow and Rain Data at 500 to 4400 m Altitude near Annapurna, Nepal, 1999 - 2001, *Arctic, Antarctic, and Alpine Research*, *36*(2), 244–248, doi:10.1657/1523-0430(2004)036[0244:CSARDA]2.0.CO;2.

Raymo, M. E., and W. F. Ruddiman (1992), Tectonic forcing of late Cenozoic climate, *Nature*, *359*(6391), 117–122, doi:10.1038/359117a0.

Reiners, P. W., T. a. Ehlers, S. G. Mitchell, and D. R. Montgomery (2003), Coupled spatial variations in precipitation and long-term erosion rates across the Washington Cascades., *Nature*, *426*(6967), 645–7, doi:10.1038/nature02111.

Roe, G. H. (2003), Orographic precipitation and the relief of mountain ranges, *Journal of Geophysical Research*, *108*(B6), doi:10.1029/2001JB001521.

Roe, G. H. (2005), Orographic Precipitation, *Annual Review of Earth and Planetary Sciences*, *33*(1), 645–671, doi:10.1146/annurev.earth.33.092203.122541.

Roe, G. H., D. R. Montgomery, and B. Hallet (2002), Effects of orographic precipitation variations on the concavity of steady-state river profiles, *Geology*, *30*(2), 143, doi:10.1130/0091-7613(2002)030¡0143:EOOPVO¿2.0.CO;2.

Royden, L. (1996), Coupling and decoupling of crust and mantle in convergent orogens: Implications for strain partitioning in the crust, *Journal of Geophysical Research*, *101*(B8), 17,679–17,705, doi:10.1029/96JB00951.

Sadler, P. (1999), The influence of hiatuses on sediment accumulation rates, *GeoResearch Forum*, *5*, 15–40.

Schaffer, J. P., E. E. Small, and R. S. Anderson (1998), Pleistocene relief production in Laramide mountain ranges, western United States, *Geology*, *26*(12), 1150, doi:10.1130/0091-7613(1998)026¡0123:PRPILM¿2.3.CO;2.

Schaller, M., F. von Blanckenburg, N. Hovius, and P. Kubik (2001), Large-scale erosion rates from in situ-produced cosmogenic nuclides in European river sediments, *Earth and Planetary Science Letters*, *188*(3-4), 441–458, doi:10.1016/S0012-821X(01)00320-X.

Scherler, D., B. Bookhagen, and M. R. Strecker (2011a), Spatially variable response of Himalayan glaciers to climate change affected by debris cover, *Nature Geoscience*, *4*(1), 1–4, doi:10.1038/ngeo1068.

Scherler, D., B. Bookhagen, and M. R. Strecker (2011b), Hillslope-glacier coupling: The interplay of topography and glacial dynamics in High Asia, *Journal of Geophysical Research*, *116*(F2), 1–21, doi:10.1029/2010JF001751.

Schumer, R., and D. J. Jerolmack (2009), Real and apparent changes in sediment deposition rates through time, *Journal of Geophysical Research*, *114*, 1–12, doi:10.1029/2009JF001266.

Shrestha, M. L. (2000), Interannual variation of summer monsoon rainfall over Nepal and its relation to Southern Oscillation Index, *Meteorology and Atmospheric Physics*, *75*(1-2), 21–28, doi:10.1007/s007030070012.

Siame, L., et al. (2004), Local erosion rates versus active tectonics: cosmic ray exposure modelling in Provence (south-east France), *Earth and Planetary Science Letters*, *220*(3-4), 345–364, doi:10.1016/S0012-821X(04)00061-5.

Singh, M., I. Singh, and G. Muller (2007), Sediment characteristics and transportation dynamics of the Ganga River, *Geomorphology*, *86*(1-2), 144–175, doi:10.1016/j.geomorph.2006.08.011.

Stewart, I. T. (2009), Changes in snowpack and snowmelt runoff for key mountain regions, *Hydrological Processes*, *23*(1), 78–94, doi:10.1002/hyp.7128.

Stone, J. O. (2000), Air pressure and cosmogenic isotope production, *Journal of Geophysical Research*, *105*(B10), 23,753–23,759, doi:10.1029/2000JB900181.

Summerfield, M. a., and N. J. Hulton (1994), Natural controls of fluvial denudation rates in major world drainage basins, *Journal of Geophysical Research*, *99*(B7), 13,871–13,883, doi:10.1029/94JB00715.

Syvitski, J. (1998), HYDROTREND: A climate-driven hydrologic-transport model for predicting discharge and sediment load to lakes or oceans, *Computers & Geosciences*, *24*(1), 51–68, doi:10.1016/S0098-3004(97)00083-6.

Szulc, a. G., et al. (2006), Tectonic evolution of the Himalaya constrained by detrital 40 Ar - 39 Ar, Sm-Nd and petrographic data from the Siwalik foreland basin succession, SW Nepal, *Basin Research*, *18*(4), 375–391, doi:10.1111/j.1365-2117.2006.00307.x.

Thiede, R. C., B. Bookhagen, J. Arrowsmith, E. R. Sobel, and M. R. Strecker (2004), Climatic control on rapid exhumation along the Southern Himalayan Front, *Earth and Planetary Science Letters*, *222*(3-4), 791–806, doi:10.1016/j.epsl.2004.03.015.

Thiede, R. C., T. a. Ehlers, B. Bookhagen, and M. R. Strecker (2009), Erosional variability along the northwest Himalaya, *Journal of Geophysical Research*, *114*(F1), doi:10.1029/2008JF001010.

Tipper, E., M. Bickle, A. Galy, A. West, C. Pomies, and H. Chapman (2006), The short term climatic sensitivity of carbonate and silicate weathering fluxes: Insight from seasonal variations in river chemistry, *Geochimica et Cosmochimica Acta*, *70*(11), 2737–2754, doi:10.1016/j.gca.2006.03.005.

Tucker, G. E., and R. Slingerland (1997), Drainage basin responses to climate change, *Water Resources Research*, *33*(8), 2031, doi:10.1029/97WR00409.

Turowski, J. M. (2010), Probability distributions of bed load transport rates: A new derivation and comparison with field data, *Water Resources Research*, *46*(8), 1–10, doi:10.1029/2009WR008488.

Turowski, J. M., N. Hovius, A. Wilson, and M.-J. Horng (2008), Hydraulic geometry, river sediment and the definition of bedrock channels, *Geomorphology*, *99*(1-4), 26–38, doi:10.1016/j.geomorph.2007.10.001.

Tustison, B., D. Harris, and E. Foufoula-Georgiou (2001), Scale issues in verification of precipitation forecasts, *Journal of geophysical research*, *106*(D11), 11–775.

Vance, D., M. Bickle, S. Ivy-Ochs, and P. W. Kubik (2003), Erosion and exhumation in the Himalaya from cosmogenic isotope inventories of river sediments, *Earth and Planetary Science Letters*, *206*(3-4), 273–288, doi:10.1016/S0012-821X(02)01102-0.

Viviroli, D., H. H. Dürr, B. Messerli, M. Meybeck, and R. Weingartner (2007), Mountains of the world, water towers for humanity: Typology, mapping, and global significance, *Water Resources Research*, *43*(7), 1–13, doi:10.1029/2006WR005653.

von Blanckenburg, F. (2005), The control mechanisms of erosion and weathering at basin scale from cosmogenic nuclides in river sediment, *Earth and Planetary Science Letters*, *237*(3-4), 462–479, doi:10.1016/j.epsl.2005.06.030.

Wagner, G. A., and G. M. Reimer (1972), Fission track tectonics: The tectonic interpretation of fission track apatite ages, *Earth and Planetary Science Letters*, *14*(2), 263–268.

Webster, P., and L. Chou (1980), Seasonal structure of a simple monsoon system, *Journal of the Atmospheric Sciences*, *37*(2), 354–367.

Whipp, D. M., and T. a. Ehlers (2007), Influence of groundwater flow on thermochronometer-derived exhumation rates in the central Nepalese Himalaya, *Geology*, *35*(9), 851, doi:10.1130/G23788A.1.

Whipple, K. X. (2009), The influence of climate on the tectonic evolution of mountain belts, *Nature Geoscience*, *2*(2), 97–104, doi:10.1038/ngeo413.

Whipple, K. X., and G. E. Tucker (1999), Dynamics of the stream-power river incision model: Implications for height limits of mountain ranges, landscape response timescales, and research needs, *Journal of Geophysical Research*, *104*(B8), 17,661–17,674, doi:10.1029/1999JB900120.

Whipple, K. X., E. Kirby, and S. S. H. Brocklehurst (1999), Geomorphic limits to climate-induced increases in topographic relief, *Nature*, *401*(6748), 39–43, doi:10.1038/43375.

Willenbring, J. K., and F. von Blanckenburg (2010), Long-term stability of global erosion rates and weathering during late-Cenozoic cooling., *Nature*, *465*(7295), 211–4, doi:10.1038/nature09044.

Willett, S. D. (1999), Orogeny and orography: The effects of erosion on the structure of mountain belts, *Journal of Geophysical Research*, *104*(B12), 28,957–28,981, doi:10.1029/1999JB900248.

Willett, S. D., N. Hovius, M. T. Brandon, and D. M. Fisher (2006), Introduction, *Geological Society of America Special Papers*, *398*, vii–xi, doi:10.1130/2006.2398(00).

Wobus, C., A. Heimsath, K. Whipple, and K. Hodges (2005), Active out-of-sequence thrust faulting in the central Nepalese Himalaya., *Nature*, *434*(7036), 1008–11, doi:10.1038/nature03499.

Wobus, C. W., K. V. Hodges, and K. X. Whipple (2003), Has focused denudation sustained active thrusting at the Himalayan topographic front?, *Geology*, *31*(10), 861, doi:10.1130/G19730.1.

Wobus, C. W., K. X. Whipple, and K. V. Hodges (2006), Neotectonics of the central Nepalese Himalaya: Constraints from geomorphology, detrital 40 Ar/ 39 Ar thermochronology, and thermal modeling, *Tectonics*, *25*(4), 1–18, doi:10.1029/2005TC001935.

Wu, S., R. L. Bras, and A. P. Barros (2006), Sensitivity of channel profiles to precipitation properties in mountain ranges, *Journal of Geophysical Research*, *111*(F1), 1–13, doi:10.1029/2004JF000164.

Wulf, H., B. Bookhagen, and D. Scherler (2010), Seasonal precipitation gradients and their impact on fluvial sediment flux in the Northwest Himalaya, *Geomorphology*, *118*(1-2), 13–21, doi:10.1016/j.geomorph.2009.12.003.

Yanites, B. J., G. E. Tucker, and R. S. Anderson (2009), Numerical and analytical models of cosmogenic radionuclide dynamics in landslide-dominated drainage basins, *Journal of Geophysical Research*, *114*(F1), doi:10.1029/2008JF001088.

Yatagai, A., and H. Kawamoto (2008), Quantitative estimation of orographic precipitation over the Himalayas by using TRMM/PR and a dense network of rain gauges, in *Proceedings of SPIE*, pp. 71,480C–71,480C–12, SPIE, doi:10.1117/12.811943.

Yatagai, A., O. Arakawa, K. Kamiguchi, H. Kawamoto, M. Nodzu, and A. Hamada (2009), A 44-year daily gridded precipitation dataset for Asia based on a dense network of rain gauges, *Sola*, *5*, 137–140, doi:10.2151/sola.2009â035.

Yin, A. (2006), Cenozoic tectonic evolution of the Himalayan orogen as constrained by along-strike variation of structural geometry, exhumation history, and foreland sedimentation, *Earth-Science Reviews*, *76*(1-2), 1–131, doi:10.1016/j.earscirev.2005.05.004.

Zech, R., M. Zech, P. W. Kubik, K. Kharki, and W. Zech (2009), Deglaciation and landscape history around Annapurna, Nepal, based on 10Be surface exposure dating, *Quaternary Science Reviews*, *28*(11-12), 1106–1118, doi:10.1016/j.quascirev.2008.11.013.

Zhisheng, A., J. E. Kutzbach, W. L. Prell, and S. C. Porter (2001), Evolution of Asian monsoons and phased uplift of the Himalaya-Tibetan plateau since Late Miocene times., *Nature*, *411*(6833), 62–6, doi:10.1038/35075035.